FACULTY OF SCIENCE
UNIVERSITY OF COPENHAGEN

NIELS BOHR INSTITUTE

How living systems adapt to changing physical environment

Ph.D. Thesis

Mads Kasper von Borries

Supervisor

Mogens Høgh Jensen

Co-supervisors

PóL Martin Bendix

Lene Broeng Oddershede

This thesis has been submitted to the Ph.D. School of the Faculty of Science, University of Copenhagen, on September 1, 2021

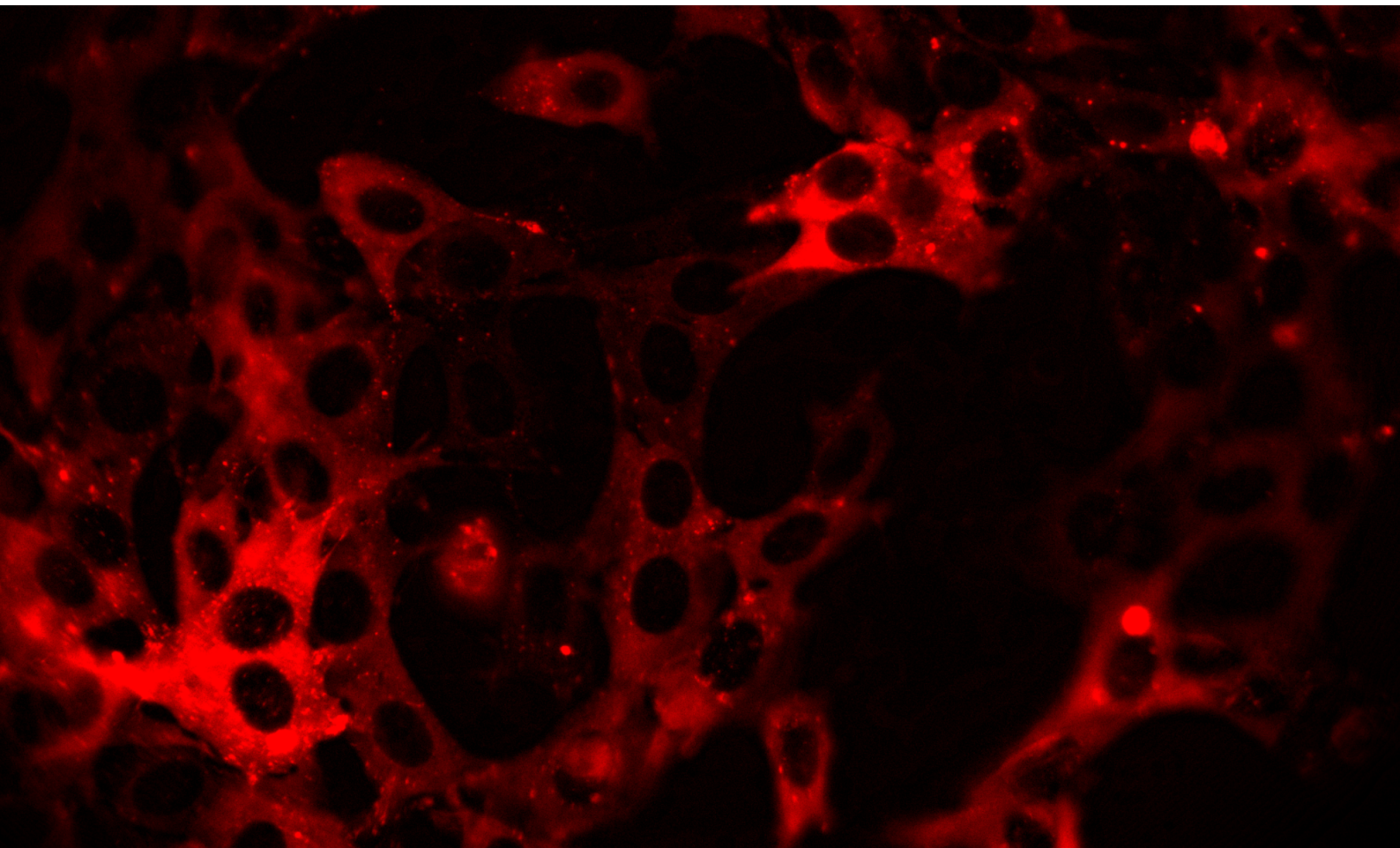

Contents

List of Figures

List of Tables

Acknowledgement

A sincere thanks to my supervisor, Mogens Høgh Jensen, and my co-supervisors, Pól Martin Bendix and Lene Broeng Oddershede. Thanks to Mogens for giving me the exceptional opportunity to do this ph. d. project, to Pól Martin for always being solution-oriented and giving great experimental advice, and thanks to Lene for supporting me with an incredible ability to be both detail-oriented and holistic thinking at the same time.

Thanks to Stanley Brown, whose immense knowledge in biochemistry and experience in the laboratory have helped me overcome many experimental challenges.

I have had numerous great social and academic experiences with the Optical Tweezers group during all these years. For that, I am grateful to all current and former members, of whom many have become my friends.

Thanks to the people in the Center for Models of Life for always spreading joy and for all the unique conversation.

The StemPhys collaboration was a great source of academic inspiration with countless exciting talks. So thanks to the biologists for discussing biophysics with us at the Niels Bohr Institute.

My family and friends have been amazingly supportive during my ph. d. project. I can always count on you, and for that, I am grateful.

A special thanks belong to my wonderful girlfriend and our two fantastic kids. Thinking about the three of you always makes me happy. With you in my mind, I push through when it is tough, and the good moments are even better.

Abstract

The response of living systems to physical cues in the environments is now recognized as a general feature of living systems. The response of living cells to physical factors allows cells to dynamically regulate the expression of genes, which has significant implications in both embryonic development and cellular disorders like cancer. These fascinating features of living cells are investigated here in single cells and in organoids, where the organisms are exposed to changing physiochemical environments, such as temperature variations, stiffness of the surrounding medium, and change in cytokines concentration.

The physical changes applied to the organoid environment were conducted by changing the viscoelastic properties of the organoid surroundings. Matrigel and nutrition medium were mixed in different concentrations, and optical tweezers were then used to quantify the physical properties of this medium. From these measurements, the α-value and the viscoelastic moduli were extracted. The organoids were then exposed to different concentrations in order to correlate changes in physical properties of the medium with morphological changes of the organoids. It was found that as Matrigel concentration increased, the elasticity of the medium increased, and under these conditions, the branching of the organoids increased significantly.

To investigate the cell adaption at a single cell level, Mouse Embryonic Fibroblast (MEF) cells were exposed to various stresses. The cells' stress indicator was the fluorescently tagged transcription factor NF-κB, which serves as a transcription factor for the cellular responses of stress, immune defense, apoptosis, cancer, aging, cell cycle, and proliferation. In order to achieve custom control over the culture and stress conditions, an in-house flow system with a microbioreactor sample was built. This flow system was carefully calibrated to facilitate control of chemical upconcentration over time and allowed for the application of low - and high - drag force experiments. In this assay, MEF cells were exposed to heat stress, 466 nm LED light and high drag forces. The cells were also exposed to a temporary gaseous environment, lack of CO_2, and cell stretching. These experiments showed no sign of NF-κB response, which would have been an indicator of the cells adapting to the changing physical environments.

Contrary, chemical induction of NF-κB pathway resulted in shuttling of this transcription factor between the nucleus and the cytoplasm. Repeated oscillations were sustained for up to 44 hours. Interestingly, it was found that the oscillation period decreased as a function of temperature in accordance with theoretical predictions, presented in this thesis.

0.1. Resumé

I dag betragtes det som en generel egenskab ved levende systemer at de kan tilpasse sig til fysiske ændringer i det omkringliggende miljø. Disse ændringer kan forplante sig helt ind i cellekernen og påvirke hvordan generne reguleres. Denne mekanisme har stor betydning, både under fosterudvikling og ved dannelsen af kræftknuder. I denne ph.d.-afhandling undersøges disse fascinerende egenskaber i både enkelte celler og organoider, hvor de levende systemer udsættes for ændringer i det fysiske og kemiske miljø – det være sig variationer i temperatur, hårdheden af det omgivende medie eller koncentrationen af signalstoffer.

Organoiders reaktion på ændringer i det omkringliggende fysiske miljø blev testet ved at ændre miljøets viskoelastiske egenskaber. Forskellige koncentrationer af Matrigel blev blandet med vækstmedie, og ved hjælp af optiske pincetter blev mediets fysiske egenskaber kvantificeret. Ud fra disse eksperimenter kunne α-eksponenten og de viskoelastiske moduli udvindes. Organoiderne blev derefter udsat for medier med forskellig viskoelasticitet for at korrelere ændringer i mediets fysiske egenskaber med organoidernes morfologi. Når matrigelkoncentrationen blev forøget, sås også en forøgelse i mediets elasticitet, og dette resulterede i at organoiderne forgrenede sig signifikant mere.

For at undersøge enkelte cellers tilpasningsevne til ændringer i det fysiske miljø, blev murine embryonale fibroblastceller udsat for adskillige stresstyper. NF-κB spiller en vigtig rolle i cellers stressrespons, og den regulerer både immunrespons, programmeret celledød, kræft, aldring, cellecyklus og celledeling. NF-κB var tilføjet en fluoroscerende markør, hvilket tillod direkte aflæsning af cellernes stresstilstand gennem live fluorescensmikroskopi. For at opnå præcis kontrol over cellernes kemiske og fysiske miljø blev et flow- og inkubatorsystem bygget in-house. Flowsystemet var nøje kalibreret til at kunne yde både lav og høj friktionskraft, og ydermere til kontrol af en specifik gradvis stigning i mediets signalstofkoncentration over tid. Fibroblastcellerne blev eksponeret for ekstreme temperaturer, 466 nm LED lys og høj friktionskraft. Ydermere blev cellerne udsat for mangel på CO_2 og mekanisk deformering. Ingen af disse påvirkninger resulterede i et NF-κB respons.

Ved kemisk stimulering af NF-κB signaleringsvejen sås oscillation af NF-κB imellem cellekernen og cytoplasma. Oscillationerne var kontinuerlige i op til 44 timer. Efter kemisk stimulering kunne perioden af NF-κB oscillationerne påvirkes ved at variere temperaturen omkring cellerne. Dette stemmer overens med de teoretiske forudsigelser præsenteret i denne afhandling.

1

Introduction to the physical environments of living systems

Living systems are constantly exposed to their surrounding environment. However, what constitutes an environment depends on who is asked. From a chemist's standpoint, the surrounding environment would be described as concentrations of molecules, pH value, and equilibriums. Biologists have for decades resorted to the explanations proposed by chemists in attempting to explain biological phenomena [1]. This has resulted in immense progress in the field of biology, and incredible discoveries have been made. This includes the discovery of genetic engineering of cells, new insight into evolutionary processes, and new types of medical treatments, such as antibiotics and the new gene-editing Crispr Cas9 technology. If a physicist was asked about what an environment constitutes, the answer would likely include properties, such as temperature, pressure, and density. Even though these physical properties are also fundamental biological concepts, their direct impact on living systems has to an extent been neglected in biological research in the late half of the 20th century. During the last couple of decades, however, new insight has revealed that physical factors significantly influence cell behavior, including the biomechanics of cells [2] [3], the morphology of organisms [4], mechanotransduction [5], to more specific findings, such as a change in stem cell differentiation from mechanical cues or geometrical constrains [6] [7]. It is of great scientific importance to continuously explore the impact of physical parameters on the response of living systems, and in particular, how organisms react to perturbations of the

physical environment with respect to their natural conditions.

The direct impact of physical properties in living systems is found in many forms, and in the following, it is reminded that single cells and multicellular organisms will both react to, as well as develop different external physical parameters for specific use-cases. The elastic modulus of blood cells has been shown to affect circulation times, where cells of higher elasticity are being entrapped in organs, while softer cells are bypassing [8]. In this example, organs react to different physical properties of cells and are selective in the cells they capture. However, it is not only multicellular organisms that react to the physical properties of the surrounding. Single cells have been shown to have the same ability since the rigidity of substrates have been shown to direct differentiation and promote proliferation in fibroblast cells [9]. Cells and organs do not only react to different physical properties but also have a wide range of different physical properties themselves. It has been shown that single cells have different elasticity [2] [10] and that red blood cells have an ability to adapt to narrow vessel passages due to their complex viscoelastic properties [11]. The last famous example is our own body consisting of skin capable of withstanding high tensile forces, hard bones, hence having extremely high elasticity, and fluent blood pumping in our veins. With these examples, a story is told of living organisms, both reacting to the physical environment and adapting physical properties for specific purposes - both at the single-cell level and in multicellular organisms.

It is fascinating to test how physical changes in the environment affect the biological response in pancreatic organoids and the NF-κB signaling pathway in mouse embryonic fibroblast (MEF) cells. When pancreas organoids are cultured in an extracellular matrix (ECM), they grow in three dimensions, resembling natural organ development. Changing the physical properties of the environment in this system will give results relevant to multicellular organisms and how environmental changes affect developmental biology. Testing how physical properties affect the NF-κB signaling pathway in MEF cells will give insight into how mature cells are affected and respond via the essential transcription factor, NF-κB.

Organoid research shows a promising future due to its wide applicability as a model system. From one or a few cells being suspended in a 3D culture, they can grow into functioning as model organs and capture essential multicellular and anatomical characteristics [12], and they have even been shown to develop into fully functioning organs [13]. It also serves as a promising candidate for curing diseases, and organ tissue replacement [14]. Organoids are extremely sensitive to the surrounding environment, and the morphology and even cell development are depending on it. Designer matrices have many benefits and have the potential to become an essential tool for organoid research and for medical applications [15]. A vital

aspect of the designer matrices is their physical properties and how these affect organoid growth. This project aims to help answer these questions by providing an in-depth quantification of the most commonly used matrix, the naturally extracted Matrigel, and relate that to how organoids develop when varying the physical properties of the solutions.

To investigate how single cells respond to physical and chemical changes in the environment, the stress response of the NF-κB signaling pathway in living fibroblast cells was tested. NF-κB is an essential regulator of a wide range of stresses. NF-κB has several proteins in its protein family, e.g., p65, the NF-κB protein studied in this ph. d. project. When p65 is activated and in a complex with other NF-κB proteins, it can translocate into the nucleus and regulate genes. The NF-κB family can induce various stress responses, immune responses, cancer responses, aging responses, inflammation responses, and even developmental cues. Regulating this many cellular processes, NF-κB has naturally been proposed as a path to the treatment of many diseases. For example, it has been proposed to treat inflammatory bowel disease by inhibiting an NF-κB dependent signaling pathway [16]. Also, NF-κB regulation is suggested as a treatment of ovarian carcinogenesis [17]. Upregulating NF-κB is generally described as a treatment for cancer due to its pro-apoptotic properties [18], however, it has also been described as a two-sided coin from its cell survival properties [19]. An essential feature of the NF-κB signaling pathway is its ability to oscillate. The NF-κB activation causes translocation into the nucleus, where it upregulates hundreds of proteins. One of those proteins, the IκB, is an inhibitor of NF-κB in the nucleus and will therefore translocate NF-κB back into the cytoplasm. This process is the fundamental mechanism behind the NF-κB shuttling. A better knowledge of how the NF-κB oscillations pathway reacts to stress will improve the knowledge of the signaling pathway as a whole and, therefore, has the potential of helping treat many diseases. In this ph. d. project, numerous different stresses are applied to MEF cells to achieve a deeper understanding of the NF-κB activation and subsequent oscillation.

Experimentation with these two systems will give specific results about how organoids adapt to changing physical environments and how NF-κB is influenced by physical stress, both with and without stimulation from the cytokine TNF-α. However, since these two systems function at different size scales, where one is unicellular and the other is multicellular, it will be possible to assess how living systems of different sizes adapt to physical changes in the environment.

2

Impact of viscoelasticity on organoid morphology

2.1. Introduction

Extracellular matrices (ECMs) have gained increasingly larger interest for research the recent years. A reason being that they can serve as biopolymer scaffolds for three-dimensional cell- and organoid growth. ECMs are primarily made of water, proteins, and polysaccharides. The content of ECMs vary according to the extraction method, where several protocols are used [20] [21] [22]. The ECM affects many functions in the cellular interior as well as its reactions to surroundings. In cell migration, it was shown that the cell preferred to stay in a region of higher stiffness substrate compared to a softer one [23], with theoretical models predicting the sensing of the stiffness of the three-dimensional scaffolds under cell migration [24]. A correlation between elasticity of surroundings and proliferation of invasive breast cancer cells has also been shown, concluding that a higher elasticity will lead to a higher proliferation rate [25]. Furthermore, it was found that breast cancer cells had increased viscosity under the invasion of collagen matrices [26]. These examples highlight the importance of both viscous and elastic properties of the cell media for eukaryotic cells.

The most commonly used ECM for organoid growth is Matrigel [27] [28] [29]. It resembles the basal lamina, and it is secreted by the Engelbreth-Holm-Swarm (EHS) mouse sarcoma cells [30][31] [32]. It consists of more than 1800 peptides, whereas the vast majority of

proteins are Laminin (~ 60 %); Collagen IV (~ 30 %); and Nidogen (~ 2 %), with the remaining being proteoglycans and other proteins. Laminin can withstand high tensile force and is therefore thought to be responsible for a high elasticity of Matrigel, which is thought to be beneficial for three-dimensional organoid culturing [33].

Several techniques have been used to measure the viscoelastic properties of ECMs, including atomic force microscopy (AFM), shear rheology, video microscopy, and optical tweezers. While the first two have their practical limitations, with AFM being confined to primarily topological measurements at the surface of the ECM and shear rheology being too large to measure small forces and local positions inside of single cells. Video microscopy overcomes these issues, however, it is limited to a frequency range below that of optical tweezers. Optical tweezers serve as a reliable source of viscoelasticity measurements in bulk or at the surfaces of ECMs and at a frequency range of up to 50 kHz.

2.2. Theoretical background for optical tweezers

Light can be described as the moving particles, photons, that have a momentum given by $p = h/\lambda$, where h is Planck's constant and λ is the photon wavelength. When a single photon interacts with matter, either the wavelength or its direction has been changed. This causes a change in momentum for both the photon and for the matter of which it has interacted. It is this change of momentum that a bead utilizes when a bead is confined by a laser in an optical tweezers setup, as seen in figure 2.1.

Optical tweezers can simultaneously manipulate and monitor the surroundings of the bead and, therefore, is an excellent tool for scientific experiments at the nano- and micrometer scales. To mention a few, it can use gold nanoparticles to heat local parts of cells [34]; pull tethers from cell membranes [35]; unzip DNA double helix into single DNA strands; measure the exerted force on nano- and microscale objects when pushing and pulling[36]; and measure diffusion, and viscoelastic properties inside living cells [37]. Theory for the two latter will be presented below.

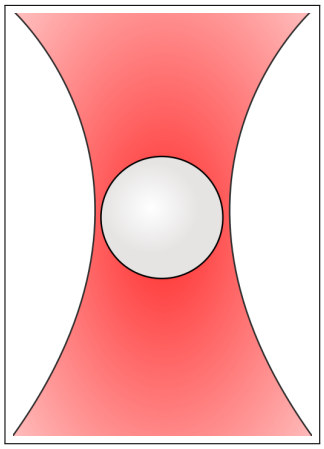

Figure 2.1: Illustration of an optical tweezers trap. Light intensity is illustrated by the red gradient, where the darker red near the center of the trap emphasises the higher light intensity in this region. With the right experimental arrangements, the bead – colored grey in this illustration – is attracted to this region.

The interaction between a bead and a trapping laser beam can be described in two distinct regimes by two theories, namely, Rayleigh scattering and Mie scattering, where the ratio d/λ, where d is the diameter of the bead, determines which theory mainly describes the interaction[38].

Mie scattering describes the refraction that occurs when the di-

ameter of the bead is much larger than the wavelength, $d >> \lambda$.
Here, the momentum exerted on the bead can be understood from the photon changing direction.

When the bead diameter is much smaller than the photon's wavelength, $d << \lambda$, the scattering is described by Rayleigh theory. Here, the medium with the highest refractive index will be pulled towards the highest intensity region of the light. The attracting force is termed the gradient force and is described by

$$\mathrm{F}_{grad} = \alpha \nabla E^2, \tag{2.1}$$

where α is the polarizability of the bead, and E is the electric field of the interacting photons. In the optical tweezers experiments described in this thesis, the diameter of the bead is approximately equal to the wavelength with $d = 960$ nm and $\lambda = 1064$ nm, so in this case, both Mie- and Rayleigh scattering are considerable. However, for a bead to be confined in the optical trap, the force originating from the Rayleigh scattering must exceed the force originating from the Mie scattering. Experiments have shown that the combined forces acting on the bead when $d \simeq \lambda$ are approximately a harmonic potential

$$F = \kappa x, \tag{2.2}$$

where κ is the spring constant that can be found through calibration and x is the distance from the center of the trap. The spring constant is known to be smaller along the direction of the laser beam than perpendicular to it [39].

Following, the theory needed for understanding how physical properties were investigated in this thesis will be presented.

2.2.1. Background for measuring diffusion using optical tweezers

One of the most essential laws of physics is Newton's second law which, for a constant mass, states that the force applied to an object is directly proportional to the mass times the accelerations applied to this object:

$$F = ma = m\frac{dv}{dt}. \tag{2.3}$$

If a particle is inside a medium, it will be influenced by a stochastic force, $F_{random}(t)$, that is caused by heat in the system. This generates particle movement, but when this movement

happens, a drag force

$$F_{drag} = \gamma v, \tag{2.4}$$

where γ is a drag coefficient, is exerted on the particle in the opposite direction of its movement. At low Reynolds numbers, γ can from the Stokes equation be described by

$$\gamma = 6\pi\eta R, \tag{2.5}$$

where η is the dynamic viscosity and R is the radius of the spherical particle. From these assumptions, the Langevin equation, describing the forces acting on the particle, is derived by combining eq. 2.3,2.4, and 2.5:

$$F = 6\pi\eta R v + F_{random}(t). \tag{2.6}$$

The harmonic potential from eq. 2.2 that describes the forces exerted by the optical tweezers is inserted into the equation. A bead trapped inside optical tweezers will have its net forces equal to zero. Hence the equation of motion looks as follows:

$$0 = m\gamma v + \kappa x(t) + F_{random}(t) \tag{2.7}$$

$$F_{random}(t) = m\gamma v + \kappa x(t). \tag{2.8}$$

Using Einstein-Ornstein-Uhlenbeck theory [40], where the stochastic force is described as a Gaussian distribution dependent on the temperature, T, and the noise term, η,

$$F_{random}(t) = (2k_B T\gamma)^{1/2}\eta(t). \tag{2.9}$$

Combining eq. 2.8 and 2.9 the Langevin equation including all terms used for this the following:

$$(2k_B T\gamma)^{1/2}\eta(t) = m\gamma v + \kappa x(t). \tag{2.10}$$

For convenience, some of the symbols in this equation are replaced before taking the Fourier transform in order to eventually find the positional power spectrum. The corner frequency, f_c, is defined as

$$f_c \equiv \kappa/(2\pi\gamma) \quad \Leftrightarrow \quad \kappa \equiv f_c 2\pi\gamma. \tag{2.11}$$

Note that a spring constant, κ, for the optical trap can be found from the corner frequency. The Einstein relation is

$$D = k_B T/\gamma. \tag{2.12}$$

Combining eq. 2.5, 2.11, and 2.12 with the form of the Langevin equation found in eq. 2.10, makes the final Langevin equation before taking the Fourrier transform:

$$v(t) + 2\pi f_c x(t) = (2D)^{1/2}\eta(t). \tag{2.13}$$

The Fourrier transform, $\tilde{x}$, of $x(t)$ is taken:

$$\tilde{x}_k = \frac{2D^{1/2}\tilde{\eta}_k}{2\pi(f_c - if_k)}, \tag{2.14}$$

Here f_k is a frequency of an integer, k [41]. From a Fourier transform, a power spectrum can be calculated as

$$P_k^{(ex)} = |\tilde{x}|^2/T_{msr}, \tag{2.15}$$

where T_{msr} is the time of a measurement. The power spectrum is found to be [42] [43]:

$$P_k^{(ex)} \equiv \frac{D|\tilde{\eta}(t)|^2}{2\pi^2 T_{msr}(f_c^2 - if_k^2)}. \tag{2.16}$$

$\eta(t)$ is approximated as white noise, and $|\tilde{\eta}(t)|^2$ can be described as $\langle \tilde{\eta}_k^* \tilde{\eta}_l \rangle = T_{msr}\delta_{k,l}$. This leaves us with the final expression for the power spectrum:

$$P_k \equiv \left\langle P_k^{(ex)} \right\rangle = \frac{D}{2\pi^2(f_c^2 - if_k^2)}. \tag{2.17}$$

Taking a power spectrum of a bead in a medium can give much knowledge about the system. Fitting this equation can provide the corner frequency, which in eq. 2.11 is showing how the spring constant of the trap can be calculated. Another physical property of a medium that can be calculated is viscoelasticity. In eq. 2.17, if the exponent of f_c is 2, it is assumed that the surrounding medium is purely viscous. If a fit is performed on a power spectrum in the range illustrated in 2.2 with the equation

$$P_k \propto \frac{1}{f_k^{(1+\alpha)}}, \tag{2.18}$$

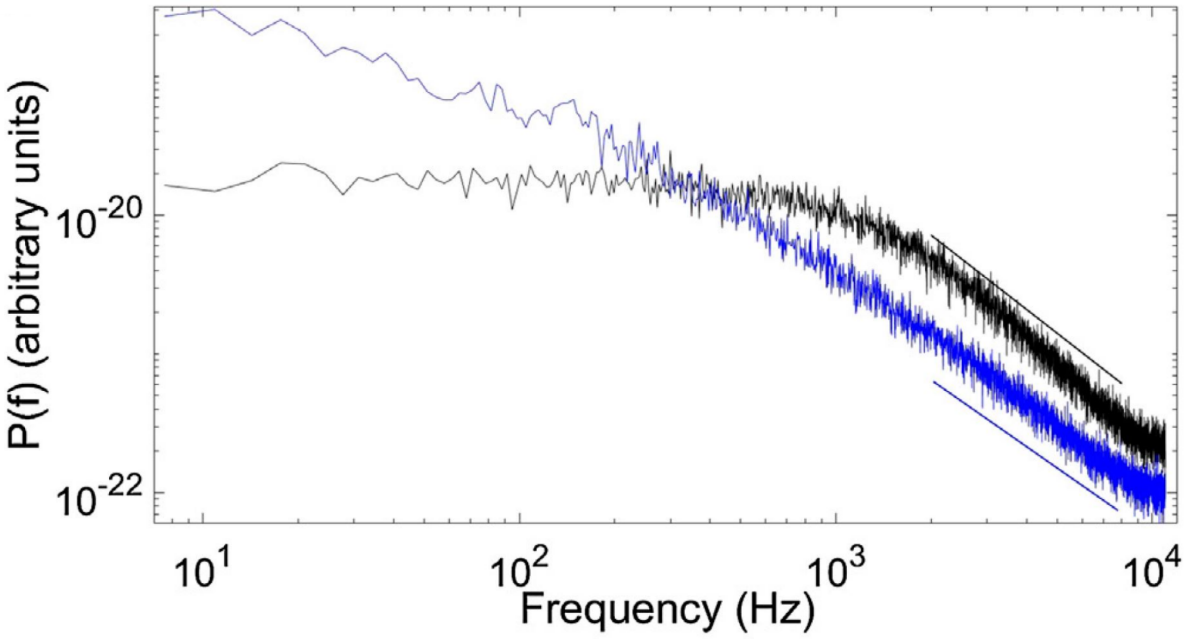

Figure 2.2: Power spectra for a bead in a purely viscous medium in black and a viscoelastic medium in blue. The lines illustrates the range where a fit would give the alpha values.

then an α-value of 1 will correspond to an exponent of two, and the medium undergoes Brownian motion and is purely viscous. If the α-value is 0, the exponent is 1, and in this case, the bead is completely confined in the medium. This means that the surroundings only exert an elastic response and the medium acts like a solid. If the α-value is between 0 and 1, the medium is neither viscous nor solid but both, and is termed viscoelastic [44]. Therefore, it is possible to determine the physical properties of the surroundings of a tracer bead by fitting this equation to the power spectrum of its movements.

However, the physical properties found from the α-value often do not give a fulfilling description of the physical properties. This is because the α-value only gives a measure of how viscous the medium is compared to its elasticity. The method does not quantify the magnitude of the viscous nor of the elastic part of the response. The following derivation will give a method for quantifying the elastic- and the viscous responses of a medium surrounding a bead.

2.2.2. Loss- and storage modulus

When a bead is displaced in a medium, the medium will be displaced as well. The displacement of the medium can be described as a shear strain, $\epsilon = \Delta x/l$, where Δx is the magnitude of the displacement and l is the initial length. See figure 2.3. This displacement requires a force, F, per area, A, that is displaced. This is described by the shear stress, $\tau = F/A$. The

shear modulus, G, describes the relationship between τ and ϵ as

$$G = \frac{\tau}{\epsilon} = \frac{F/A}{\Delta x/l}, \tag{2.19}$$

which makes the shear modulus an essential material property. A viscoelastic material can be described by the frequency dependent complex shear modulus

$$G(f) = G'(f) + iG''(f), \tag{2.20}$$

$G(f)$ where the real part, $G'(f)$ is termed the storage modulus, quantifying the stored energy, and the imaginary part $G''(f)$ is termed the loss modulus, quantifying the energy dissipated in the system.

The Fourrier transform of x(t), $\tilde{x}(f)$, is related to the stochastic force, $F(f)$, by the compliance of the medium [45] [46], $\chi(f) = \chi'(f) + i\chi''(f)$, with the response function

$$x(f) = \chi(f)F(f). \tag{2.21}$$

The compliance of the medium is related to the complex shear modulus through the generalized Stokes-Einstein relation [47]

$$G(f) = \frac{1}{6\pi r\chi(f)}. \tag{2.22}$$

. From here, the complex shear modulus can be divided into storage modulus, $G'(f)$, and loss modulus, $G''(f)$:

$$G'(f) = \frac{1}{6\pi r}\frac{\chi'(f)}{\chi'(f)^2 + \chi''(f)^2} \tag{2.23}$$

$$G''(f) = \frac{1}{6\pi r}\frac{\chi''(f)}{\chi'(f)^2 + \chi''(f)^2}. \tag{2.24}$$

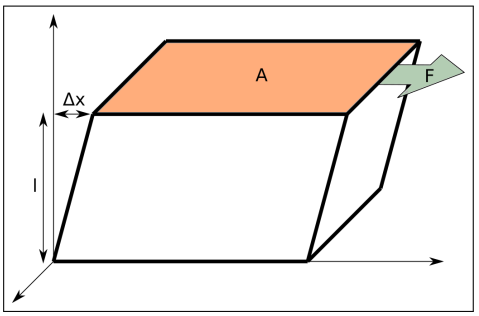

Figure 2.3: Shear stress, τ is exerted in the direction parallel to the orange region, A, which will cause a shear strain, ϵ. Shear strain is given by $\Delta x/l$ and shear stress is given by F/A, while the shear modulus, G is a material property, given by the the ratio of τ/ϵ

Through the fluctuation dissipation theorem, $\chi''(f)$ can be related to the power spectrum, P_k[48] as

$$\chi''(f) = \frac{\pi f}{2k_B T}P(f). \tag{2.25}$$

Using the Kramers-Kronig relation the $\chi'(f)$ is found to be

$$\chi'(f) = \frac{2}{\pi} p.v. \int_0^\infty d\tilde{f} \frac{\tilde{f}\chi''(\tilde{f})}{\tilde{f}^2 - f^2}. \tag{2.26}$$

which means that with this method the viscosity and the elasticity can be quantified through the loss- and storage modulus, respectively.

When using this method, however, the spring constant, κ, and thereby the laser power of the optical trap, should be as low as possible. This will lower the corner frequency, and the fitting range will increase since the fit is conducted on frequencies higher than the corner frequency. When calculating loss- and storage modulus from these equations, values from the power spectrum between the corner frequency and the filtering frequency described in [49] are used.

It can be useful to compare the two moduli, in order to calculate if the loss- or the storage modulus is more dominant. The loss tangent is the ratio

$$\tan(\delta) = G''/G'. \tag{2.27}$$

If $\tan(\delta) < 1$, the loss modulus is larger than the storage modulus and the medium is primarily solid, and if $\tan(\delta) > 1$, the loss modulus is larger than the storage modulus and the medium is predominantly viscous.

With this, a sufficient theory for analyzing optical tweezers experiments has been presented. First, the important α-value was derived. Later, it was shown how passive optical tweezers measurements could be used to obtain the loss- and storage moduli, which are essential to quantify the elastic- and viscous properties of media surrounding a tracer bead. Information about how the tracer bead is fused into the samples and how the optical tweezers setup is built will be given in the following section.

2.3. Materials and methods

Here, an overview of the materials and methods used for the optical tweezers measurements and the organoid culturing experiments is given.

2.3.1. Matrigel and nutrition medium

The Corning Matrigel [28] that was selected for these experiments was the Growth Factor Reduced, Basement Membrane Matrix, Phenol Red-free, LDEV-free ECM. It was mixed with Dulbecco's Modified Eagle Medium/Nutrient Mixture F-12 (DMEM) with Sodium Pyruvate

and Sodium Bicarbonate.

2.3.2. Preparing samples for the optical tweezers

The procedure for creating the sample chambers revolved around keeping the Matrigel at a temperature between 0 °C and 4 °C, since below this temperature, the Matrigel is solid, and above this temperature, the Matrigel becomes gel-like. Chambers consisting of two glass slides sealed with vacuum grease were created. Together with the nutrition medium, it was kept in a refrigerator until it was cooled down to approximately 5 °C. Matrigel was thawed on ice, and when it reached a liquid state, it was mixed with a nutrition medium and a 0.96 μm polystyrene bead solution. The bead solution was less than 1 % of the volume and is considered negligible. The ratio between the nutrition medium and Matrigel was varied as described in the results section. To avoid subsequent heating, pipetting was performed immediately. After that, the mixture was injected into the sample chamber, and the chamber was sealed with vacuum grease. After this, the temperature of the sample would reach room temperature, and for the rest of the experiment, the sample was kept at room temperature.

In order to start measuring immediately after sample preparation, the optical tweezers setup was already prepared by aligning the optical tweezers focus with the focus of the microscope. After samples were inserted, a polystyrene bead was found and trapped by the optical tweezers, as explained in 2.2. Five beads were trapped at each time point for each sample, and three measurements were conducted on each bead.

2.3.3. Organoid experiments

Pancreas progenitors were extracted from dissected mice at E 10.5. By pipetting, mesenchyme was removed. Trypsin 0.5% was used to separate the pancreatic bud into smaller clusters and single cells. These were seeded in solutions of Matrigel and nutrition medium, and the organoids were cultured at 37 °C in three dimensions for seven days.

A Leica AF6000 with HCX PL FLUOTAR 10x/0.30 Ph1 Dry and Leica DFC365 FX cameras were used to obtain images of the organoid. The low numerical aperture and low magnification resulted in images where several organoids were present in each image. The image quality of the organoids was suited for analysis over a relatively long z length.

2.3.4. Organoid analysis

The images for the growth analysis were analyzed in ImageJ by measuring the radius of the organoids. It was assumed that the organoids were circular when measuring the radius, and when calculating the volume, the organoids were considered spherical. This meant that from

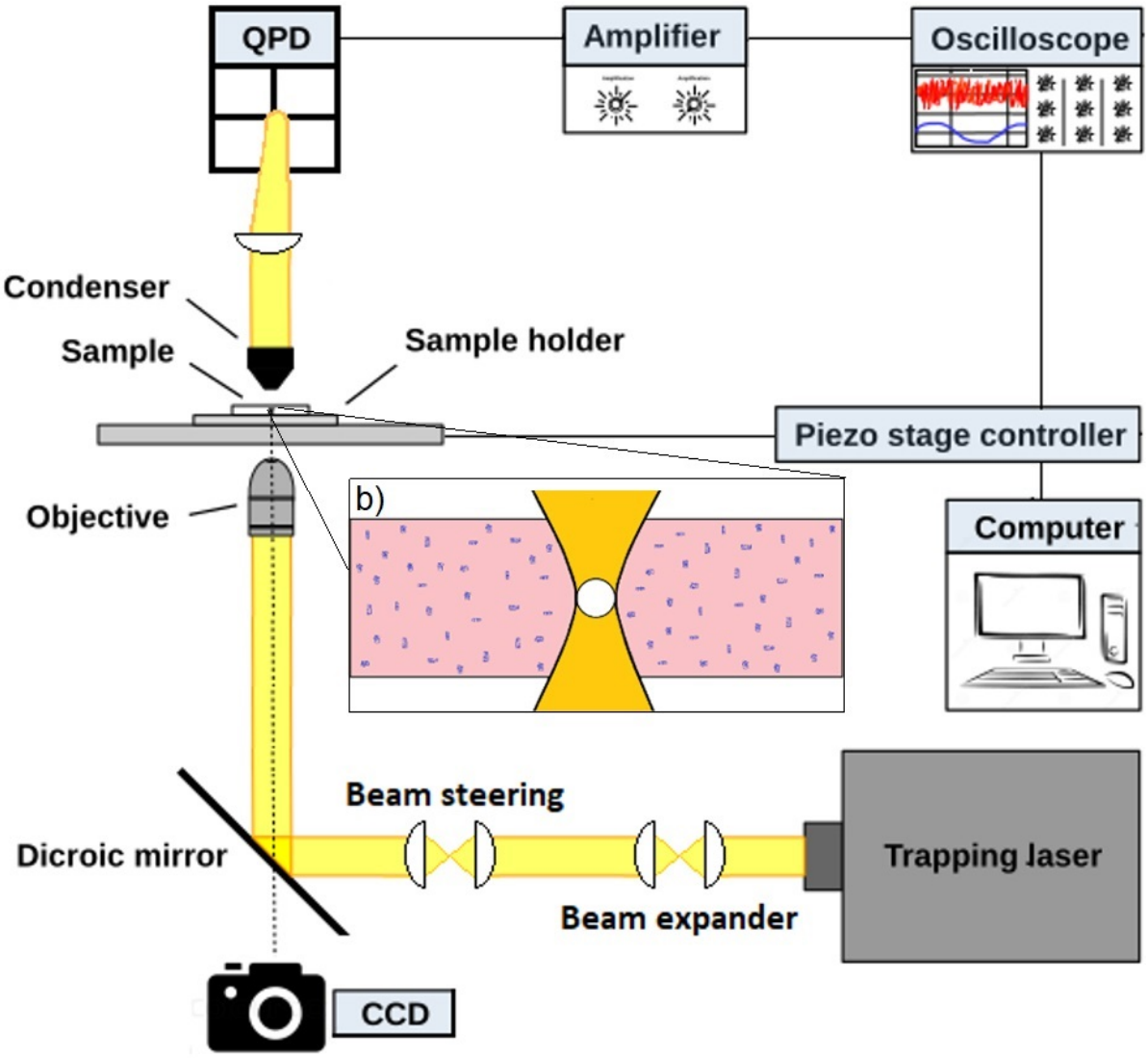

Figure 2.4: Sketch of the optical tweezers setup. A 1064 nm laser is trapping the polystyrene bead inside the sample. The trapping is monitored by a CCD camera connected via the microscope to the computer. The light interacting with the tracer particle is directed onto the QPD, which allows the user to monitor the fluctuations of the tracer article and save the fluctuation on the computer.

the radius measurements, a relative volume growth could be calculated by the radius cubed divided by the radius cubed at day one, r^3/r_{day1}^3.

The branching is calculated by selecting the perimeter of an organoid at its largest cross-sectional area in ImageJ. The perimeter squared was normalized to the area at this cross-section, perimeter^2/area. This means that if an organoid has perimeter^2/area = 4 π, it has no branching at all, and all values above 4 π means that there is some degree of branching. This ratio is independent of organoid size and is larger when an organoid branches more.

2.3.5. Optical tweezers setup

An illustration of the optical tweezers setup is presented in figure 2.4. This allowed for the trapping of the polystyrene bead and measurements in the bulk of the Matrigel samples. In the bottom right if figure 2.4, a 1064 nm laser Nd:YVO4, Spectra-Physics J20-BL10-106Q laser is situated. From here, the laser beam is directed toward a set of beam expander lenses and then to a set of beam steering lenses. Then, the beam is sent into an inverted microscope (Leica, TCS SP5) and reflected on the dichroic mirror, which allows for light to reach the CCD camera (Imagesource, DFK 31AF03) so images of the sample can be captured. The immersion objective (PL APO, NA = 1.2, 63X, w) will narrow the laser beam into its focal point inside the sample. The sample is situated in the sample holder, positioned in the piezo stage (Newport, XY Translation Stage Model M406), which allows for three-dimensional control via the computer. The bead is trapped in the focal point of the laser with an effect of 200-300 mW. After the light has interacted with the sample and, in particular, the bead, it is focused by the condenser, where the light beam is converted into a beam of photons moving in parallel. The beam is then collected by the Hamamatsu, Si PIN photodiode S5981 quadrant photodiode (QPD). The output of the QPD is four voltages that can be converted into the position of the trapped bead, through a series of calibration steps. In these experiments, however, the position need not be known in absolute units since the scaling of the power spectrum versus frequency provides the scaling exponent, α, of interest. The QPD signal is sent to the amplifier and subsequently to the oscilloscope, which allows the user to monitor the fluctuations of the trapped bead. The quantification of the fluctuations of the trapped bead is then sent to the computer as a digital signal.

2.4. Viscoelasticity of Matrigel

Results on how the physical properties of Matrigel vary with concentration were obtained from the viscoelasticity measurements quantified by the α-value measurements and the loss- and storage moduli. These data are then related to organoid growth experiments to see how Matrigel concentration will change organoid morphology.

2.4.1. α-value measurements

In the solutions of Matrigel and nutrition medium, the nutrition medium was assumed to have viscoelastic properties similar to water and hence was assumed to have a constant storage modulus throughout all measured frequencies and an α-value of 1. So when analyzing a mixture of the two with the α-value theory, if the α-value is below 1, and the bead is not

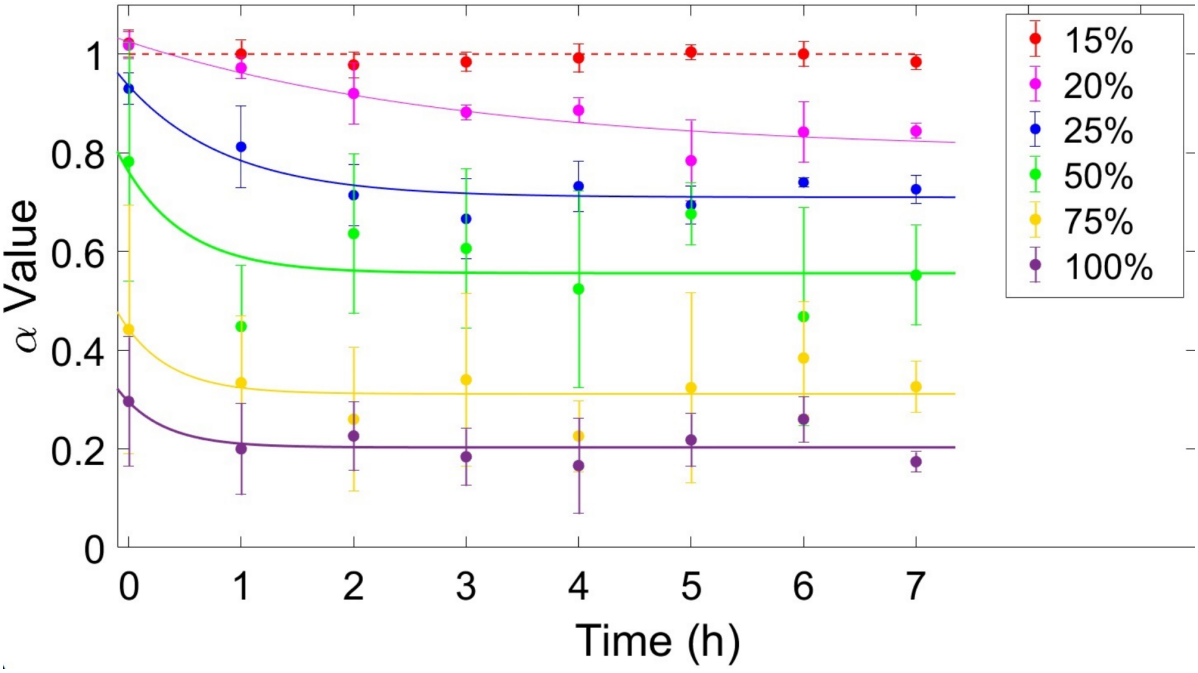

Figure 2.5: α-values as a function of time for different Matrigel concentrations. Purple is 100 % Matrigel; yellow is 75 %; green is 50 %; Blue is 25 %; Magenta is 20 %; and red is 15 % Matrigel. Exponential fits of the α-values are shown with solid lines, while the dotted red line is a linear fit. The exponentially decreasing fits reaches an asymptotic value, α_{final}.

undergoing free diffusion, the elastic properties are assumed to originate from the Matrigel. In figure 2.5, 15 measurements distributed on five beads were conducted for each time point, in the concentration 15 %, 20 %, 25 %, 50 %, 75 %, and 100 % Matrigel with the remaining of the solution being nutrition medium. In the solutions, beads were trapped by optical tweezers, power spectrum analysis was conducted on the signal of the bead movement, and an exponential fit was made from 2 kHz (well above corner frequency) to 8 kHz (well below cut-off frequency for the quadrant photodiode [49]). At t = 0 h the 15 % and 20 % solutions are exposed to free diffusion with an α-value at approximately 1. When increasing the concentration, the α-value decreases and enters the subdiffusive regime. At 100 % Matrigel concentration, the α-value is 0.3 at t = 0 h. For all concentrations except the 15 % Matrigel, the α-value drops over time to a constant value called α_f. Interestingly, at lower Matrigel concentrations, it took longer before α_f was reached. At 20 %, α_f is reached after 5 - 7 h, at 25 %, it is reached after 2 - 3 h, while at the higher concentrations, it is already reached after one hour. As with the initial α-value, α_f also drops with increasing Matrigel concentration. In figure 2.6, α_f is plotted versus Matrigel concentration. It is clearly seen that α_f drops as a function of Matrigel concentration. This result can be used when culturing cells and organoids in three dimensions. In such culture conditions, the living material is suspended in the biological polymer. If an object, such as a bead or an organoid, in the solution, is freely diffusing, and it has a higher density than the Matrigel, it will sink to the bottom. If so, the

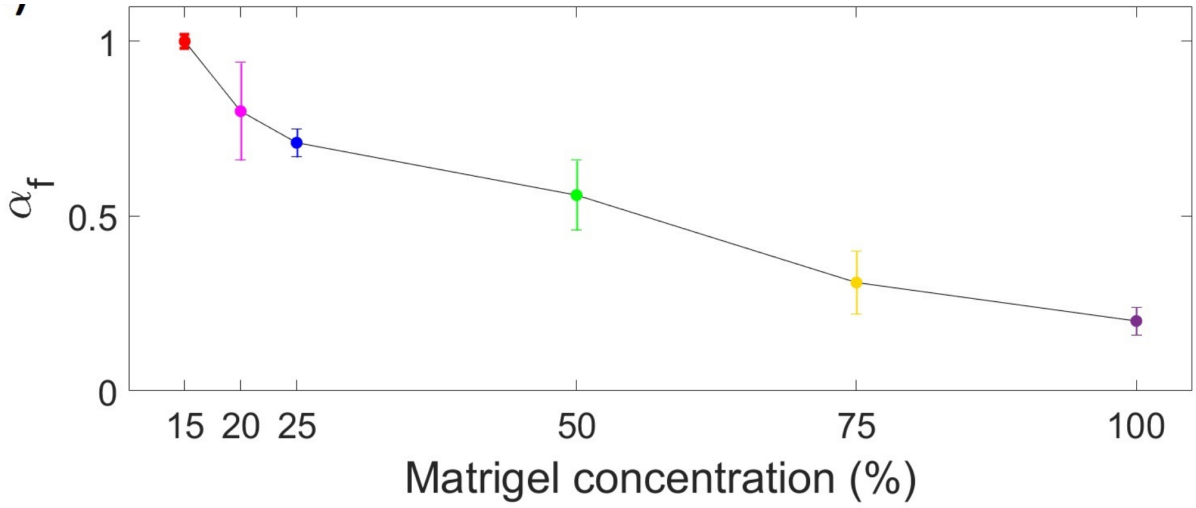

Figure 2.6: α_f is the asymptotic value that the fits in 2.5 are reaching. In the figure, α_f is plotted versus Matrigel concentration, and it is observed that α_f is decreasing when Matrigel concentration is increasing. The tracer particle experiences completely free diffusion at 15 % Matrigel at all times, with an α_f value at 1.00 ±0.02, however at 100 % Matrigel concentration it is close to completely confinement, after the asymptotic value is reached, with an α_f value at 0.2 ±0.04.

three-dimensional culture conditions are unsuccessful, and the organoid will tend to grow along the bottom. When α_f in the figure is at 1.0 in the 15 % Matrigel concentration, this serves to show why three-dimensional culturing in this concentration will most likely fail.

With the α-value measurements clearly expressing that solutions with higher Matrigel concentration will result in a more elastic medium, the next step was to quantify the elasticity and viscosity of the solutions by finding the loss- and storage moduli.

2.4.2. Viscoelasticity measurements of Matrigel

From the equation, 2.23 and equation 2.24 the loss- and storage moduli, G' and G", were calculated for trapped tracer beads in water. The results are plotted in figure 2.7. For a bead trapped in water, elastic part ,G', will originate from the trap [48] and the viscous part, G", will originate from the water. The storage modulus is constant throughout most frequencies and is found to be 6.57 ± 0.9 Pa. This value is essential for determining the storage modulus of Matrigel since this value will be included in the Matrigel measurements. To calculate a storage modulus from the optical tweezers measurements, this storage modulus then has to be subtracted. In the plot, the theoretical value of G" is plotted. Note that it increases as a function of frequency. When G" was extracted for water in these experiments, there is a strong correlation with the theoretical prediction. This shows that the measurements are reliable and that the system gives the expected loss modulus.

With the value for the strength of the optical trap and the knowledge that G" is correctly quantified in water, viscoelasticity experiments were initiated. The viscoelasticity was measured for the following solutions: 20 %, 25 %, 50 %, 75 %, and 100 % Matrigel. In figure 2.8

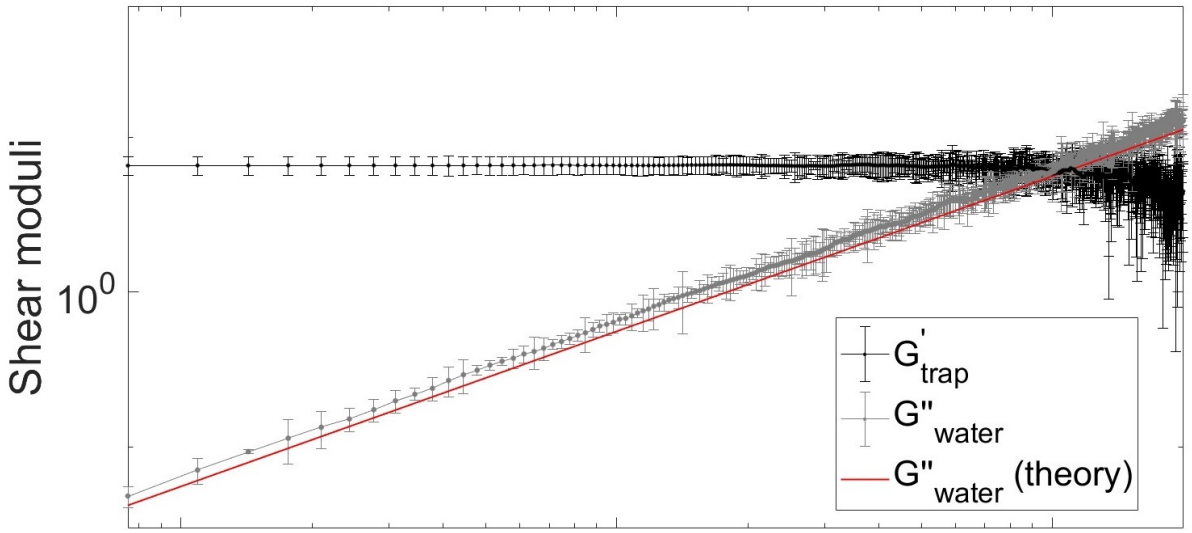

Figure 2.7: Shear moduli for water. Black dots are storage modulus originating from the optical trap, and grey dots are loss modulus versus frequency. The red line is the theoretical loss modulus of water, which is in agreement with the data.

A), the storage modulus for the solutions is presented. For all concentrations, the storage modulus increases as a function of frequency. This is expected for a viscoelastic material, and as in the results for α-value, it is confirmed that the mixtures of Matrigel and nutrition medium are viscoelastic. When the concentration increases, the total level of the storage modulus also increases. Again this supports the α-value experiments in that a higher Matrigel concentration will increase the elastic response. In figure 2.8 B) the loss tangent tan(δ) is plotted versus frequency for the same concentrations as in A). If tan(δ) $=G''(f)/G'(f) < 1$, the behavior of the medium is solid-like. If tan(δ) > 1, the behavior of the medium is fluid-like and if tan(δ) = 1 the medium has equal fluid-like and solid-like properties. In B), it can be seen that tan(δ) increases as a function of frequency. This means that G" increases relative to G' even though G' also increases versus frequency, as seen in A). For all frequencies tan(δ) is dominated by viscous forces for the 20 % Matrigel solution, while for the 100 % Matrigel solution, the medium is dominated by elastic forces until the end of the measured frequencies and first crosses over with tan(δ) > 1 at approximately 1750 Hz. This cross-over frequency is plotted versus Matrigel concentration in the inset in B). When the Matrigel increases, the cross-over frequency increases. This means that the higher the Matrigel concentration, the larger range of frequencies the medium is solid-like, which is expected from the other experimental result addressing the physical properties of Matrigel.

By this, the viscoelastic properties of Matrigel were adequately quantified. The next step would be to see how these changing physical properties in the surrounding environment of the organoids would affect organoid morphology.

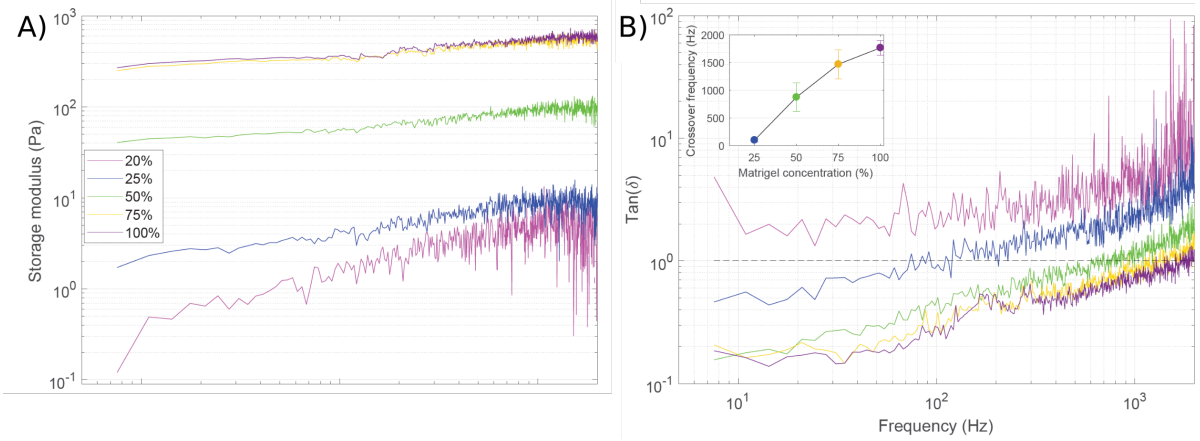

Figure 2.8: A) storage modulus as a function of frequency for different concentrations of Matrigel. At all measured frequency values, the storage modulus increases with Matrigel concentration until a Matrigel concentration at 75 %. From this concentration, the storage modulus has approximately equal values when increasing the Matrigel concentration to 100 %. B) Tan(δ) for the same Matrigel concentration as in A) is plotted versus frequency. A dotted line at one illustrates that when below this Tan(δ) value, the solutions are primarily solid, while the solution is primarily liquid above this Tan(δ) value. Notice that the 20 % Matrigel concentration is primarily liquid at all measured frequencies, while the 100 % Matrigel concentration is solid at the vast majority of measured frequencies. In the insert, the cross-over frequency is plotted. The frequency value at which the solution is primarily liquid increases as a function of concentration.

2.4.3. Organoid culture experiments

Organoid experiments were conducted to investigate how the changing physical properties of changing Matrigel concentrations would affect the organoid morphology. In figure 2.9 A) the growth of three organoids in 25 %, 50 %, and 75 % at day 2, 4, 5, and 7 after seeding at e10.5. It can be seen how the organoids increase their volume as well as starting branching over time. Notice here that the organoids in 25 % Matrigel has dropped to the bottom of the three-dimensional culture, which results in cells growing along the surface in the background of the image at day 7. In order to quantify the volume growth in the organoid experiments, the relative growth r^3/r^3_{day1} was calculated with number of measurements, n = 12, n = 33, and n = 29, for the 25 %, 50 %, and 75 % Matrigel concentrations, respectively. The results are plotted in figure 2.9 A) where the growth for the different solutions is evident. When applying Student's t-test on the differences across volume growth for different Matrigel concentrations, the populations were not shown to be different. In B), the branching of the organoids was quantified with a measure of perimeter^2/area at days 4 and 7. D'Argostino tests of the individual distributions showed that several of the six populations in figure B) was not normally distributed. Therefore, Mann-Whitney U tests were conducted to quantify the differences in the populations. It was shown that already at day 4 the populations of 50 % and 75 % Matrigel were significantly different, with more branching in the 75 % Matrigel concentration. On day 7, there was a significant difference in branching between organoids grown at 50 % compared to those grown at 75 % and a significant difference between 25 % and 75 % with a higher degree of branching at higher Matrigel concentrations.

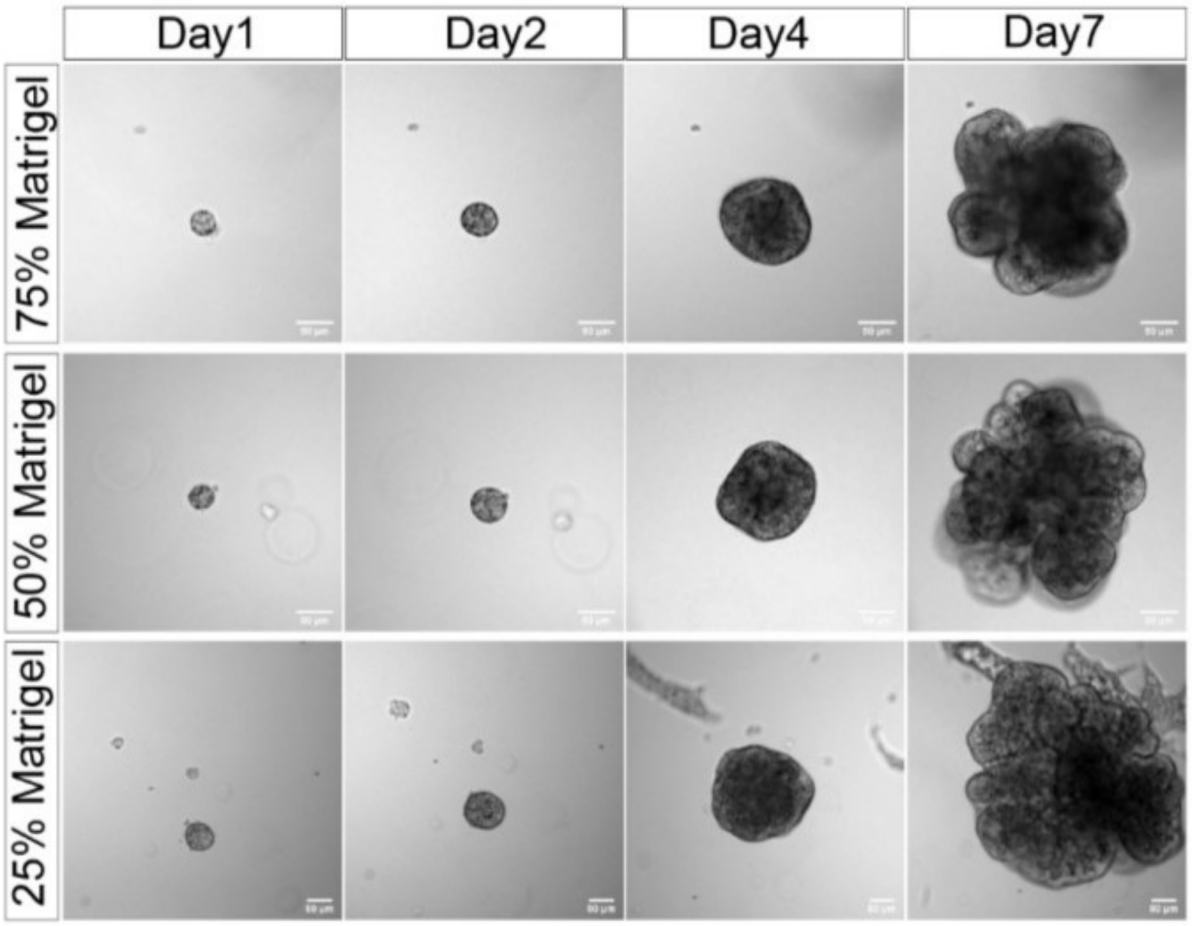

Figure 2.9: Pancreatic organoids cultured after E 10.5 Matrigel concentration of 25 %, 50 % Matrigel and 75 % Matrigel. The experiments were performed by Siham Yennek at DanStem at the Panum Institute. Images are captured on days 1; 2; 3; and 7, after E 10.5. On days 1 and 2, the organoids look the same across the different Matrigel concentrations. On day 4, more branching is observed in the organoid in the 75 % Matrigel concentration than in the 25 % and 50 % on day 4. On day 7 the 50 % organoid in the 50 % Matrigel concentration shows more branching than the one in 25 %, while the organoid in the 75 % Matrigel solution shows more branching than both.

When these results are compared to the physical properties of Matrigel from the optical tweezers experiments, there is a clear tendency. When increasing the elastic properties of Matrigel, measured by decreased α-value, increased storage modulus, and decreased $\tan(\delta)$, the organoids are branching more. However, despite different physical properties across the Matrigel solutions, the overall volume of the organoids did not change significantly. From these results, it can be speculated that once an organoid has penetrated a region of the Matrigel, it can expand more easily in that direction, which will result in increased branching in higher Matrigel concentrations.

2.5. Conclusion

It was proved possible to quantify the viscoelastic properties of Matrigel with both power spectrum analysis and with calculations of loss- and storage moduli. The measured loss modulus

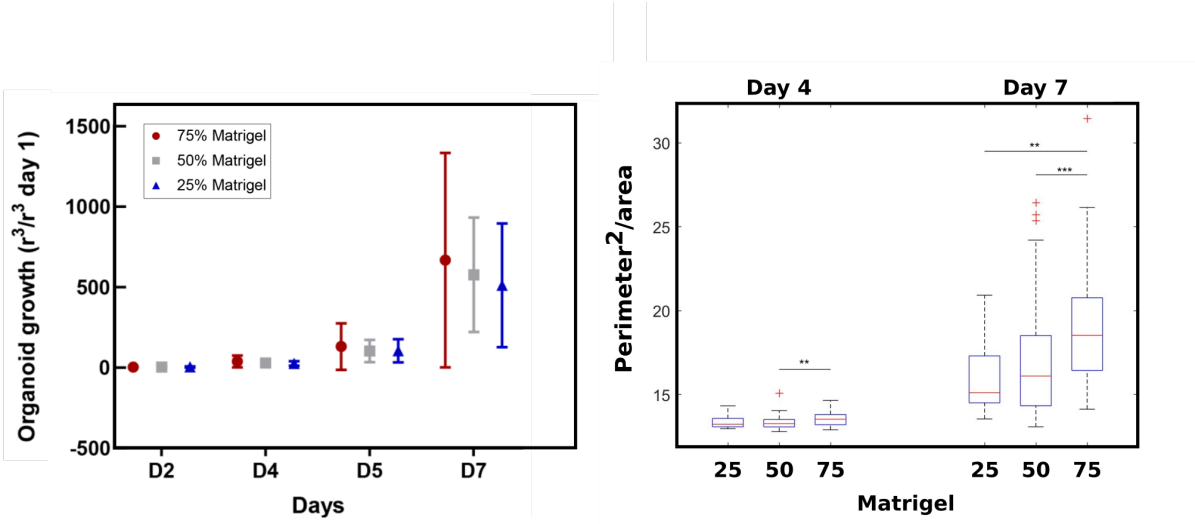

Figure 2.10: A) Organoid volume growth at days 2; 4; 5; and 7 after being seeded at E 10.5 on day 1. Growth of organoid is calculated by r^3/r^3_{day1} with error bars of one standard deviation. Red circles are data for organoids grown in 75 % Matrigel, while data for 50 % Matrigel is grey squares, and data for 25 % Matrigel is blue triangles. No statistical differences were measured with Student's t-test, and the number of organoids used for the analysis is 12; 33; and 29 for the 25%, 50%, and 75% Matrigel, respectively. B) Branching of organoids calculated from the same image data as in A). On day 4 the organoids in 75 % Matrigel concentration show significantly more branching than the organoids in 50 %. At day 7 the organoids in 75 % Matrigel are branching significantly more than the organoids in the % Matrigel concentration while branching significantly more than in the 25 % Matrigel concentration solution. The number of organoids used for analysis is 12; 66; and 49 for 25%; 50%; and 75% Matrigel, respectively, with each experiment conducted twice.

was compared to the theoretical values, and it was found that there was a high correlation. This technique makes it possible to extract detailed information of physical properties in the bulk of some types of biological samples.

The power spectrum experiments showed that the α-values decreased when Matrigel concentration increased and thereby that the samples had become more elastic. Furthermore, it was shown that the α-values decreased over time and reached a final value after between 1 and 7 hours. At higher Matrigel concentration, the final α-value was reached earlier.

It was found that a higher degree of polymers in a sample, controlled by a higher Matrigel concentration, caused the sample to have increased elasticity. Also, it was shown that the storage modulus increased as a function of frequency, however, from the tan(δ) it was revealed that the viscosity increased even more.

Tests of organoid growth in different Matrigel concentrations showed that the branching was significantly increased in higher Matrigel concentrations after growing in these conditions for 4 to 7 days. It was also shown that varying the Matrigel concentration did not impact the volume growth of the organoids.

The results in this section serve as important tools for bioengineering artificial growth matrices. The physical properties of a naturally extracted matrix, Matrigel, were analyzed in detail, and these findings were then related to organoid morphology to understand what effects the physical properties have. It was found that physical change in the environment

would affect this multicellular organism and that an active adaption by the organoids was accomplished.

3

The flow system

In biophysical experiments, the ability to engineer experiments from the bottom up can be beneficial. This allows experimentalists to design equipment with the exact properties needed for specific experiments and thereby remove constraints that companies have added to their products to generalize for a broader user base.

Initially, this project aimed to create TNF-α oscillations in the experiments. To create continuously changing waveforms, it was clear that this could only be achieved with a flow system. Though there were many flow systems to choose from on the market [50] [51] [52], it was estimated that non had the software necessary for truly creating flow functions without limitations. Therefore it was decided that a part of this project would be to build a flow system, where both software and hardware were developed in-house.

This experimental setup will then be used for a range of different stress experiments on the MEF cells to test how these, via their NF-κB signaling pathway, are adapting to physical changes in the environment.

In the following explanation on how the hardware of the flow system was designed, how the software was built, how culture conditions were improved until the flow system was capable of support cell growth for weeks, a collective overview of the final flow setup, and then finally, the flow kinetics and the upconcentrations of chemicals injected into the flow system is given.

3.1. Hardware of the flow system

In collaboration with Axel Boisen from the technical department at the Niels Bohr Institute, the hardware of the pumps was designed. At this time, the aim was to make the pumps as versatile as possible, and so, the following criteria were pursued: To fit as many syringe sizes as possible, to fit as many syringe brands as possible, to have resolution down to nL scale while being able to extremely high drag forces on cells, and to be programmable by a computer.

For those purposes, it was decided that this pump would be a displacement pump contrary to the alternative, a pressure-driven pump. The two final designs are seen in figure 3.1. All 3D printed parts are made from a hard polymer. The pumps consist of a 3D printed bottom piece, where rails (sliding bars) and a ball screw (linear actuator) are attached. 3D printed slots of hard polymer for a wide variety of syringes are mounted onto one side. One pump was designed with a single syringe slot, and one was designed with double syringe slots. When a syringe is in use, a 3D printed pushing module pushes the plunger of the syringe. This pushing module slides on the sliding bars and is displaced by the rotating ball screw. On the opposite side of the syringe slot, a 3D printed module for holding the stepper motor is attached. The stepper motor[53] is mounted onto this piece and connected to the ball screw. Each stepper motor step is executed after a signal is sent from a connected Phidgets PCB. The Phidgets PCB is connected to a power outlet and a computer via a USB cable. Through the Phidgets PCB, the computer allows for the programming of the stepper motor.

A stepper motor functions by changing the magnetic field of electromagnets, causing a permanent magnet to move one step. In order to know how the velocity of the stepper motor translates into the volume of displaced medium per time, the following is calculated:

Each step is 1.8 °, excluding the built-in gearbox. The Phidgets PCB[54], in combination with the stepper motor, have rotational resolution of $1/16$ of a step, called 'fine steps' in the following calculations. So rotation per fine step is

$$\frac{1.8\frac{\text{degrees}}{\text{full step}}}{360\frac{\text{degrees}}{\text{rotation}}} \cdot \frac{1}{16}\frac{\text{full step}}{\text{fine step}} = \frac{1}{3200}\frac{\text{rotation}}{\text{fine step}}. \tag{3.1}$$

And so, the number of fine steps necessary for the motor to rotate once is

$$1 \text{ rotation} = 3200 \text{ fine step}. \tag{3.2}$$

The rotation of the stepper motor translates into the movement of the 3D printed pushing module through the ball screw. The connection between the ball screw and the stepper motor

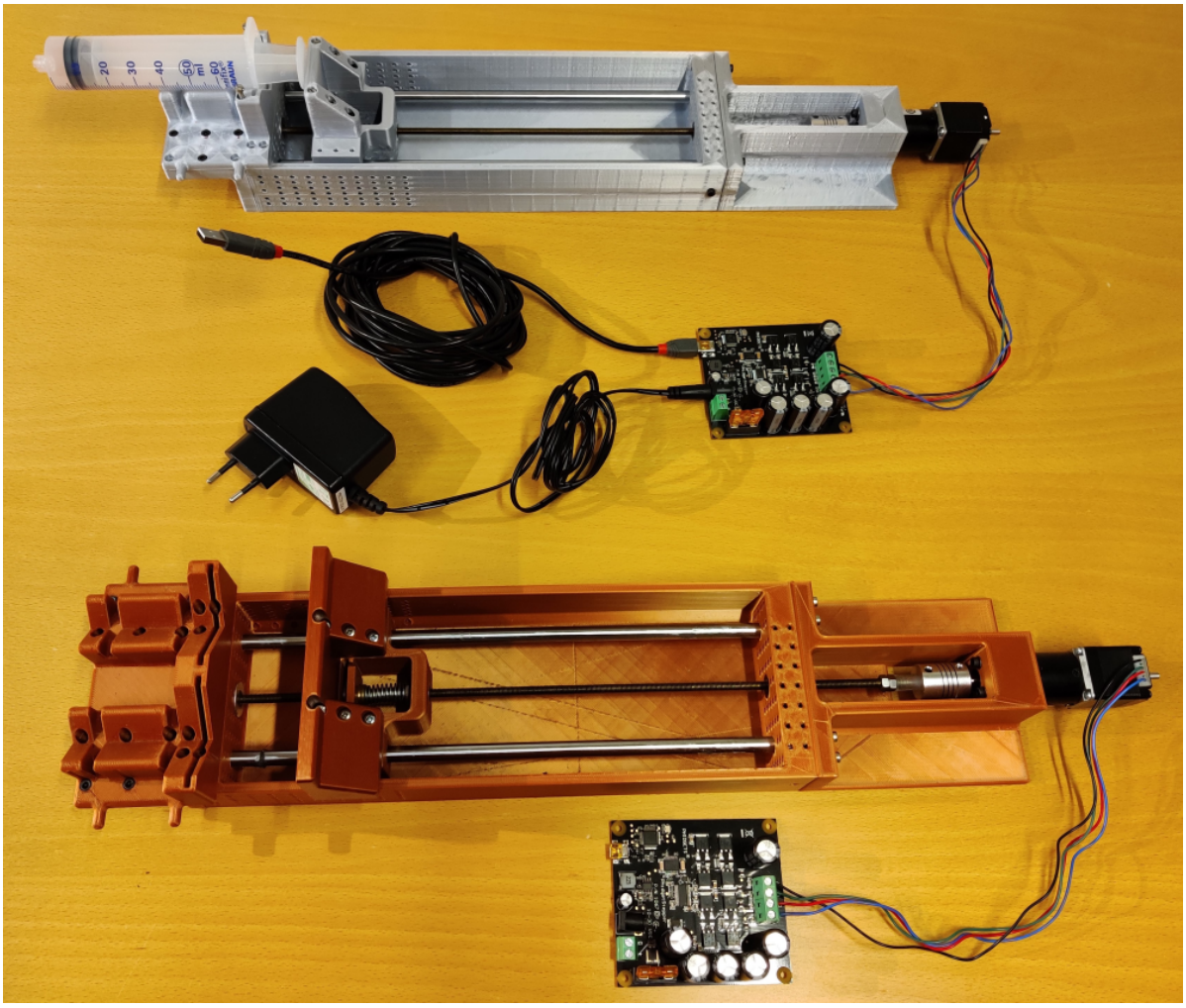

Figure 3.1: Two in-house build pumps were used for flow experiments. Each pumps consists of a Phidget PCB, stepper motor with gearing 1:100, bottom 3D print, metal rails, and 3D printed pushing module. The top pump is made from silver-colored polymer, it has a single syringe slot, and on the photo, its PCB board is connected to a USB cable and a power cable. The bottom pump is a cobber-colored polymer, it has two syringe slots, and its PCB is not connected to any cables on the photo.

goes through a 100:1 gearbox. Moreover, it is known that for every 8 mm the ball screw has 10 threads, so the relation between fine steps and displacement of the pushing module is

$$100\frac{\text{rotation}}{\text{thread}} \cdot \frac{10}{8}\frac{\text{thread}}{\text{mm}} \cdot 3200\frac{\text{fine step}}{\text{rotation}} = 4.00\text{E}5\frac{\text{fine step}}{\text{mm}} = 4.00\text{E}8\frac{\text{fine step}}{\text{m}}. \tag{3.3}$$

Throughout these experiments a 60 ml syringe was used and in this calculation the dimensions of this syringe is used. Since the cross sectional area of the tube determines the volume traveling into the flow system per time, it should be noted that the size of the syringe can serve as an extra gearing, where using syringe with a larger cross sectional area will increase the volume per time flowing into the system and vice versa. In this syringe the cross sectional area was calculated to be 6.15 E-4 m^2. So the volume displaced per fine step is calculated

to be

$$\frac{6.15\mathrm{E}-4\mathrm{m}^2}{4.00\mathrm{E}8\frac{\text{fine step}}{\mathrm{m}}} = 1.54\mathrm{E}-12\frac{\mathrm{m}^3}{\text{fine step}} \Rightarrow 1.54\frac{\mathrm{nL}}{\text{fine step}}. \tag{3.4}$$

These numbers are tested and confirmed by relating measured rotations of the thread to the output flow volume. The motor was capable of rotational velocity between 1 fine step/s and 4000 fine steps/s, which means that the hardware could perform the desired tasks since it was capable of injecting in both nL range and µL range. The velocity could be set from a computer, which meant that the hardware of the pump was completed. An extra pump was built to mix chemicals later in the flow system and allow for oscillating chemical concentration.

3.2. Software of the flow system

The aim of the pump-controlling software was to allow for simultaneous movements of the two pumps and also for each one to move independently. When the software was built, it was expected that two different kinds of flow patterns would be needed. One flow with a constant speed is followed by another constant speed. This would allow for chemicals to reach the sample relatively quickly, and then, subsequently, a low flow speed could be exerted to lower drag force while keeping the chemicals at a constant level, or a high flow speed could subsequently be applied to exert a high drag force. The other flow pattern that was desired would first have a constant flow speed, which would be followed by an oscillating flow speed, following a waveform. Hence, the software was developed to create these flow speed patterns.

Labview, a graphical programming language, was chosen for the hardware programming due to its intuitive user interface and because this program specializes in hardware programming. The final version of the software is presented in figure 3.2. The Labview VI, where the actual programming takes place, is seen as the many boxes connected by wires. In the bottom left corner, the user interface, which in Labview is called the Front Panel, is inserted. In the following, a brief description of how the program works is given.

As seen in the Front Panel, there are separate controls for each pump. For each pump, the flow speed of an 'Initial Constant Flow' is set for a specific time span. Underneath that control, the oscillating flow is set. Here, the total duration of the oscillating flow is set. The amplitude is specified by setting the maximum and minimum values of the waveform, where the wave's minimum value can be negative and positive. The period is set to be any value much larger than 1 second since this is the time resolution of the velocity change. Lastly, the starting phase is also specified.

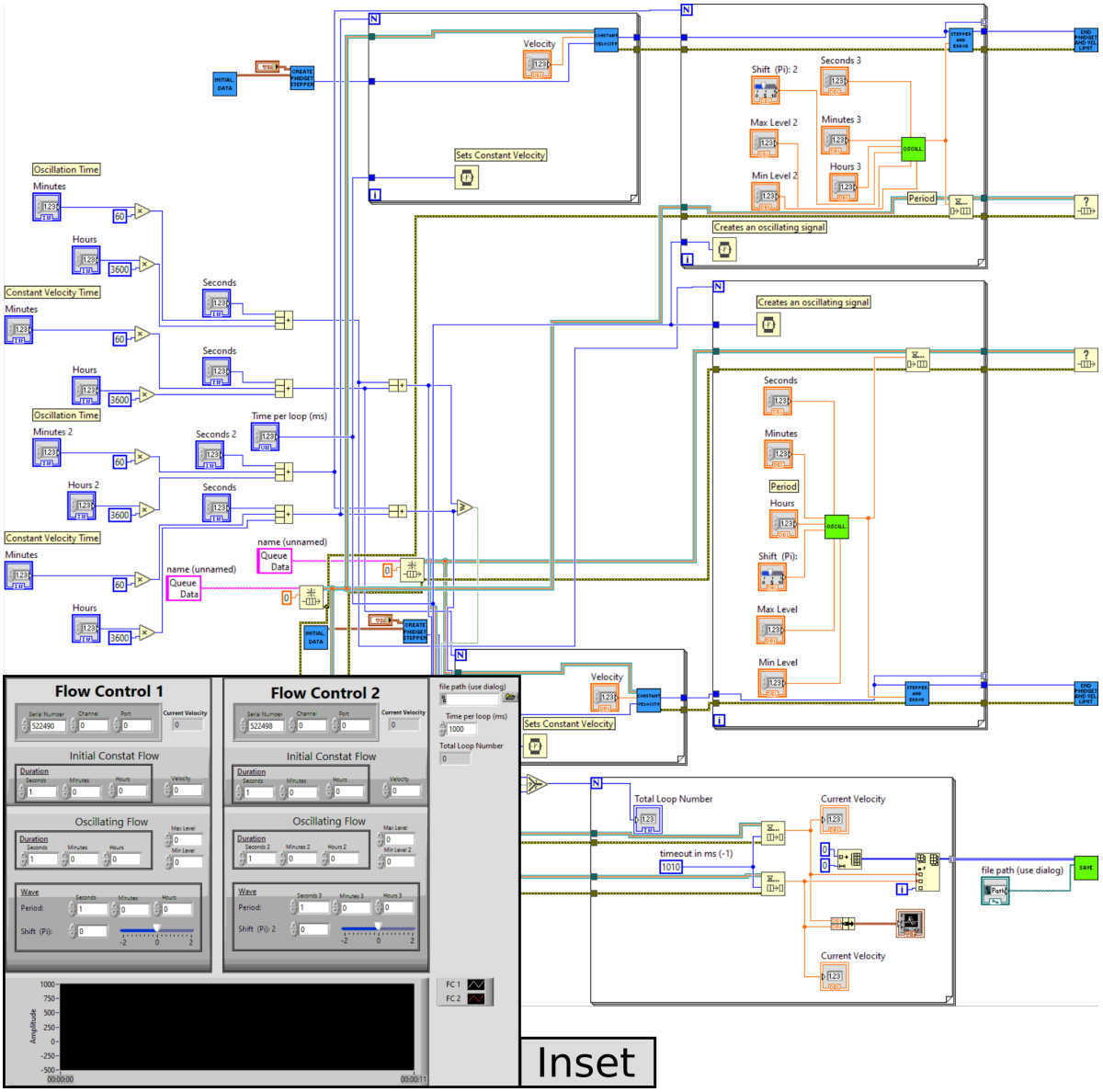

Figure 3.2: Labview software created for chemical oscillations, capable of controlling two syringes simultaneously (a) Front panel where flow conditions specific to a given experiment are preset. Flow Control 1 and Flow Control 2 control pump 1 and pump 2, respectively. Each pump has a sequence consisting of an initial flow at a constant flow rate, followed by a flow of oscillating velocity. In the initial phase, the length of the signal and stepper motor velocity can be preset. In the oscillating flow phase, the duration of this phase, the minimum and maximum values of the amplitude of the stepper motor velocity, the period, and the phase can be preset. In the top right corner file path is set. Beneath that, 'Time per loop' gives the time resolution of the waveforms. Beneath that, a 'Total Loop Number' counts the total number of velocity changes of the oscillating pumps. At the bottom, the velocity waveforms of stepper motors are shown. (b) The VI block diagram is programmed to allow for the functions described in (a).

The image behind the inset is the actual program. Here, information is sent from left to right, and each little box in the program represents one or more functions. All of the dark blue and bright green boxes contain several other boxes and were built for this program. In the left-most part of the program, several blue boxes function as inputs from the front panel, where the time durations for the different flow patterns are set. Towards the right, there are 5 large boxes with black edges surrounding many small boxes. Each of these is a loop with repeated actions. The two furthest to the left - one partly behind the Front Panel and one in the center top, are where the pump is performing constant flows. The CONSTANT VELOCITY and the OSCILL. boxes are where the actual instructions are sent to the Phidget PCB, which initiates the pump.

After the hardware and the software were built, the flow system was tested. As it turned out, it was very challenging to keep cells alive in the microbioreactor. Extensive initial experiments needed to be made before cells would thrive. In the following, steps taken to improve culture conditions, and especially to reduce gas formation, are described.

3.3. Improving flow culture conditions

When the flow setup was built, preliminary experiments of water flowing at room temperature showed that liquids could flow through the flow system. It was decided to start flow experiments with cells growing in a flow chamber [55] with culture medium being injected. However, it turned out that an extensive and essential task was imminent before the flow system could be utilized: To avoid cell necrosis in the flow system.

3.3.1. Necrosis and flow at the JuliStage setup

To perform flow experiments in a well controlled atmosphere and at well controlled temperatures, it was decided to insert the flow system into an incubator. For those experiments, the Juli stage [56] was utilized, which is a compact fluorescence microscope, small enough to be situated inside of an incubator. This is meant to give the advantage that CO_2 level, humidity, and temperature can be controlled more precisely. Initial experiments by the Juli Stage performed in the Nuaire CO_2 incubator at 37 °C were then initiated. However, it was soon realized that cell death and gas formation would occur. During the first experiments, it was difficult to separate these two phenomena since most mammal cells will die if they are not surrounded by a liquid culture medium, and the two phenomena occurred approximately simultaneously. Within few hours, the entire flow chamber would at some point have been filled up with gas. For each bubble entering the flow chamber, the majority of cells would be swiped away in the direction of the flow. Furthermore, those remaining would be visibly dam-

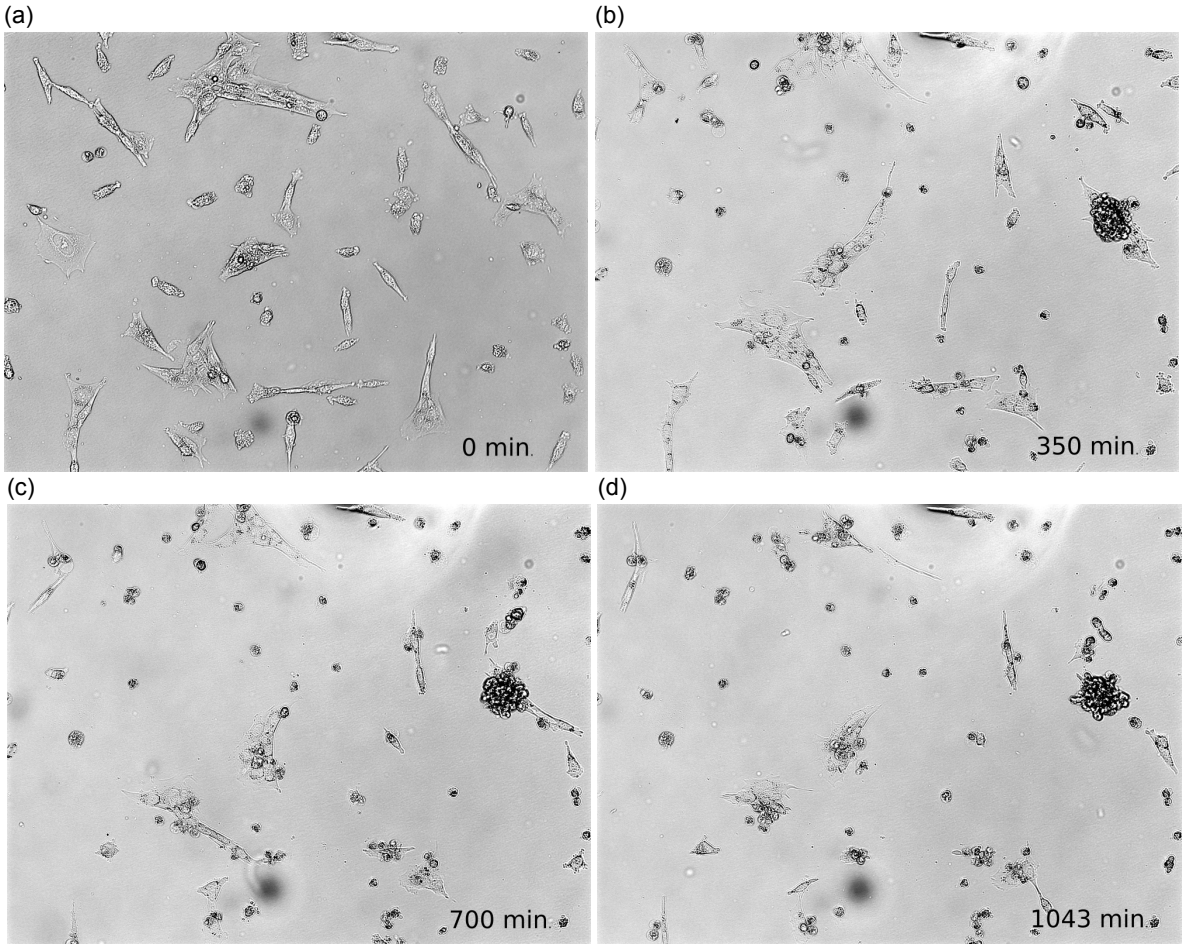

Figure 3.3: LED with 466 nm excitation wavelength is used in the JuliStage setup at the lowest power available. The bright-field images are captured at t = 0 min.; t = 350 min.; t = 700 min.; and t = 1043 min. At t = 0 min. the cells look healthy and are attached to the substrate. As time progresses, the number of cells undergoing necrosis is increasing, and after t = 1043 min., cells were unable to recover.

aged. However, before the bubbles entered the chamber, cells already showed preliminary signs of cell injury by contracting and becoming spherical, separating from each other and detaching from the surface. Since it was suspected that more than one variable was causing cell death, the eminent task would be to separate the variables and solve them sequentially. To eliminate variables originating from the flow that caused cell death, experiments in micro dishes were performed, where culture and image conditions could be examined. In the following, the measures are taken first to prevent cell death in micro dishes, and secondly, to prevent bubble formation in the flow system.

Cells underwent necrosis, and it was suspected that the 466 nm excitation lamp and emission wavelength at 525 nm in the JuliStage setup were causing DNA damage to an extent where cells could not recover. To test if the 466 nm excitation was causing necrosis, experiments in µ-wells were performed, where the cells were only exposed to the 466 nm excitation. Besides the light exposure, cell were cultured in otherwise normal conditions

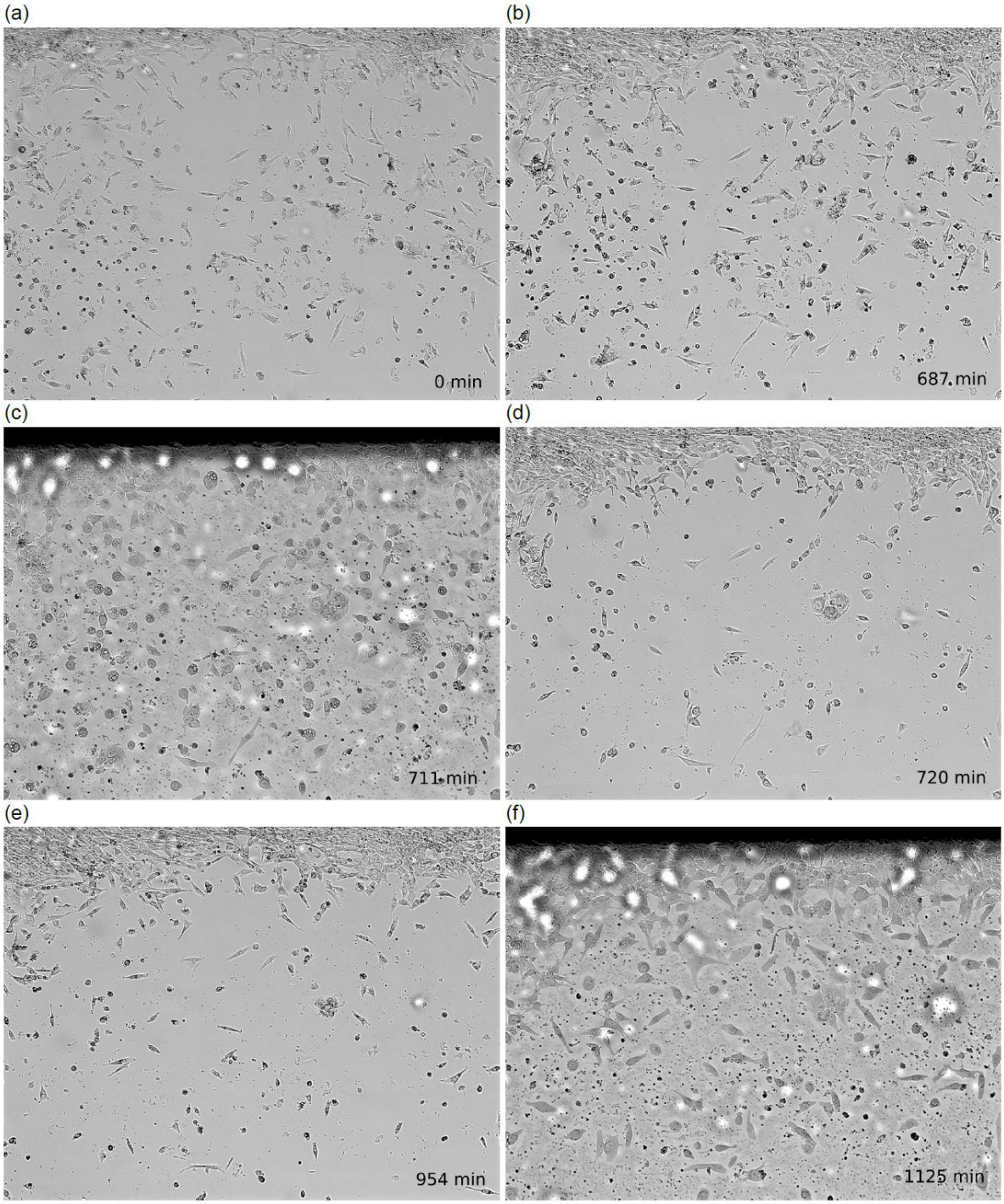

Figure 3.4: Fibroblast cells in the JuliStage, exposed to gas built-up in the flow chamber, causing decreasing confluency. At t = 0 min. cells look healthy. At t = 687 min. the cells have increased confluency, which is a clue that cells are living in a healthy environment. At t = 711 min. the field of view is filled with gas. At t = 720 min., only 33 min. after cells showed signs of increasing confluency, the substrate in the field of view has approximately halved its confluency. At t = 954 min. the sample is similar to the previous image, and in the last image at t = 1125 min., cells are again exposed to gas. Each time a bubble passes the cells, the confluency decreases, and the probability of cells undergoing necrosis increases.

(a)

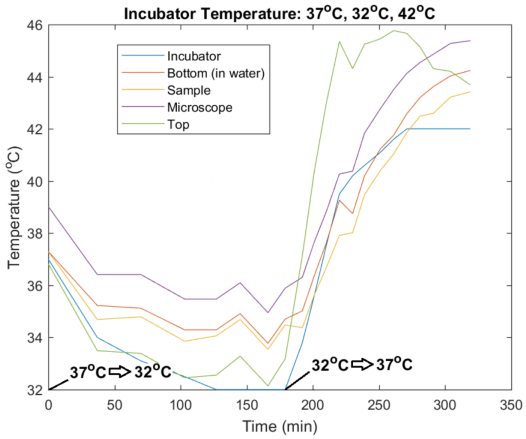

(b)

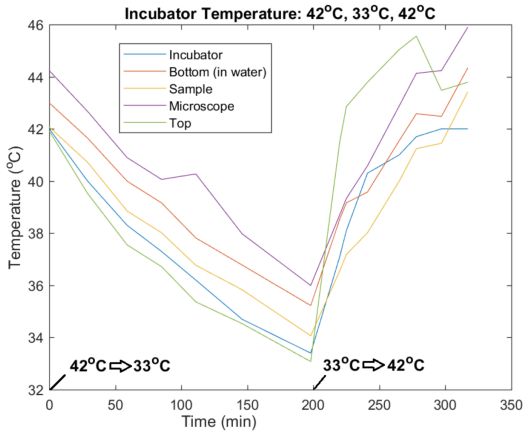

Figure 3.5: Temperature experiments in incubator with JuliStage microscope recording inside. Throughout the experiment the incubator temperature is set to different values. During the experiments the temperature at five different positions are recorded: 'Incubator' is the value that the incubator is set to, 'Bottom in water' is the thermometer in the water bath in the bottom of the incubator. 'Sample' is a thermometer inserted into a micro dish with 3 ml of water. 'Microscope' is a thermometer attached in close proximity with the LED lamp on the microscope. During the experiment images are taken at full excitation power with an exposure time of 1.0 second every 10 minutes. a) 24 hours prior to the experiment the incubator is set to 37 °C. At t = 0 min. the incubator is set to 32 °C. At t = 180 min. temperature is set to 42 °C. b) 24 hours prior to the experiment the incubator is set to 42 °C. At t = 0 min. the incubator is set to 37 °C. At t = 200 min. temperature is set back to 42 °C.

with medium [57] as described in the methods section 4.6.1, 37 °C, and 5 % CO_2. The results are presented in figure 3.3. The lowest possible excitation power is presented here at arbitrary level 1 out of 20 provided by the JuliStage setup. At t = 0 min, the cells appear flat and attached to the surface of the µ-dish. As time progresses, at t = 350 min. and at t = 700 min., the cells detach from the surface and start to change shape from flat to more spherical. At t = 1043 min. most cells are completely spherical. After these experiments, the cells were unable to recover. These results were compared to results where the 466 nm excitation lamp was absent. This was initially tested in µ-wells. Throughout the experiment, cells would spread out, multiply, become spherical, and undergo necrosis. After the µ-well experiments showed that this excitation would cause cell death, the experimental setup was changed back to the flow system. An example of this is seen in figure 3.4, where images are captured with both red LED light with excitation wavelength at 543 nm and emission wavelength at 580 nm and bright field. Between the images in A) at t = 0 min. and B) at t = 687 min., the cells are spreading out and multiplying. This is a time interval approximately equivalent to the time span in figure 3.3 A) to C) at 700 min. These figures show two out of many examples of cell necrosis when using the 466 nm excitation lamp, and cell division and a general thriving cell culture when this was absent. From this, it is concluded that the 466 nm excitation lamp causes necrosis.

The problem of necrosis prior to the gas formation of the chamber was then solved. How-

ever, designing a setup that did not produce gas turned out to be an extensive task. In figure 3.4 B), at t = 711 min, the area of the flow chamber imaged by the microscope is completely filled up with gas. In D), the field of view again only contains medium, but here the amount of cells compared to B) is much less, despite the time span from B) to D) is only 33 min. This means that the gas bubble that passed through the chamber mechanically removed cells. In E), at t = 954 min., no bubbles have passed the chamber since D). The remaining cells do not seem to spread out and multiply but instead shown early signs of necrosis. In figure F) the chamber is again filled with gas. After this time point, cells were not able to recover. Several similar experiments showed that the fibroblast cell culture could not withstand frequent exposure to gas, and the cells would eventually undergo necrosis. Also, while the chamber is filled with gas, the bright field- and fluorescence images have too poor quality to be used for data analysis. This meant that the gas formation problem would have to be solved in order to use the flow setup.

Through several flow experiments on the JuliStage, where the gas formation problem was worked on, it was clear that the task was larger than first anticipated. At this time, it was still unclear whether the incubator containing the JuliStage would allow for fast and precise temperature variation. It was realized that it would be a risk to spend time solving the gas formation problem in this setup without knowing if the temperature control would be acceptable. Therefore, it was decided to test this before the gas formation problem was solved.

3.3.2. Temperature in the incubator during fluorescence microscopy

Cells affected by heat stress is a major part of this project. So, it was necessary to find a method to control heat precisely and conveniently and change the temperature in time intervals ranging from minutes to days, with temperatures ranging from 32 °C to 42 °C for persistent temperature variation experiments and up to 45 °C for heat shock experiments. One method investigated was to control the heat by a Nuaire CO_2 incubator[58] with a Juli^{TM} Stage fluorescence microscope situated inside [56]. Using this method was advantageous considering its culture conditions, high humidity, precise control of CO_2, and temperature. Also, the time it takes to heat up and cool down the incubator is important since this will affect the experimental productivity and hinder certain experiments. To test this, two experiments where the incubator temperature was set to specific values and changed twice during a time span of 350 minutes. In figure 3.5 A), the temperature was stable at 37 °C for several days, then 32 °C, and finally 42 °C. In figure 3.5 B) the temperature was stable at 12 hours at 42 °C, then changed to 33 °C, and just before reaching that temperature, it was set to 42 °C.

(a) (b)

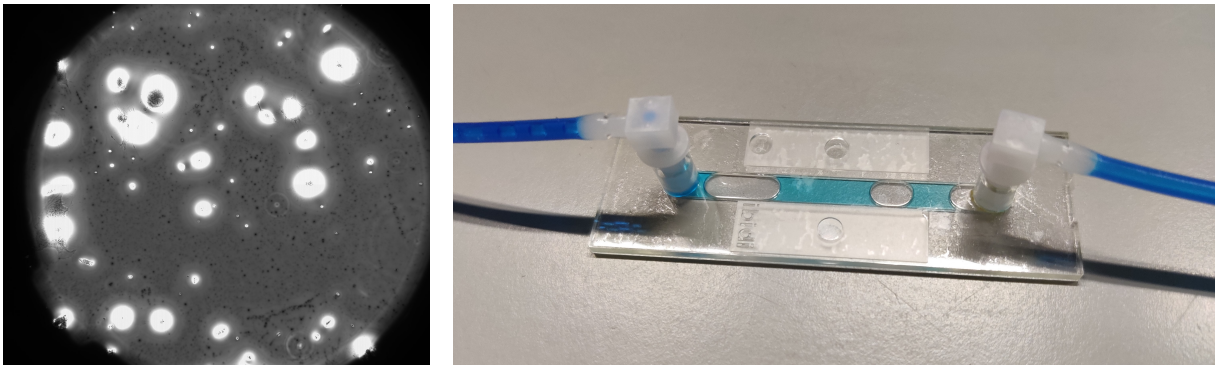

Figure 3.6: Gas formation in flow system. a) Bright-field image of a sample with gas formation. Prior to the bubble entering the chamber, fibroblast cells were thriving in the culture medium. At the time of the captured image, the part of the sample where the image is taken is completely filled with gas. b) Flow slide with gas formation forming bubbles in the order of magnitude of millimeters. The liquid in this sample is water with methylene blue for illustrative purposes.

Four multi-meters with connected thermocouplers were calibrated using ice baths to achieve 0.0 °C and boiling water to achieve 100.0 °C. A concern was that the microscope LED would heat the sample while conducting experiments. Therefore one thermocoupler was inserted into a µ-dish with 3 ml of water. This would monitor how a cell sample would change the temperature during heat experiments. Other thermocouplers were inserted into the water bath in the bottom of the incubator, taped onto the ceiling of the inside of the microscope, and attached in close proximity to the LED on the microscope. In 3.5 a) and b) the temperature is set to 37.0 °C and 42.0 °C 24 hours before the experiment starts. At this time all measured temperatures inside the incubator were within 0.2 °C of the incubator temperature, except the temperature measured close to the LED, in both experiments, and except for the thermocoupler in the water bath in figure 3.5 b). In figure 3.5 a) the temperature in the sample was 34.2 °C when the incubator reached 32.0 °C which is a difference at 2.2 °C. When heating up the incubator by setting the temperature to 42.0 °C, the sample temperature would reach 43.4 °C and thereby overshoot by 1.4 °C. In figure 3.5 b) when decreasing the temperature from 42.0 °C to 32.0 °C, the difference between the incubator temperature and the sample temperature was less significant, reaching a maximum difference at 1.2 °C. Again, the temperature was increased from 32.0 °C to 42.0 °C, but this time from another initial condition. Again the sample temperature would overshoot with 1.4 °C, and likely even higher had the experiment continued.

These results proved it difficult to use the incubator as a method of varying temperature during experiments for several reasons. First, when cooling down from 37 °C to 32 °C, the sample will cool down slowly and have an elevated temperature when the incubator reaches its target temperature. Secondly, if the influence of heat shock of the cells is tested, it takes 100 min to cool down, meaning that cells will be exposed to heat stress for much longer than

Experiments that failed to reduce bubbles	
Experiment	**Possible reason for reducing bubbles**
Decreasing flow velocity	- Reduce turbulence - Adjust to heat
Straightening tubing	- Reduce turbulence
Decreasing LED power	- Reduce heat
Changing LED color	- Reduce heat
Changing from culture medium to water	- Culture medium might be more prone to develop gas - Gas from respiration of non-visualized micro organisms
Experiments that succeeded in reducing bubbles	
Increasing height of input and output	- increasing pressure in the sample - increasing pressure in tubing before sample
Degassing medium before use	- remove submicroscopic gas bound in medium
Inserting bubble trap	- removing large bubbles prior to sample
Gas permeable tubing	- letting gas escape from tubing under high-pressure
Medium at near peak temperature before bubble trap	- larger bubbles form before bubble trap - enables bubble trap to extract bubbles

Table 3.1: Overview of experiments that failed or succeeded in reducing bubbles, caused by gas formation inside the system.

intended, which would likely cause necrosis. Thirdly, the possibility of oscillating temperature in the same timescale as NF-κB shuttling was considered. A full NF-κB shuttling period can be down to less than 60 minutes, meaning that both heating and cooling of the incubator would be too slow for creating a 1:1 coupling between temperature fluctuations and NF-κB fluctuations.

The setup consisting of the JuliStage inside the Nuaire ES NU-5710 incubator was concluded to be inadequate for the temperature variation experiments that were to be performed in this project. Hence, it was decided to move the experiments and the flow system to a Nikon Eclipse TI[59], where a Warner temperature controller, to control the heat inside the Oko gas Incubator[60], would be attached to the microscope stage.

3.3.3. Gas formation and necrosis at the Nikon Eclipse microscope

From the first experiments on the Nikon Ecplipse TI microscope, it was clear that the problem of gas formation in the flow system was still present. Moreover, the problem of cell necrosis had returned.

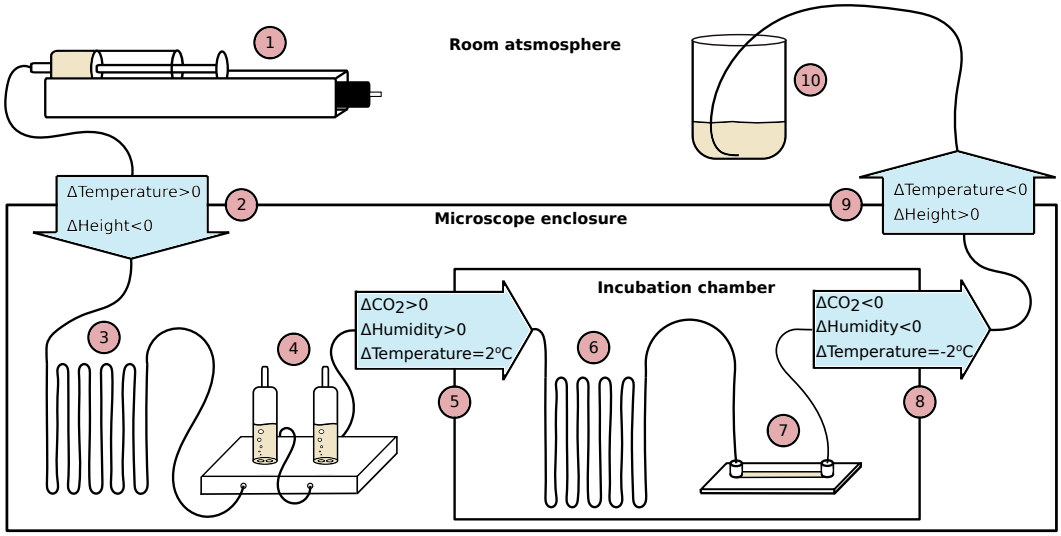

Figure 3.7: Schematic of flow system with numbers indicating the order that the medium flows through the system. Gas permeable silicone tubing is represented by a solid line. 1) Pump injects medium into the system at a rate controlled by a computer via Labview software. 2) medium flows into the microscope enclosure. Medium changes temperature from room to target -2.0 ^{o}C and changes from the starting height to the same level as all other devices inside the microscope enclosure (ΔHeight ~ -40 cm) 3) 1.0 m of extra tubing lets the medium reach target temperature -2.0 ^{o}C before entering the bubble trap. 4) Two bubble traps are capturing excess gas in the tubing. 5) Medium enters the incubation chamber, and the atmosphere changes from room atmospheric CO_2 and room atmospheric humidity to 5 % CO_2 and high humidity, while also the temperature increases by + 2.0 ^{o}C so that it reaches the target temperature. 6) Extra tubing allows for the medium to adjust to 5 % CO_2 and target temperature. 7) Perfusion chamber, where NF-κB experiments are performed and data is collected. 8) Medium exits incubation chamber. CO_2 and humidity changes to atmospheric levels. The temperature changes to target temperature -2.0 ^{o}C. 9) Medium exits microscope enclosure and temperature changes from target temperature -2.0 ^{o}C to room temperature, while the height of the medium is increased (ΔHeight ~ +30 cm). 10) Medium flows out of the outlet and into a glass beaker.

An example of gas formation in a flow chamber in the Nikon Eclipse TI setup is seen in figure 3.6 A). This image is taken several hours after necrosis. For illustrative purposes, Methylene Blue was dissolved in water and pumped into the chamber in figure 3.6 B). This will give the reader an intuition about how large the gas bubbles in the flow chamber were, compared to the size of the sample.

In order to solve necrosis and gas formation in the Nikon Eclipse TI setup, a test scheme with a total of 28 experiments was planned. This scheme is presented in Appendix figure 6.4 and 6.4 and will not be discussed in detail. However, the intentions and logic behind it will be briefly explained. The aim of the scheme was to achieve acceptable culture conditions and no gas formation for at least 8 hours. In the scheme, several possible explanations for cell death and gas formation are mentioned in the beginning. A list of experiments addressing the most likely explanations for the problems was created. From the outcomes of the experiments, which were either positive (validating hypothesis) or negative (rejecting hypothesis), it was then noted how to proceed. Color coding was used, and the confirmed outcome was marked green while the disconfirmed outcome was marked red. In some of the experiments, if a particular outcome was confirmed, other experiments could be skipped. These experiments were colored yellow. By following the test scheme strictly, possible explanations for the gas

Experiment	Motor speed	Channel height	Volume flow rate	Average flow velocity
$Flow_1$	20 steps/s	600 µm	0.0308 µL/s	10.27 µm/s
$Flow_2$	4000 steps/s	200 µm	6.16 µL/s	6160 µm/s

Table 3.2: Initially calculated variables for $Flow_1$ and $Flow_2$

formation and necrosis were either validated and solved or rejected. By the end of the list, the flow experiments could run for days without gas formation in the flow chamber while cells were multiplying.

From the experiments on the JuliStage, it was known that the 466 nm excitation lamp would cause unrepairable damage to the cells. However, while testing in the Nikon Eclipse TI microscope, it was found that the main contributor to necrosis was the pH value. Despite sending the medium through tubes unable to transport liquid through its barrier, the atmospheric environment would still change the pH value to basic at pH ~ 10. This change in pH-value happened even with the addition of the buffer HEPES to the medium.

The experiments in the testing scheme would significantly decrease the gas formation in the flow system. It is worth mentioning that a few experiments were performed leading up to the creation of the testing scheme, and a few experiments were perfecting the flow conditions afterwords, but mainly the gas formation problem was solved by following this scheme. In table 3.1 the conclusions from these gas formation experiments are summarized. In conclusion, the five additions to the protocol significantly decreasing gas formation in the chamber were the following: Increasing height of input and output; degassing medium before use; inserting bubble trap immediately before flow chamber; using gas permeable tubing, and heating the medium close to its target temperature immediately before entering the flow chamber.

After extensive testing, a flow setup was now proposed, that would allow for precise experimental control, without unwanted necrosis and gas formation. The improvements were incorporated into the working flow system, presented in figure 3.7. By then, the only control needed to start experiments was precise temperature control.

3.3.4. Temperature control at Nikon Eclipse

The microscope enclosure in figure 3.7 is a part of the Oko cage incubator system [61]. Here, heat is pumped into the enclosure, and a thermocoupler is measuring the temperature, which is then controlled by the computer. This system allows for a maximum temperature of 40 °C, and due to the large distance between thermocoupler and heat pump, the temperature fluctuated within a span of 1 - 2 ∘C. This maximum temperature and these relatively large

fluctuations were unacceptable for the temperature experiments in this project, and so, it was decided to attach a Warner heat controller [62] to the gas incubation chamber. The heat-generating resistances were unscrewed from the Warner heating plates, burnished to fit, and screwed onto the Oko gas incubator. This allowed for the temperature to be more stable (fluctuating less than 0.5 °) and reach temperatures above 45 °. With this final addition to the setup, experiments could be performed in the flow system. In several of the experiments, quantification of flow speed and upconcentration of chemicals in the microbioreactor was needed. How these were found is described below.

3.4. Flow in the microbioreactors

Building the hardware and software for the flow system enabled the user to determine a type of flow. As described above, the flow system could be used to create both constant and oscillatory flow speeds, however, for the scientific experiments described in this thesis, only constant flow was used, and so, it is this type of flow that is characterized in this section. In these experiments, several different flow speeds were used in the microbioreactor. Experimental variables used in these experiments include the concentration of chemicals in medium, temperature, and LED power. However, the variables directly changing the flow conditions are viscosity, chamber shape, and size, as well as flow injection speed. Temperature and concentration of chemicals like glucose [63] in the flow system will affect the viscosity. The high glucose medium used [57] contained 4.5 weight % glucose and 10 +% FBS. Density and viscosity measurements had been conducted on a very similar medium in [64], so the density of the medium could be determined to be 1.009 kg/m^3 and the dynamic viscosity to be 0.930 Pa·s. The chambers all had rectangular cross-sections, with the same length and width at 50 mm and 5 mm, respectively, meaning that regarding the chamber shape, it was only the height that was changing. Also, the variable of flow speed was changed. For the results presented in this thesis, only two different flow conditions were used. These conditions are described in table 3.2. The purpose of $Flow_1$ was to create low drag and chemically stable culture conditions, while the purpose of $Flow_2$ was to exert high shear stress on the fibroblast cells.

Throughout initial experimentation in this project, other flow chambers and flow speeds were used. In order to find a sweet spot where mechanical stress was as small as possible but flow speed was still be fast enough for the chemicals to flow into the chamber before the cell confluency of the chamber was too high, different flow speeds were tested, including 5 steps/s, 10 steps/s, 20 steps/s, 40 steps/s, 100 steps/s 200 steps/s, 400 steps/s 1000 steps/s, 2000 steps/s, and 4000 steps/s. The latter value was found to be the highest pos-

Experiment	P_{wet}	D_h	Re	L_e	-dp/dx
$Flow_1$	11.2 mm	1071 µm	0.0119	702 µm	0.0215 Pa/m
$Flow_2$	10.4 mm	384 µm	2.57	233 µm	110 Pa/m

Table 3.3: Microfluidic properties of the flow chambers. Wetted perimeter, P_{wet}, Hydraulic diameter D_h, Reynolds number, Re, Entrance Length, L_e, and pressure drop, -dp/dx.

sible value. At values higher than this, the speed inserted into the program would not match the actual motor speed since it would fluctuate between turning and having no rotational velocity. Also, the heights of the following chamber were tested: 200 µm, 400 µm, 600 µm, and 800 µm. This means that experiments with both lower flow speeds and flow speeds in between the values presented in table 3.2 were initially carried out but not used for any results presented in the thesis.

Determining the flow speed, u at different chamber positions requires knowledge of whether the flow is turbulent or laminar. To calculate this, the Reynolds number is used. For a microfluidic channel with length, L, with hydraulic diameter, D_h, the Reynolds number is calculated as

$$\mathrm{Re} = \frac{\rho u L}{\eta} = \frac{\rho u D_h}{\eta}, \tag{3.5}$$

where u is the average flow speed, ρ is density, and η is the dynamic viscosity. The hydraulic diameter is calculated from the wetted perimeter, P_{wet}, defined as the perimeter of the channel that is wet. The hydraulic diameter of a channel with the cross-sectional area, A, is defined as

$$D_h = \frac{4 \times \text{cross section area}}{\text{wetted perimeter}} = \frac{4A}{P_{\mathrm{wet}}}. \tag{3.6}$$

The Reynolds number gives the inertial to viscous forces, meaning that when

- **Re « 1** viscous effects dominate inertial effects
- **Re ≈1** inertial effects and viscous effects are comparable
- **Re » 1** inertial effects dominate viscous effects.

When increasing the Reynolds number Reynolds, at values higher than 2000 ± 1000 the laminar flow will become turbulent. From the equations above, the wetted perimeter, the hydraulic diameter, and the Reynolds number for $Flow_1$ and $Flow_2$ are calculated and presented in table 3.3. The viscosity and density of water at 37 C° is used.

This means that for Flow_1 the inertial forces dominate, and in Flow_2 the viscous forces dominate. In both flow settings, however, the Reynolds numbers are orders of magnitude lower than values where the flow will become turbulent, so both flows are considered laminar.

.

For flows in a channel that have an entrance larger than the flow channel, the flow close to the entrance will behave differently than flow far from the entrance. This is called entrance effects, and the length into the channel that these effects take place, are for low Reynolds numbers described as:

$$\frac{L_\text{e}}{D_\text{h}} \approx \frac{0.6}{1 + 0.035\text{Re}_{D\text{h}}} + 0.056\text{Re}_{D\text{h}} \tag{3.7}$$

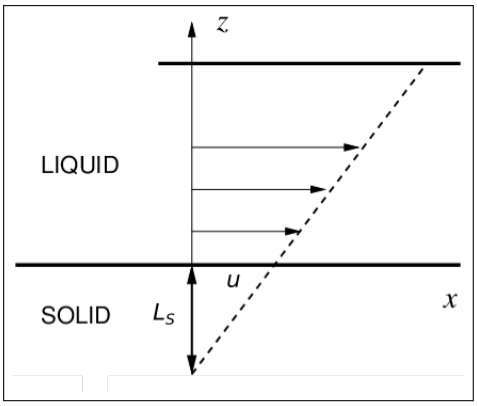

Figure 3.8: Illustration of slip length. In the bulk of the channel, furthest from the boundary, the flow speed is the largest. Decreasing the distance to the boundary decreases the flow speed, u. If the flow speed reaches zero beyond the boundary, the flow speed will have a magnitude at the boundary, correlated to the distance at which the speed reached zero. This distance is defined as the slip length, L_S.

.

The entrance lengths, presented in table 3.3, are in both cases below 1 mm, which means that the entrance lengths are much smaller than the length of the channel at 50 mm. Therefore cells growing in the microbioreactor will experience equal flow speeds and mechanical stresses throughout the vast majority of the length of the channel. In order to determine what velocities and mechanical stresses cells were exposed to, one has to make certain assumptions, described in the following.

3.4.1. Flow speed

Often when working with microfluidics, it is assumed that the flow speed of the liquid is zero at the boundaries. Such boundary conditions are called Navier boundary, and it is an assumption used due to a negligible slip in many experiments.

A slip at the boundary of the solid-liquid interface is defined as the difference in velocity between the solid wall, which in the current experiments is immobile, and the liquid at the interface equals the change of liquid velocity over y, which is normal to the wall multiplied with a proportionality constant, defined as the slip length, L_S

$$\Delta u_\text{wall} = L_S \frac{\partial u_\text{fluid}(y)}{\partial Y}\bigg|_\text{wall}. \tag{3.8}$$

The concept of slip length, L_S, is moreover illustrated in figure 3.8. In the illustration, it is seen that $u > 0$. This means that a slip between the solid-liquid interface is present when,

$L_S > 0$ and $\partial u_{\text{fluid}}(y)/\partial Y \neq 0$. Contrary, if the slip length, $L_S = 0$, there is no difference between the velocity of the wall and the velocity of the liquid flow.

Determining the slip length is a non-trivial task, and there are large disagreements between experimental and theoretical findings. The slip length is dependent on the properties of the wall and the liquid, making it even more difficult to set a value for slip length in an experiment where it is not directly measured. In [65] the slip length was measured by micro-particle image velocimetry (μPIV) in water with hydrophobic surfaces, which corresponds well with the experiments presented in this thesis. In this thesis, the slip length is estimated to be 200 nm plus/minus 200 nm. In [66] a range of different types of experiments are compared under varying conditions, and slip length is found to be below 200 nm in more than 50 % of experiments. For the purpose of finding a velocity profile and subsequently finding the force acting on fibroblast cells, the slip length is assumed to be negligible for this setup, when considering the dimensions of the flow chamber and the typical fibroblast cell sizes.

With the assumptions that the microbioreactors in this thesis have laminar flow and that the entrance length and the slip length are negligible, the flow speeds of the cross-sectional area spanned can be calculated. The liquid flows along the x-direction, and the velocity is then measured as a function of the z- and y-direction spanning the cross-section.

For a rectangular channel with no-slip, the flow speed, $u(y,z)$ is [67]

$$u(y,z) = \frac{16a^2}{\eta\pi^3}\left(-\frac{\mathrm{d}p}{\mathrm{d}x}\right)\sum_{i=1,3,5,\dots}^{\infty}(-1)^{(i-1)/2}\left[1-\frac{\cosh(i\pi z/2a)}{\cosh(i\pi b/2a)}\right]\frac{\cos(i\pi y/2a)}{i^3}, \tag{3.9}$$

where a and b are the lengths of the sides of the rectangle, and $-\mathrm{d}p/\mathrm{d}x$ is the pressure drop along the direction of the flow. In order to calculate $u(y,z)$, $-\mathrm{d}p/\mathrm{d}x$ has to be found. The volume flow rate, $\dot{Q}$ is given by [67]

$$\dot{Q} = \frac{4ba^3}{3\eta}\left(-\frac{\mathrm{d}p}{\mathrm{d}x}\right)\left[1-\frac{192a}{\pi^5 b}\sum_{i=1,3,5,\dots}^{\infty}\frac{\tanh(i\pi b/2a)}{i^5}\right]. \tag{3.10}$$

$\dot{Q}$ for Flow_1 and Flow_2 was presented in table 3.2, so $-\mathrm{d}p/\mathrm{d}x$ can be calculated from isolating this factor in the equation above

$$-\frac{\mathrm{d}p}{\mathrm{d}x} = \dot{Q}\frac{3\eta}{4ba^3}\left[1-\frac{192a}{\pi^5 b}\sum_{i=1,3,5,\dots}^{\infty}\frac{\tanh(i\pi b/2a)}{i^5}\right]^{-1}. \tag{3.11}$$

Having calculated the pressure drop, the flow speed profile can be determined from equation 3.9. The velocity of the data is presented in figure 3.9. In A) and B), the flow speeds versus

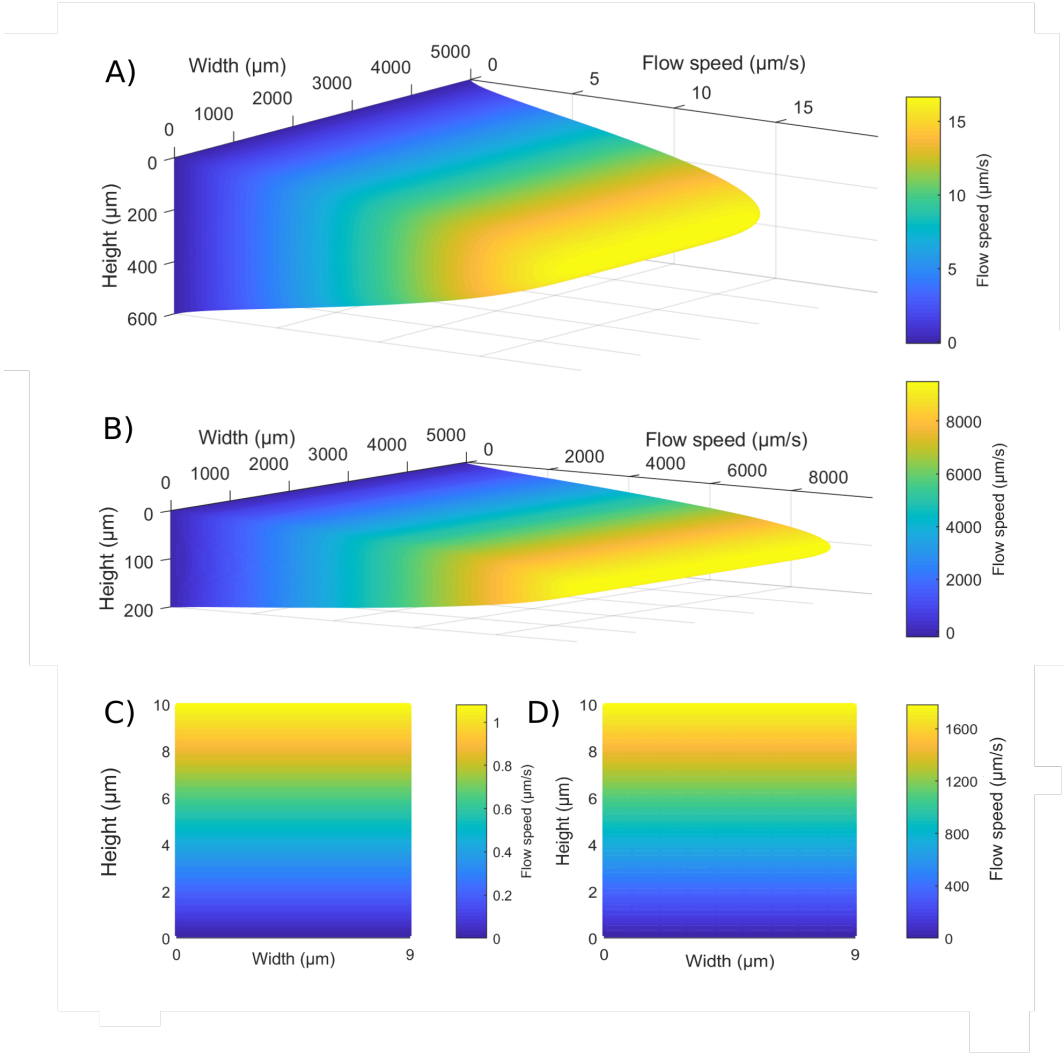

Figure 3.9: Flow speeds as a function of x- and y distance of the cross-sectional area of the flow channel. A) Flow_1 in: A channel with the dimensions 600 μm × 5000 μm with a volume flow rate, $\dot{Q}$, at 0.0308 μL/s. The maximum flow speed in the bulk of the channel is 16.66 μm/s and an average flow speed of 10.27 μm. B) Flow_2: A channel of the dimension 200 μm × 5000 μm with a volume flow rate of 6.16 μL/s. It has a maximum flow rate of 9482 μm/s and an average flow speed of 6160 μm/s. Both flows are assumed to have a flow speed at zero at the boundaries. C) A close-up of the channel near the boundary in A) at height from 0 μm to 10 μm in the middle of the width. D) A close-up of the channel near the boundary in B) at height from 0 μm to 10 μm in the middle of the width.

height and width of the flow channels are plotted for Flow_1 and Flow_2, respectively. The height dimension is enlarged compared to the width dimension of the channels for illustrative purposes. This visualizes that the height of the channel in A) is 3 times larger than the height in B). As seen in table 3.2 the volume flow rate is 200 times faster in Flow_2 compared to Flow_1. The narrower channel in Flow_2 also helps create a faster flow, resulting in a maximum flow speed of 16.66 μm/s in Flow_1 and a maximum flow speed of 9482 μm/s in Flow_2.

In figure 3.9 C) and D) the flow speeds along the width of the channels are plotted for Flow_1 and for Flow_2, respectively. From here it is extracted that the strain rate $\dot{\gamma} = \partial u/\partial y$ in this region is given by $\dot{\gamma}_1 = \Delta u/\Delta height$ = 9.85E-7ms^{-1}/10E-6 m = 0.985s^{-1} for Flow_1 and $\dot{\gamma}_2 = \Delta u/\Delta height$ = 1.63E-3 ms^{-1}/10E-6 m = 1.63E3s^{-1} for Flow_2.

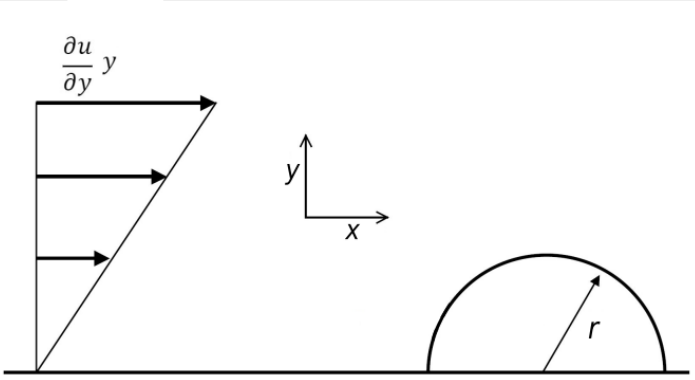

Figure 3.10: Flow on hemisphere attached to surface. Modified from [68]. A flow with a flow speed, u, in the direction x, is increasing as a function of y. A hemisphere with radius, r, serves as a simple model for a cell in order to predict a drag force from the flow speed.

The flow speeds found will serve as the foundation for calculating the mechanical stress exerted on the cell under these conditions. It is clear from figure 3.9 that the velocity is highest in the center of the channel and decreases closer to the boundaries. Therefore, for the calculation of mechanical stress exerted on the cell, assumptions on cell height and shape must be made.

3.4.2. Forces acting on fibroblast cells in the flow chamber

When the flow system was functional, the purpose was to have cells attached to the bottom surface of the chamber and observe how they react to changing electrolytes and temperature. The cells used for this purpose are 3t3 fibroblast cells. Since the cells attach to the surfaces, the flow speed they experience is that of the flow chamber walls. These cells have been shown to have a height of approximately 2.5 µm at 6 µm from the edge [69] and in other experiments, they were found to be up to 2 µm approximately at the same distance from the edges [70]. Fibroblast cells are highest at the nucleus in the center of the cell, with a height between 4.1 µm and 6.7 µm dependent on the confluency, where higher confluency will lower the maximum height [71]. From own experiments, discussed in detail in section 4.7.1 and presented in figure 4.14, the typical diameter of fibroblast cells, if the cell is assumed to be a plate, is approximately 20 µm, even though the cell can have a length of approximately 100 µm. The volume of fibroblast cells is estimated to be 2000 µm^3 [72], so from this number under the assumptions of a hemisphere the radius is estimated to be

$$V = \frac{2}{3}\pi r^3 \Rightarrow r = \left(\frac{3}{2}\frac{V}{\pi}\right)^{1/3} = \left(\frac{3}{2}\frac{2000\mu\text{m}^3}{\pi}\right)^{1/3} = 9.85\mu\text{m} \quad (3.12)$$

Experiment	Maximum flow speed on cell	Drag force on cell
$Flow_1$	98.5 µm/s	0.56 pN
$Flow_2$	1630 µm/s	930 pN

Table 3.4: Flow speed and drag force experienced by cells in the flow system

. This is in rough accordance with the other height discussed here at 4.1 µm and 6.7, so since this volume is used for a calculation below, this radius will also be used here. It is worth noting that in plot 3.9 C) and D) the height is 10 of the plot is 10 µm. This is considered the maximum height of the cell, and the flow speed at this height is therefore considered the maximum flow speed experienced by a fibroblast in these experiments.

For calculating the force exerted on a cell in the flow system, the cells are estimated to be hemispheres attached to a surface. This solution is found analytically in [68] and a modified illustration is presented in figure 3.10. As in the equations and figures above, a flow with a velocity, u, in the x-direction, has a change along the y-direction, described by $\partial u/\partial y$. The equation for the exerted force on a hemisphere is

$$F_{\mathrm{D}} = \left[2\pi\eta r^2 + \mathrm{C_D}\frac{\pi}{4}\rho r^4 \frac{\partial u}{\partial y}\right]\frac{\partial u}{\partial y}. \tag{3.13}$$

The drag forces acting on the fibroblast cells is calculated for the two flows from the formula above, with the values from the tables:

$$F_{\mathrm{Flow1}} = 0.56\mathrm{pN} \tag{3.14}$$

$$F_{\mathrm{Flow2}} = 930\mathrm{pN}. \tag{3.15}$$

A comparison of the drag force to the gravity force is useful to determine whether a given drag force is significant compared to the forces that a cell will normally be exposed to. Therefore, the gravitational force of a single fibroblast cell is calculated. The weight density of a fibroblast cell is 1050 kg/m^3 [73] and the density of high glucose medium containing 19 % FBS at 37 °C is 1009 kg/m^3 [64]. The difference in density of fibroblast cells and water is then

$$\Delta\rho = \rho_{\mathrm{fibroblast}} - \rho_{\mathrm{water}} = 1050\frac{\mathrm{kg}}{\mathrm{m}^3} - 1009\frac{\mathrm{kg}}{\mathrm{m}^3} = 41\frac{\mathrm{kg}}{\mathrm{m}^3}. \tag{3.16}$$

The volume of a fibroblast cell is 2000 µm^3 = 2 E -15 m^3 [72] and so the difference in mass

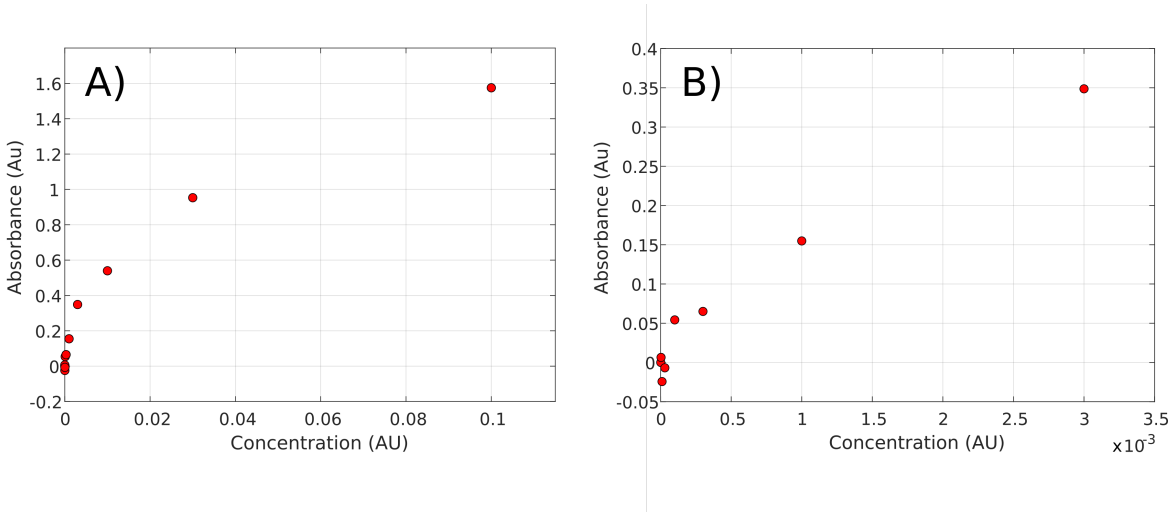

Figure 3.11: Absorbance versus concentration of Methylene Blue in curvettes. A) Absorbance versus concentration in this range is not linear, so the concentration is too high for relating concentration linearly to absorbance. B) Absorbance versus concentration in this range is linear, and the absorbance can be linearly related to concentration in the flow experiments.

of the fibroblast cell compared to water with the same volume is

$$\Delta m = \Delta \rho V = 41 \frac{\text{kg}}{\text{m}^3} \cdot 2\text{E-}15\text{m}^3 = 82\text{E-}15\text{kg}. \tag{3.17}$$

From Newton's second law of motion, with the gravitational acceleration g = 9.82 m/s^2, the net gravitational force acting on a single fibroblast cell is calculated to be

$$F_{\text{gravity}} = gm = 9.82 \frac{\text{m}}{\text{s}^2} \cdot 82\text{E-}15\text{kg} = 0.805\text{pN}. \tag{3.18}$$

So the force exerted by Flow_1 is $\frac{0.56\text{N}}{0.805\text{N}} \cdot 100\% = 69.3\%$ of the gravitational force while Flow_2 is $\frac{930\text{N}}{0.805\text{N}} = 1152$ times larger than the gravitational force. The maximum flow speed experiences by a cell and its total drag force in the flow are presented in table 3.4. These calculations were a useful tool when quantifying the magnitude of the drag forces. With the following quantification of the upconcentration of chemicals in the microbioreactor, the understanding of the flow system was adequate for experimentation.

3.4.3. Upconcentration in the chamber

After the flow speed and the force exerted on cells from the flow were determined, knowledge of the upconcentration of chemicals inside the chamber was of interest. Knowing the shape of the upconcentration curve and the approximate concentration at a time point would allow for a satisfying understanding of the flow system and how it affected cells during experiments.

To experimentally extract the upconcentration curve, measurements of concentration inside the chamber would have to be made. Inside a fluorescent microscope, the seemingly ob-

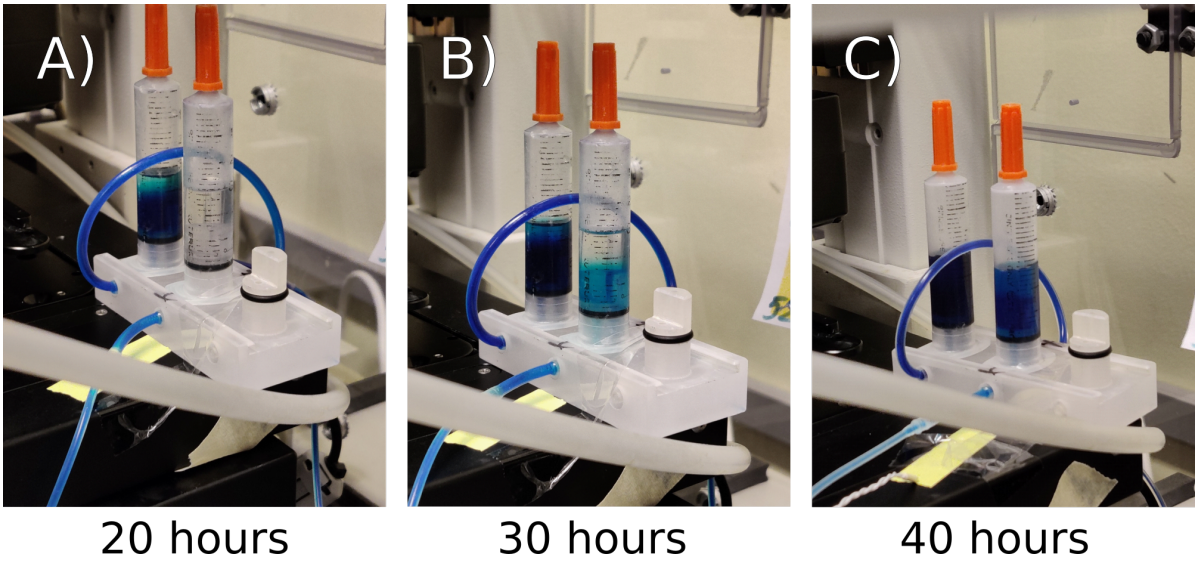

Figure 3.12: Upconcentration of chemicals in the bubble traps after being pumped into the flow system. In A), after 20 hours, Methylene Blue has reached the first bubble trap but has not yet reached the second. In B), Methylene Blue has reached both bubble traps but is more upconcentrated in the first. C) The concentration of Methylene Blue is higher in both bubbles traps compared to A) and B), and is still higher in the first bubble trap compared to the second.

vious choice for concentration measurements is a fluorescent dye, however, fluorescent dyes will typically have a relatively short half-life at 37 °C, and this experiment would continue for approximately a week at up to 37 °C. Another disadvantage with a fluorescent dye is the lack of knowledge of concentrations at different positions inside the flow chamber. When an upconcentration curve is eventually found, why it has a particular shape is better answered when having this knowledge. For those reasons, it was decided to use the light-absorbing dye Methylene Blue [74].

To determine the concentration from the absorption, Lambert-Beer's law was used:

$$A = \epsilon c l, \tag{3.19}$$

where A is absorbance, ϵ is the absorptivity, c is the concentration and l is the length of the optical path. It was possible to find the absorbance of Methylene Blue in dilution, from the relationship between absorbance, A and transmittance, T, given by[75]

$$A = log10(1/T) = log10(I_0/I), \tag{3.20}$$

Where I_0 is the incident light, and I is the transmitted light.

Lambert-Beer's law is only linear up to a certain concentration [76], so the linear range between concentration and absorbance was found.

Finding a concentration range of Methylene Blue, where an absorbance could be measured but where significant light could still transmit, was achieved by diluting methylene Blue in

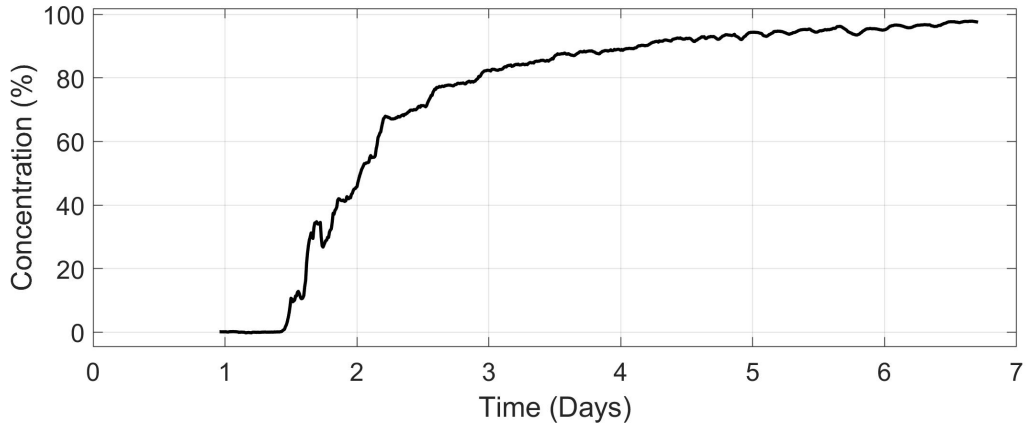

Figure 3.13: Concentration of chemicals injected into the flow chamber versus time during flow experiments. Data is from a single experiment where Methylene Blue (aq) was injected into the flow chamber. Transmittance was measured and calculated into absorption, then was then calculated into concentration in %. When the flow system was used to inject TNF-α into a flow chamber, NFκB oscillations were analyzed from day 1.5 when the TNF-α concentration started increasing.

water. This arbitrary concentration was then diluted into concentrations spanning 10^7 orders of magnitude. From this initial experiment, ten dilutions of arbitrary concentration were then prepared. With the initial Methylene Blue dilution having the value 1, the following concentration were prepared: 0; 1E-6; 3E-6; 1E-5; 3E-5; 1E-4; 3E-4; 1E-3; 3E-3; and E-2. The light source allowing for transmitted light was the microscope lamp from the Nikon microscope at 6 V. The collected data was from CCD camera that measured the brightness of the pixels in a bright field image. Since there is a linear relationship between the brightness of a pixel in the camera and light intensity [77], the initial transmittance could be found by taking the average intensity of all pixels in the image at a certain time point and relate that to the average light intensity, in a calibration experiment with a slide containing pure water. The absorbance for the ten different concentrations is plotted in figure 3.11 A). From this plot, it was estimated that the concentration was not in a linear range. In B), the eight lowest concentrations from plot A) are plotted. This range is estimated to be linear, so the maximum value 3E-3 was chosen as the concentration of Methylene Blue to characterize the upconcentration of the chemicals in the flow system.

For this experiment, it was relevant to test the upconcentration of chemicals of Flow_1, since this was used for the addition of TNF-α. All tubing and the flow chamber were filled with water, and the bubble traps were filled to 3 ml each. The 60 ml syringe was filled with Methylene Blue diluted in water with the concentration found from the experiments presented above. The pump was set to a constant value matching the velocity of Flow_1. As seen in figure 3.12, the bubble traps functioned as reservoirs, where the chemical —in this experiment Methylene Blue —is diluted. It is thereby not the same chemical concentration flowing out of a bubble trap as the one flowing in. Chemicals are diluted in each of the two bubble traps,

and so, the chemical concentration flowing out of the second bubble trap is lower than the chemical concentration flowing out of the first. In figure 3.12 A), the experiment has been running for 20 hours. Here the chemicals have reached one bubble trap but remain to be diluted in the second bubble trap. In B) after 30 hours, the first bubble trap has a darker color than in A), and Methylene Blue is now observed in the second bubble trap. In C) after 40 hours, both bubble traps are observed to be upconcentrated relative to A) and B). From these images, it is clear that the concentration of a chemical flowing into the flow chamber is upconcentrated over time and that the upconcentration is not being achieved in one step.

How this upconcentration looks in further detail is measured by absorbance and is plotted in figure 3.13. The time points before day 1 have been removed because bubbles would allow for transmittance even higher than pure water, resulting in a negative concentration value when bubbles flowed through the flow chamber. At approximately 36 hours into the experiment, the concentration of Methylene Blue starts to increase. The upconcentration has its highest gradient at the beginning of the experiment and is thereafter converging towards a value at 100 %. 60 hours after the concentration started to increase, at 60 hours or 2.5 days, the concentration is approximately 70 % of the total concentration, and after 6 days, the concentration is approximately 95 %. To relate this to the increase of TNF-α, where the flow system is filled with TNF-α free medium before initiation of the experiment, and TNF-α with a concentration of 1 ng/ml is pumped into the flow system, it would upconcentrate as follows. The medium would not contain TNF-α for the first 1.5 days. After this, it would start to increase. At day 2.5 the TNF-α value would be at 0.75 ng/ml, and after 6 days, it would be at 0.95 ng/ml.

From these experiments, the general understanding of how chemicals were upconcentrated in the microbioreactor was improved, and quantification of injected chemicals over time had been performed. If it is desired to change the shape of the upconcentration curve, this is possible by changing the initial volume of the bubble traps or decreasing or increasing the number of bubble traps. However, as is explained in section 4.3 and figure 4.5, the chemical upconcentration observed in these experiments is in accordance with the natural upregulation of the cytokine TNF-α, which is used for activating NF-κB in this thesis, so it upconcentration curve was chosen for the TNF-α experiments in the flow system.

3.5. Conclusion

A functional displacement pump with in-house designed software was successfully built. Experiments were conducted to improve the understanding of temperature regulation inside an incubator with a fluorescence microscope situated inside. These findings assumed that

changing to another setup where heaters could be built into a gas incubator was beneficial. Here, building a complete flow system was initiated, and despite extensive challenges with gas formation in the system, these problems were eventually solved, and a well-functioning flow system was built. Gas was reduced by increasing input and output height, degassing medium before experiments, inserting bubble trap, using gas-permeable tubing, and having the medium reach a relatively high temperature before entering the bubble trap. With a successful flow system, different flow kinetics could be characterized. Two flows with a flow speed difference of approximately a factor of 600 were calculated analytically, and from that, the difference in force that these flows would exert on cells was calculated. Finally, experiments on the upregulation of chemicals were conducted, and it was found that 1.5 days after initiation of the experiments, chemicals reached the chamber. After this, the upregulation was steepest initially and converged toward full concentration for the remaining 7 days of the experiment.

This flow system will be used in the following for exposing cells to controlled levels of TNF-α as well as for exposing cells to variable flow stresses.

4

Stressing the NF-κB signaling pathway

The NF-κB signaling pathway functions as a general stress response in eukaryotic cells. In biological experiments, changing the physical environment is considered a stress, so using NF-κB fluorescent MEF cells as a model for testing how living systems adapt to changes in their physical environment was extremely interesting. This chapter gives an overview of intra- and extracellular signaling, the NF-κB signaling pathway, how NF-κB is activated by stress and TNF-α, fundamental dynamical systems and chaos theory, several interesting NF-κB measurements, and finally, theoretical predictions based on these experiments.

4.1. Cell signaling

For the understanding of NF-κB gene regulation, a brief explanation of intra- and extracellular communication and protein regulation is provided. A background on multicellular communication will be elucidated, as well as how molecules transfer signals, how signaling pathways fundamentally operate, and lastly, how proteins are upregulated from DNA via messenger RNA (mRNA), which is often described as the central dogma.

4.1.1. Cell communication

Multicellular organisms require intercellular communication in order for all cells in the organism to function as a whole. Extracellular signaling molecules are emitted from individual cells and received by others, exemplified by the hormone Adrenaline, which is transported

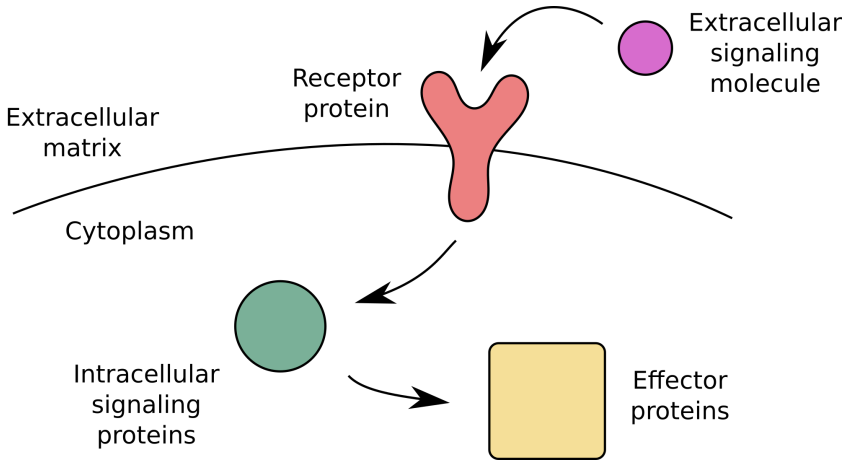

Figure 4.1: Intracellular signaling from an external signal in a multicellular organism. An extracellular signaling molecule in the extracellular matrix can form a temporary complex with the membrane receptor protein. The signal is chemically transducted to intracellular signaling molecules that give the signal to effector proteins. This will initiate intracellular processes, such as gene regulation.

via the bloodstream and hereby affects cardiac output, pupil dilation, blood flow to muscles, and blood glucose level. Another example is the cytokine Fibroblast Growth Factor 1 secreted by macrophages and received by nearby fibroblast cells, giving them the signal to promote endothelial cell organization or proliferation. In these two examples, the body will function as one organism rather than individual cells acting to survive individually.

There are four forms of extracellular signaling; contact-dependent signaling, which requires cells to be in close proximity for signaling molecules to activate a response in the next cell; paracrine signaling, where cytokines or other growth factors are excreted into the surrounding cytoplasm and subsequently act on nearby cells; synaptic signaling, sometimes also defined as a type of paracrine signaling, where electric signals are transferred in neurons in the form of ions, which release a neurotransmitter response in proximity with another cell, and finally; endocrine signaling, where hormones or in fewer cases cytokines are excreted into the bloodstream in order to communicate throughout the multicellular organism over longer distances. In these four forms of extracellular signaling, the signal is received by receptors located in the membrane of the receiving cell that will react to the input. Another form of signaling that also uses membrane receptors is autocrine signaling, where signaling molecules are excreted from a cell and received by its own receptors.

4.1.2. Molecular signal transfer

For a signal to be transferred from one signaling molecule to another, a chemical cue must be transferred. This chemical cue can have several forms depending on the signaling molecule. A common form of signal transduction is when a protein is phosphorylated or dephosphory-

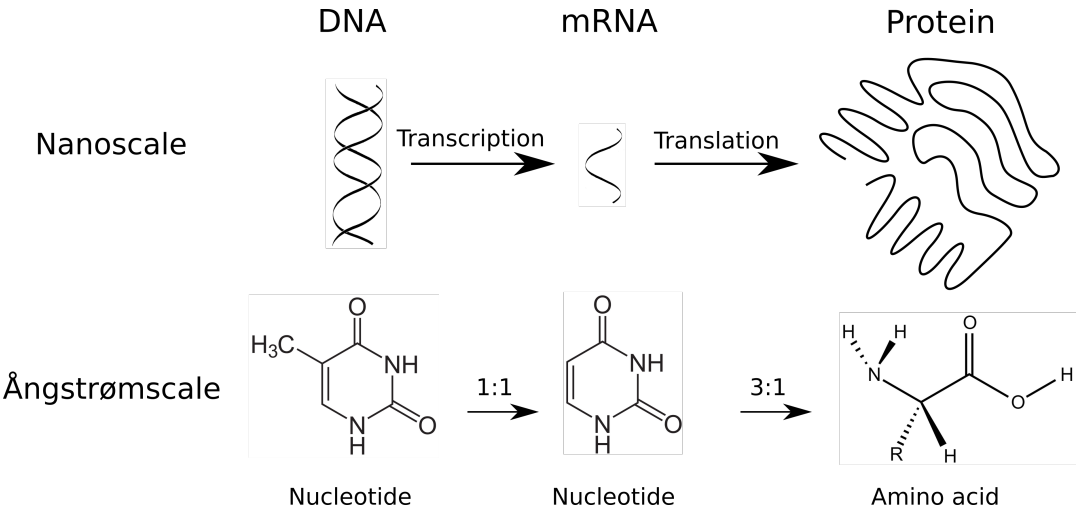

Figure 4.2: Central Dogma of biology at nano- and Ångstrøm length scales. At the nanoscale, the DNA is in double helices and is transcribed into single-stranded mRNA. These are translated into proteins of complex three-dimensional structures, which are translated into proteins. At Ångstrømscale, nucleotides from the DNA are transcribed into mRNA nucleotides at the ratio 1:1. Nucleotides are then translated into protein forming amino acids in the ratio 3:1.

lated by an enzyme. In these processes, a phosphate group is either covalently attached or its covalent bond is broken. Another signal transduction method is ligand binding, where a smaller molecule (the ligand) binds to larger molecules by either covalent bonding or by intermolecular forces. These structural changes will cause other molecules to react differently to the complex. This can, for example, be a receptor that now has the potential to bind to the complex, which it did not have before, or a proteasome that will start degradation of a protein because it has been tagged for degradation by the addition of a phosphate group.

4.1.3. Fundamental signaling pathway

When a chemical signal is received by a cell via an extracellular signaling molecule, this can bind as a ligand to a receptor protein, as seen in figure 4.1.

From here, a signaling cascade is initiated where the receptor protein transfers a signal to an intracellular signaling protein. This intracellular signaling protein will either transfer a signal to one or more effector proteins directly or activate other intracellular signaling proteins or small intracellular mediators. Some of the activated signaling proteins will activate one or more effector proteins, which can affect the cell's behavior. This includes altering gene expression, metabolism, enzymatic activity, and cell movement.

4.1.4. Gene regulation

Central Dogma, visualized in figure 4.2 describes the process where DNA is converted into a useful product, and as this description will focus on, from DNA into mRNA and then from mRNA into a protein.

When an effector capable of alternating the gene expression has been given a chemical cue to regulate a gene, it will affect one or more transcription factors to either bind or detach to or from a specific region of the Deoxyribonucleic Acid (DNA). The DNA is shaped like a double helix that is built up of single nucleotides forming base pairs.

Transcription factors are like any other protein built from amino acids. In a specific region of the protein, the amino acids have a sequence that constitutes a domain that will create a three-dimensional motif that will have the ability to attach to a specific region of the DNA sequence. The DNA sequence can either be a silencer or an enhancer and decrease or boost nearby genes' transcription. If the gene is upregulated and the transcription factor increases gene expression, the transcription factor is called a transcription activator or an activator protein. If the transcription factor decreases a gene that it is bound to, it is called a transcription repressor. Approximately 100 different proteins are required for starting transcription, including general transcription factors, a mediator, and an RNA Polymerase. RNA Polymerase binds to a part of the DNA called the promoter and will initiate copying of DNA into RNA and hence start the transcription. There are three DNA polymerases, but the one responsible for building messenger RNA (mRNA), which is the basis for all protein translation, is DNA Polymerase II. In DNA Polymerase II mRNA assembles, it then detaches from DNA and is thereafter exposed to post-transcriptional modifications before, while, or after translocating into the cytoplasm.

. In the cytoplasm, mRNA interacts with a ribosome. Here, the mRNA codon, nucleotide sequences consisting of a series of three nucleotides, will bind to a transfer RNA (tRNA) that has a complementary codon. Besides the three nucleotides forming the complementary codon, the tRNA carries amino acids, which will become linked to the growing protein being created in the ribosome. This means that the information in the mRNA is translated from a sequence of nucleotides into a sequence of amino acids. The sequence of amino acids will, in some cases, be a mature protein, but in some cases, the amino acid chain is not completed into a fully functional protein and will have to undergo post-translational modifications to form the mature protein.

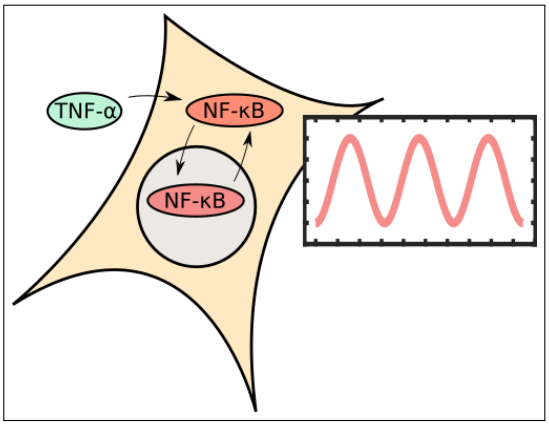

Figure 4.3: Simple illustration of NF-κB oscillations. TNF-α initiates a signaling pathway resulting in shuttling of NF-κB between cytoplasm and nucleus. Measuring nuclear to cytoplasm ratio over time will result in an oscillating curve as illustrated in the inset.

From the understanding of fundamental intra- and extracellular communication and of

the central dogma, the NF-κB mechanics and how its signaling pathways are affected by stress and TNF-α can now be explained.

4.2. Mechanics of NF-κB oscillations

The NF-κB activation is both assumed to have canonical signaling pathways and non-canonical signaling pathways [19], which are often seen as entirely separated, even though experiments have shown that these can couple and be initiated simultaneously by, e.g., TNF-α [78]. In figure 4.4 the canonical and the non-canonical signaling pathways are illustrated. Initiation of the cascades comes from surface receptors in both cases. However, all canonical signaling pathways phosphorylate the IκB Kinase (IKK) complex, consisting of IKK-α, IKK-β, and IKK-γ. This activation will then phosphorylate IκB that is in complex with the two NF-κB subunits p65 and p50, which at this step is situated in the cytoplasm. IκB stands for inhibitor of NF-κB, and when in complex, it will inhibit the translocation of NF-κB into the nucleus. The phosphorylation of IκB will cause ubiquitination, which functions as a tag for degradation by the 26S proteasome. The NF-κB complex will then translocate into the nucleus, where it binds to DNA and upregulate in the order of a thousand different peptides. It will upregulate the production of IκB, and form complexes with the NF-κB complexes, which will translocate back into the cytoplasm. This means that NF-κB is initially located in the cytoplasm, then upconcentrated in the nucleus, and finally upconcentrated in the cytoplasm again. This is the biological origin of the oscillations, which was illustrated in figure 4.3.

In a positive feedback loop, when single cells in multicellular organisms have fluctuating levels of chemicals in their surroundings, such as ions, signaling molecules, and proteins, and from that up- or down-regulate the output of genes, the chemical fluctuations lower the signal to noise ratio, and thereby makes it more difficult for a cell to react appropriately. It has been suggested that cells will be more robust to noise by oscillating [79][80][81] because the output oscillations will be less affected by temporary fluctuations of the activating chemicals. There must be a negative feedback in the signaling pathway to have an oscillating signaling pathway, which is the case for the NF-κB system.

Besides making the signaling pathway more robust, oscillating mechanics create more possibilities in varying its gene output. It has been shown that the gene output can change for each oscillation from a constant cytokine input. The patterns of the gene transcription networks are described as motifs [82] and are determined from a combination of positive and negative feedback loops [80]. When transferring a signal from one signaling molecule to the next, positive feedback will have a positive chemical input and turn this into positive chemical output. From the Hill coefficient of the reaction, the relationship between chemical

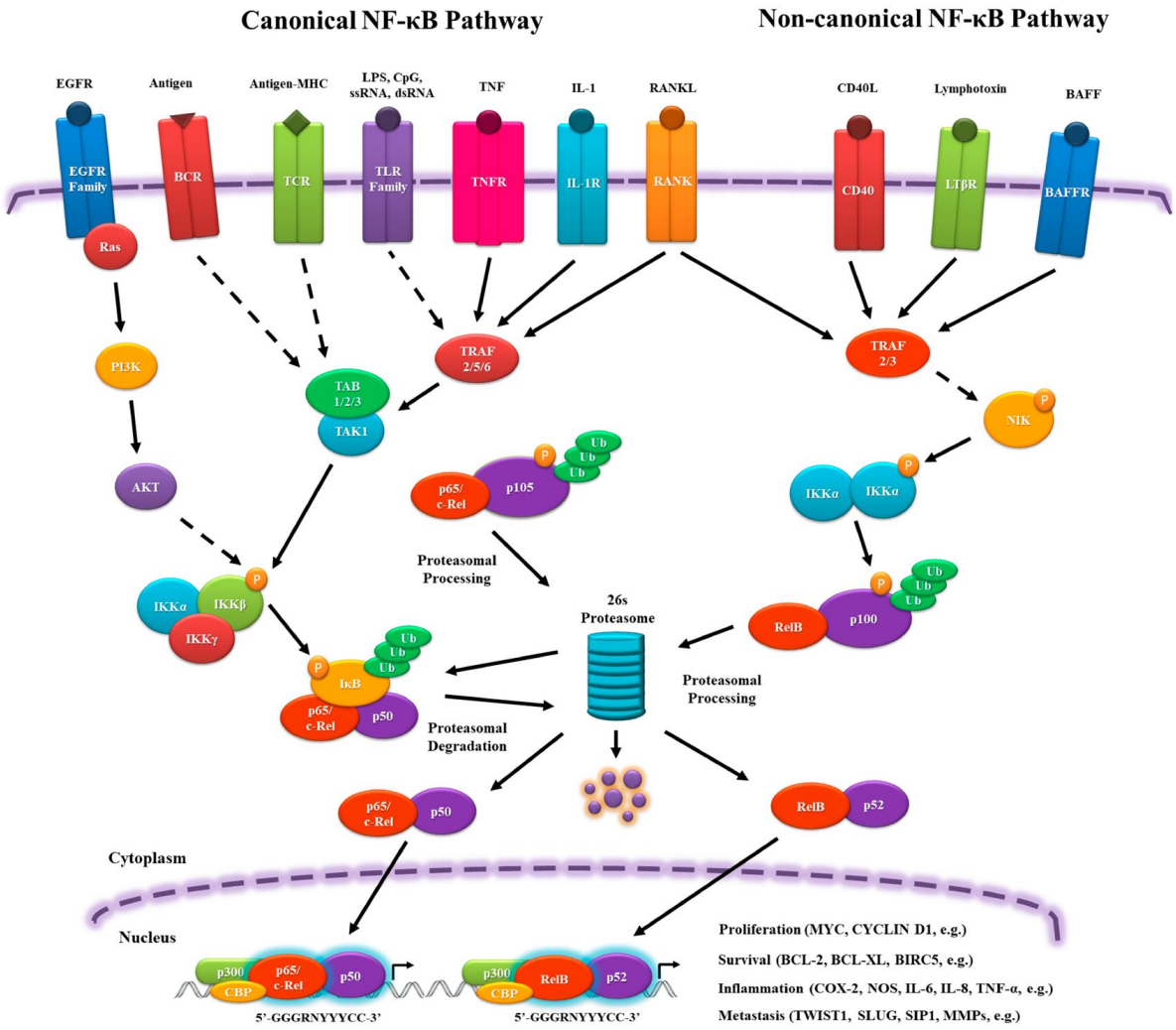

Figure 4.4: The canonical and the non-canonical NF-κB signaling pathway, taken from [19]. The canonical NF-κB signaling pathway to the left involving the kinases IKK-α, IKK-β, and IKK-γ. One out of several proposed non-canonical NF-κB signaling pathways to the right. A cascade of proteins from the initiation by the extracellular signaling molecule phosphorylates IKK-β, resulting in the phosphorylation of IκB and the subsequent translocation of the NF-κB complex —in this case p65 and p50 —into the nucleus. In the nucleus, NF-κB will upregulate hundreds of proteins, including IκB that will bind to NF-κB, which translocate the complex back into the cytoplasm.

input and output can be determined [83]. From this, positive feedback can either enhance or lower the magnitude of chemical input while also making it insignificant until a particular threshold value. Negative feedback loops are gene regulatory networks with motifs that down-regulate their own gene regulatory molecules, and therefore down-regulate their own production. If, for a longer time period, the input is constant, the gene output will eventually increase, resulting in oscillations of gene output, as illustrated in figure 4.3. The details of the canonical NF-κB signaling pathway will be discussed from a theoretical perspective in section 4.5.3. Suppose a signaling pathway consists of both negative- and positive feedback loops. In that case, the pathway can be adjusted to have the right sensitivity for the input signal, the right concentration of the output signal, having a temporal sensitivity, temporal

output dependence, and being robust to noise. Such a system will enable digital activation and binary decision-making [84]. This is the case for the NF-κB system.

Many different signals can activate the NF-κB signaling pathway. Some of which are reactive oxygen species (ROS), cytokines such as TNF-α and interleukins, and a range of different stresses. It also has a role in the immune defense, such as regulation of natural killer cells [85], it is involved in cancer and aging response, where it can cause apoptosis to hinder damaged cells in multiplying, it is involved in cell cycle, in proliferation [86][87], and it has been suggested to have an inhibitory role in bone homeostasis [88], to mention a few. The digitization of the signaling pathway is essential for signal transduction of NF-κB with these many functions and activation methods.

For cells in tissues, many biological oscillators show synchronous behavior at the population level [89] [90]. This is contrary to the NF-κB signaling pathway, where it has been suggested that an IκB-ϵ dependent mechanism will result in NF-κB oscillations between cells being in antiphase [91]. This behavior can provide advantages specific to the NF-κB signaling pathway.

From a mathematical standpoint, the concepts of oscillations, coupling, and chaos will be expanded on in the theory section 4.5. This theory is fundamental for understanding theoretical modeling, and thereby the predictions that the theoretical field can make. However, a description of certain physical and chemical properties is imminent that can activate the NF-κB signaling pathway.

4.3. TNF-α

TNF-alpha plays a vital part in the immune defense. It is a pro-inflammatory cytokine primarily released by macrophages when these have detected an infection. Its membrane receptors are called TNFR1 and TNFR2, and when TNF-alpha forms a complex with one of these, the NF-κB signaling pathway is initiated. An example of a molecule interpreted as an infection by the macrophages is the lipopolysaccharide (LPS), which is abundant in bacteria. If this is detected, macrophages will start TNF-α production. Another cause for starting TNF-α production is the detection of T cells. The upregulation of TNF-α after these two stimuli has been measured [92]. These experiments are presented in figure 4.5 and served as a guideline for increasing TNF-α in the experiments in this thesis, and so it was attempted to mimic this increase over time. The upconcentration of chemicals versus time in the in-house built flow system was successful in resembling the natural upconcentration, as seen in 3.13. In the experiment, the TNF-α concentration was measured in macrophages at t = 1 h; 2 h; 4 h; 8 h; and 24 h, after stimulating the cells with 10 ng/ml LPS or T cells in the concentration 1:1

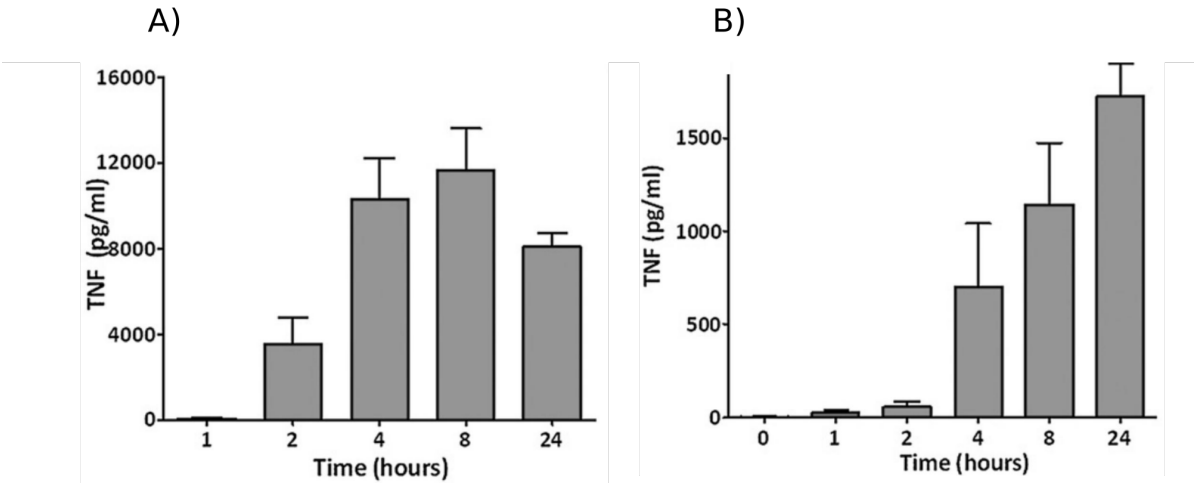

Figure 4.5: Production of TNF-α in macrophages after stimulation by 10 ng/ml LPS in A) and after stimulation by T-cells in the ratio 1:1 with the macrophages [92]. The TNF-α production increases for between 8 and 24 hours when stimulated by LPS and for at least 24 hours when stimulated by t cells. The natural upconcentration was mimicked by the in-house built flow system, as seen in figure 3.13

to macrophages. When cells were stimulated with LPS, the highest TNF-α value is 12 ng/ml, and the peak is between t = 8 h and t = 24 h. In the T cell experiments, the highest measured TNF-α value is 1.6 ng/ml. In this experiment, the TNF-α concentration increases throughout the entire experiment, but the peak value is assumed to be near 24 hours.

In the experiments in this ph. d. project, TNF-α is used to activate NF-κB. In those experiments, TNF-α is kept at a temperature at approximately 37 °C. Therefore it is crucial to know the stability of TNF-α at this temperature. The stability of human TNF-α at 37 °C has been investigated [93]. It was cultured for 0; 2; 5; 8; 12; 17; 22; or 28 days, and it was found that there is no detection of storage at various TNF-α concentrations after up to 17 days. On day 28, the TNF-α concentration was approximately 75 % of the starting concentration. This means that the TNF-α proteins in these experiments are assumed to have no degradation.

In the experiments, it was also tested how stress affects the NF-κB signaling pathway. Therefore a background on stress-dependent NF-κB signaling is given here.

4.4. Stress dependent signaling of NF-κB

Cellular stress exists in many forms, and NK-κB has been found to react to several of these. An essential form of cellular stress is when DNA is damaged, where it is known that misregulation is implicated in a wide range of diseases ranging from cancer to inflammatory and immune disorders [94][95]. It has been proposed that after DNA damage IKK-γ is ubiquitinated in the nucleus and subsequently exported to the cytoplasm, where it will start degradation

of IκB and subsequently cause nuclear activation of NF-κB that can then promote inflammation. As a response to ribotoxic stress, the NF-κB response has been tested with exposure to UV light, where it has been found that a PERK-dependent pathway will inhibit the synthesis of IκB, resulting in activation of nuclear NF-κB [96]. More than one shear stress-dependent pathway has also been suggested. A hemodynamic shear stress-dependent pathway was proposed after endothelial- and smooth muscle cells were exposed to flows creating a pressure between 0.01 Pa and 0.1 Pa. This resulted in a significant upregulation of IκB in both nucleus and cytoplasm and is assumed to be connected to an upconcentration of nuclear NF-κB. For comparison, a wall shear pressure of 0.1 Pa is generally considered to affect cells in vitro [97]. Moreover, shear stress has been found to activate NF-κB in osteoblasts through a phospholipase pathway that releases intracellular calcium ions [94]. There have been proposed connections to oxidative stress [98] and stress originating from sound waves [99], but for the findings in this thesis, the connection to heat stress is essential.

4.4.1. Biological effects of temperature variations

Keeping a temperature of approximately 37 °C is essential to mammals. This critical task is mainly achieved by the mitochondria, which functions as heat generators in mammals. Relatively small derivation from the normal temperature will have major consequences, among others, change rates of chemical reactions, diffusion, stability of membranes, and the DNA of cells. Therefore, it can be difficult to determine a specific reason for a biological event caused by changes in temperature. Nevertheless, some signaling molecules in the NF-κB signaling pathway are affected by these changes. For example, it was found that the IκB transport into the nucleus was reduced at lower temperatures [100].

Heat shock proteins (HSP) prevent aggregation of misfolded proteins, ensure correct tridimensional conformation during synthesis or heat stress, and eliminate incorrectly folded proteins if repair is impossible [101]. There are six classes of HSP, each with names after their molecular weight. These include: large HSP or HSP100, HSP90, HSP70, HSP60, HSP40 and small HSP. When HUVEC cells were exposed to heat shock of up to 90 min. at 43 °C, with subsequent activation of NF-κB, HSP27 dependent signaling was proposed [102]. Another study [101] shows that HSP70 primed in plasma membrane monocytes will enhance expression of pro-IL-1β, TNF-α, and IL-6 while phosphorylating IκB and thereby activating NF-κB. From these findings, it seems that NF-κB and HSPs are closely correlated and that NF-κB is an indicator of heat shock.

In [103] they report on a study on how NF-κB activation is influenced by keeping cells at various constant temperatures. This paper reports on findings quite similar to part of those

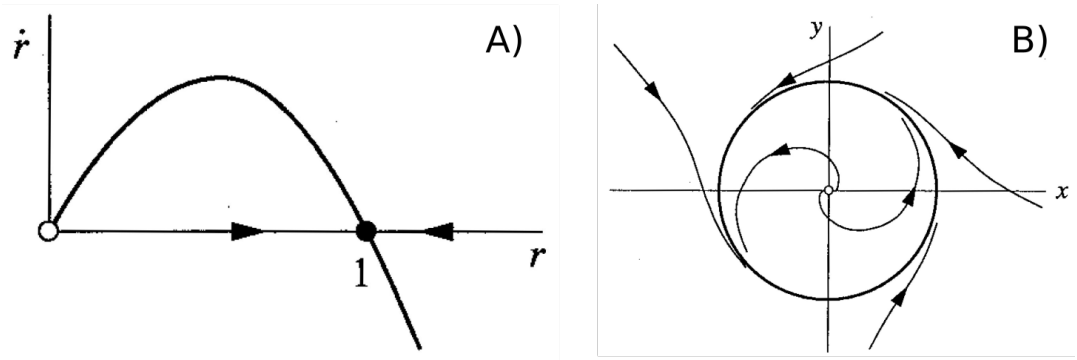

Figure 4.6: Limit cycle in B) described by the system in A), where where change of r, $\dot{r}$, is plotted versus r. At $0 < r < 1$, $\dot{r}$ is positive, and the solution will increase towards 1. At $r > 1$, $\dot{r}$ is negative and r will decrease towards 1. B) The solution in A) is given an angular velocity, resulting in a two dimensional plot, where the solution is rotating and will converge towards the radius 1.

reported in the present thesis. We were in contact with the lead author of [103] and informed him of our plans and initial studies before he published [103], but he never informed us of his intentions to publish a similar result, and this paper was only observed by us in the spring of 2021. From their experiments they calculated a gradient for how period changes with temperature, which they found to be dp/dT = - 8.0 min/°C for 34 °C - 37 °C and dp/dT = - 9.8 min/°C for 37 °C - 40 °C.

Background for the biological understanding of the NF-κB signaling pathway was given here. NF-κB was put into biological context, its functions were described, and many examples of how it can be activated were given. However, the NF-κB oscillations can be explained from another background, namely, the mathematical theories of dynamical systems and chaos, which gives a complete understanding and enables theoretical predictions.

4.5. NF-κB theory

Oscillations of NF-κB are well described by dynamical system- and chaos theory. An introduction to oscillatory dynamics and chaos is therefore provided here.

In a system, described by the function f, where a variable, for example, a position, x, is dependent on time, this system will often be described as a function of time. But it turns out that the system is easily described by letting the change of position, $\dot{x}$ be dependent on the position

$$\dot{x} = f(x). \tag{4.1}$$

In such an equation, where a time variable is excluded, it will often be easy to obtain a qualitative understanding, and calculations and especially modeling of a dynamical system

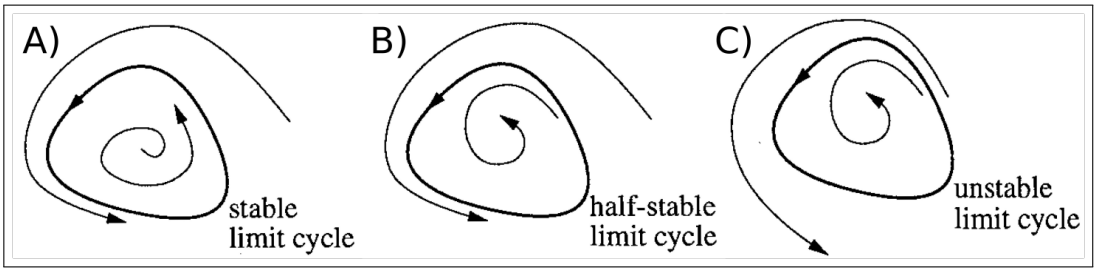

Figure 4.7: A) Stable limit cycle. The solutions will go towards the limit cycle. B) Half stable limit cycle. The solution outside of the limit cycle will go towards the limit cycle, and the solution inside the limit cycle will go towards 0, or the solution outside of the limit cycle will go towards infinity, and the solution inside the limit cycle will go towards the limit cycle. C) An unstable limit cycle. The solution inside the limit cycle will go towards zero, and the solution outside the limit cycle will go towards infinity.

will be simplified. If such an equation is modeled, and the time needs to be found, a time interval is assigned to each step taken described by $\dot{x}$, and the total time is found from adding up all steps.

Dynamical systems theory can be used to calculate variable changes in more than one dimension. An example of this is limit cycles in an x,y-plane. In a system, where r is the distance from the origin, and the rotational velocity is described by θ, the change of distance to the center, $\dot{r}$, is given by

$$\dot{r} = r(1 - r^2), \qquad \theta = 1. \tag{4.2}$$

In this system $\dot{r}$ is increasing towards 1 when $0 < r < 1$ and decreasing when $r > 1$, and will be constant when $r = 1$, as seen in figure 4.6 A). In the x,y-plane the solution to the equation will look as sketched in figure 4.6 B). The circle is called a limit cycle, and solutions will converge towards its value while rotating. Since solutions above and below the value of 1 will get increasingly close to 1, the limit cycle is stable, meaning that the solutions will be attracted to it and continuously converge.

As shown in figure 4.7 it is, besides the stable limit cycles, possible to construct both half-stable and unstable limit cycles. In a half-stable limit cycle, as seen in figure 4.7 B, when $r > 1$, the limit cycles will attract, but when $r < 1$ it will repel, or vice versa. In an unstable limit cycle, as seen in figure 4.7 C), a solution will always be repelled from the limit cycle and go towards infinity when $r > 1$, and converge towards 0, when $r < 1$.

These limit cycles describe systems where solutions will either be constant or converge or diverge towards fixed values. In the following example, rotating solutions are also discussed. However, a parameter is included in the differential equations, which, when varied, can result in a change of stability.

.

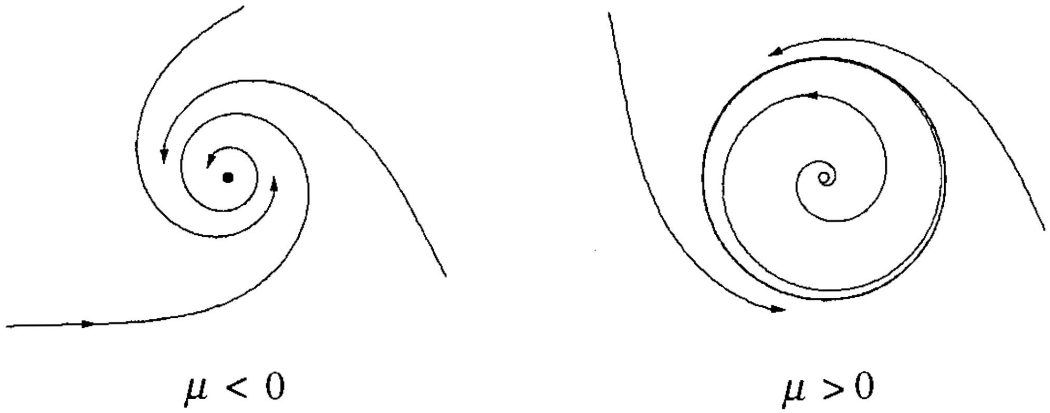

Figure 4.8: Supercritical Hopf bifurcation [104]. When $\mu < 0$ all solutions rotate around a stable fix point in the center. At $\mu = 0$ a Hopf bifurcation happens so that at $\mu > 0$ the stable fix point has turned into a stable limit cycle.

4.5.1. Hopf bifurcations

In a two-dimensional system with a stable fix point, the stability can change with a parameter, μ. The type of stability and the type of transition when changing μ can be described by the eigenvalues of the Jacobian, λ_1 and λ_2 [104]. If the eigenvalues have negative real parts, the system is stable, and if one or both of the eigenvalues have positive real parts, the system can destabilize. When such a system destabilizes, a Hopf bifurcation takes place. Here, the two types of Hopf bifurcations, supercritical and subcritical, are explained.

In a system described by the differential equations

$$\dot{r} = \mu r - r^3, \tag{4.3}$$

$$\dot{\theta} = \omega + br^2, \tag{4.4}$$

r is the radius, and θ is the angel. If the parameter μ is negative, the solution will rotate and move increasingly closer to the center, as seen in figure 4.8 for $\mu < 0$. If μ increases, there will be a cross-over point, where the stable fix point in the center will become an unstable fixpoint, and a stable circle with an increasingly larger radius will appear. This has happened in figure 4.8 for $\mu > 0$. This system is described as undergoing a Hopf bifurcation, with the bifurcation at $\mu = 0$.

A similar system can be described, where the bifurcation will describe the stability change from a stable fix point in the center and a stable limit cycle surrounding it, to only having a stable limit cycle. This system is described by the equations

$$\dot{r} = \mu r + r^3 - r^5 \tag{4.5}$$

$$\dot{\theta} = \omega + br^2. \tag{4.6}$$

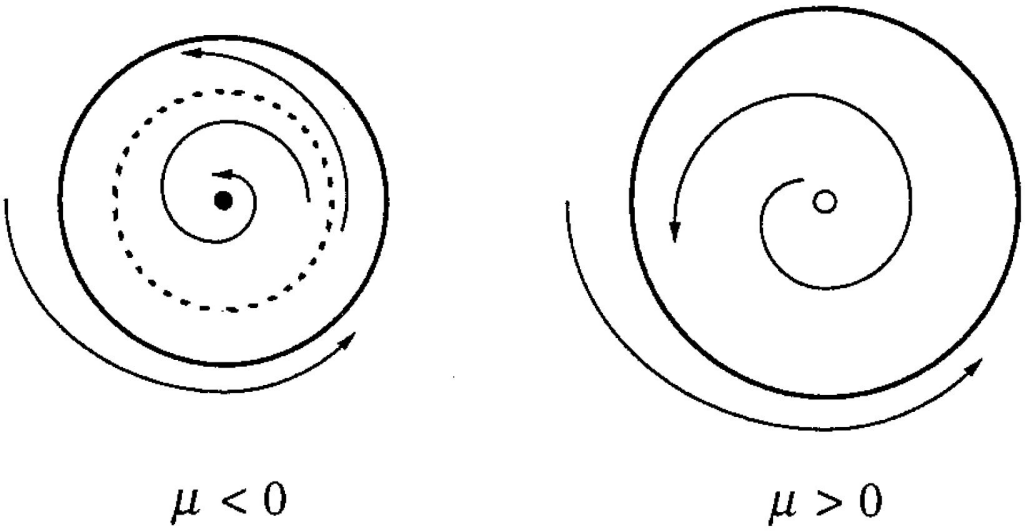

Figure 4.9: Subcritical Hopf bifurcation [104]. At $\mu < 0$, a stable fix point is present in the center, an unstable limit cycle surrounds that, and a stable limit cycle is shown as the outermost circle. At $\mu = 0$ a bifurcation occurs so that at $\mu > 0$ an unstable fix point in the center is surrounded by an unstable limit cycle.

If $\mu < 0$, the system has one fix point in the center, one unstable limit cycle surrounding the fixpoint, and surrounding the unstable limit cycle is a stable limit cycle, as seen in figure 4.9. As μ increases, the unstable limit cycle decreases its radius. At $\mu = 0$, the unstable limit cycle has reached the fixpoint, and a subcritical bifurcation occurs. At $\mu > 0$, the system has lost its stable fix point in the center and now has an unstable fix point instead. This means that all solutions will move towards the stable limit cycle.

Even though this behavior might seem like a surprise, the most surprising of the dynamic systems is when chaos is introduced. In the following, the Lorentz equations describe how chaotic behavior can appear in some dynamical systems.

4.5.2. The Lorentz equations

The first chaotic system discovered was described by the Lorentz equations

$$\dot{x} = \sigma(y - x), \tag{4.7}$$

$$\dot{y} = rx - y - xz, \tag{4.8}$$

$$\dot{z} = xy - bz, \tag{4.9}$$

where $\sigma, r, b > 0$. At certain parameter values, the solution will approach a limit cycle, like the one presented in 4.10 A). This is a stable limit cycle, just as the limit cycles presented in 4.6 B) and figure 4.7 A), but where those are two-dimensional, this is a three-dimensional limit cycle. This means that it has the property that if the solution is initialized in any

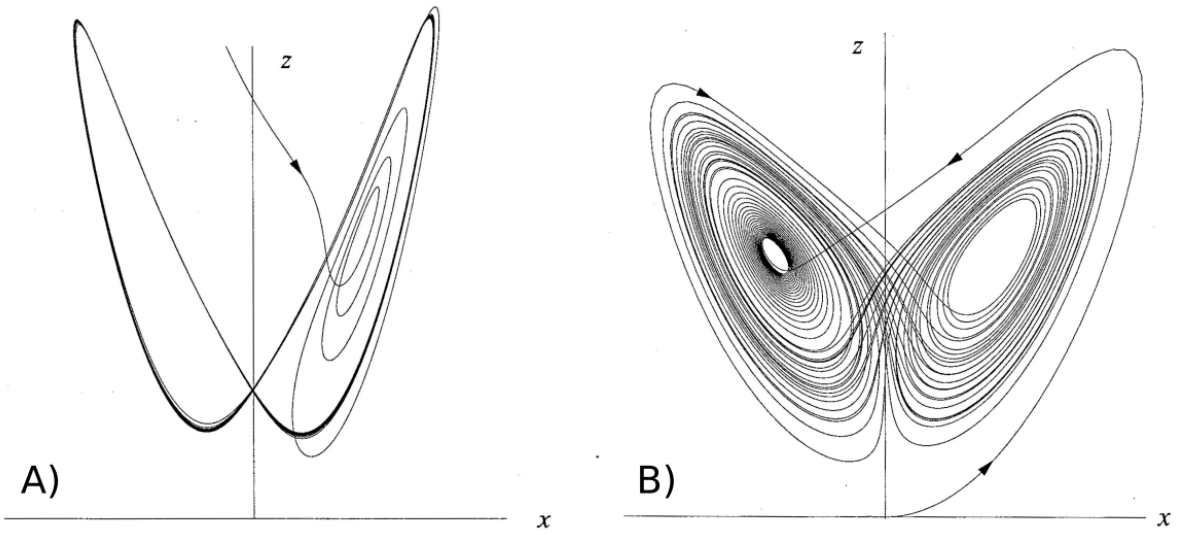

Figure 4.10: A) limit cycle in three dimensions. B) Chaotic behavior from the Lorentz equations resulting in the solution converging towards the limit cycle but repeatedly jumps out again. When in a chaotic regime, an initial condition inside of the limit cycle as in A) or an initial condition outside of the limit cycle as in B) will result in the same chaotic behavior.

position in the three-dimensional space, it will converge towards the limit cycle. However, if in this system the values σ, r and b are changed so that the Liapunov exponents are positive [104], the behavior will become chaotic. A chaotic system is presented in figure 4.10 B), and it shows that a solution will constantly converge toward the limit cycle, followed by drastic shifts towards positions that yet again are further away from the limit cycle. Such a system is called a chaotic attractor, and it has the property that it is hard to predict an exact solution. Therefore, when encountering real-world problems like these, modeling is used to predict the system's overall behavior. Despite the challenges associated with finding solutions at a specific number of steps, modeling this system will give a clear overall understanding of the system. In this case, the solution change position until the pattern looking like butterfly wings precipitates. So from such modeling, it cannot be predicted exactly where a solution is at a certain step, but it can be said that it is extremely likely that the solution is somewhere in the region of the butterfly wing pattern. Already in 2001, it was shown that genetic regulation could be described by limit cycles and that it was possible to tune the system to get into the chaotic regime [105]

As described below, both oscillations and chaotic behavior have been observed in theoretical models of the NF-κB system.

4.5.3. Dynamics and chaos in the NF-kB signaling pathway

Following the discovery of NF-κB oscillations[106], theoretical models capable of describing these oscillations were constructed[107]. In the following years, the equations describing

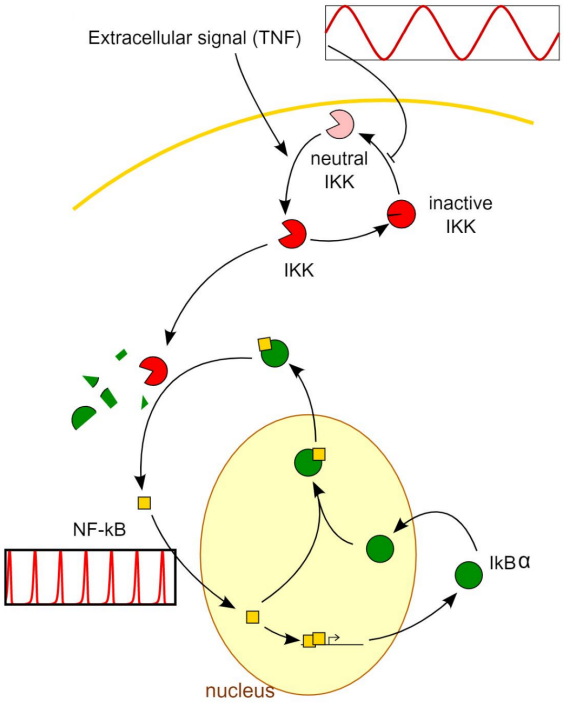

Figure 4.11: Theoretical model of the NF-κB signaling pathway described by five differential equations [108]. These equations allows for an oscillating TNF-α input to be coupled to the intracellular oscillations of NF-κB.

the system were further developed [108], reaching the five differential equations used in this work:

$$\frac{dN_n}{dt} = k_{Nin}(N_{tot} - N_n)\frac{K_I}{K_I + I} - k_{Iin} I \frac{N_n}{K_N + N_n} \tag{4.10}$$

$$\frac{dI_m}{dt} = k_t N_n^2 - \gamma_m I_m \tag{4.11}$$

$$\frac{dI}{dt} = k_{tI} I_m - \alpha [IKK]_a (N_{tot} - N_n)\frac{I}{K_I + I} \tag{4.12}$$

$$\frac{d[IKK]_a}{dt} = k_a [TNF]([IKK]_{tot} - [IKK]_a - [IKK]_i) - k_i [IKK]_a \tag{4.13}$$

$$\frac{d[IKK]_i}{dt} = k_i [IKK]_a - k_p [IKK]_i \frac{k_{A20}}{k_{A20} + [A20][TNF]} \tag{4.14}$$

With these differential equations, the NF-κB system can be modeled and show how effects such as oscillating TNF-α input and noise will affect the oscillations.

There are five differential equations in these equations, where each describes the rate of change of a variable. dN_n is the nuclear NF-κB; dI_m is the IκB messenger RNA; I is the IκB; IKK_a is the active IKK, and IKK_i is the inactive IKK.

The signaling pathway is illustrated in figure 4.11. Free NF-κB in the nucleus is up-regulating several hundreds of genes. When it forms a complex with IκB it translocates to the cytoplasm. Here it will stay until IκB is phosphorylated and subsequently degraded by

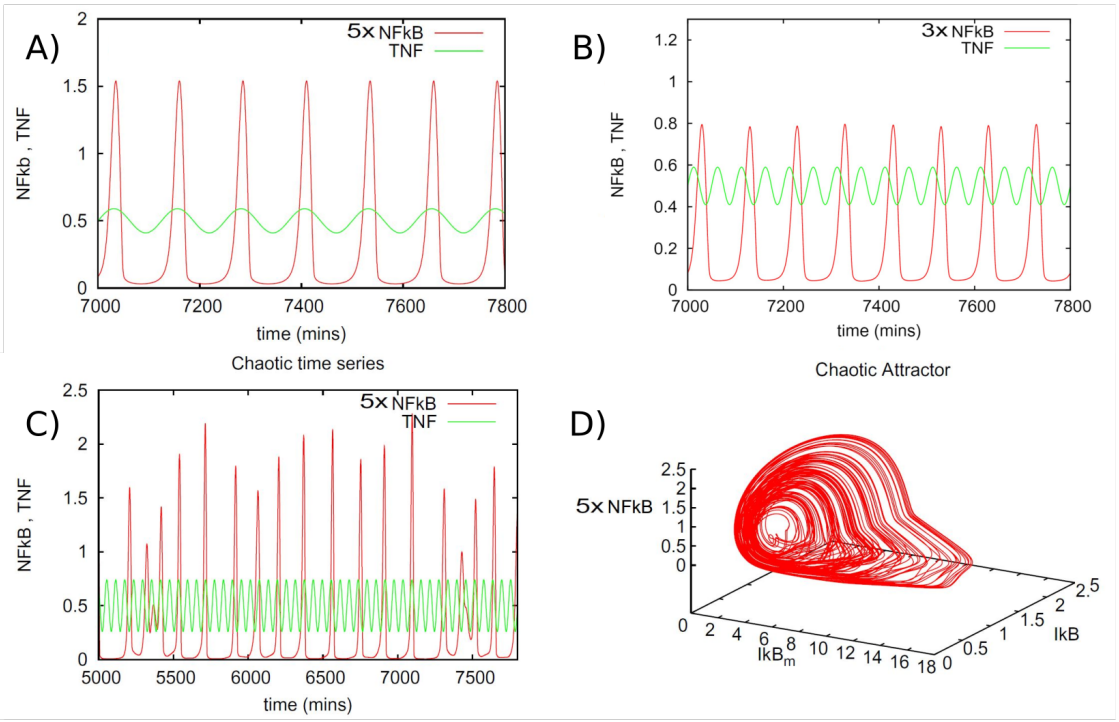

Figure 4.12: Theoretically coupled limit cycles and chaotic behavior in the NF-κB signaling pathway. A) TNF-α and NF-κB are coupled in a 1:1 ratio. B) TNF-α and NF-κB are coupled in a 2:1 ratio. C) Tuning the TNF-α to have a higher amplitude causes the NF-κ signaling to enter a regime, where amplitudes and periods are chaotic. D) Parameter space with dimensions NF-κB, IκB messenger, and IκB.

proteasomes. The phosphorylation is conducted by active IKK. In this model, IKK has three states: Active, inactive, and neutral, which in the equations are termed $[IKK]_a$, $[IKK]_i$ and ($[IKK]_{tot}$-$[IKK]_i$-$[IKK]_a$), respectively. TNF-α stimulates the signaling pathway in two ways; it increases the activation of active IKK from neutral IKK; and when in a complex with A20, it inhibits the conversion of inactive IKK into neutral IKK.

In this model, a constant TNF-α input will result in the oscillation of the nuclear and cytoplasmic NF-κB.

In [108] it was found that oscillating the TNF-α input will result in different exotic behavior of the NF-κB oscillations. In figure 4.12 A) and B) it is shown, that with the equations described above, oscillating the TNF-α signal will at some parameter values result in a coupling between the TNF-α signal and the NF-κB oscillations. In figure 4.12 A) the frequency of TNF-α and NF-κB is the same at $1/2.08$ h^{-1}, and there is a 1:1 coupling. In figure 4.12 B) the frequency of TNF-α is $1/0.83$ h^{-1} and NF-κB has a frequency of $1/2.5$ h^{-1}, and there is a 3:1 coupling. The oscillations will couple at different ratios at different parameter values, described by Arnold tongues [109]. However, as shown in figure 4.12 C), at some parameter value, the NF-κB signaling pathway will enter a chaotic regime. In this case, the amplitude increases from 0.09 in A) and B) to 0.24 in C). Here NF-κB signal undergoes chaotic behavior,

and both the amplitude and the frequency are unpredictable, as in the Lorenz equations described in section 4.5.2. In 4.12 D), the chaotic behavior seen in C) is presented in parameter space. It is seen how the solutions exist in a cone shape and are not bound to a specific limit cycle, as would have been the case if the solutions of A) and B) were plotted.

The ability to couple the TNF-α oscillations to the NF-κB cell oscillations were experimentally demonstrated [110] in a microfluidics setup. By simulations, it was shown that increasing intrinsic noise in the system would increase transcription output [111].

Entrainment of the NF-kB signal with microfluidics has since been repeated [112]. It was shown that a higher forcing amplitude would cause more entrained NF-κB oscillations. It was possible to show synchronous cell oscillations down to a forcing period of 60 min, where the TNF-α amplitude was in the range of 0 ng/ml to 10 ng/ml. After turning off forcing, cell synchronization stops. In order to understand how the gene output was related to the entrained NF-κB oscillations, the gene output was measured by microarray analysis. Cells were entrained into a period of 180 min, which resulted in the mRNA concentrations of early genes, mainly encoding for cytokines and cytokine receptors such as IκB, would oscillate with the same frequency. This suggests that by entraining the NF-κB oscillations, the gene output will couple to the NF-κB oscillations. Other gene clusters with intermediate or late genes would show different gene expression patterns. For example, genes encoding for proteins involved in the immune system would increase for the first three hours and thereafter decrease at a lower rate, while genes encoding for proteins in the extracellular matrix would increase over the entire range of the experiment at more than 9 hours.

The impact of chaos in NF-κB oscillations was thoroughly investigated [111]. It was found that when increasing the forcing amplitude of TNF-α, the NF-κB oscillations would first jump into a multi-cycle and then into a chaotic regime, which is understood by the concept of Arnold Tongues. Furthermore, it was tested how entering the chaotic regime would impact the regulation of high-affinity and low-affinity genes. It was discovered that entering a chaotic regime would change the relative gene output favoring the low-affinity genes. It was furthermore suggested that chaos might up-regulate specific complexes of proteins and be beneficial for cell heterogeneity.

4.6. Methods

For the NF-κB experiments with MEF cells, the most essential assay was the flow system, which was described in depth in chapter 3. Here, the procedure for initiating the experiments in this system is explained. Also, the remaining methods from the final setups are described, namely, the single well experiments, cell culturing, microscope, heat control, and

data analysis.

4.6.1. Cell culturing

The cells utilized in the NF-κB experiments were 3t3 mouse embryonic fibroblast (MEF) cells from [84]. To monitor NF-κB transcription factor p65, the cells were stably transducted with DsRed as the genome sequence, subsequent to the p65 gene, meaning that DsRed was coexpressed with p65 to form the p65-DsRed fusion protein. Moreover, a GFP tag was stably transducted to be coexpressed with histones, more precisely the H2B protein, to clearly being able to locate nuclei inside the cells, however, because this exposure caused necrosis, as decsribed in the flow chapter section 3.3, GFP was not used as a fluorescent tag in this thesis. Transductions were performed with the lentivirus.

The incubator used for cell culturing was the HERA CELL VIOS 160i CO_2 incubator. Until the initiation of the experiments, cells were cultivated at 37 °C and 5 % CO_2 with a Gibco^{TM} DMEM culture medium with high glucose, L-Glutamine, phenol red, no Sodium Pyruvate, no HEPES, + 10 % fetal bovine serum and + 1 % Penicillin-Streptomycin (PS).

4.6.2. µ-well experiments

The single well experiments were conducted in Collagen-coated, γ-radiated, 35 mm, No. 1.5 glass bottom µ-well dishes [113]. They were seeded 48 hours prior to the initiation of the experiments and kept in culture conditions as described above. When initiating the experiments the µ-wells were transferred to the microscope 15 min prior to this. In the Oko Lab cage incubator [61] the CO_2 was kept constant, and the temperature was at the specific target temperature for the experiment. The medium used during the experiments was the Gibco^{TM} DMEM culture medium with high glucose, HEPES, L-Glutamine, no phenol red, and no Sodium Pyruvate with + 10 % FBS and + 1 % PS. Two minutes prior to the start of the experiment, where the time-lapse microscope routine was initiated, 40 ng TNF-α to a total concentration of 40 ng/ml. Approximately 10 positions inside each µ-well were imaged, and all positions were captured every 10 min, using bright-field microscopy and the red laser channel, activating DsRed. For the double addition experiments, the procedure was identical up to this step. However, in those experiments, another addition of TNF was added at t = 38 min., two minutes before the fourth image capturing time point. At this time, 50 ng was added to the concentration to a total of 5 ml medium. This resulted in a total TNF-α mass of 90 ng, and a final concentration of 18 ng/ml.

4.6.3. Flow experimental procedure

Before each flow experiment, extensive measures were taken to reduce gas formation in the flow system. The process of reducing gas formation and the concrete solutions aimed at reducing gas is described in flow section 3.3.3. A simple sketch of the setup is found in 4.13 and the procedure for flow experiments are described in the following.

MEF cells were seeded on in Ibidi sticky slides [114] on D 263 M Schott glass, No. 1.5H [115] 48 hours prior to the experiments. Approximately three hours before the start of the experiment, the 40 ml medium was degassed for 90 min. After this, it was filtered with 0.2 µ-filter, which was extremely important to prevent bacteria after the medium was exposed to the open degassing environment. After this, the 50 ml falcon tube was sealed and heated to room temperature with the lid on to prevent gas from re-entering. The medium was divided into two parts of 20 ml degassed medium, where 1 ng TNF-α per ml was added to one portion. The tubing and sample were thereafter assembled inside the flow hood, and Phenol Red free medium was injected so that the entire flow system, including the two bubble traps, was filled up. The inlet was sealed, tubes were clamped, and the assembled tubing and bubble traps were brought to the microscope, and without disassembly, it was inserted through the microscope enclosure and into the incubator cage. The outlet was then let out to a glass beaker on top of the microscope. The medium containing TNF-α was filled into a 60 ml syringe, sealed, and brought to the microscope. The seals of the tubing inlet and the syringe outlets were both removed and quickly assembled. The syringe was placed in the pump, and the motor-controlled injection was initiated. The time-lapse microscope was initiated after this, even though it took approximately 36 hours before oscillations were visible.

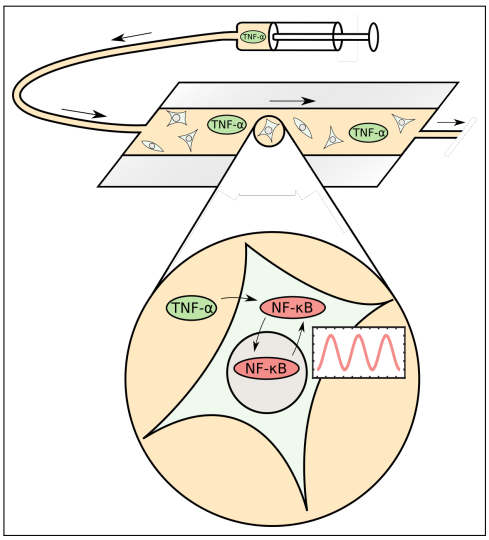

Figure 4.13: Simple schematic of the flow setup. From a syringe, TNF-α-containing medium is injected into the flow chamber. Here, NF-κB in the MEF cells will start to oscillate between the nucleus and the cytoplasm.

4.6.4. Microscopy

For the experiments described in this chapter, a Nikon Eclipse TI [59] fluorescent microscope was used. For activating the DsRed protein, an excitation filter at 575 nm built into the microscope was used, with light originating from a Lumencor Sola Light Engine solid-state illumination source [116]. The built-in emission filter at 641 nm captured the DsRed emission

wavelengths. Both bright field and fluorescence images were captured by an Andor Neo sCMOS model DC-152Q-COO-FI [117] camera.

4.6.5. Heat control

The temperature inside the incubation chamber was controlled by a Warner Duel Automatic Temperature Controller TC-344B [62], with a total of four resistances, where two were closer to the sample, and two were closer to the surrounding glass cage. Two resistances closest to the cage were set to constantly provide 6 V, while the two closest to the sample were set to automatically target a temperature, monitored by a thermometer attached to the top of the flow chamber or onto the bottom of the cage incubator when performing μ-well experiments. This temperature was in all experiments set to be two °C higher than the temperature of the Oko heating unit H201-T-0016 [61]. Before these experiments, μ-well calibration experiments had shown that medium inside the μ-wells was 1.0 °C lower than the temperature on the bottom of the cage incubator, so the temperature controller was set to a target temperature of 1.0 °C higher than the temperature that the experiment was aiming at targeting.

4.6.6. Data analysis

Before cells were analyzed, single cells were selected with clear oscillations, and where cells were not mistaken for other cells during the time span of the measurement. A crop of the smallest possible area was taken of the image series. For the analysis of the selected cells, a Matlab program was built to analyze the NF-κB oscillations. In the Matlab program, values for a circle radius of the intensity measurement in the nucleus and a value for the circle radius of the cytoplasm were chosen. The radius for these circles in pixel was set to be between 3 and 5, specified after evaluating the cell size. In the images, this pixel interval corresponds to an interval of between 1.0 μm and 1.7 μm, which again correspond to areas of between 27 pixels and 79 pixels or 3.1 μm^2 and 8.7 μm^2. It turned out that it was advantageous to have two analysis methods so that one would serve to give a qualitative understanding of the oscillations, which was more time consuming to conduct, and one would give a quantitative analysis of the oscillations, which was faster and less precise but which, however, utilized power spectrum analysis to improve the period precision. Both utilized the method described above, but they differed in the following ways:

4.6.7. Quantitative Period Extraction Method

In the Quantitative Period Extraction Method, only two intensity measurement on each image was conducted. One in the cytoplasm and one in the nucleus. Each cell was analyzed

for between 90 min and 770 min., which corresponds to between 2 and 11 oscillations. The nuclear to cytoplasm intensity ratio was calculated for each time point, and its mean was subtracted to center the ratio around zero. Subsequently, a power spectrum was performed. In the power spectrums, a peak would always be present near the observed oscillations frequency. This peak would represent the oscillation frequency, and the period for each cell was found from taking the inverse of this value.

4.6.8. Qualitative Period Extraction Method

The Qualitative Period Extraction Method would give a more precise analysis by measuring four different positions in each cell nucleus and each cell cytoplasm, totaling eight intensity measurements per image. The data were then smoothed by the Matlab Smooth function with a span of 4. In order to subtract noise at a larger time scale than the oscillations, the Matlab Smooth function was used once more: The result from the Smooth function with a span of 13 data points was subtracted to all data points that before was smoothed by 4.

4.6.9. Amplitude analysis

In order to quantify the amplitudes from the NF-κB oscillations, a Matlab script was explicitly designed for this purpose. Before this analysis was initialized, the periods were already found from the Quantitative Data Analysis Method. To find the number of oscillations in a nuclear to cytoplasm intensity data series, the length of the time series was divided by the period. This gave the number of data points per oscillation. This number was rounded to an integer value so that it could be used in the script. From these data points, the mean was extracted, and afterward, the root mean square (RMS) was calculated. This gave a measure on how much the wave deviated from the mean at zero, and thereby it could be related to the amplitude, where the RMS is approximately 0.71 of the amplitude.

4.7. Pilot experiments

Since NF-κB is considered a cell response for various stresses, pilot experiments were conducted to see what types of stresses would cause activation of NF-κB. If it was possible to activate NF-κB by stress alone, the plan was to oscillate the stress input to investigate whether this would couple to the NF-κB oscillations.

4.7.1. Apoptosis, necrosis, and healthy cells

In the wide variety of stresses that were tested, the outcomes of the experiments are here divided into categories. First, there is the possibility that cells are healthy and show NF-κB activation. This will be expanded on in section 4.8. Secondly, the experiments that did not show NF-κB oscillations are divided into three categories, with two categories describing different cell deaths. Examples of these are seen in figure 4.14 and figure 4.15. They are divided into healthy cells without NF-κB activation in figure 4.14 A) - C), cells undergoing necrosis in 4.14 D) - F), and cells undergoing apoptosis in 4.14 G) - I).

When cultivated under appropriate conditions, each cell will spread out and increase its surface area attached to the substrate surface. Also, from division, healthy cells are multiplying. These two behaviors will increase the confluency over time, as seen in figure 4.14 A) - C), where the confluency increases significantly over 670 min. In 4.14 D) - F) and example of necrosis is presented. Here, cells are primarily looking healthy at t = 0 min. As time progresses, the surface area of the cells attached to the surface decreases, while the cell volume is typically increasing. The shape of the cells becomes more spherical, and the cells start to detach from the surface. This, together with a lack of cell division, is seen as decreased confluency at t = 670 min compared to t = 0 min. In 4.14 G) - I) and example of apoptosis is observed. During the process, cells will decrease their cell volume while maintaining their attached surface area at the beginning. Cells will obtain a more spiky shape, increasing their number of spikes from approximately 3 to more than 10. During apoptosis, fibroblast cells will not divide, and after few hours, they will undergo programmed cell death. In figure 4.14 I), the two cells in the center are late in the apoptotic process, and their membranes are degenerating, and small pieces of the cells' membrane and interior are detaching from the rest of the cell. Despite being this late in the apoptotic response, the cells are still attached to the surface, with approximately 50 % of the original attached surface area.

The NF-κB response was investigated and evaluated after the four scenarios of necrosis, apoptosis, healthy cell growth without NF-κB activation, and healthy cell growth with NF-κB activation. Healthy cell growth where NF-κB remains upconcentrated in the cytoplasm is seen in figure 4.15 A). This is an example of unactivated NF-κB. During necrosis, seen in figure 4.15 B), biological cell mechanisms will stop functioning, and NF-κB will no longer be reserved to the cells' cytoplasms. Instead, the transcription factor will become increasingly more spread out in between cytoplasm and nucleus. In apoptosis, as shown in figure 4.15 C), the NF-κB in the left cell that is later in the apoptotic process will permanently be evenly distributed between cytoplasm and nucleus. The cell to the right in the image, however, is not

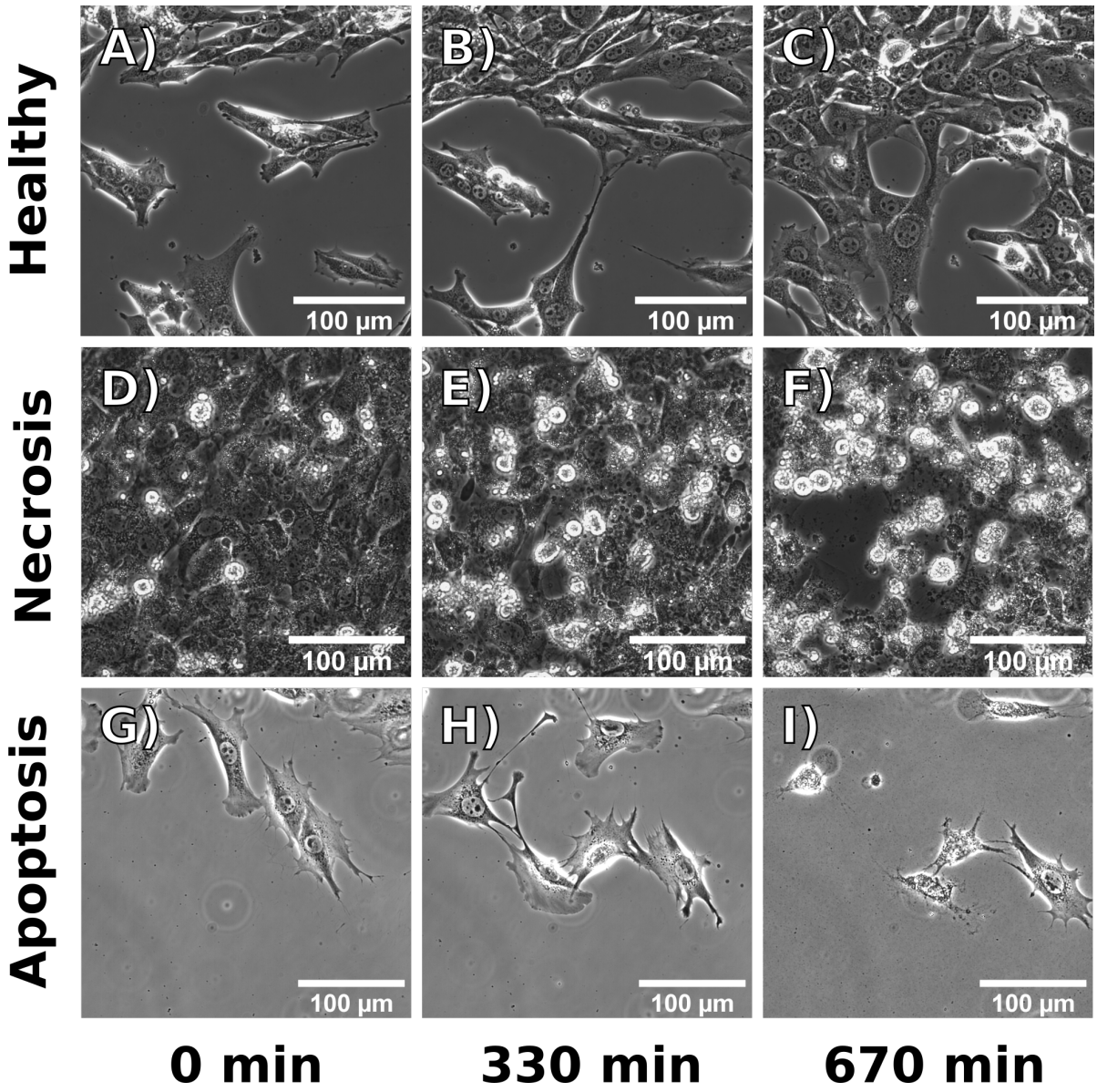

Figure 4.14: Fibroblast cell survival. Healthy cells growing in A), B), and C), where cells are multiplying and the confluency increases. Cells undergoing necrosis in D), E), and F), where cells become spherical and detach from the substrate. Cells are undergoing apoptosis in G), H), and I) and initiate programmed cells death. Cells are degenerating while one is remaining attached to the surface.

as late in apoptosis. In this cell, NF-κB is still located in the cytoplasm. These images serve as a general example of how cells react under apoptosis. NF-κB would be upconcentrated in the cytoplasm until a certain level of apoptosis was reached, and after this, NF-κB would be delocalized.

4.7.2. Physical, chemical and biological stress

A range of different pilot stress experiments was conducted in this project. Those that, in combination with TNF-α, resulted in NF-κB oscillations are described in section 4.8, while

Experiment	**Outcome**
Heat shock 90 min., 39 °C	No NF-κB response
Heat shock 90 min., 41 °C	No NF-κB response
Heat shock 90 min., 43 °C	Necrosis + no NF-κB response
Heat shock 15 min., 45 °C	Necrosis + no NF-κB response
37 °C to 48 °C in 2 hours	Necrosis
Single cell stretch	No NF-κB response
10 cell stretches	No NF-κB response
LED exposure at 466 nm	Necrosis or no NF-κB response, depending on exposure time
No CO_2 until cell death	Necrosis
Flow stress at ∼927 nN for 5 min	No NF-κB response
Flow stress at ∼927 nN for 15 min	No NF-κB response
Flow stress at ∼927 nN for 1 hour	No NF-κB response + lower confluency + necrosis
Flow stress at ∼927 nN for 2 hours	No NF-κB response + lower confluency + necrosis
Different magnitudes of flow stress at less than 927 nN for various time intervals	No NF-κB response or lower confluency + necrosis, depending on time span and magnitude of flow
Flow shock	Lower confluency by > 99 % + No NF-κB response
Bubbles flowing across chamber	No NF-κB response + lower confluency or necrosis + lower confluency, depending on the size, flow speed and time span of the bubbles
100 ng/ml TNF-α in µ-wells	Apoptosis
10 ng/ml TNF-α in µ-wells	observed NF-κB oscillations
1 ng/ml TNF-α in µ-wells	observed NF-κB oscillations
0.1 ng/ml TNF-α in µ-wells	weakly observed NF-κB oscillations
0.01 ng/ml TNF-α in µ-wells	No measurable NF-κB activation
10 ng/ml TNF-α in flow	Apoptosis
1 ng/ml TNF-α in flow	observed NF-κB oscillations
0.1 ng/ml TNF-α in flow	weakly observed NF-κB oscillations

Table 4.1: Overview of experiments where NF-κB was exposed to chemical or physical stress.

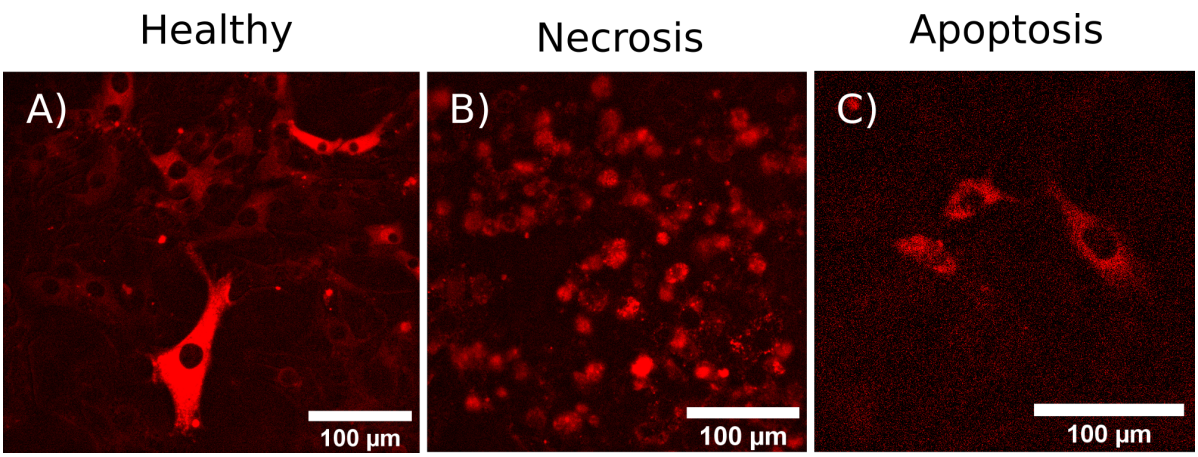

Figure 4.15: NF-κB response in healthy cells without physical or chemical stress in A). Here, NF-κB is upconcentrated in the cytoplasm. NF-κB in the necrotic cells in B) shows an evenly distribution throughout the cytoplasm and nucleus. In C) the NF-κB is upconcentrated in the cytoplasm of the apoptotic cells, while NF-κB in the left-most cell is starting to delocalize

the rest are described immediately below. The outcomes of these experiments are collected in table 4.1.

Heat shock

Heat shock experiments were conducted in time spans of either 90 min or 15 min. at temperatures of 39 °C, 41 °C, or 43 °C for 90 min., and at 43 °C or 45 °C for 15 min. At 39 °C and 41 °C for 90 min. cells were healthy and did not show any NF-κB activation. When increasing the temperature to 43 °C for 90 min and 43 °C or 45 °C for 15 min., some cells became necrotic while others survived. None of the surviving cells showed NF-κB oscillations.

Cell stretching

Cells were stretched with the Strex STB100 cell stretcher. Experiments where cells were stretched once and kept in a fully stretched position while imaged, was carried out. Also, experiments where cells were fully stretched and returned to original conditions 10 times in 10 min., were conducted. In both cases, cells survived, but no NF-κB response was observed.

466 nm LED exposure

Cells were exposed to the 466 nm excitation LED lamp in the JuliStage setup with various imaging frequencies and LED powers. At the lowest power available in the setup at above 7 min. exposure intervals, cells survived, but NF-κB activation was not observed. At the same power but with exposure intervals below 7 min., cells would undergo necrosis.

Culturing without CO_2

Cells were cultured without CO_2 until necrosis was observed. No NF-κB response was observed during this process.

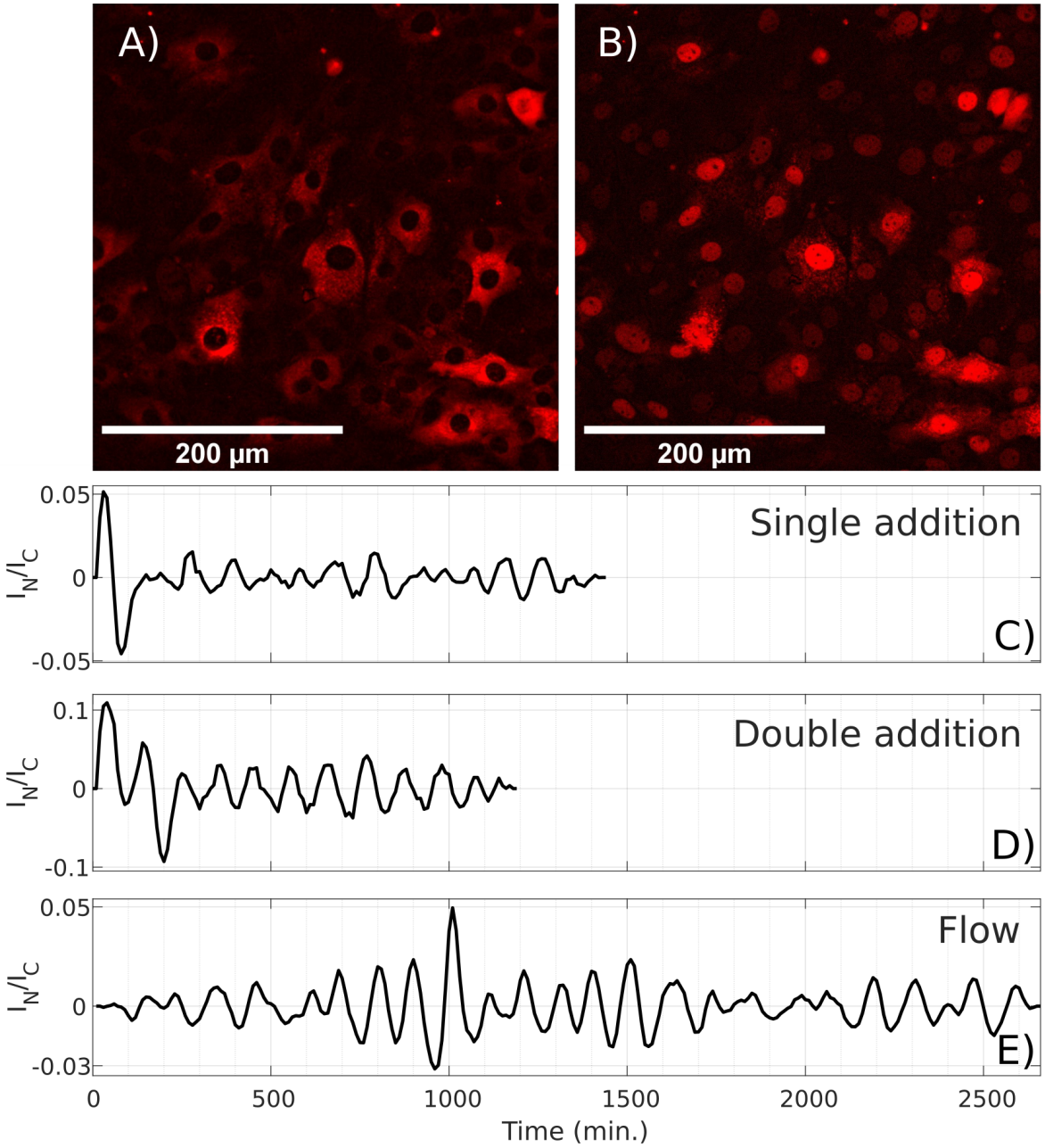

Figure 4.16: Fluorescence microscopy data showing NF-κB oscillations in Mouse Embryonic Fibroblast (MEF) cells. A) NF-κB is primarily located in the cytoplasms in a µ-well experiment at t = 0 min. after 10 ng TNF-α/ml exposure at t = −2 min. B) NF-κB is primarily located in the nuclei in the same µ-well experiment as in A), but at t = 20 min., which is a clear indicator of nuclear translocation of NF-κB. C) Nuclear to cytoplasm ratio (I_N/I_C) versus time was measured after adding 10 ng TNF-α/ml to µ-wells at t = −2 min. D) I_N/I_C versus time where 10 ng TNF-α/ml was added at t = −2 min and the concentration was again increased at t = 38 min to a total of 18 ng TNF-α/ml. E) Flow experiments where the TNF-α concentration was converging towards 1 ng/ml during the entire range plotted.

Gas formation

In the order of 100 experiments were terminated due to gas formation in the flow system. Some of these gave helpful information about avoiding gas formation in the flow system or scientific discoveries regarding cell oscillations before the bubbles were observed in the chamber. When bubbles were flowing through the flow chamber, mechanical forces were

exerted on the cells by the bubbles. This was concluded from cells detaching while the bubble boundaries were crossing the cells. After detaching, cells would typically stay in the boundary of the bubbles and flow out of the flow chamber with them. Besides a mechanical force, cells are also exposed to gas instead of medium when gas flows into the chamber. The chemical conditions are therefore also changing. When small quantities of gas entered the chamber, cells would seem unaffected, but at larger quantities, cells would undergo necrosis, detach from the surface, and flow out of the chamber, or, if cells were oscillating with NF-κB, the oscillations would terminate.

Flow stress

Flow stress was performed with two methods: By creating a flow with a specific flow speed and well-estimated force per cell as described in flow section 3; and by letting pressure build up inside the flow system while having clamps attached to the outlet, so liquid was prevented in flowing out, and after that detaching the clamp, so that the pressure was equalized within few seconds, creating an extremely high flow peak, compared to the other flow experiments with higher experimental control. The latter experiment removed most cells instantaneously. Only a few cells along the corners would remain, and these did not show NF-κB activation. Several flow speeds and time spans were tested in the flow experiments with a constant flow speed for a more extended time period. The highest flow speed of 1630 μm/s at the positions of the cells, with a force of ~ 930 pN per cell, was used for the following time spans: 5 min. and 15 min., in which cells survived but no NF-κB activation was observed, and 1 hour and 2 hours, in which confluency was lowered. After this, most remaining cells could not recover when the flow was stopped, so it was concluded that they had undergone necrosis. The few cells that survived did not show any NF-κB activation.

TNF-α

In the pilot experiments, a TNF-α concentration varying within a factor of 10,000 was tested to find concentrations at an appropriate level for further experiments in the project. In μ-well experiments, it was found that cells would undergo apoptosis with a TNF-α level of 100 ng/ml. At a concentration of between 0.1 ng/ml and 10 ng/ml, cells survived. At 10 ng/ml, the signal-to-noise ratio was highest, and at 0.1 ng/ml, the low signal-to-noise ratio resulted in oscillations that were difficult to measure in the analysis programs. Therefore 10 ng/ml was chosen for the μ-dish experiments described later in this chapter. When the flow system was tested with 10 ng TNF-α/ml, cells underwent apoptosis, even though the same TNF-α level did not cause apoptosis in the μ-well experiments. NF-κB oscillations were observed in the flow system with 0.1 ng/ml and 1 ng/ml TNF-α. Since 1 ng/ml resulted in the best signal-

to-noise ratio of the oscillations, this value was chosen for the rest of the flow experiments described in this chapter.

4.8. NF-κB oscillations

It was found that under the appropriate culturing conditions, found in section 3.3, and with a TNF-α concentration in a range, where oscillations were visible but still did not result in apoptosis, as described in section 4.7.1 and 4.7.2, NF-κB oscillations were observed. Three different assays were used for these findings: A flow experiment, in which the TNF-α concentration was converging towards a level of 1 ng/ml for flow experiments, as presented in figure 3.13. A single addition experiment in µ-wells, where 10 ng/ml was added at t = −2 min., and a double addition experiment, where 10 ng TNF-α was added at t = −2 min., with a second TNF-α increase to a total of 18 ng/ml at t = 38 min.

In a µ-well experiment presented in figure 4.17 A) and B) of the same field of view, nuclear translocation of NF-κB is observed. The images are from single addition µ-well experiments with 10 ng TNF-α/ml, and it shows the fluorescent signal from the p65-DsRed protein, which in the following will be termed the NF-κB signal. In A) at t = 0 min. the signal is primarily located in the cytoplasm and in B) at t = 20 min. NF-κB is primarily located in the nucleus. TNF-α is added to the solution at t = −2 min. Afterward, NF-κB translocates into the nucleus, observed at t = 20 min. in B). From the hundreds of hours of experiments, without NF-κB translocation, described in section 4.7.2, and from the fundamental NF-κB dynamics, described in section 4.5, the translocation of NF-κB is concluded to origin from the TNF-α stimulus.

A major part of this project was to obtain a deep understanding of how NF-κB oscillations changed under various conditions. To obtain a deeper understanding of this, graphs of the ratio of nuclear NF-κB to cytoplasmic NF-κB versus time were essential. It was required to analyze data of high-quality cell oscillations under various conditions and to have a large number of cells under various conditions for the statistical analysis. To solve this problem, two analysis methods were therefore developed. A Qualitative Period Extraction Method, described in the methods section 4.6.8, and a Quantitative Period Extraction Method, described in methods section 4.6.7. The Qualitative Period Extraction Method analyzed each image in much greater detail and did subsequent noise subtraction, while the Quantitative Period Extraction Method analyzed each image much quicker without doing subsequent noise subtraction. Instead, in the latter, power spectrum analysis was performed to obtain periods from the lower quality oscillation data. The raw image data was, however, the same in the two analysis methods. They were obtained with the Nikon Eclipse TI time-lapse microscope,

as described in methods section 4.6.4, with an image capturing interval of 10 min. In the following, a description of the two analysis methods is provided.

4.8.1. Qualitative NF-κB oscillation analysis

All graphs in figure 4.17 are analyzed by the Qualitative Periods Extraction Method. In figure 4.17 C) a μ-well experiment similar to the experiment in A) and B) is plotted. It is seen how NF-κB oscillates between cytoplasm and nucleus throughout the entire range of the experiment of 1440 min., equivalent to 24 hours and 0 min. By counting the number of oscillations in this experiment, which is 15, a period can be calculated to be $\frac{1440\text{min}}{15\text{oscillations}} = 96\text{min/oscillation}$. In this experiment, the first oscillation is observed to have a higher amplitude, while all following oscillations have approximately equivalent amplitudes.

In figure 4.17 D) a double addition experiment is plotted. In the double addition experiments, the TNF-α concentration is increased twice. At t = −2 min. 10 ng TNF-α/ml is added; at t = 0 min. the time-lapse microscope initiates the imaging routine. At t = 38 min., 2 min. prior to the fourth data point, the TNF-α concentration is increased from 10 ng/ml to 18 ng TNF-α/ml. In the graphs, the two initial oscillations have higher amplitudes than the subsequent oscillations, whereas the first has a higher amplitude than the second. Throughout the entire experiment spanning 1190 min., equivalent to 19 hours and 50 min., a total of 12 oscillations are observed. This results in a period of $\frac{1190\text{min}}{12\text{oscillations}} = 99\text{min/oscillation}$.

Figure 4.17 E), a plot of cellular NF-κB oscillations in a flow experiment is presented. In this experiment, the medium flowing into the system has a TNF-α concentration of 1 ng/ml. An experiment of the upconcentration of a chemical in terms of % was presented in the flow chapter, section 3.4.3. t = 0 in figure 4.17 E) corresponds to 36 hours in the graph of chemical upconcentration. We see that when TNF-α is upconcentrated in the flow system, until 1000 min. in figure 4.17 E), the amplitudes are increasing. During this time span, the TNF-α increases from 0 ng/ml to approximately 0.5 ng/ml %. The amplitude was approximately constant throughout the remaining experiment of 2650 min., equivalent to 44 hours and 10 min. Throughout the entire experiment, the period is approximately constant. A total of 25 oscillations are counted, resulting in a period of $\frac{2500\text{min}}{25\text{oscillations}} = 100\text{min/oscillation}$.

These experiments were analyzed with the Qualitative Period Extraction Methods, which enabled a general understanding of the NF-κB oscillations. It was observed that the oscillations were roughly shaped as sinusoidal waveforms. This was different from other experiments, where oscillations closer resembled spikes [112] [107].

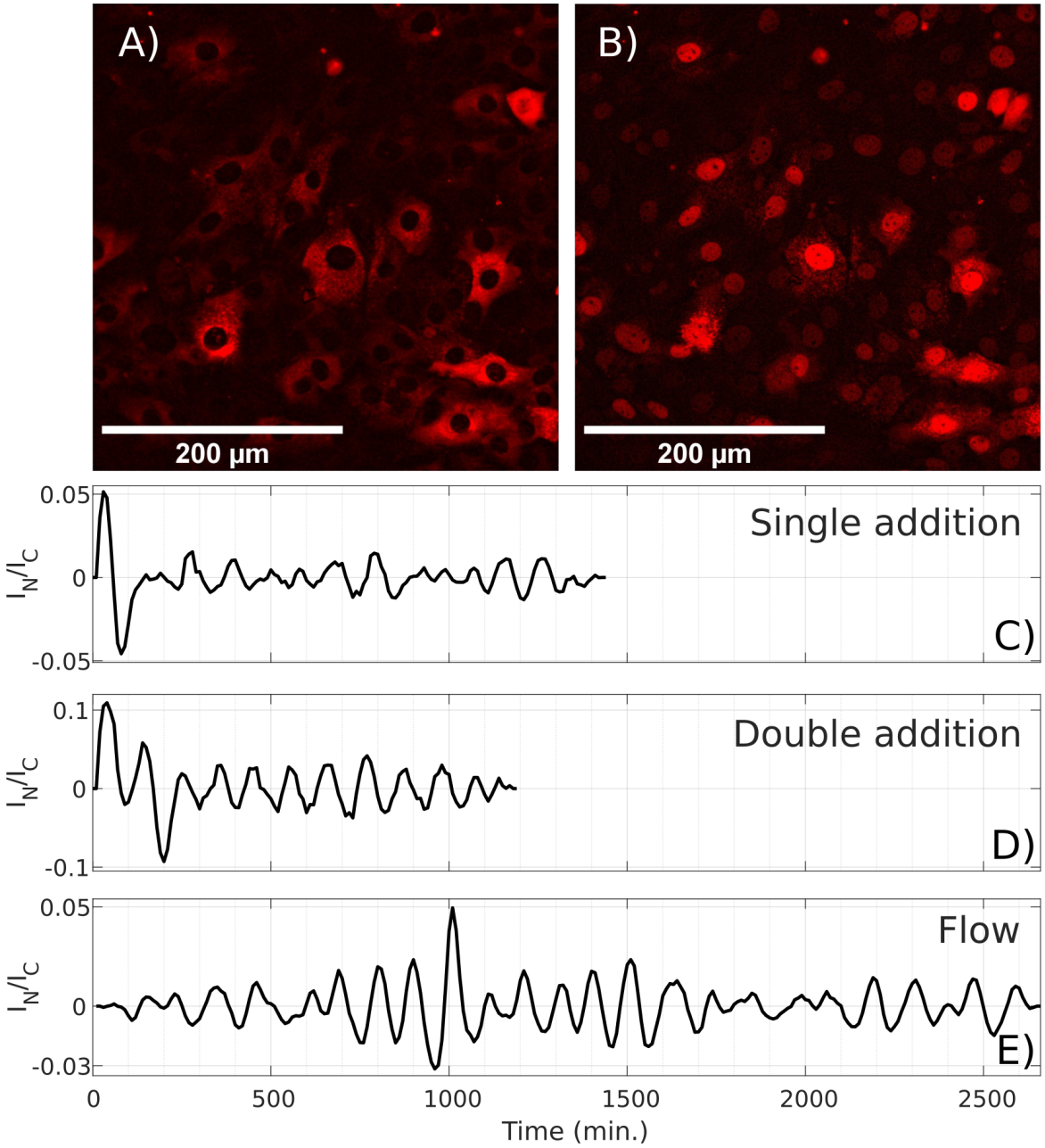

Figure 4.17: Fluorescence microscopy data showing NF-κB oscillations in Mouse Embryonic Fibroblast (MEF) cells. A) NF-κB is primarily located in the cytoplasms in a µ-well experiment at t = 0 min. after 10 ng TNF-α/ml exposure at t = −2 min. B) NF-κB is primarily located in the nuclei in the same µ-well experiment as in A), but at t = 20 min., which is a clear indicator of nuclear translocation of NF-κB. C) Nuclear to cytoplasm ratio (I_N/I_C) versus time was measured after adding 10 ng TNF-α/ml to µ-wells at t = −2 min. D) I_N/I_C versus time where 10 ng TNF-α/ml was added at t = −2 min and the concentration was again increased at t = 38 min to a total of 18 ng TNF-α/ml. E) Flow experiments where the TNF-α concentration was converging towards 1 ng/ml during the entire range plotted.

4.8.2. Quantitative NF-κB oscillation analysis

For the statistical data analysis, the raw image data was analyzed with the Quantitative Period Extraction Method. An example of a data series analyzed by this method is presented in figure 4.18. The data is obtained in double addition experiments and shows the I_N/I_C ratio in a time span of 200 min in each experiment. The experiment in A) is performed at 32.0 °C

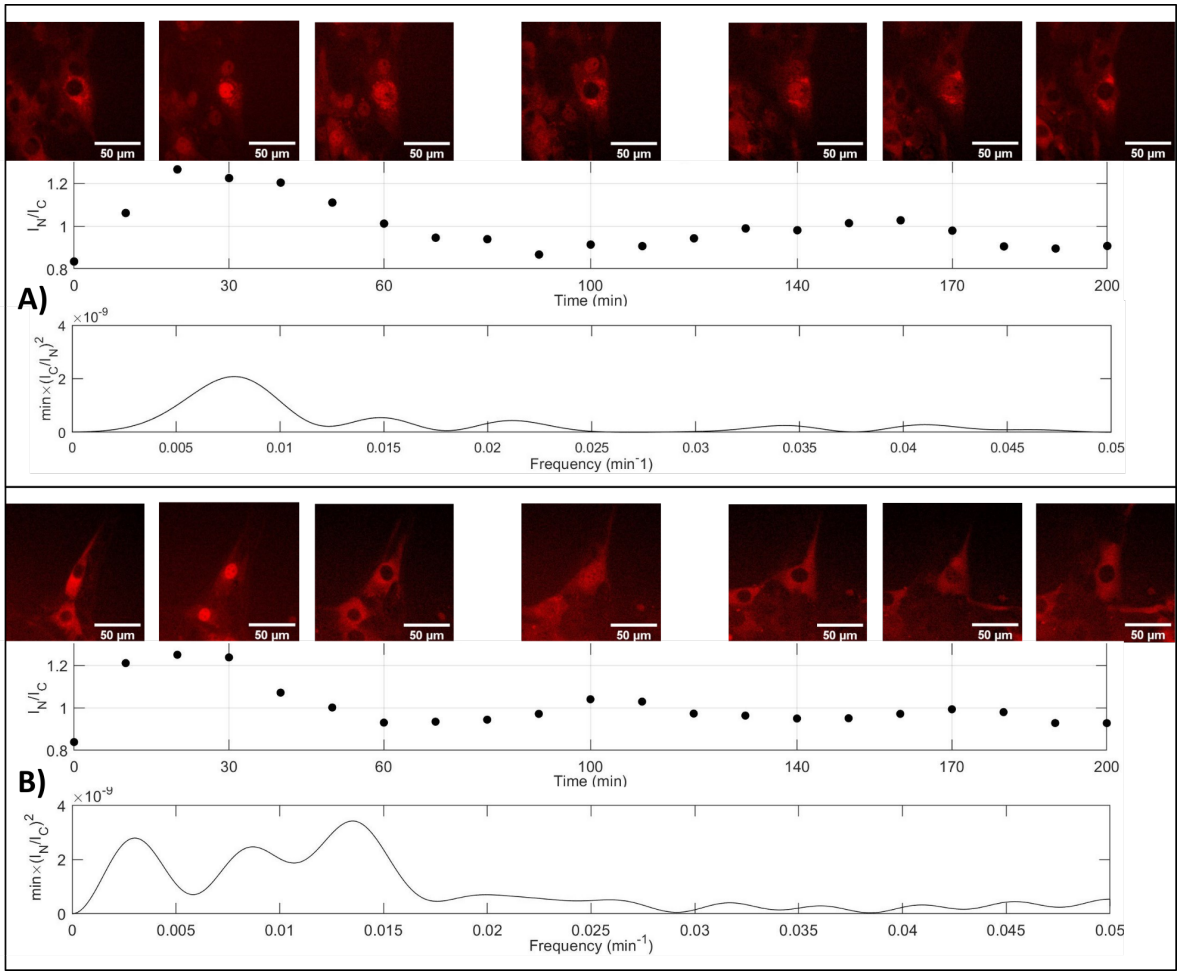

Figure 4.18: A) TOP: Time-lapse of a single fibroblast cell in the center of the image with NF-κB fluorescently labeled with DsRed. At T = 32.0 °C the cell is exposed to 10 ng TNF-α/ml at t = −2 min and a new concentration increment to a total of 18 ng TNF-α/ml at t = 38 min. NF-κB is shuttling from cytoplasm to nucleus and back twice during the presented time span of 200 min. Each image corresponds to the time point in the plot below. A) MIDDLE: I_N/I_C ratio of the first 200 min. of the data series. Data is extracted in 10 min. intervals, with image examples every 30 or 40 min. A) BOTTOM: Power spectrum of the I_N/I_C ratio of the data presented in MIDDLE. For reference, the longer time series of 510 min. of the same cell is shown in suppl. figure 6.1. To extract an oscillation period for this cell, a peak correlated to the MIDDLE time series was chosen. At this peak, the inverse of the frequency value equals the period: 7.76 E-3 $\text{min}^{-1})^{-1}$ = 129 min., which fits well with the longer time-series shown in figure 6.1. In B) TNF-α concentration is increased twice as in A) but in this case at a temperature of 39.5 °C. A total of three oscillations are shown in images in B) TOP and in the I_N/I_C plot in B) MIDDLE. B) BOTTOM is a power spectrum of B) MIDDLE, with the highest peak at 1.35 E-2 min^{-1} corresponding to a period of (1.35 E-2 $\text{min}^{-1})^{-1}$ = 74.1 min.

and the experiment in B) at 39.5 °C. A single fibroblast cell is followed in TOP of A) and B) during the presented 200 min. The nuclear NF-κB to cytoplasmic NF-κB is quantified from the measured light intensities from the nucleus and the cytoplasm. These relative intensities are plotted in the MIDDLE of figure A) and B). There are 30 or 40 min. between each image in TOP, while data points in MIDDLE are separated by 10 min., which is the time interval between each captured image from the raw image data. In BOTTOM of A) and B) power spectrum analyses are performed on the data from MIDDLE.

From the few data points utilized for each intensity measurement in each image, the source of error is relatively large in these experiments. In A) MIDDLE, it seems that there

are two oscillations in 190 min, which would correspond to a period of 95min/oscillation. However, as seen in the appendix in figure 6.1, when analyzing 490 min. of the oscillation data, four oscillations are observed, which corresponds to a period of 123min/oscillation. When a power spectrum analysis of the first 200 min. of this data series is performed, which is presented in A) BOTTOM, it is observed that one peak is higher than the others. This peak has the value 8.26 E−3 min^{-1}. To find the corresponding period, the reciprocal value is taken. The period is found to be (8.26 E−3 min^{-1})$^{-1}$= 121 min, which is remarkably close to the 123 min. measured at longer time scales, but relatively different from the 95 min first calculated. This serves as an example of how a more accurate period is found on data of poor quality with the power spectrum analysis, compared to counting oscillations.

In B) TOP and MIDDLE, three full oscillations are observed during the first 200 min. This corresponds to a period of 67min/oscillation. In BOTTOM, the highest peak has the frequency value of 1.32E-2 min^{-1}. This corresponds to a period at (1.32E-2 min^{-1})$^{-1}$ = 74.1 min. Here, the latter value is interpreted as the correct period due to the argument presented above.

In this power spectrum, there is another relatively large peak at the frequency value of 0.003 min^{-1}. A peak between 0.001 min^{-1} and 0.005 min^{-1} is present in most power spectra. However, this is not the peak representing the oscillation. In some of the data series, these peaks are higher than the peak, giving the cell oscillation frequency, so the peak was always evaluated relative to a visual judgment of the fluorescence images. In more than 50 % of data series, the highest peak corresponds to the observed oscillation time, but in some cases, the second, or even the third, highest peak corresponds to the period of the NF-κB oscillation.

With the Quantitative Period Extraction Method, the cell oscillation periods from the single addition-, the double addition- and the flow experiments were successfully extracted.

4.8.3. NF-κB oscillation as a function of temperature

To analyse whether oscillation periods were temperature-dependent, the extracted periods were plotted versus temperature. In figure 4.19 all periods extracted with the Quantitative Period Extraction Method are separated into assay by color and plotted versus the temperature that the individual experiments were conducted at. From this plot, it is seen that the periods decrease when the temperature is increased. It is also noted that despite the varying experimental conditions in the three assays, the behavior of period versus temperature is very similar across the experiments. At 37.0 °C the periods are 105.3 min. ± 21.3 min., 114.7 min. ± 29.7 min., and 100.8 min. ± 10.9 min. for the single addition, double addition, and flow experiments, respectively, with the number of oscillating cells $n_{37single}$ = 12, $n_{37double}$ = 10, and n_{37flow} = 10. From this, it is concluded that there is no significant differ-

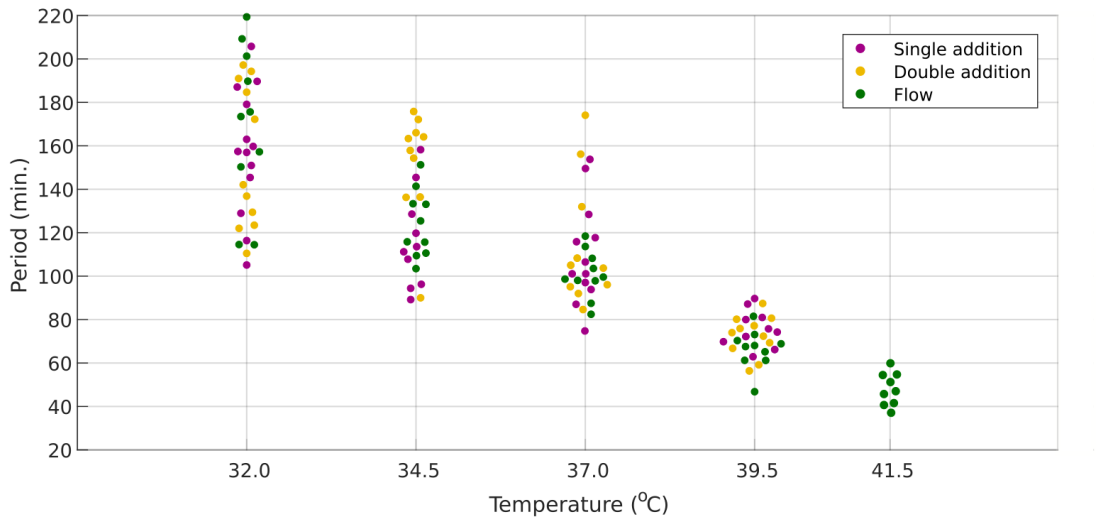

Figure 4.19: Oscillation period of p65 in fibroblast cells versus temperature for the three different assays: Single addition experiment, where 10 ng TNF-α/ml was added at t = −2 min, double addition experiment, where 10 ng TNF-α/ml was added at t = −2 min and then 8 ng TNF-α/ml at t = 38 min, and lastly, flow experiments, where cells were exposed to flow in a microbioreactor with a TNF-α concentration converging towards 1 ng/ml. All experiments were conducted at 32.0 °C, 34.5 °C,37.0 °C, 39.5 °C, and 42.0 °C.

ence across the various experiments at body temperature, with Student's t-test resulting in p-values > 0.05 when comparing the three populations two by two. The period at 32.0 °C is 157.3 min. ± 29.1 min., 154.8 min. ± 33.2 min., and 170.5 min. ± 36.7 min. for single addition, double addition, and flow experiments, respectively, with the number of oscillating cells $n_{32single}$ = 13, $n_{32double}$ = 11 and n_{32flow} = 10. Again, no statistical differences were found at this temperature. There was, however, a major difference across the assays, namely, that higher temperatures in the flow assay could be reached, compared to the two µ-well assays, as explained below.

It was initially attempted to obtain data at 42.0 °C for all three assays, but after four attempts with the flow assay and two of each of the µ-well assays, where cells became necrotic, it was concluded that this was not possible. Experiments at 41.5 °C were then tested for all assays. The two µ-well assays resulted in necrotic cells. However, at this temperature, the flow assay showed oscillating cells. The average of the periods at 41.5 °C is 48.28 min. ± 7.73 min. for the flow experiments, with the number of oscillating cells $n_{41.5flow}$ = 9.

When grouping the assays as a weighted average, the periods are 160.4 min. ± 32.4 min., 106.8 min. ± 22.0 min. and 48.28 min. ± 7.73 min. for the 32.0 °C, 37.0 °C and 41.5 °C, respectively, and so for the change in temperature investigated, ΔT = 9.5 °C, the change in period is 112.1 min, and the periods at 32 °C is a factor of 3.3 larger than the periods at 41.5 °C. Thus, when varying the temperature approximately +/- 5 °C from body temperature, these variations change the oscillation periods far more than the type of assay, which includes different TNF-α concentrations and different culture conditions. The decrease

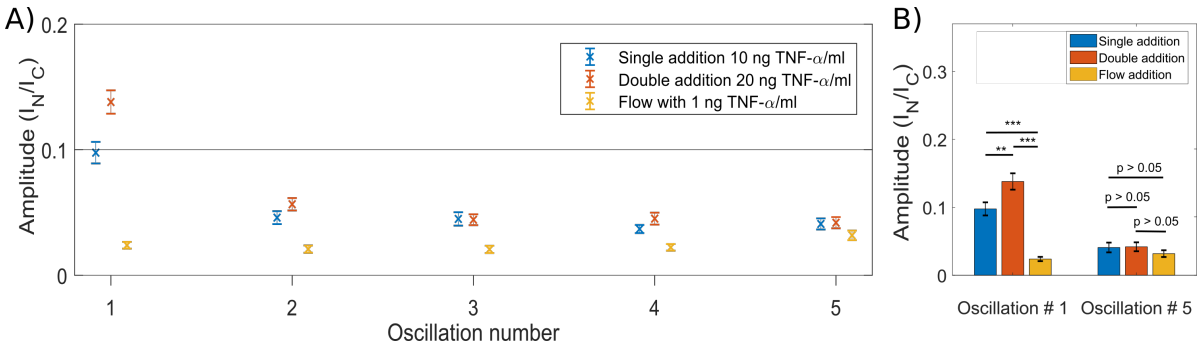

Figure 4.20: A) SEM of I_N/I_C amplitudes of the three different assays vs. oscillation number. B) Student's t-tests investigating statistical differences between populations of different assays in oscillations 1 and 5, seen in A). Error bars are SEM.

in oscillation period as a function of temperature was also quantified with a linear fit, found in the appendix figure 6.2. Here, the average for each temperature is used as the fitting points. The linear fit gives the equation: $p = -11.9T + 540.3$, with period, p, in min. and temperature, T, in °C. From this linear fit, it is extracted that the period decreases by 11.9±2.8 min/°C. Moreover, an exponential fit was performed on the same data points. The fit is presented in appendix 6.3 and gives the equation $p = 93.53\exp(-0.4698T)$.

In figure 4.19 the span of the distribution of the oscillation periods decreases as temperature increases. This suggests that the NF-κB oscillation periods become increasingly more defined as temperature increases and that increased noise, originating from the temperature increase, does not cause a less defined period. A D'Agostino test was conducted on the period distribution at 32.0 °C, and it was found that this was a normal distribution with a rather low p-value of 0.0724, and the distribution is considered to be normal from this test. D'Agostino test for periods of the individual assays at 32 °C resulted in p-values at 0.9289, 0.0693, and 0.6851 in the single addition, double addition, and flow experiments, respectively, so none of the experiments can be concluded to consist of several normal distributions. These experimental findings then suggest that the measured periods have the same origin.

The power spectrum analysis assumes that all oscillations in each data series have the same period, where each data series consists of between 2 and 11 oscillations with varying amplitude. So in order to evaluate amplitudes individually, data series were separated into single oscillations with the time span of the periods. Each amplitude is extracted from these smaller time series by taking the root mean square (RMS) of the signal.

All amplitudes were extracted as explained in the Methods section 4.6.9 and analyzed with Student's t-tests.

The oscillation amplitudes, calculated as the root mean square of I_N/I_C, are plotted as a function of the oscillation number in figure 4.20 A) and B). In figure 4.20 A) the data from specific assays are separated and plotted with standard error of the mean (SEM). The first

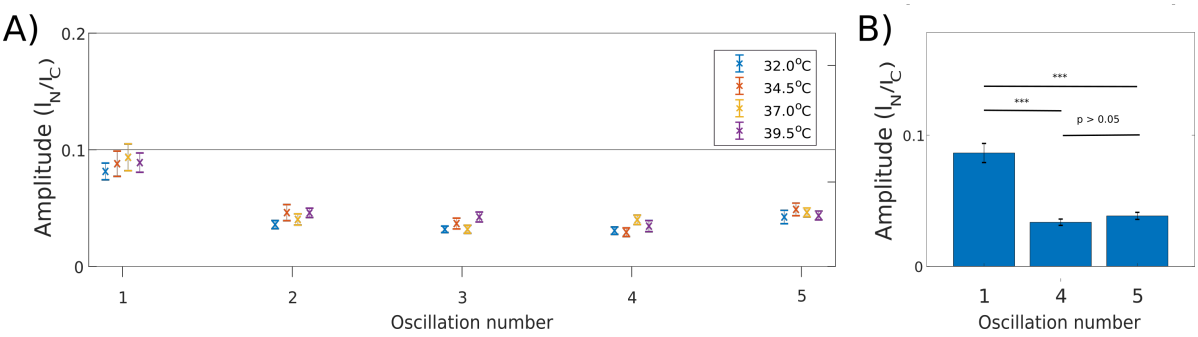

Figure 4.21: A) SEM of I_N/I_C amplitudes at different temperatures vs. oscillation number, with different asssays grouped. B) Student's t-test of weighted averages in A) investigating differences between oscillation 1, 4, and 5 with temperature and assays grouped. Error bars are SEM.

oscillation has an RMS amplitude of 0.098 for the single addition experiments, 0.14 for the double addition experiments and 0.024 for the flow experiments. This is matching the oscillations analysed by the Qualitative Period Extraction Method, presented in figure 4.17. As seen in figure 4.20 B), these populations are significantly different at the first oscillation with the p-values $p_{1single} \rightarrow p_{1double}$ = 7.1 E-3, $p_{1single} \rightarrow p_{1flow}$ = 6.8 E-11 and $p_{1double} \rightarrow p_{1flow}$ = 8.8 E-16 and the number of data points in each test $n_{1single}$ = 47, $n_{1double}$ = 42 and n_{1flow} = 43. It seems that a higher concentration of TNF-α will produce a larger NF-κB amplitude. Starting from the initial oscillation, the difference in amplitude between the three assays are decreasing: The single and double addition experiments have decreasing amplitudes, whereas the flow experiments have a constant amplitude. Differences between assays at oscillation number 5 is tested with a Student's t-test in figure 4.20 B) and it is found that there is no significant difference between the populations with the p-values $p_{5single} \rightarrow p_{5double}$ = 0.92, $p_{5single} \rightarrow p_{5flow}$ = 0.33 and $p_{5double} \rightarrow p_{5flow}$ = 0.26 and the number of data points in each test $n_{5single}$ = 11, $n_{5double}$ = 14 and n_{5flow} = 11. In the flow experiment the TNF-α level is kept constant, however, in the µ-well experiments all TNF-α is added instantly and subsequently has the time to be consumed by cells, and will therefore decrease over time. So it is speculated that this is the origin of the decreasing NF-κB oscillations in the µ-well experiments. Degradation of TNF-α cannot explain this, since it is known that the degradation of TNF-α is minimal at this temperature [93].

When plotting amplitude as a function of oscillation number, grouped for assay and plotted separately for different temperatures, as shown in figure 4.21 A), it is seen that amplitudes for all temperatures are decreasing towards a steady state. This is tested with a Student's t-test in figure 4.21 B), where both oscillation number four and oscillation number five are significantly different from the first oscillation, but do not significantly differentiate from each other. The p-values found from a Student's t-test are: $p_1 \rightarrow p_4$ = 9.09 E-7, $p_1 \rightarrow p_5$ = 1.59 E-4 and $p_4 \rightarrow p_5$ = 0.329 with the number of data points in the tests n_1 = 132, n_4 = 52 and n_5 =

36. Importantly, no statistical evidence for differences between temperatures was found.

These experimental results showed interesting properties of the NF-κB signaling pathway, namely, that the NF-κB oscillations periods decreased as a function of temperature in all tested assays. In the following section, these data were used to model temperature dependency of a TNF-α stimulated NF-κB signaling pathway.

4.9. Theoretical temperature dependency on the NF-κB system

The experiments served as a foundation for developing a theoretical model where temperature variations were incorporated. The following work was performed by Mathias Heltberg from the Niels Bohr Institute. For the equations presented in eq. 4.5.3, the rates can be described as diffusion-limited or reaction-limited. All default values of these rates can be found in the appendix figure 6.6. Whether a reaction is diffusion- or reaction-limited can be determined from the magnitude of the reaction rate, as is discussed in the pre-print article in Appendix 6.4. If the reaction rate is high, the amount of time for two molecules to bind is limited by the time it takes for them to encounter, which is understood by diffusion. Hence this type of reaction can be approximated to be diffusion-limited, described by the Smoluchowski equation. If the reaction rate is low, the time it takes for two molecules to bind is not limited by the rate of the encounter but rather by the time for the binding to occur, which is understood from the Arrhenius equation.

The reaction limited change in a reaction rate is found to be

$$k_n^+ = k_0^+ \left(1 + \ln\left(\frac{1}{k_0^+}\right)\frac{1}{A}\frac{\Delta T}{T_0}\right). \tag{4.15}$$

Here k_n^+ is the reaction rate given by a change in temperature, k_0^+ is the initial reaction rate before the temperature was changed, A is the pre-exponential factor of the Arrhenius equation, ΔT is the temperature change, and T_0 is the initial temperature. It is seen that the temperature change is linearly related to k_n^+. With this result, it is possible to correlate a slow chemical reaction to the change in temperature.

If a reaction is fast, the limiting factor is not the reaction itself but instead the time it takes for molecules to encounter, described by diffusion. The change of reaction rate in a diffusion-limited regime was approximated to be

$$k_n^+ = k_0^+ \left(1 + \frac{\Delta T}{T_0}\right). \tag{4.16}$$

Again, the reaction rate is linearly related to the change in temperature. These equations

made it possible to simulate temperature changes in the NF-κB system. from the parameters listed in Appendix figure 6.6. The parameters k_{Nin}, k_t, and α were set to be diffusion-limited due to their high reaction rates, while the remaining rates were reaction-limited.

These changes in reaction rates were used to simulate the NF-κB oscillations during temperature changes, with the outcome as presented in figure 4.22. In A), nuclear NF-κB is plotted versus time for 30 °C, 35 °C, and 40 °C. It can be seen that when increasing the temperature, both the period and the amplitudes of the oscillations decrease. In B), IκB, messenger IκB, and NF-κB form the phase space in which the solutions for 30 °C, 35 °C, and 40 °C are plotted. It is observed how the path around the circumference of the limit cycle decreases when the temperature drops, thereby explaining the decreased amplitudes and periods in A). As in the Quantitative Period Extraction Method, described in Methods section 4.6.7, power spectrum analysis was used to determine the periods in C), though, here, the periods were simulated. It can be seen that multiples of the oscillation appear, but the first peak, which is also the highest, represents the NF-κB frequency. From power spectra analysis, periods were found for all temperatures from 30.0 °C to 44.0 °C for three different arbitrary TNF-α concentrations as shown in D). The data obtained for the experiments, presented earlier in figure 4.19, are plotted here for comparison, and it is seen that there is an excellent agreement between experimentally and theoretically obtained data. Both data decrease versus temperature with very similar values, and they both have a converging tendency above 40 °C. In E), the mean of the absolute derivative of NF-κB is plotted versus an arbitrary TNF-α concentration for 30 °C, 35 °C, and 40 °C. When this measure suddenly increases, the system is undergoing a supercritical Hopf bifurcation. At lower temperatures, the Hopf bifurcation appears earlier, meaning that here, less TNF-α is needed to create NF-κB oscillations.

The article pre-print in Appendix 6.4 discusses how this model can predict genetic up- and down-regulation from temperature changes. It shows how high-affinity genes will be upregulated while low-affinity genes will be down-regulated as the temperature increases.

These results proved it possible to derive a theoretical model, rooted in experiments, capable of predicting fascinating phenomena not yet shown experimentally.

4.10. Conclusion

In the experiments, MEF cells were exposed to a wide variety of stresses in *in vitro* experiments conducted in µ-wells and in an in-house built flow system.

The flow system enabled a chemical increase in TNF-α to mimic the natural upconcentration. With this flow system, fibroblast cells were grown in the flow system for days, with clear

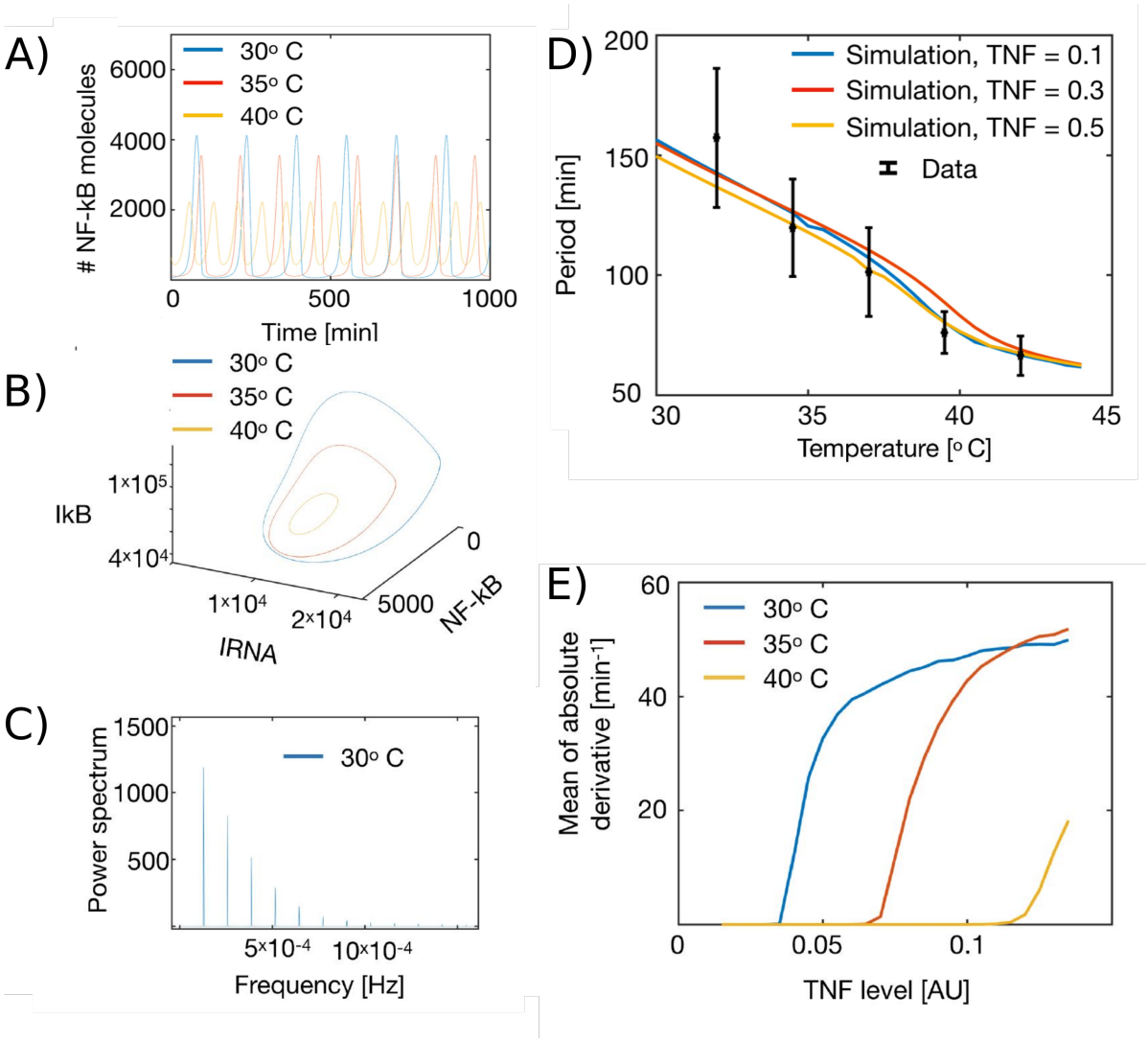

Figure 4.22: NF-κB simulations influenced by temperature. A) Nuclear NF-κB after tnf-α stimulation at 30 °C, 35 °C and 40 °C. As temperature increases, amplitude and period decrease. B) limit cycles for 30 °C, 35 °C and 40 °C in phase space. The perimeter of the limit cycle decreases as temperature increases. C) Power spectrum analysis of an NF-κB oscillation at 30 °C. D) Period versus temperature for NF-κB oscillations stimulated with three different arbitrary TNF-α concentration and compared to experimental data. In both cases period decrease as a function of temperature. E) Mean of absolute derivative versus TNF-α concentration for 30 °C, 35 °C and 40 °C. As temperature increases, the TNF-α level where the Hopf bifurcation occurs increases.

NF-κB oscillations sustained for up to 44 hours. This suggests stable culturing conditions and reliable measurements for the extraction of cell oscillation data.

A wide variety of stresses were utilized as a possible source of NF-κB activation, including heat shock, cell stretching, DNA or ribosomal damage by 466 nm LED excitation lamp, flow stress as well as physical and chemical stress, applied by gas in the flow system. In these experiments, no positive results were obtained about activation of NF-κB.

It was observed that at a particular TNF-α concentration, cells became apoptotic and that the apoptotic TNF-α level was different for experiments conducted in the flow system compared to experiments conducted in µ-wells. This is exemplified by the value of 10 ng TNF-α/ml, where cells underwent apoptosis in the flow experiments but were healthy and

exhibited oscillations in the μ-well experiments.

Applying TNF-α to the fibroblast cells resulted in observable NF-κB oscillations in the following three assays: Flow experiments, where TNF-α value converged towards 1 ng/ml, single addition μ-well experiments, where 10 ng TNF-α/ml was added prior to imaging, and the double addition μ-well experiments, where the TNF-α value was upconcentrated twice to a total of 18 ng/ml. The experiments resulted in NF-κB oscillation periods that were indistinguishable across the different assays.

Furthermore, the oscillations were exposed to different temperatures, and the periods and amplitudes from these experiments were measured. Oscillation experiments with the three assays were conducted at 32.0 °C, 34.5 °C, 37.0 °C, and 39.5 °C, while 41.5 °C was only reached in the flow assay. It was found that the oscillation periods decreased with 11.9±2.8 min/°C.

The experiments showed that the first oscillation of the single- and double addition experiments had significantly higher amplitude than the first oscillation in the flow system. The second peak in the double addition experiment was observed to increase compared to the second peak of the other assays. This occurred soon after the second exposure to increased TNF-α concentration. From these observations, it is concluded that NF-κB repeatedly translocates when whenever the TNF-α concentration is increased.

When the data were separated for each temperature, no significant difference was found between the populations, so no conclusions can be reached regarding amplitude dependence on temperature.

The variance of distributions of oscillation periods decreased with higher temperature. Therefore, it is concluded that the oscillation period is more precisely determined at higher temperatures.

With a background in the experimental findings of this thesis, theoretical derivations that originated from the Smoluchowski and the Arrhenius equations, were used to change the reaction rates of the NF-κB simulations, so they became temperature-dependent. The reaction rates were either diffusion − or reaction − limited, depending on the magnitude of their reaction rates. The experimental results were compared to the theoretical simulations, and an excellent agreement was found. Furthermore, the theoretical simulations were used to predict that the TNF-α level, at which Hopf bifurcations will occur, increase with temperature. Furthermore, this model can predict how genes are regulated as a function of temperature, from whether genes are of high or low affinity.

5

Conclusion and outlook

Extensive studies were carried out to assess how living systems adapt to physical changes in the environment. Both positive and negative results were obtained, exemplified by the MEF cells that could not adapt to various physical stresses, resulting in necrosis, and experiments, where MEF cells did adapt to temperature changes, by increasing the oscillation period of NF-κB. Also, physical change impacted organoid morphology, where a higher Matrigel stiffness resulted in increased branching.

When organoids were suspended in different Matrigel concentrations, data obtained by optical tweezers clearly showed changes in viscoelastic properties. While the organoids did not adapt by changing growth rate, where it was found that organoid size was the same throughout a large span of viscoelasticities of the matrix, the branching of the organoids increased significantly in Matrigel solutions with lower α-value and loss tangent, and higher storage modulus. An exciting way forward with the discovered viscoelastic properties is to design artificial matrices with these physical properties.

The response of living systems was also tested at single cell level when exposing cells to various physical factors. Experimentation with MEF cells was performed, and it was measured whether the transcription factor NF-κB would be activated or even show sustained oscillations. An activation of NF-κB would give information about the MEF cells' ability to adapt to the physical environment. From earlier findings, NF-κB was found to serve as a general stress response, and, when disregarding the chemical and biological stresses, the physical stresses that are thought to activate NF-κB is shear stress, heat stress, and DNA-

and ribotoxic stress by blue – or UV – light. The experimental assay used for the majority of these experiments was an in-house-built flow system. It was shown how this system would cover the entire flow range, from being low enough for drag forces to be neglected, at a force magnitude lower than the gravitational force, to being extremely high, at more than a factor of a thousand larger than the force magnitude of the gravitational force. It was showed that cells would thrive for days in the microbioreactor of the flow system and that TNF-α upconcentrated here was following natural conditions. From that, it is concluded that the flow system worked exceptionally well for conducting stress and TNF-α experiments on MEF cells, with NF-κB as the stress indicator. In this ph. d. project, experiments with several types of stresses, including those mentioned above, were carried out, and surprisingly, it was found that no activation of NF-κB was observed from the stresses alone. These findings emphasize the importance of the exact living system when carrying out experiments where the physical environment is changed. NF-κB activation by an environmental change in one cell type does not translate into NF-κB activation in another cell type when the same environmental change is applied. It seems that it is difficult to generalize the specific impact that a physical environmental change has on organisms, and therefore, future experiments need to be designed for specific living systems.

In the experiments where MEF cells were exposed to physiochemical stress, interesting phenomena were observed. When TNF-α was applied to the MEF cells, NF-κB was activated, and the system sustained oscillations for up to 44 hours. It was found that the oscillation period decreases as a function of temperature with 11.9 ± 2.8 min/°C, and the period was changed by a factor of 3.32 within the interval from 32.0 °C to 41.5 °C. These findings were compared to computer simulations, where the fundamental equations, the Arrhenius equation and the Smoluchowski equation, were used for the assumptions on how chemical reaction rates changed with temperature. These simulations strongly correlate with the experimental data, so from these findings, we see that already established mechanisms can explain temperature effects on biological systems, and new biological models, such as changes in signaling pathways, are not needed for temperature effects to be explained. A major part of the new research in NF-κB is related to coupling an activating stimulus to the NF-κB oscillations. With a basis in the findings from this project, experiments, where the temperature oscillates in order to couple to the NF-κB oscillations, would be interesting.

From the experiments conducted in this thesis, it seems that the understanding of how living systems adapt to physical changes in the environment has merely just begun. The ways in which organisms can be exposed to changing physical environments are countless, and with these findings as an example, it would seem that fascinating science is guaranteed.

6

Appendix

6.1. Supplementary figures

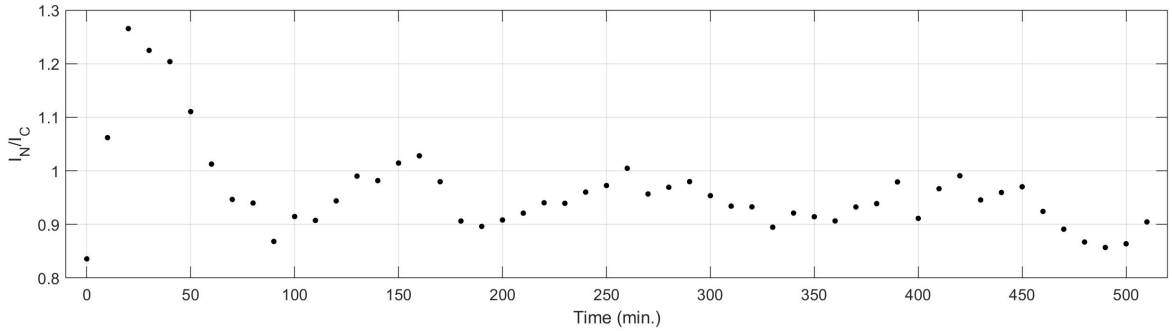

Figure 6.1: NF-κB oscillation at 32 C° full length after exposure to TNF-α at −2 min. and again at 38 min. First addition results in a TNF-α concentration of 10 ng/ml and the second of 18 ng/ml.

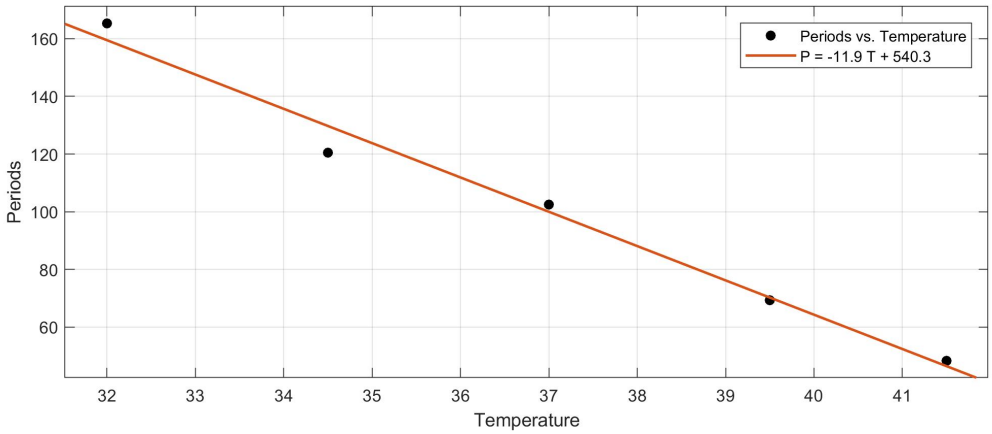

Figure 6.2: NF-κB oscillation periods versus temperature with a linear fit, showing that Δperiod/Δtemperature = -11.9±2.8 min/°C

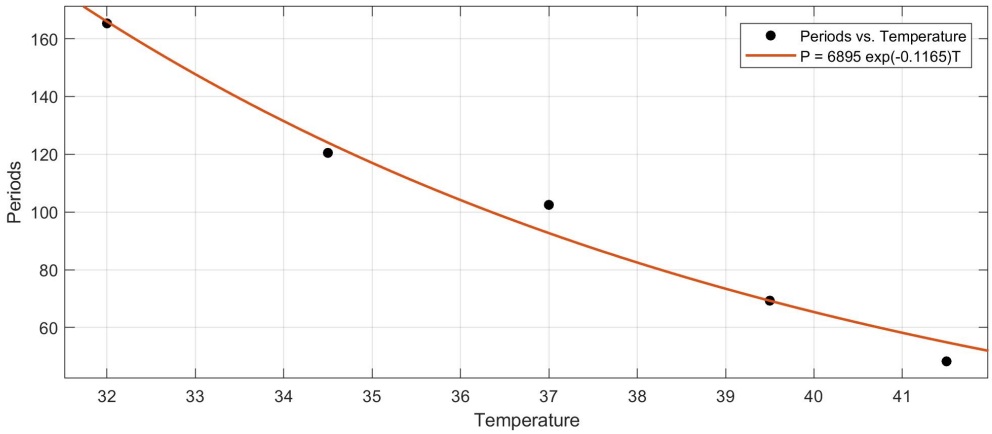

Figure 6.3: NF-κB oscillation periods versus temperature with exponential fit.

Creating a functional microfluidics device		
Goal: Havning healthy cell culture for at least 8 hours - preferably up to weeks		
Problems:	1) Gas i system	Bubbles filling up entire chamber is forming
	2) Cell death	Cells are dying inspite of no TNF-alpha and no significant source of
Approach to solve problems:	Gas in the system could be a reason for cell death, so I will start by solving the gas problem, so when I afterwoods solve cell death, then I know that it isn't the bubbles causing death. Also if there're no bubbles, then I can more easily control other parameters such as flow, gas diffusion into tube, mini oxygen bubbles and pH.	
Possible solutions:		
Comments in this scheme: If anything else than "unrelated" is written it means that this effect (or the lack thereof) can cause gas/cell death		
	Gas	**Cells death**
Tube related		
Double layer of tubing	Inner tube is gas permeable	Possible
Gas permeabilty of tube	Types of PTFE	Possible
Toxicity of tube	Unrelated	Silicone/PTFE (test in T-flask)
Medium related		
Medium creating bubbles	Try with water only	Not directly related
pH due to degassing	Necessary	pH test while degassing
HEPES buffer	Another/no buffer	Another/no buffer
Cells		
Cells excreting CO2	Unlikely	Unlikely
Setup		
Levels changing preassure	No cell testing	Unrelated
Turbulence	Create very low Reynolds numer laminar flow to test	Unrelated
Insert tiny air bubbles	Increasing this problem	Might help by providing O_2
Interfaces	Sealed?	Unrelated
Humidity in incubator	Possible	Possible
Atmosphere (Oxygen and CO_2)	Test levels to observe bubbles	Test levels to observe cell death
Surface treatments		
Surfactants (STS or other)	Minimizing surface tension	Unrelated

	Experiments: Note: I will use CO2, oxygen and high humidity in all experiment	**The color green means that this is outcom is confirmed. Red means the outcome is disputed. Yellow means the experiment has been skipped.**			
		Outcome:			
	Solving gas formation/bubbles	**Positive (yes)**	**Negative (no)**	**Was the problem minimized?**	**Experimental Notes:**
1	pH is changing in vacuum chamber?	Cell death is not due to changes in pH when in vacuum chamber	Cell death is probably due to wrong pH - find new medium that will work or adjust pH in current medium		This was done in the vacuum chamber. The medium froze solid while measuring and the pH indicator went more light green, which should mean more acidic, but I'm pretty sure that it was just color being flushed off after being in the liquid for a while. Because when I added a new pH indicator, it shouwed exactly 7.
2	Temperature is correctly measured?	Temperature is OK. Keep temperature measuring wires on slide	Change wires and check again		I glued the tip of the thermometer to the tip of the wires and put it on 37 degrees. The thermometer also showed exactly 37 degrees.
3	Is flow system bubble-free when only used with water?	Bubbles are there due to a combination of medium and other factors - continue with medium without additives	Bubble problem is fundamental - continue with water		Bubbles appeared. These were actual bubbles and not the entire chamber filling up with gas. You could see approximately 2-20 stationary bubbles on each 4x image - they were there in the beginning for some reason. Surprising observation was that the smaller bubbles on each image disappeared slowly over time while large bubbles became bigger over time. Therefore it seems that in the water experiments, the total amount of gas is approximately the same gas is transferred from small to big bubbles - seems like slightly more gas is generated over time.
4	With water: Are existing bubbles reduces from slide when slide is placed lower than other parts? I continued experiment 3 without changing the water - only moving syrringe and outlet up.	Leveling and pressure is a good way to reduce bubbles. If no leakage: Continue with HEPES and additives. If leakage: See if medium without additives and no leveling will reduce bubbles (experiment 6)	Move to experiment 6	It seems that the problem was minimized since there wasn't an increased amount of gas.	No leakage. It still seems that a contant amount of gas was present, but smaller bubbles dissapeared and larger got even larger.
5	Is flow system bubble-free when used without HEPES and other additives?	Perfect - move to cell death and continue with this setup	Continue with medium with additives		Didn't do this.

Figure 6.4: Page 1 of test scheme for removing gas formation (bubbles) and preventing cell death. This is considered laboratory notes. Green is a positive experimental outcome. Red is a negative experimental outcome. Yellow experiments are skipped.

6	Are bubbles minimized when slide is placed lower than other parts?	And leakage: Solve leakage and continue with that setup. And no leakage: Perfect - move to cells death, experiment 11, and continue with this setup.	Continue with old levels	Yes, significantly - considered solved!	When I started this experiment I sucked air into the system from the outlet to get rid of water. Also I didn't filter the HEPES medium. These two thing can cause bacteria. Syrringe was warmed up in incubator for approximately 10 minutes before starting the experiment. Thermometer was not attached at the right place so just when the system was filled with medium and I started recording, the thermostat was moved near to the slide, meaning that temperature went from 34.4 to 37 shortly after. I did the experiments and saw two tiny, tiny bubbles at less than 1 mm in diameter. The gas problem has been improved by an order of a thousand or more. Yes! No leakage, which is unexpected since when I stated doing experiments, I had leakage when placing the slide below other parts. This is actually why I decided to place outlet under slide thereafter. Maybe Ibidi did changes in connections. After this I have been testing medium (no HEPES) in flow with lower level for 3 days regarding the cell death experiments and still very, very little bubbles are forming. Three tiny bubbles in the whole slide
7	Are bubbles gone when tubing between bubbletrap-bubbletrap and bubbletrap-slide is non gas permeable?	Perfect - move to cell death and continue with this setup	Continue with gas permeable tubing		
8	Are bubbles gone when a surfactant has been used?	Perfect - move to cell death and continue with this setup	Continue without surfactant		
9	Are bubbles gone when using non gas permeable tubes all the way?	I need to create setup where I add oxygen by pumping into T-junction since it can't diffuse through membrane anymore	Continue with gas permeable tubing		
10	Are bubbles gone when using double tubing?	Perfect - move to cell death and continue with this setup	Continue with single tube		
	Are bubbles gone when using a combination of everything that minimized the bubbles?	Perfect - move to cell death and continue with this setup	Try the last available option to get rid of bubbles		
	Solving cell death				
11	Does the microfluidics system affect the pH? Test with pH indicator paper.	Try with medium without HEPES for flow. Do 12 and 13	Go to 14.		The pH of medium with and without HEPES is approximately 7 (maybe a bit under including HEPES and a bit above without Hepes, but for sure between 6 and 8). I also tested both media after degassing and they had the same Ph. However, when the medium has been in the flow system for about 16 hours the pH of the HEPES medium is about 10, or a bit under. This is essential.
12	Does the medium without HEPES have a pH at 7 after being used in flow system?	Get som of that without Phenol Red and go to 14.	Talk to people and maybe use another buffer.		pH is at 10 too. So both with and without HEPES it's at 10.
13	Is the medium becomming basic when inside the incubator but not in flow system? (Test a sealed container with HEPES buffer inside incubator.	Another medium migt also become basic.	Use something else than HEPES		Hepes medium was tested and it also became basic - pH between 8 and 9. Maybe it would increase even more if it had more time to "develop". There's not so much diffusion in the petri dish as in the silicone tubes.
14	Does both kinds of media become basic in the timelapse incubator and both media stay at pH 7 in the good incubator?	Something is probably wrong with the CO2 flow in the timelapse incubator. Make it work.	Something is wrong with either both media or both incubators		pH at about 9 in both samples already after 3 hours when situated inside the timelapse incubator. In the cell lab incubator they are at 7.
15	Are pH values of media in petri dishes still at 9-10 after 3 days?	I'm sure the atmosphere in the large incubator doesn't have the right atmospheric contents if the pH become neutral when being put into the incubation cage	Media can become neutral after a long time		
16	Do media that have turned basic (pH 9-10) become neutral after being put into the mini-incbator inside the timelape?	See if it is possible to get the flow system incoorperated into the mini incubator	Test neutral medium from start		Already after 45 minutes the HEPES medium is at pH 7 and the one without HEPES is between 7 and 8
17	Can I do flow system setup inside the mini incubator where there're no bubbles and the pH is neutral?	It seems like everything is working. Test for phototoxicity.	Either oxygen level, flow speed or tubing is likely to kill cells		I do not use new tubing in this experiment. I will test the pH at the outlet because it's convenient, but since it might have a good pH value at the sample inside the mini incubator, I will have to test the pH value at the slides as well by breaking up the flow system at test the medium.
18	Test pH value at 4 different locations inside flow system. Are they as expected?	Good.	Mixing along tubing might be higher than expected.		Just after syrringe: 7-8. Just before mini incubator: 9. Just after slide (inside incubator): 7, at outlet: 9-10.
19	Do cells thrive until at least 8 hours when all tubing is new and the bubbletrap has just been autoclaved and we're inside the mini incubator?	Continue for as long as possible. Move to last experiment.	Next		
20	Atmosphere testing. Do cells thrive until at least 8 hours when increasing oxygen?	Continue for as long as possible. Move to last experiment.	Next		
21	Atmosphere testing. Do cells thrive until at least 8 hours when increasing CO2?	Continue for as long as possible. Move to last experiment.	Next		
22	Atmosphere testing. Do cells thrive until at least 8 hours when using PTFE tubing?	Use PTFE from now on.	Back to silicone tubing. Next.		
23	Do cells thrive until at least 8 hours when I don't use HEPES?	Continue for as long as possible. Move to last experiment.	Next		
24	Do cells thrive until at least 8 hours when I use another buffer?	Continue for as long as possible. Move to last experiment.	Next		
25	Consider flow speed. Does it need to be faster/slower?	?	?		
26	Create double tubing experiment or tiny oxygen bubble experiment. These are going to be more complicated so talk to people and consider carefully what to do.	?	?		
27	Do cells thrive until at least 8 hours when I autoclave the tubing and reuse it?	Autoclave most times from now on. Test next for phototoxicity	Use new tubing everytime from now on. Next.		
28	Do cells thrive when imaged with BF-autofocus, BF and 100% DsRed at 5 locations every 5 min.?	Do science.	Find the limit of phototoxicity		

Figure 6.5: Page 2 of test scheme for removing gas formation (bubbles) and preventing cell death. This is considered laboratory notes. Green is a positive experimental outcome. Red is a negative experimental outcome. Yellow experiments are skipped.

6.2. Parameters

Parameter in paper	Default value
k_{Nin}	$5.4\ \text{min}^{-1}$
k_{Iin}	$0.018\ \text{min}^{-1}$
k_t	$1.03\ (\mu\text{M})^{-1}.\text{min}^{-1}$
k_{tl}	$0.24\ \text{min}^{-1}$
K_I	$0.035\ \mu\text{M}$
K_N	$0.029\ \mu\text{M}$
γ_m	$0.017\ \text{min}^{-1}$
α	$1.05\ (\mu\text{M})^{-1}.\text{min}^{-1}$
N_{tot}	$1.\ \mu\text{M}$
k_a	$0.24\ \text{min}^{-1}$
k_i	$0.18\ \text{min}^{-1}$
k_p	$0.036\ \text{min}^{-1}$
k_{A20}	$0.0018\ \mu\text{M}$
$[IKK]_{tot}$	$2.0\ \mu\text{M}$
$[A20]$	$0.0026\ \mu\text{M}$

Figure 6.6: Parameters for simulations of the NF-κB system

Bibliography

[1] Samir Mitragotri and Joerg Lahann. Physical approaches to biomaterial design. *Nature materials*, 8(1):15–23, 2009.

[2] Subra Suresh. Biomechanics and biophysics of cancer cells. *Acta Materialia*, 55(12): 3989–4014, 2007.

[3] Karen A Beningo and Yu-li Wang. Fc-receptor-mediated phagocytosis is regulated by mechanical properties of the target. *Journal of cell science*, 115(4):849–856, 2002.

[4] Kevin D Young. The selective value of bacterial shape. *Microbiology and molecular biology reviews*, 70(3):660–703, 2006.

[5] AS French. Mechanotransduction. *Annual review of physiology*, 54(1):135–152, 1992.

[6] Antonio Graziano, Riccardo d'Aquino, Maria Gabriella Cusella-De Angelis, Francesco De Francesco, Antonio Giordano, Gregorio Laino, Adriano Piattelli, Tonino Traini, Alfredo De Rosa, and Gianpaolo Papaccio. Scaffold's surface geometry significantly affects human stem cell bone tissue engineering. *Journal of cellular physiology*, 214(1): 166–172, 2008.

[7] Florian Rehfeldt, Adam J Engler, Adam Eckhardt, Fariyal Ahmed, and Dennis E Discher. Cell responses to the mechanochemical microenvironment—implications for regenerative medicine and drug delivery. *Advanced drug delivery reviews*, 59(13):1329–1339, 2007.

[8] Timothy J Merkel, Stephen W Jones, Kevin P Herlihy, Farrell R Kersey, Adam R Shields, Mary Napier, J Christopher Luft, Huali Wu, William C Zamboni, Andrew Z Wang, et al. Using mechanobiological mimicry of red blood cells to extend circulation times of hydrogel microparticles. *Proceedings of the National Academy of Sciences*, 108(2):586–591, 2011.

[9] Stephanie Nemir and Jennifer L West. Synthetic materials in the study of cell response to substrate rigidity. *Annals of biomedical engineering*, 38(1):2–20, 2010.

[10] Martha E Grady, Russell J Composto, and David M Eckmann. Cell elasticity with altered cytoskeletal architectures across multiple cell types. *Journal of the mechanical behavior of biomedical materials*, 61:197–207, 2016.

[11] Gaël Prado, Alexander Farutin, Chaouqi Misbah, and Lionel Bureau. Viscoelastic transient of confined red blood cells. *Biophysical journal*, 108(9):2126–2136, 2015.

[12] Giuliana Rossi, Andrea Manfrin, and Matthias P Lutolf. Progress and potential in organoid research. *Nature Reviews Genetics*, 19(11):671–687, 2018.

[13] Paul Weiss and AC Taylor. Reconstitution of complete organs from single-cell suspensions of chick embryos in advanced stages of differentiation. *Proceedings of the National Academy of Sciences of the United States of America*, 46(9):1177, 1960.

[14] Madeline A Lancaster and Juergen A Knoblich. Organogenesis in a dish: modeling development and disease using organoid technologies. *Science*, 345(6194), 2014.

[15] Michael J Kratochvil, Alexis J Seymour, Thomas L Li, Sergiu P Paşca, Calvin J Kuo, and Sarah C Heilshorn. Engineered materials for organoid systems. *Nature Reviews Materials*, 4(9):606–622, 2019.

[16] Pegah Dejban, Nasrin Nikravangolsefid, Mohsen Chamanara, Ahmadreza Dehpour, and Amir Rashidian. The role of medicinal products in the treatment of inflammatory bowel diseases (ibd) through inhibition of tlr4/nf-kappab pathway. *Phytotherapy Research*, 35(2):835–845, 2021.

[17] Ayesha B Alvero. Recent insights into the role of nf-kappab in ovarian carcinogenesis. *Genome Medicine*, 2(8):1–3, 2010.

[18] Fazlul H Sarkar and Yiwei Li. Nf-kappab: a potential target for cancer chemoprevention and therapy. *Front Biosci*, 13(1):2950–2959, 2008.

[19] Bruno RB Pires, Rafael CMC Silva, Gerson M Ferreira, and Eliana Abdelhay. Nf-kappab: two sides of the same coin. *Genes*, 9(1):24, 2018.

[20] Qi Xing, Zichen Qian, Wenkai Jia, Avik Ghosh, Mitchell Tahtinen, and Feng Zhao. Natural extracellular matrix for cellular and tissue biomanufacturing. *ACS Biomaterials Science & Engineering*, 3(8):1462–1476, December 2016.

[21] Shiri Uriel, Edwardine Labay, Megan Francis-Sedlak, Monica L. Moya, Ralph R. Weichselbaum, Natalia Ervin, Zdravka Cankova, and Eric M. Brey. Extraction and assembly of tissue-derived gels for cell culture and tissue engineering. *Tissue Engineering Part C: Methods*, 15(3):309–321, September 2009.

[22] Michael P. Francis, Patrick C. Sachs, Parthasarathy A. Madurantakam, Scott A. Sell, Lynne W. Elmore, Gary L. Bowlin, and Shawn E. Holt. Electrospinning adipose tissue-derived extracellular matrix for adipose stem cell culture. *Journal of Biomedical Materials Research Part A*, 100A(7):1716–1724, 2012.

[23] Chun-Min Lo, Hong-Bei Wang, Micah Dembo, and Yu li Wang. Cell movement is guided by the rigidity of the substrate. *Biophysical Journal*, 79(1):144 – 152, 2000. ISSN 0006-3495.

[24] Min-Cheol Kim, Yaron R. Silberberg, Rohan Abeyaratne, Roger D. Kamm, and H. Harry Asada. Computational modeling of three-dimensional ecm-rigidity sensing to guide directed cell migration. *Proceedings of the National Academy of Sciences*, 115(3):E390–E399, 2018. ISSN 0027-8424.

[25] Marta Cavo, Marco Fato, Leonardo Peñuela, Francesco Beltrame, Roberto Raiteri, and Silvia Scaglione. Microenvironment complexity and matrix stiffness regulate breast cancer cell activity in a 3d in vitro model. *Scientific Reports*, 6(1), 2016.

[26] Lena Wullkopf, Ann-Katrine V West, Natascha Leijnse, Thomas R Cox, Chris D Madsen, Lene B Oddershede, and Janine T Erler. Cancer cells' ability to mechanically adjust to extracellular matrix stiffness correlates with their invasive potential. *Molecular biology of the cell*, 29(20):2378–2385, 2018.

[27] Chris S Hughes, Lynne M Postovit, and Gilles A Lajoie. Matrigel: a complex protein mixture required for optimal growth of cell culture. *Proteomics*, 10(9):1886–1890, 2010.

[28] Corning. Corning matrigel. URL `https://www.corning.com/worldwide/en.htmlx`.

[29] Hynda K Kleinman and George R Martin. Matrigel: basement membrane matrix with biological activity. In *Seminars in cancer biology*, volume 15, pages 378–386. Elsevier, 2005.

[30] Ma. Lin, Li. Jingwu, Nie. Qiang, Zhang. Qiuyang, Zhang. Qiuyang, Liu. Sen, Ge. Dongxia, and You. Zongbing. Organoid culture of human prostate cancer cell lines lncap and c4-2b. *Am J Clin Exp Urol*, 5:25–33, 2017.

[31] Jarno Drost, Wouter R Karthaus, Dong Gao, Else Driehuis, Charles L Sawyers, Yu Chen, and Hans Clevers. Organoid culture systems for prostate epithelial and cancer tissue. *Nature Protocols*, 11(2):347–358, 2016.

[32] Temitope R. Sodunke, Keneshia K. Turner, Sarah A. Caldwell, Kevin W. McBride, Mauricio J. Reginato, and Hongseok "Moses" Noh. Micropatterns of matrigel for three-dimensional epithelial cultures. *Biomaterials*, 28(27):4006 – 4016, 2007.

[33] Chiara Greggio, Filippo De Franceschi, Manuel Figueiredo-Larsen, and Anne Grapin-Botton. In vitro pancreas organogenesis from dispersed mouse embryonic progenitors. *Journal of visualized experiments: JoVE*, (89), 2014.

[34] Liselotte Jauffred, Akbar Samadi, Henrik Klingberg, Poul Martin Bendix, and Lene B Oddershede. Plasmonic heating of nanostructures. *Chemical reviews*, 119(13):8087–8130, 2019.

[35] Liselotte Jauffred, Thomas Hønger Callisen, and Lene Broeng Oddershede. Viscoelastic membrane tethers extracted from escherichia coli by optical tweezers. *Biophysical journal*, 93(11):4068–4075, 2007.

[36] Christine M Ritter, Josep Mas, Lene Oddershede, and Kirstine Berg-Sørensen. Quantifying force and viscoelasticity inside living cells using an active–passive calibrated optical trap. *Optical Tweezers: Methods and Protocols*, pages 513–536, 2017.

[37] Josep Mas, Andrew C Richardson, S Nader S Reihani, Lene B Oddershede, and Kirstine Berg-Sørensen. Quantitative determination of optical trapping strength and viscoelastic moduli inside living cells. *Physical biology*, 10(4):046006, 2013.

[38] D Nemecek and GJ Thomas. Handbook of molecular biophysics. methods and applications, 2009. Accessed: 2016-04-11.

[39] A Rohrbach. Stiffness of optical traps: Quantitative agreement between experiment and electromagnetic theory. *Physical Review Letters*, 95:168102–(1–4), 2005.

[40] Ryogo Kubo, Morikazu Toda, and Natsuki Hashitsume. *Statistical physics II: nonequilibrium statistical mechanics*, volume 31. Springer Science & Business Media, 2012.

[41] Kirstine Berg-Sørensen and Henrik Flyvbjerg. Power spectrum analysis for optical tweezers. *Review of Scientific Instruments*, 75(3):594–612, 2004.

[42] Karel Svoboda and Steven M Block. Biological Applications of Optical Forces. *Annual Review of Biophysics and Biomolecular Structure*, 23(1):247–285, 1994.

[43] Frederick Gittes and Christoph F Schmidt. Signals and Noise in Micromechanical Measurements. *Methods in Cell Biology*, 55:129–156, 1998.

[44] Christine Selhuber-Unkel, Pernille Yde, Kirstine Berg-Sørensen, and Lene B Oddershede. Variety in intracellular diffusion during the cell cycle. *Physical biology*, 6(2): 025015, 2009.

[45] M. Fischer. Optical tweezers in viscoelastic media. *Ph. D Thesis*, 2007.

[46] G Pesce, A C De Luca, G Rusciano, P A Netti, S Fusco, and A Sasso. Microrheology of complex fluids using optical tweezers: a comparison with macrorheological measurements. *J. Opt. A: Pure Appl. Opt.*, 11:034016, 2009.

[47] B Schnurr, F Gittes, FC MacKintosh, and CF Schmidt. Determining microscopic viscoelasticity in flexible and semiflexible polymer networks from thermal fluctuations. *Macromolecules*, 30(25):7781–7792, 1997.

[48] Giuseppe Pesce, AC De Luca, G Rusciano, PA Netti, S Fusco, and A Sasso. Microrheology of complex fluids using optical tweezers: a comparison with macrorheological measurements. *Journal of Optics A: Pure and Applied Optics*, 11(3):034016, 2009.

[49] Kirstine Berg-Sørensen, Lene Oddershede, Ernst-Ludwig Florin, and Henrik Flyvbjerg. Unintended filtering in a typical photodiode detection system for optical tweezers. *Journal of applied physics*, 93(6):3167–3176, 2003.

[50] Godfrey Pasirayi, Vincent Auger, Simon M Scott, Pattanathu KSM Rahman, Meez Islam, Liam O'Hare, and Zulfiqur Ali. Microfluidic bioreactors for cell culturing: a review. *Micro and nanosystems*, 3(2):137–160, 2011.

[51] fluigent Smart Fluidics. fluigent. URL `https://www.fluigent.com/?gclid=CjwKCAjw092IBhAwEiwAxR1lRvAnwcXz8AWKJBNFiJJ6uMPloeYEs_WJv_DOwsG5sI8ukZc_1uNfYBoC8Q8QAvD_BwE`.

[52] m2p labs. m2p bioreactors. URL `https://www.m2p-labs.com/bioreactors/products/get-more-data/`.

[53] Phidgets. 28sth32 nema-11 bipolar stepper with 100:1 gearbox, . URL `https://www.phidgets.com/?tier=3&catid=24&pcid=21&prodid=341`.

[54] Phidgets. Phidgetstepper bipolar hc, . URL `https://www.phidgets.com/?tier=3&catid=23&pcid=20&prodid=1029`.

[55] Ibidi. Complete flow chamber, . URL `https://ibidi.com/channel-slides/50--slide-i-luer.html`.

[56] NanoEnTek. Juli stage. URL `http://www.julistage.com/product-overview/`.

[57] Fisher Scientific. Density of water with sugar. URL https://www.fishersci.com/shop/products/dmem/21063029.

[58] Nuaire. In-vitrocell es nu-5710. URL https://www.nuaire.com/in-vitrocell-nu-5710-direct-heat-co2-incubator-sterilization-cycle.

[59] Nikon. Nikon microscopes. URL https://www.microscope.healthcare.nikon.com/.

[60] OkoGasIncubator. Oko gas incubator. URL http://www.oko-lab.com/live-cell-imaging/cage-incubator.

[61] OkoCageIncubator. Oko cage incubator. URL http://www.oko-lab.com/live-cell-imaging/cage-incubator.

[62] Warner. Warner temperature controller. URL https://www.warneronline.com/dual-channel-temperature-controller-tc-344c.

[63] Engineering Toolbox. Viscosity of water with sugar. URL https://www.engineeringtoolbox.com/sugar-solutions-dynamic-viscosity-d_1895.html.

[64] Christine Poon. Measuring the density and viscosity of culture media for optimized computational fluid dynamics analysis of in vitro devices. *BioRxiv*, 2020.

[65] Peichun Tsai, Alisia M Peters, Christophe Pirat, Matthias Wessling, Rob GH Lammertink, and Detlef Lohse. Quantifying effective slip length over micropatterned hydrophobic surfaces. *Physics of Fluids*, 21(11):112002, 2009.

[66] Eric Lauga, Michael P Brenner, and Howard A Stone. Microfluidics: the no-slip boundary condition. *arXiv preprint cond-mat/0501557*, 2005.

[67] Nam-Trung Nguyen, Steven T Wereley, and Seyed Ali Mousavi Shaegh. *Fundamentals and applications of microfluidics*. Artech house, 2019.

[68] Dominique Legendre, Catherine Colin, and Typhaine Coquard. Lift, drag and added mass of a hemispherical bubble sliding and growing on a wall in a viscous linear shear flow. *Philosophical Transactions of the Royal Society A: Mathematical, Physical and Engineering Sciences*, 366(1873):2233–2248, 2008.

[69] Christian Rotsch, Ken Jacobson, and Manfred Radmacher. Dimensional and mechanical dynamics of active and stable edges in motile fibroblasts investigated by using atomic force microscopy. *Proceedings of the National Academy of Sciences*, 96(3):921–926, 1999.

[70] Chia-Wei Lee, Chun-Chieh Wang, and Chau-Hwang Lee. Mechanoprofiling on membranes of living cells with atomic force microscopy and optical nano-profilometry. *Advances in Physics: X*, 2(3):608–621, 2017.

[71] Srujana Neelam, Peter Robert Hayes, Qiao Zhang, Richard B Dickinson, and Tanmay P Lele. Vertical uniformity of cells and nuclei in epithelial monolayers. *Scientific reports*, 6(1):1–10, 2016.

[72] Bionumbers. Human cell sizes, . URL http://book.bionumbers.org/how-big-is-a-human-cell/.

[73] Bionumbers. Fibroblast cell density, . URL https://bionumbers.hms.harvard.edu/bionumber.aspx?id=106496&ver=3&trm=density+fibroblast&org=.

[74] Pub Chem. Methyleneblue. URL https://pubchem.ncbi.nlm.nih.gov/compound/Methylene-blue.

[75] Sigma Aldrich. Tranmittance. URL https://www.sigmaaldrich.com/DK/en/technical-documents/technical-article/analytical-chemistry/photometry-and-reflectometry/transmittance-to-absorbance.

[76] Alexander Yu Tolbin, Victor E Pushkarev, Larisa G Tomilova, and Nikolay S Zefirov. Threshold concentration in the nonlinear absorbance law. *Physical Chemistry Chemical Physics*, 19(20):12953–12958, 2017.

[77] James B Pawley. Points, pixels, and gray levels: digitizing image data. In *Handbook of biological confocal microscopy*, pages 59–79. Springer, 2006.

[78] Sanjeev Choudhary, Mridul Kalita, Ling Fang, Kershaw V Patel, Bing Tian, Yingxin Zhao, Chukwudi B Edeh, and Allan R Brasier. Inducible tumor necrosis factor (tnf) receptor-associated factor-1 expression couples the canonical to the non-canonical nf-κb pathway in tnf stimulation. *Journal of Biological Chemistry*, 288(20):14612–14623, 2013.

[79] Raymond Cheong, Alex Rhee, Chiaochun Joanne Wang, Ilya Nemenman, and Andre Levchenko. Information transduction capacity of noisy biochemical signaling networks. *science*, 334(6054):354–358, 2011.

[80] Pawel Paszek, Dean A Jackson, and Michael RH White. Oscillatory control of signalling molecules. *Current opinion in genetics & development*, 20(6):670–676, 2010.

[81] Tony Yu-Chen Tsai, Yoon Sup Choi, Wenzhe Ma, Joseph R Pomerening, Chao Tang, and James E Ferrell. Robust, tunable biological oscillations from interlinked positive and negative feedback loops. *Science*, 321(5885):126–129, 2008.

[82] Uri Alon. Network motifs: theory and experimental approaches. *Nature Reviews Genetics*, 8(6):450–461, 2007.

[83] Alexander Y Mitrophanov and Eduardo A Groisman. Positive feedback in cellular control systems. *Bioessays*, 30(6):542–555, 2008.

[84] Savaş Tay, Jacob J Hughey, Timothy K Lee, Tomasz Lipniacki, Stephen R Quake, and Markus W Covert. Single-cell nf-κb dynamics reveal digital activation and analogue information processing. *Nature*, 466(7303):267–271, 2010.

[85] Cristina M Tato, Nicola Mason, David Artis, Sagi Shapira, Jorge C Caamano, Jay H Bream, Hsiou-Chi Liou, and Christopher A Hunter. Opposing roles of nf-κb family members in the regulation of nk cell proliferation and production of ifn-γ. *International immunology*, 18(4):505–513, 2006.

[86] Frank Christian, Emma L Smith, and Ruaidhrí J Carmody. The regulation of nf-κb subunits by phosphorylation. *Cells*, 5(1):12, 2016.

[87] Sudhir Gupta. A decision between life and death during tnf-α-induced signaling. *Journal of clinical immunology*, 22(4):185–194, 2002.

[88] Ying Lu, Qinghua Zheng, Wanlu Lu, Junli Yue, Wei Zhou, Xuedong Zhou, Lan Zhang, and Dingming Huang. Compressive mechanical stress may activate ikk-nf-kb through proinflammatory cytokines in mc3t3-e1 cells. *Biotechnology letters*, 37(9):1729–1735, 2015.

[89] Li Sun, Guozhe Yang, Mone Zaidi, and Jameel Iqbal. Tnf-induced gene expression oscillates in time. *Biochemical and biophysical research communications*, 371(4):900–905, 2008.

[90] Andrew C Liu, David K Welsh, Caroline H Ko, Hien G Tran, Eric E Zhang, Aaron A Priest, Ethan D Buhr, Oded Singer, Kirsten Meeker, Inder M Verma, et al. Intercellular coupling confers robustness against mutations in the scn circadian clock network. *Cell*, 129(3):605–616, 2007.

[91] Jeffrey D Kearns, Soumen Basak, Shannon L Werner, Christine S Huang, and Alexander Hoffmann. Iκbε provides negative feedback to control nf-κb oscillations, signaling

dynamics, and inflammatory gene expression. *The Journal of cell biology*, 173(5):659–664, 2006.

[92] Gideon Agbanoma, Ching Li, Darren Ennis, Andrew C Palfreeman, Lynn M Williams, and Fionula M Brennan. Production of tnf-α in macrophages activated by t cells, compared with lipopolysaccharide, uses distinct il-10–dependent regulatory mechanism. *The Journal of Immunology*, 188(3):1307–1317, 2012.

[93] Gene and Cell Technologies. Human tnf-a stability testing. URL `https://www.geneandcell.com/blogs/molecular-biology-methods/human-tnf-alpha-stability-testing`.

[94] Simon Mitchell, Jesse Vargas, and Alexander Hoffmann. Signaling via the nfκb system. *Wiley Interdisciplinary Reviews: Systems Biology and Medicine*, 8(3):227–241, 2016.

[95] Ellen O'Dea and Alexander Hoffmann. The regulatory logic of the nf-κb signaling system. *Cold Spring Harbor perspectives in biology*, 2(1):a000216, 2010.

[96] Ellen O'Dea and Alexander Hoffmann. Nf-kb signaling. *Wiley Interdisciplinary Reviews: Systems Biology and Medicine*, 1(1):107–115, 2009.

[97] DM Wang and JM Tarbell. Modeling interstitial flow in an artery wall allows estimation of wall shear stress on smooth muscle cells. 1995.

[98] Catherine Vida Park. *The role of NF-kB in the response to reoxygenation-induced oxidative stress*. PhD thesis, Newcastle University, 2018.

[99] Kaori Sugioka, Koichi Nakagawa, Ryo Murata, Nobuyasu Ochiai, Takahisa Sasho, Momoko Arai, Hiroaki Tsuruoka, Seiji Ohtori, Takashi Saisu, Takefumi Gemba, et al. Radial shock waves effectively introduced nf-kappa b decoy into rat achilles tendon cells in vitro. *Journal of Orthopaedic Research*, 28(8):1078–1083, 2010.

[100] Shrikesh Sachdev, Sriparna Bagchi, Donna D Zhang, Angela C Mings, and Mark Hannink. Nuclear import of iκbα is accomplished by a ran-independent transport pathway. *Molecular and cellular biology*, 20(5):1571–1582, 2000.

[101] Pierre Martine and Cédric Rébé. Heat shock proteins and inflammasomes. *International Journal of Molecular Sciences*, 20(18):4508, 2019.

[102] Yanan Liu, Gengbiao Zhou, Zhenglian Wang, Xiaohua Guo, Qiulin Xu, Qiaobing Huang, and Lei Su. Nf-kb signaling is essential for resistance to heat stress-induced early stage apoptosis in human umbilical vein endothelial cells. *Scientific reports*, 5: 13547, 2015.

[103] CV Harper, DJ Woodcock, C Lam, M Garcia-Albornoz, A Adamson, L Ashall, W Rowe, P Downton, L Schmidt, S West, et al. Temperature regulates nf-κb dynamics and function through timing of a20 transcription. *Proceedings of the National Academy of Sciences*, 115(22):E5243–E5249, 2018.

[104] Steven H Strogatz. *Nonlinear dynamics and chaos with student solutions manual: With applications to physics, biology, chemistry, and engineering*. CRC press, 2018.

[105] Albert Goldbeter, Didier Gonze, Gérald Houart, Jean-Christophe Leloup, José Halloy, and Genevieve Dupont. From simple to complex oscillatory behavior in metabolic and genetic control networks. *Chaos: An Interdisciplinary Journal of Nonlinear Science*, 11 (1):247–260, 2001.

[106] DE Nelson, AEC Ihekwaba, M Elliott, JR Johnson, CA Gibney, BE Foreman, G Nelson, V See, CA Horton, DG Spiller, et al. Oscillations in nf-κb signaling control the dynamics of gene expression. *Science*, 306(5696):704–708, 2004.

[107] Sandeep Krishna, Mogens H Jensen, and Kim Sneppen. Minimal model of spiky oscillations in nf-κb signaling. *Proceedings of the National Academy of Sciences*, 103(29): 10840–10845, 2006.

[108] Mogens H Jensen and Sandeep Krishna. Inducing phase-locking and chaos in cellular oscillators by modulating the driving stimuli. *FEBS letters*, 586(11):1664–1668, 2012.

[109] Mathias L Heltberg, Sandeep Krishna, Leo P Kadanoff, and Mogens H Jensen. A tale of two rhythms: Locked clocks and chaos in biology. *Cell systems*, 12(4):291–303, 2021.

[110] Ryan A Kellogg and Savaş Tay. Noise facilitates transcriptional control under dynamic inputs. *Cell*, 160(3):381–392, 2015.

[111] Mathias L Heltberg, Sandeep Krishna, and Mogens H Jensen. On chaotic dynamics in transcription factors and the associated effects in differential gene regulation. *Nature communications*, 10(1):71, 2019.

[112] Samuel Zambrano, Ilario De Toma, Arianna Piffer, Marco E Bianchi, and Alessandra Agresti. Nf-κb oscillations translate into functionally related patterns of gene expression. *Elife*, 5:e09100, 2016.

[113] MatTek. Mattek microwell dishes. URL `https://www.mattek.com/products/glass-bottom-dishes/`.

[114] Ibidi. Sticky slide 0.6 mm or 0.2 mm, . URL https://ibidi.com/sticky-slides/63-sticky-slide-i-luer.html#/33-pcs_box-15/58-channel_height-06_mm.

[115] Ibidi. 1.5 (170 +/- 5 µm) d 263 m schott glass, . URL https://ibidi.com/sticky-slides/66-coverslips-for-sticky-slides.html#/35-pcs_box-100/54-surface_modification-15h_170_m_5_m_d_263_schott_glass_unsterile.

[116] Lumencor. Lumencor sola light engine, . URL https://lumencor.com/products/sola-light-engine/.

[117] Lumencor. Andor neo scmos, . URL https://andor.oxinst.com/products/scmos-camera-series/neo-5-5-scmos.

6.3. Paper 1

frontiers in Physics

ORIGINAL RESEARCH
published: 30 October 2020
doi: 10.3389/fphy.2020.579168

Quantification of Visco-Elastic Properties of a Matrigel for Organoid Development as a Function of Polymer Concentration

Mads Borries[1†], *Younes Farhangi Barooji*[1†], *Siham Yennek*[2], *Anne Grapin-Botton*[2], *Kirstine Berg-Sørensen*[3,4#] *and Lene B. Oddershede*[1*]

[1] *Niels Bohr Institute, University of Copenhagen, Copenhagen, Denmark,* [2] *The Novo Nordisk Foundation Center for Stem Cell Biology, University of Copenhagen, Copenhagen, Denmark,* [3] *Department of Physics, Technical University of Denmark, Kongens Lyngby, Denmark,* [4] *DTU Health Technology, Lyngby, Denmark*

The biophysical properties of polymer based gels, for instance the commonly used Matrigel, crucially depend on polymer concentration. Only certain polymer concentrations will produce a gel optimal for a specific purpose, for instance for organoid development. Hence, in order to design a polymer scaffold for a specific purpose, it is important to know which properties are optimal and to control the biophysical properties of the scaffold. Using optical tweezers, we perform a biophysical characterization of the biologically relevant Matrigel while systematically varying the polymer concentration. Using the focused laser beam we trace and spectrally analyze the thermal fluctuations of an inert tracer particle. From this, the visco-elastic properties of the Matrigel is quantified in a wide frequency range through scaling analysis of the frequency power spectrum as well as by calculating the complex shear modulus. The viscoelastic properties of the Matrigel are monitored over a timespan of 7 h. At all concentrations, the Matrigel is found to be more fluid-like just after formation and to become more solid-like during time, settling to a constant state after 1–3 h. Also, the Matrigel is found to display increasingly more solid-like properties with increasing polymer concentration. To demonstrate the biological relevance of these results, we expand pancreatic organoids in Matrigel solutions with the same polymer concentration range and demonstrate how the polymer concentration influences organoid development. In addition to providing quantitative information about how polymer gels change visco-elastic properties as a function of polymer concentration and time, these results also serve to guide the search of novel matrices relevant for organoid development or 3D cell culturing, and to ensure reproducibility of bio-relevant Matrigels.

Keywords: optical trapping, viscoelasticity, polymer network, complex shear moduli, organoid development

OPEN ACCESS

Edited by:
Halina Rubinsztein-Dunlop, The University of Queensland, Australia

Reviewed by:
Khoi Tan Nguyen, Vietnam National University, Vietnam
Jianming Wen, Kennesaw State University, United States

***Correspondence:**
Lene B. Oddershede
oddershede@nbi.ku.dk

[†]These authors have contributed equally to this work

[#]Present address:
Kirstine Berg-Sørensen
Department of Health Technology, Technical University of Denmark, Kgs Lyngby, Denmark

Specialty section:
This article was submitted to Optics and Photonics, a section of the journal Frontiers in Physics

Received: *01 July 2020*
Accepted: *22 September 2020*
Published: *30 October 2020*

Citation:
Borries M, Barooji YF, Yennek S, Grapin-Botton A, Berg-Sørensen K and Oddershede LB (2020) Quantification of Visco-Elastic Properties of a Matrigel for Organoid Development as a Function of Polymer Concentration. Front. Phys. 8:579168. doi: 10.3389/fphy.2020.579168

INTRODUCTION

Cells in an organism are surrounded by a matrix, often made of biopolymers, whose physical properties dramatically influence cell behavior. For instance, the visco-elastic properties of the extracellular matrix (ECM) has been shown to play an important role in fundamental cellular processes such as cell migration [1, 2], proliferation [3–5], and differentiation [6–8], as well as for the spreading of cancerous cells [5, 9, 10]. For this reason, much effort has been put into developing physics-based tools, experimental and theoretical, to enable characterization of the biophysical properties of polymer solutions. Atomic force microscopy (AFM) and shear rheology are two common experimental techniques which allow for quantification of the elastic properties of the ECM [11, 12]. However, both methods still struggle to measure the stiffness changes of the ECM during imaging of cells in culture media and none of them have the ability to measure deep inside organisms or tissue in a non-invasive manner. Optical tweezers and video-microscopy are two other techniques, which has proven capable of quantifying visco-elastic properties, also inside living cells and organisms, through passive monitoring of an optically trapped tracer particle. These methods have the advantage that they provide both the elastic and viscous responses of a polymer matrix over a large frequency range, including the range relevant for polymer dynamics [13, 14].

Cellular development can be influenced, or controlled, by proper matrix choice. This is instrumental for the development of organoids, which are 3D cell models, derived from a few cells, which allow for *in vitro* expansion of an organ for potential medical usage. Matrigel is the most commonly used polymer matrix for successful organoid development. In this paper, we use Matrigel as a biologically relevant polymer matrix with the purpose of systematically investigating how the physical properties of the polymer matrix change as a function of polymer concentration. Thereby, we continue work which was sparked by investigating the elastic properties of actin network by MacKintosh et al in 1995 [15]. More than 1800 peptides have been identified in Matrigel, however, the main components are Laminin (~ 60%), Collagen IV (~ 30%) and entactin/nidogen (~ 8%), while the remaining ~ 2% consists of a wide range of macromolecules, including proteoglycans. A major difference in protein composition, when comparing the basal lamina or Matrigel to another ECM as, e.g., the connective tissue, is a higher proportion of Laminin compared to Collagen IV. Laminin is a macromolecule with structural functions that especially can withstand tensile forces, while Collagen IV assembles into very large, stiff structures. As a result of this, Matrigel has much more tensile resilience than compressive resilience. Its physical properties then correlate with its role as an element that for example, connects skin cells to connective tissue. One reason why Matrigel is particularly relevant is that mixtures of Matrigel and media have resulted in unprecedented achievements in organoid growth in 3-dimensional structures [16, 17].

Here, we systematically quantify the viscoelastic properties of Matrigel preparations at different polymer concentrations using a passive optical tweezers based method which can be carried out non-invasively during confocal imaging of the sample. These results have interest also for other types of polymeric solution where it is an outstanding question how the viscoelastic properties depend on the polymer concentration. It is also demonstrated how the physically different matrices result in different growth of embedded organoids.

MATERIALS AND METHODS

Optical Setup

An overview of the optical tweezers based setup used for the experiments is provided in **Figure 1**. The optical trap is constructed from an infrared laser (1064 nm, Nd:YVO4, Spectra-Physics J20-BL10-106Q) directed into an inverted microscope (Leica, TCS SP5), equipped with a proper dicroic mirror. Both the laser and the microscope light are focused onto a sample placed in a sample holder through a water immersion objective (PL APO, NA = 1.2, 63X, w). The sample holder is placed on a movable piezo stage (Newport, XY Translation Stage Model M406), that is used to position the sample with respect to the focus of the optical trap. After interacting with the weakly trapped bead, the back-scattered light is collected by the condenser and imaged onto a Quadrant Photo Diode (QPD) (Hamamatsu, Si PIN photodiode S5981) in the back focal plane. In addition, the sample plane is imaged with a CCD camera (Imagesource, DFK 31AF03), monitoring the sample. The measurement output of the QPD, the raw data, consists of four voltages that are transformed into appropriate sums and differences linearly related to the position of the bead inside the trap [18, 19]. The laser was operated at 200–300 mW of which approximately 20% reached the sample plane.

Power Spectral Analysis Method

Optical tweezers exert a harmonic force, $F = \kappa x$, on a trapped bead, where κ is the spring constant and x is the distance from the bead's equilibrium position within the trap. For the bead sizes used here (~ 1μm), the spring constant is similar in the two directions perpendicular to the propagation of the laser light and smaller in the direction parallel to the laser light [20]. For a trapped bead with radius of r in a normal viscous fluid (e.g., water) with viscosity of η, power spectral analysis shows that the power spectrum $P(f)$ at frequency f is ideally given by [21, 22].

$$P(f) = \frac{k_B T}{6\pi\eta r\beta^2} \frac{1}{\left(f_c^2 + f^2\right)}, \tag{1}$$

where f_c is the corner frequency, $k_B T$ is thermal energy and β is the calibration factor which is relating position measurement in Volts by the QPD to meters.

When the surrounding medium is a visco-elastic medium rather than a newtonian fluid, for frequencies well above the corner frequency of the trap, the power spectrum can be described by:

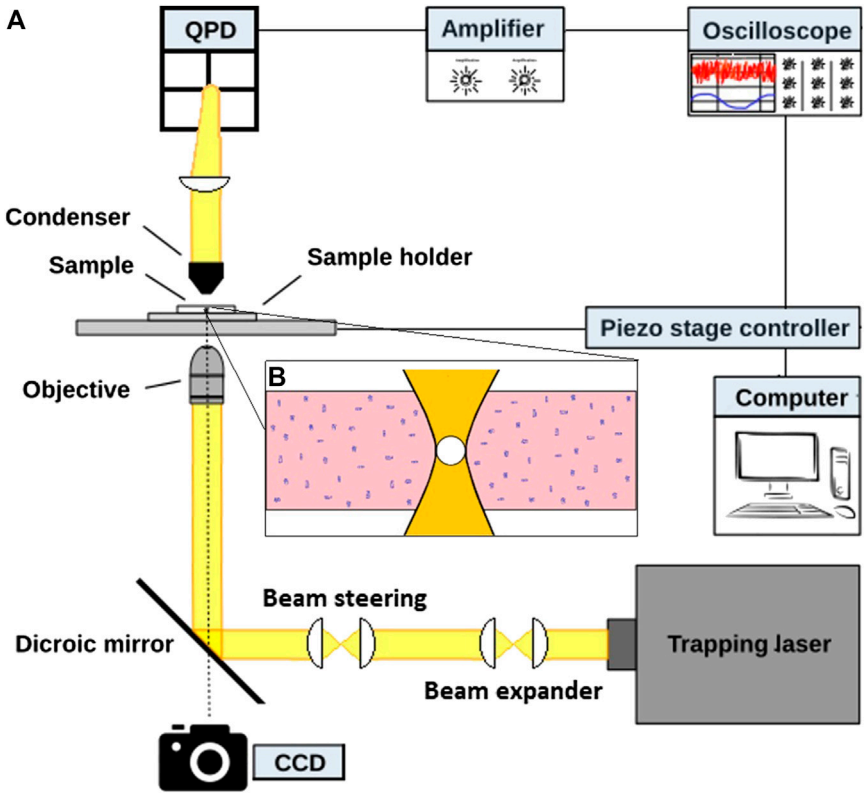

FIGURE 1 | Sketch of the setup. **(A)** 1,064 nm laser light is directed into an inverted microscope. The microscope objective focuses the laser onto a sample (b) placed on a movable piezo stage. After interacting with the sample, the back-scattered light is collected by a condenser and focused onto a Quadrant Photo Diode (QPD). A CCD camera monitors the sample. **(B)** Sketch of a sample containing Matrigel solution and an optically trapped tracer particle.

$$P(f) \propto f^{-(\alpha+1)}. \tag{2}$$

For tracer motion within a medium, the value of α relates to the behavior of the tracer particle as follows:

- $\alpha = 0$: The particle is **completely confined** by the surrounding medium.
- $0 < \alpha < 1$: The particle undergoes **sub-diffusion**, the lower the value of α, the more elastic the medium, and the closer to 1 the more viscous the medium.
- $\alpha = 1$: The particle performs **free diffusion** described as Brownian motion, and the surrounding medium is purely viscous.
- $\alpha > 1$: The particle undergoes **super-diffusion**, indicating that there are active processes and that particle movement is propelled by external forces.

Complex Shear Moduli

The frequency dependent complex shear modulus, $G(f) = G'(f) + iG''(f)$ can be found from the power spectral density and analysis of the response function of the trapped particle. The frequency dependent shear modulus, $G(f)$, has as its real part the elastic modulus, $G'(f)$, which describes the stored energy in the complex medium. Conversely, the imaginary part, the loss modulus, $G''(f)$, is a measure of the energy dissipated by deformation of the complex material. For a microparticle inside a viscoelastic medium, the Fourier transform of the stochastic thermal force, $F(f)$, and the Fourier transformed of the position of the particle, $x(f)$ are related through linear response theory [23],

$$x(f) = \gamma(f)F(f), \tag{3}$$

where $\gamma(f)$ is the compliance of the medium [24]. The medium compliance is a complex function which in turn is related to the viscoelastic modulus through the Generalized Stokes-Einstein relation,

$$G(f) = \frac{1}{6\pi r\gamma(f)}. \tag{4}$$

Thus, the different physical quantities are extracted as follows:

$$G'(f) = \frac{1}{6\pi r}\frac{\gamma'(f)}{\gamma'(f)^2 + \gamma''(f)^2} \tag{5}$$

$$G''(f) = -\frac{1}{6\pi r}\frac{\gamma''(f)}{\gamma'(f)^2 + \gamma''(f)^2} \tag{6}$$

$$\gamma''(f) = \frac{\pi f}{2k_B T}P(f) \tag{7}$$

$$\gamma'(f) = \frac{2}{\pi}\int_0^\infty \cos(2\pi f t)\mathrm{d}t \int_0^\infty \gamma''(f)\sin(\tilde{f}t)\mathrm{d}\tilde{f} \qquad (8)$$

where the last results follows from the Kramers-Kronig relation. This method is less challenging in comparison with active methods (oscillatory microrheology) [25], however, since the trap stiffness is not accounted for, the laser power should not be too high. And since the photodiode detection system may act as an unintended filter [26], the frequency span of the method lies between the corner frequency of trap and the filtering frequency of the photodiode, this frequency interval spanning several orders of magnitude and encompassing frequencies relevant for polymer dynamics. With these concerns accounted for, the frequency dependent viscoelastic characteristics of the medium can be determined as described above. The loss tangent, $\tan(\delta) = G''/G'$, relates to the overall behavior of the medium at the particular frequency, i.e., it describes the solid (or gel like) ($G''/G' < 1$)- or fluidlike ($G''/G' > 1$) behavior of the viscoelastic material.

Preparation of Matrigel Matrix and Sample Chamber

The major components of the ECM include water, proteins, and polysaccharides and different types of ECMs for cell culturing are commercially available, extracted from different types of tissue using different protocols [27–29]. ECM preparations of particular viscoelastic properties can be produced with different compositions by including a variety of proteins and biopolymers. Matrigel^R is a commercial ECM extracted from Engelbreth-Holm-Swarm mouse tumor cultures [30–33]. It is commonly used as a basement membrane matrix to support proliferation of stem cells while they remain in an undifferentiated state [34]. In addition, combinations of Matrigel and other ECM mixtures [35–37] are widely used as external matrix in culturing of 3D spheroids and organoids.

The Matrigel (Corning® Matrigel®, Growth Factor Reduced, Basement Membrane Matrix, Phenol Red-free, LDEV-free) was mixed with the nutrition medium Dulbecco's Modified Eagle Medium/Nutrient Mixture F-12 (DMEM) (Gibco™, GlutaMAX™, Additives: Sodium Pyruvate & Sodium Bicarbonate). The latter is a medium that has proven to support growth of several kinds of cells and organoids, such as the pancreas organoid, providing the addition of small quantities of additional growth factors [16, 17]. The nutrition medium contains a high concentration of amino acids, vitamins and glucose.

Sample chambers, with an inner height between 300 and 500 μm, were prepared by sticking two glass slides together using vacuum grease and the chambers were then cooled down. Frozen Matrigel was put on ice to slowly thaw. Since Matrigel becomes gel-like at above approximately 4°C, the temperatures of the solutions had to be kept between 0 and 4°C. The nutrition medium was cooled to the same temperature and mixed with a 0.96 μm polystyrene bead solution. Matrigel and the nutrition medium with polystyrene beads were mixed together using pipettes and injected in the sample chambers. The chambers were then sealed completely with vacuum grease. A chamber was placed on the microscope stage and beads were trapped to conduct a measurement once per hour during 7 h.

Trapping of Beads Inside Matrigel Sample

Immediately after sample preparation, the samples were taken to the optical tweezers setup. Beforehand the laser trap was calibrated to have its focus (**Figure 1B**) at the same axial position as the microscope objective's focus and to have its lateral center in the center of the field of view of the objective. At this position, the tracer beads were physically trapped in a harmonic potential. Before turning on the laser, the dispersed beads were localized and positioned in the center of the microscope objective's focus point. The laser was then activated, it was operated at relatively low laser powers and the bead was hence trapped in a weak harmonic potential. While the bead was trapped and performing thermal fluctuations, its positions were recorded by QPD. In each chamber, for each concentration and at each point in time, five beads were trapped. And for each bead, three microrheology measurements were conducted.

Mouse Pancreatic Organoid Culture and Measurement

Mouse pancreatic organoids were cultured as previously described [16, 17]. Briefly, pancreatic progenitors were isolated from the dorsal pancreatic bud of a litter of mouse embryos at embryonic day (e)10.5, typically 10 embryos. The epithelial part of the bud was dissected from the surrounding mesenchyme and remaining digestive tract with microneedles, dissociated to single cells and small clusters using Trypsin 0.5% (about 5,000 cells from 10 pooled embryos) and mixed with growth factor-depleted Matrigel on ice. Drops of 8 μl of the cell:Matrigel mixture were deposited on culture plates, allowed to gel at 37°C and cultured in organoid medium [16, 17] for 7 days. In these conditions clusters of cells proliferate and self-organize to form organoids. Three concentrations of Matrigel were tested: 75%, 50%, and 25%. Images of organoid cultures were acquired after day 1, day 2, day 4, day 5 and day 7 in culture on a Leica AF6000 (HCX PL FLUOTAR 10x/0.30 Ph1 Dry, Leica DFC365 FX camera) in such a way that every single organoid could be tracked over time. Organoid area was measured over time using the freehand selection tool on ImageJ. The radius (r) of the measured areas was calculated assuming a spherical shape, and organoid growth was determined by plotting r^3 of organoids over time, normalized to r^3 of the same organoid at day 1. This analysis corrects for the dependency of the final size of the organoid on the initial seed size observed at day 1.

To quantify the branching of the growing organoids, the focus plane of the objective yielding the largest area for each organoid was used to determine the area of individual organoids. At this plane, the length of the outer membrane surrounding the entire organoid, the perimeter, was quantified by Fiji routines. The ratio perimeter^2/area was calculated for each organoid in order to have a dimensionless measure of branching, that is, size-independent.

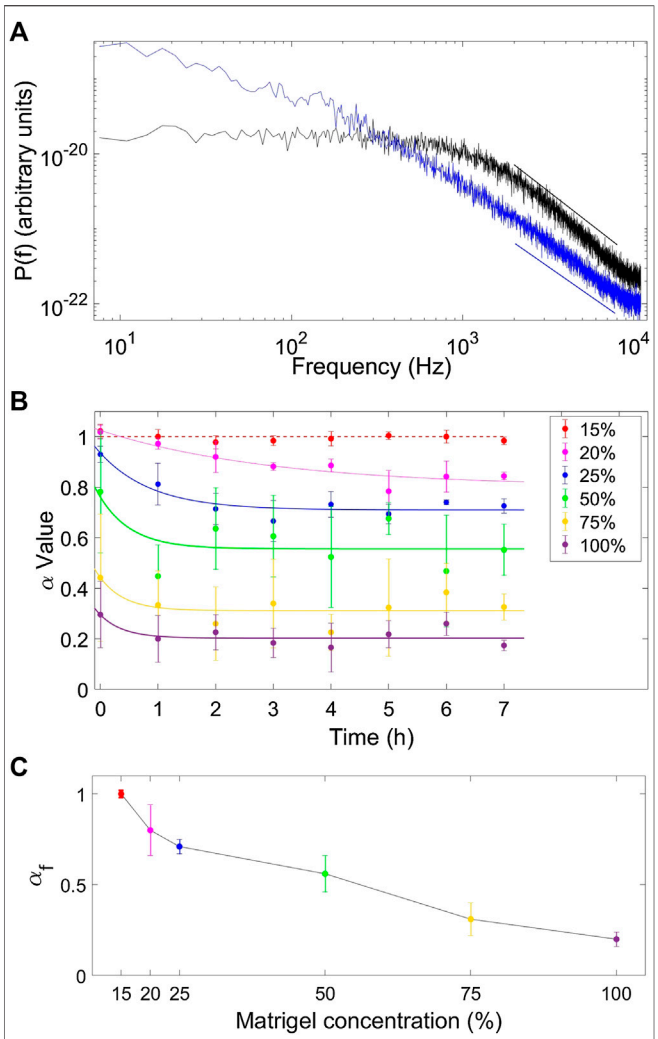

FIGURE 2 | Determination of scaling properties and evaluation of how these change as a function of time and concentration. **(A)** Power spectrum of an optically trapped particle in water (black, $\alpha = 1$) and in a Matrigel mixture (ratio 75% medium to 25% matrigel) (blue, $\alpha = 0.71$) 7 h after preparation of the sample. The straight lines show fits of **Eq. 2** to data, fits were carried out on data blocked as described in refs. 38 and 39. **(B)** Values of α as a function time for tracer particles embedded in different concentrations of matrigel solution (15% red, 20% magenta, 25% blue, 50% green, 75% orange, and pure Matrigel solution (100%) purple). Solid lines show exponential fits to the experimental data which indicate that α reaches an asymptotic value, α_f, after a few hours. **(C)** The value of α_f decreases with Matrigel concentration: $\alpha_f = 1.00 \pm 0.02$ for 15% Matrigel, $\alpha_f = 0.80 \pm 0.14$ for 20% Matrigel, $\alpha_f = 0.71 \pm 0.04$ for 25% Matrigel, $\alpha_f = 0.56 \pm 0.10$ for 50% Matrigel, $\alpha_f = 0.31 \pm 0.09$ for 75% Matrigel, and $\alpha_f = 0.20 \pm 0.04$ for 100% Matrigel.

RESULTS AND DISCUSSION

Viscoelastic Properties of the Matrigel Changes as a Function of Time and Concentration

To characterize the viscoelastic properties of each sample, we retrieved α by fitting **Eq 2** to the experimentally obtained power spectral data (PSD) in the frequency range 2000 Hz < f < 8,000 Hz. The miminum frequency, 2 kHz, was chosen well above the corner frequency, f_c, in order to avoid the frequency interval where the optical trap had a confining effect. The maximum frequency, 8 kHz, was chosen well below the cut-off frequency, f_{3dB}, of the quadrant photodiode [26].

Figure 2A shows two examples of the PSD as a function of frequency on a double-log plot for a trapped bead in water (a purely viscous liquid, black in **Figure 2A**) and in a 25% Matrigel solution (a viscoelastic medium, blue in **Figure 2A**). The two PSDs in **Figure 2A**) illustrate the difference in scaling properties of a tracer particle embedded in a purely viscous media as opposed to embedment in a viscoelastic media. Beads moving in a mixture with only 15% Matrigel solution behave as if they had been in a normal Newtonian liquid like water as their motion was characterized by $\alpha \sim 1$. Higher concentrations of Matrigel (20%, 25%, 50%, 75%, and 100%) lead to values of α significantly less than 1, indicating that the mixture of Matrigel and nutrition medium for these concentrations of Matrigel have both viscous and elastic properties.

Over time, the fitted value of α decreased from an initial value α_0 to a final asymptotic value, α_f (see **Figure 2B**). This temporal behavior of α was well fitted by an exponential function, $\alpha(t) = \alpha_0 e^{-t/\tau} + \alpha_f$, as seen in **Figure 2B**), where the parameter τ is a

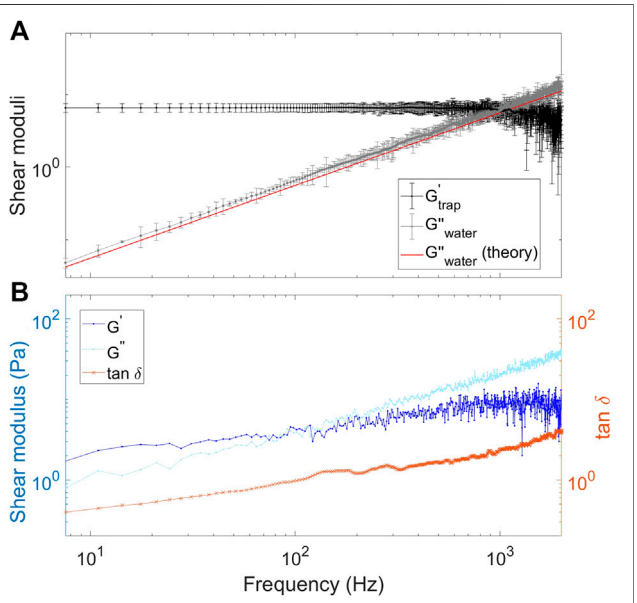

FIGURE 3 | Extraction of complex shear moduli for tracer particles in water or Matrigel solutions. **(A)** Extracted complex shear moduli for a bead trapped in water. The black symbols and black line show the storage modulus. The gray symbols and gray line show the loss modulus, the results being in agreement with theory (red line) for a viscous liquid. **(B)** Extracted storage modulus, G'(blue), and loss modulus, G''(light-blue), for a bead trapped in a Matrigel solution (75 medium:25 Matrigel). Both G' and G'' increase as a function frequency. At low frequencies, the Matrigel solution exhibits solid-like behavior. At around 100 Hz the loss modulus equals the storage modulus, and at frequencies higher than 100 Hz the solution exhibits liquid like behavior. The orange line shows the loss tangent which is below or above 1 for solid- or liquid-like behavior, respectively.

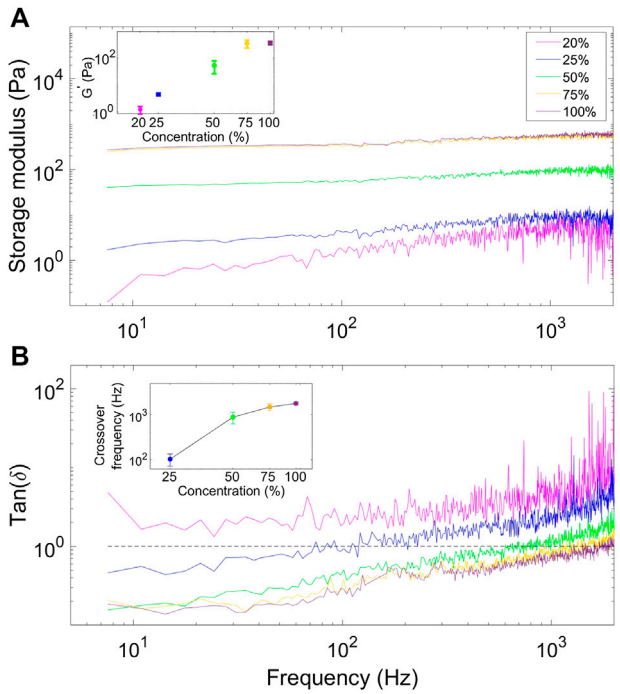

FIGURE 4 | Analysis of how the elastic properties of the matrix change with polymer concentration. **(A)** Storage moduli of mixtures with different Matrigel concentrations (20% magenta, 25% blue, 50% green, 75% orange, and pure Matrigel solution (100%) purple). At all frequencies, the storage moduli increase with Matrigel concentration. The inset shows the value of the storage modulus at f = 100 Hz as a function of Matrigel concentration. **(B)** Loss tangents as a function of frequency for different Matrigel concentrations. The insert shows the value of the crossover frequency, the frequency at which $\tan(\delta) = 1$, as a function of concentration. The cross-over frequency marks the frequency at which the solution shifts from solid- to liquid-like behavior. The data were collected 7 h after the sample preparation.

relaxation time. The asymptotic value of the exponent, α_f, decreases as the concentration of Matrigel increases, thus indicating that the polymeric mixture becomes more rigid as a function of time (**Figure 2C**).

Complex Shear Moduli of Matrigel Change With Concentration

The viscoelastic properties of the Matrigel were also investigated through their complex shear moduli as described in Methods, however, with the extra consideration that the contribution from the optical trap should also be considered. For a particle trapped inside the medium, $G'(f)$ as calculated directly from the data is an effective modulus which contains both the contribution from the elastic modulus of the surrounding medium and the contribution from the trap [24], G'_{trap}. Therefore, the contribution from the trap should be subtracted from the effective value calculated from the raw data. To determine the storage modulus of the trap, we extracted the elastic modulus for a bead trapped in water as a purely viscous medium, otherwise following an identical procedure. The resulting storage modulus of the trap ($G'_{\mathrm{trap}} = 6.57 \pm 0.9\,Pa$) is shown in **Figure 3A**). The experimental data shows the expected behavior of the loss modulus for water; in particular, we observe that $G''_{\mathrm{trap}}(f)$ scales with $\alpha = 1$ as expected for a purely viscous medium where $G'' = 2\pi\eta f$ (**Figure 3A**). The apparent decrease in the shear moduli for the highest frequencies is an artifact resulting from the finite experimental maximum frequency when evaluating the integrals in **Eq. 8**, as also described in ref. 40.

Once the storage moduli of water are known, the shear moduli corresponding to the Matrigel solution can be extracted. As discussed above, in a solution with a 15% concentration of Matrigel, the bead experiences a medium with properties very similar to water, see also **Figure 2B**), which is probably due to the very low concentration of polymers. For a 20% Matrigel mixture, the loss modulus dominates the storage modulus in the entire measured frequency interval, thus implying that the solution has a dominantly liquid like behavior ($\tan(\delta) > 1$). The mixtures with 25% Matrigel concentration and higher show solid like behavior ($\tan(\delta) < 1$) at low frequencies whereas the behavior changes to a liquid-like phase ($\tan(\delta) > 1$) after the crossover point ($G'' = G'$), see **Figure 3B**).

Figure 4A) demonstrates that the storage modulus of Matrigel mixtures increases with Matrigel concentration over the entire frequency range, the inset in a) shows the value of the loss modulus at f = 100 Hz as a function of concentration. The same conclusion can be drawn from inspecting the loss tangent as a function of frequency for different Matrigel concentration; the loss tangent clearly increases with Matrigel concentration over the entire frequency range (**Figure 4B**). The inset in **Figure 4B**) shows the cross over frequency, i.e., the frequency at which $\tan(\delta) = 1$, as a function of Matrigel concentration, further cementing the observation that the higher the polymer concentration, the more solid-like the matrix.

Effect of Matrigel Concentration on Organoid Expansion

To test whether variations of the mechanical properties of a Matrigel polymer matrix affects pancreas organoid growth and branching patterns, we seeded pancreatic progenitors isolated from e10.5 embryos in Matrigel-based matrices with Matrigel concentrations in the range of 25–75%. As previously reported for 75% Matrigel, we observed that organoids grew during the entire 7-day period of observation. After day 4 they started to form bulges reminiscent of the branching patterns seen in the body (**Figure 5A**). While the growth (measured by normalized volume) was in the same range for organoids embedded in 25%, 50% or 75% Matrigel matrices (**Figure 5B**), their branching visually appeared greater in higher Matrigel concentrations (**Figure 5A**).

To further analyze the branching of organoids as a function of time, the morphology of the growing organoids was determined by measuring their area and perimeter. If the perimeter compared to area is large, compared that of a disk, there is a high degree of organoid branching. In order to have a measure for branching,

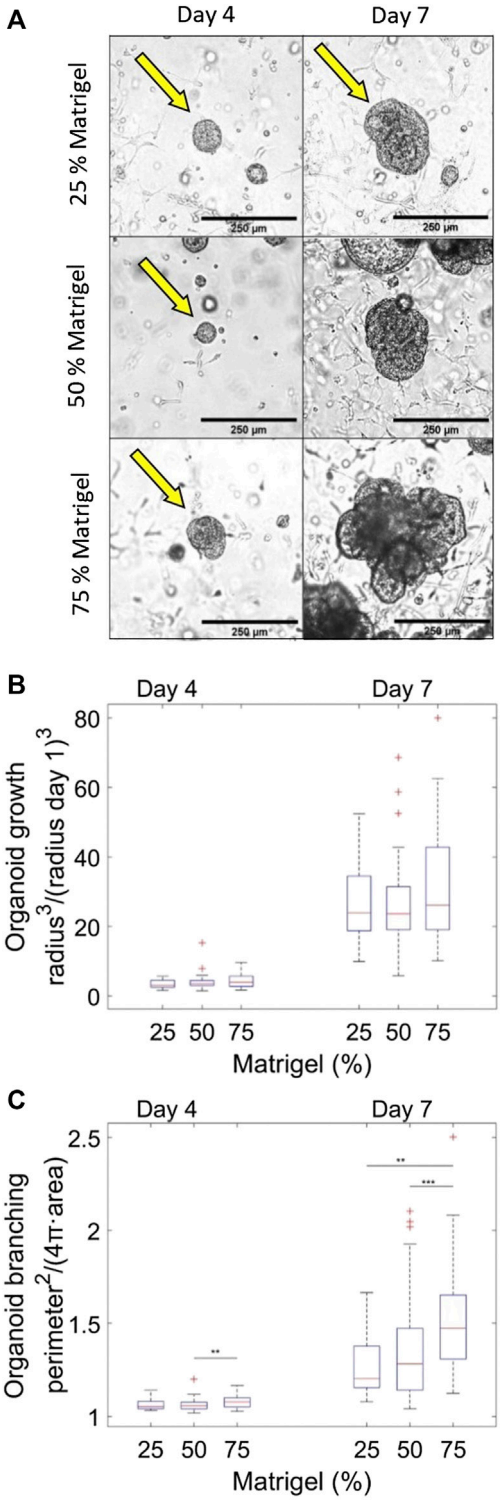

FIGURE 5 | Quantification of organoid branching in Matrigel matrices of different concentrations. **(A)** Representative pictures of organoid growth over time in 75%, 50%, and 25% Matrigel matrices at Day 4 and Day 7, respectively. If more objects are present in an image, arrows point to examples of organoids used for data analysis. **(B)** Quantification of organoid growth in Matrigel matrices with different concentrations (25%, 50%, 75%).

(*Continued*)

that is, independent of the overall size or the organoid, the perimeter^2/area ratio, which is dimensionless, was calculated for each organoid at each Matrigel concentrations at day 4 and at day 7. This ratio was normalized by 4π, which is the value of the ratio for a perfect disk. Hence, the measure depicted in **Figure 5C**) is perimeter^2/area for an organoid divided by the same ratio for a disk. If the measure exceeds 1, the organoid has some degree of branching. This measure of branching is plotted in **Figure 5C**) as a function of time elapsed since seeding of the organoids in the Matrigel matrix. Notice that even at the first time point (D4), the elastic properties of the matrix have reached their static behavior (cf **Figure 2B**).

D'Agostino tests performed on the distributions shown in **Figure 5C** showed that a fair fraction of the distributions were not normally distributed. Hence, to evaluate whether the distributions were statistically significantly different, Mann-Whitney U tests were performed. At day 4 after seeding, organoids embedded in Matrigel matrices at all tested concentrations showed minimal branching with an average normalized perimeter^2/(4πarea) value between 1.06 and 1.08. At this early developmental stage there is, however, already significantly more branching in the 75% Matrigel concentration than in the 50% Matrigel concentration (p = 5.7e-3). At day 7, organoids embedded in the 75% Matrigel matrix have visibly and statistically significantly more branching than those embedded in the 50% (p = 2.9e-04) and the 25% Matrigel matrices (p = 1.8e-3). The average values of normalized perimeter^2/(4πarea) at day 7 for the 25%, 50%, and 75% Matrigel concentrations are 1.27 ± 0.17, 1.36 ± 0.27, and 1.53 ± 0.29, respectively, with median values of 1.20 interquartile range (IQR) 0.22, 1.28 IQR 0.33, and 1.47 IQR 0.34, respectively.

These results show a correlation between the biophysical properties of the medium that organoids are seeded in and the developing morphology of organoids. When the Matrigel concentration is higher, the matrix becomes stiffer, as measured both by the power spectral method and through shear- and storage moduli. A higher degree of branching during pancreas organoid growth is observed for matrices of higher stiffness.

While one may have expected that the stiffness of the environment may either promote growth [41] or limit it by its resistance to compression, this was not observed in the range tested. Instead, the more rigid matrix affects the degree of organoid branching, with more branching observed at higher

FIGURE 5 | The organoid growth is monitored over time. The average of the normalized volumes r/(r Day 1) and the standard deviations are plotted for each condition and each time point. n = 12, 33, and 29 organoids grown in 25%, 50%, and 75% Matrigel, respectively, distributed in two independent experimental repeats. **(C)** Effect of Matrigel concentration on branching quantified by the dimensionless measure: Normalized perimeter^2/area which is plotted as a function of time and for different Matrigel concentrations (25%, 50%, and 75%). At Day 7, there is a significant increase in branching as the Matrigel concentration is increased. n = 12, 66, and 49 organoids for 25%, 50%, and 75% Matrigel, respectively, distributed in two independent experimental repeats.

Matrigel concentrations. It is possible that when an organoid has penetrated a certain region of a rigid medium, the organoid expands more easily at this position and hence creates branches here. More of the organoid's growth will then appear at this position compared to the case of a less rigid growth medium where a more uniform expansion is easier. This may be alike what was reported during the formation of cortical gyri where a mechanical instability due to tangential expansion of cells has non-linear consequences [42].

CONCLUSION

Optical tweezers-based micro-rheology provides a simple method to quantify visco-elastic properties in a highly localized manner and potentially deep within a sample over a large frequency range. Here, we tracked thermal fluctuations of tracer particles inside Matrigel solutions while systematically varying polymer concentrations. This allowed for extraction of the visco-elastic properties of the polymer matrix at different polymer concentrations; the visco-elastic properties were quantified though the scaling properties of the tracer particle's positional power spectrum and by calculating the complex shear moduli.

The visco-elastic properties of a Matrigel-based polymer matrix were found to be highly dependent on polymer concentration, the higher the polymer concentration, the more elastic (less viscous) the matrix. Also, we found that the visco-elastic properties of the Matrigel matrix change over time, with the matrix being more viscous when it is first made and after a few hours it becomes more elastic and settles to a permanent degree of elasticity.

Organoids embedded in a higher Matrigel concentration developed a larger degree of branching, however, their overall size did not change with Matrigel concentration. Being aware of the fact that organoid growth morphology is dependent on Matrigel concentration will be important for bioengineering of proper growth matrices and for understanding how tissues mechanically interact with their environment.

DATA AVAILABILITY STATEMENT

The raw data supporting the conclusions of this article will be made available by the authors, without undue reservation.

AUTHOR CONTRIBUTIONS

The study was designed by LBO, MB, YFB, KBS and AGB. The experimental data was acquired and analyzed by MB, YFB and SY. All authors discussed all results and participated in writing the manuscript.

ACKNOWLEDGMENTS

The authors acknowledge financial support from the Danish National Research Council, grant number DNRF116. The Novo Nordisk Foundation Center for Stem Cell Biology is supported by a Novo Nordisk Foundation grant number NNF17CC0027852.

REFERENCES

1. Lo CM, Wang HB, Dembo M, Wang YL. Cell movement is guided by the rigidity of the substrate. *Biophys J* (2000) **79**:144–52. doi:10.1016/S0006-3495(00)76279-5
2. Kim MC, Silberberg YR, Abeyaratne R, Kamm RD, Asada HH. Computational modeling of three-dimensional ECM-rigidity sensing to guide directed cell migration. *Proc Natl Acad Sci USA* (2018) **115**:E390–9. doi:10.1073/pnas.1717230115
3. Wells RG. The role of matrix stiffness in regulating cell behavior. *Hepatology* (2008) **47**:1394–400. doi:10.1002/hep.22193
4. Shin JW, Mooney DJ. Extracellular matrix stiffness causes systematic variations in proliferation and chemosensitivity in myeloid leukemias. *Proc Natl Acad Sci USA* (2016) **113**:12126–31. doi:10.1073/pnas.1611338113
5. Cavo M, Fato M, Peñuela L, Beltrame F, Raiteri R, Scaglione S. Microenvironment complexity and matrix stiffness regulate breast cancer cell activity in a 3D *in vitro* model. *Sci Rep* (2016) **6**, 35367. doi:10.1038/srep35367
6. Smith LR, Cho S, Discher DE. Stem cell differentiation is regulated by extracellular matrix mechanics. *Physiology* (2018) **33**:16–25. doi:10.1152/physiol.00026.2017
7. Hwang JH, Byun MR, Kim AR, Kim KM, Cho HJ, Lee YH, et al. Extracellular matrix stiffness regulates osteogenic differentiation through MAPK activation. *PLoS One* (2015) **10**:1–16. doi:10.1371/journal.pone.0135519
8. Olsen AL, Bloomer SA, Chan EP, Gaça MDA, Georges PC, Sackey B, et al. Hepatic stellate cells require a stiff environment for myofibroblastic differentiation. *Am J Physiol Gastrointest Liver Physiol* (2011) **301**:G110–8. doi:10.1152/ajpgi.00412.2010
9. Wullkopf L, West AKV, Leijnse N, Cox TR, Madsen CD, Oddershede LB, et al. Cancer cells' ability to mechanically adjust to extracellular matrix stiffness correlates with their invasive potential. *Mol Biol Cell* (2018) **29**:2378–85. doi:10.1091/mbc.E18-05-0319
10. Bordeleau F, Mason BN, Lollis EM, Mazzola M, Zanotelli MR, Somasegar S, et al. Matrix stiffening promotes a tumor vasculature phenotype. *Proc Natl Acad Sci USA* (2017) **114**:492–7. doi:10.1073/pnas.1613855114
11. Soofi SS, Last JA, Liliensiek SJ, Nealey PF, Murphy CJ. The elastic modulus of matrigel$_{TM}$ as determined by atomic force microscopy. *J Struct Biol* (2009) **167**:216–9. doi:10.1016/j.jsb.2009.05.005
12. Koutsopoulos S, Zhang S. Long-term three-dimensional neural tissue cultures in functionalized self-assembling peptide hydrogels, matrigel and collagen I. *Acta Biomater* (2013) **9**:5162–9. doi:10.1016/j.actbio.2012.09.010
13. Tolić-Nørrelykke IM, Munteanu EL, Thon G, Oddershede L, Berg-Sørensen K. Anomalous diffusion in living yeast cells. *Phys Rev Lett* (2004) **93**:078102. doi:10.1103/PhysRevLett.93.078102
14. Wessel A, Maheshwar G, Grosshans J, Schmidt C. The mechanical properties of early drosophila embryos measured by high-speed video microrheology. *Biophys J* (2015) **108**:1899–1907. doi:10.1016/j.bpj.2015.02.032
15. MacKintosh F, Kas J, Janmey P. Elasticity of semiflexible biopolymer networks. *Phys Rev Lett* (1995) **75**:4425–8. doi:10.1103/PhysRevLett.75.4425
16. Greggio C, De Franceschi F, Figueiredo-Larsen M, Grapin-Botton A. *In vitro* pancreas organogenesis from dispersed mouse embryonic progenitors. *J Vis Exp* (2014) (89):51725. doi:10.3791/51725
17. Greggio C, De Franceschi F, Grapin-Botton A. Concise reviews: in vitro-produced pancreas organogenesis models in three dimensions: self-organization from few stem cells or progenitors. *Stem Cell* (2015) **33**:8–14. doi:10.1002/stem.1828

18. Gittes F, Schmidt CF. Interference model for back-focal-plane displacement detection in optical tweezers. *Opt lett* (1998) **23**:7–9. doi:10.1364/ol.23.000007
19. Allersma MW, Gittes F, DeCastro MJ, Stewart RJ, Schmidt CF. Two-dimensional tracking of ncd motility by back focal plane interferometry. *Biophys J* (1998) **74**:1074–85. doi:10.1016/S0006-3495(98)74031-7
20. Rohrbach A. Stiffness of optical traps: quantitative agreement between experiment and electromagnetic theory. *Phys Rev Lett* (2005) **95**:168102. doi:10.1103/PhysRevLett.95.168102
21. Svoboda K, Block SM. Biological applications of optical forces. *Annu Rev Biophys Biomol Struct* (1994) **23**:247–85. doi:10.1146/annurev.bb.23.060194.001335
22. Gittes F, Schmidt CF. Signals and noise in micromechanical measurements. *Methods Cell Biol* (1998) **55**:129–56. doi:10.1016/S0091-679X(08)60406-9
23. Schnurr B, Gittes F, MacKintosh F, Schmidt C. Determining microscopic viscoelasticity in flexible and semiflexible polymer networks from thermal fluctuations. *Macromolecules* (1997) **30**:7781–92. doi:10.1021/MA970555N
24. Pesce G, De Luca AC, Rusciano G, Netti PA, Fusco S, Sasso A. Microrheology of complex fluids using optical tweezers: a comparison with macrorheological measurements. *J Opt A Pure Appl Opt* (2009) **11**:034016. doi:10.1088/1464-4258/11/3/034016
25. Mizuno D, Head DA, MacKintosh FC, Schmidt CF. Active and passive microrheology in equilibrium and nonequilibrium systems. *Macromolecules* (2008) **41**:7194–202. doi:10.1021/ma801218z
26. Berg-Sørensen K, Oddershede L, Florin EL, Flyvbjerg H. Unintended filtering in a typical photodiode detection system for optical tweezers. *J Appl Phys* (2003) **93**:3167–76. doi:10.1063/1.1554755
27. Xing Q, Qian Z, Jia W, Ghosh A, Tahtinen M, Zhao F. Natural extracellular matrix for cellular and tissue biomanufacturing. *ACS Biomater Sci Eng* (2016) **3**:1462–76. doi:10.1021/acsbiomaterials.6b00235
28. Uriel S, Labay E, Francis-Sedlak M, Moya ML, Weichselbaum RR, Ervin N, et al. Extraction and assembly of tissue-derived gels for cell culture and tissue engineering. *Tissue Eng C* (2009) **15**:309–21. doi:10.1089/ten.tec.2008.0309
29. Francis MP, Sachs PC, Madurantakam PA, Sell SA, Elmore LW, Bowlin GL, et al. Electrospinning adipose tissue-derived extracellular matrix for adipose stem cell culture. *J Biomed Mater Res* (2012) **100A**:1716–24. doi:10.1002/jbm.a.34126
30. Lin M, Jingwu L, Qiang N, Qiuyang Z, Qiuyang Z, Sen L, et al. Organoid culture of human prostate cancer cell lines LNCaP and C4-2B. *Am J Clin Exp Urol* (2017) **5**:25–33. doi:10.1002/ijc.33315
31. Molina-Jimenez F, Benedicto I, Thi VLD, Gondar V, Lavillette D, Marin JJ, et al. Matrigel-embedded 3D culture of huh-7 cells as a hepatocyte-like polarized system to study hepatitis C virus cycle. *Virology* (2012) **425**:31–9. doi:10.1016/j.virol.2011.12.021
32. Drost J, Karthaus WR, Gao D, Driehuis E, Sawyers CL, Chen Y, et al. Organoid culture systems for prostate epithelial and cancer tissue. *Nat Protoc* (2016) **11**: 347–58. doi:10.1038/nprot.2016.006
33. Sodunke TR, Turner KK, Caldwell SA, McBride KW, Reginato MJ, Noh HM. Micropatterns of matrigel for three-dimensional epithelial cultures. *Biomaterials* (2007) **28**:4006–16. doi:10.1016/j.biomaterials.2007.05.021
34. Hughes CS, Postovit LM, Lajoie GA. Matrigel: a complex protein mixture required for optimal growth of cell culture. *Proteomics* (2010) **10**:1886–90. doi:10.1002/pmic.200900758
35. Kuo CT, Wang JY, Lin YF, Wo AM, Chen BPC, Lee H. Three-dimensional spheroid culture targeting versatile tissue bioassays using a PDMS-based hanging drop array. *Sci Rep* (2017) **7**:4363. doi:10.1038/s41598-017-04718-1
36. Anguiano M, Castilla C, Maska M, Ederra C, Pelaez R, Morales X, et al. Characterization of three-dimensional cancer cell migration in mixed collagen-matrigel scaffolds using microfluidics and image analysis. *PLoS One* (2017) **12**:e0171417. doi:10.1371/journal.pone.0171417
37. Cui X, Hartanto Y, Zhang H. Advances in multicellular spheroids formation. *J R Soc Interface* (2017) **14**:20160877. doi:10.1098/rsif.2016.0877
38. Berg-Sørensen K, Flyvbjerg H. Power spectrum analysis for optical tweezers. *Rev Sci Instrum* (2004) **75**:594–612. doi:10.1063/1.1645654
39. Hansen PM, Tolić-Nørrelykke IM, Flyvbjerg H, Berg-Sørensen K. Tweezercalib 2.0: faster version of matlab package for precise calibration of optical tweezers. *Comput Phys Commun* (2006) **174**:518–20. doi:10.1016/j.cpc.2005.11.007
40. Loosemore VE, Forde NR. Effects of finite and discrete sampling and blur on microrheology experiments. *Opt Express* (2017) **25**:31239–52. doi:10.1364/OE.25.031239
41. Gjorevski N, Sachs N, Manfrin A, Giger S, Bragina ME, Ordóñez-Morán P, et al. Designer matrices for intestinal stem cell and organoid culture. *Nature* (2016) **539**:560–4. doi:10.1038/nature20168
42. Tallinen T, Chung J, Biggins J, Mahadevan L. Gyrification from constrained cortical expansion. *Proc Natl Acad Sci USA* (2014) **111**12667–72. doi:10.1073/pnas.1406015111

Conflict of Interest: The authors declare that the research was conducted in the absence of any commercial or financial relationships that could be construed as a potential conflict of interest.

6.4. Paper 2

Temperature controls NF-κB oscillations and presents a road map to chaotic dynamics

Mads von Borries[1,+] Mathias L. Heltberg[1,+], Pol Martin Bendix[1,*], Lene Oddershede[1,*], and Mogens H. Jensen[1,*1,*]

[1]1 *Niels Bohr Institute, University of Copenhagen, Blegdamsvej 17, DK-2100, Copenhagen, Denmark*

* *Co-corresponding author*

\+ *co-first author*

(Dated: August 31, 2021)

The nuclear concentration of the most important transcription factors has been revealed to show intriguing dynamical features. In particular the protein complex NF-κB, that is expected to play a vital role in the control of the immune system, shows oscillatory behaviour following stimulation with the ligand TNF. However, how cells can control these oscillations and how the period and amplitude might affect the downstream gene production is still an unsolved question. In this paper, we investigate how oscillations in the nuclear concentration of NF-κB are affected by the temperature in the surroundings. We find that cells can survive and sustain oscillations under temperature variations of $\pm 5^oC$ and that the frequency of the oscillations increases with temperature. From this we investigate the oscillations through a mathematical model, where all rate parameters are affected as predicted by results derived from the Smoluchowski equation and find a remarkable correspondence between the model predictions and the experimental results. We find that the downstream protein production of genes stimulated by NF-κB and reveal a crossover behaviour, where low affinity genes are down-regulated at low temperatures whereas proteins from high affinity genes are up-regulated at high temperatures. Finally we show that oscillations in the temperature can control the NF-κB oscillations through entrainments and that temperature variations of $\pm 3^oC$ suggest an effective way to induce chaotic dynamics which might be of significant importance to future work.

I. INTRODUCTION

The fine-tuned regulation of protein production is fundamental to all living organisms. This production is complicated and includes a number of components, but central to the stimulation of genes is the concentration of transcription factors inside the nucleus. In the past two decades, it has been revealed that the nuclear concentration of a number of central transcription factors, can be highly dynamic and it is expected that this dynamics might be an important element in the complex gene regulation of cells. One example of such a transcription factor, is the p53 tumour suppressor that has a period of ≈ 5 hours [8, 11, 12] and another, which is the scope of the present work, is NF-κB, which oscillates with a period $\approx$ 1.5 hours and has been shown to control the production of a number of proteins related to the immune response [2–4, 6, 7, 9]. It is at present debated what the functional role (if any) of these oscillations is, but it seems certain that the downstream genes are affected by this dynamics [2, 3, 5, 10, 16].

The NF-κB signaling pathway is one of the most essential signaling pathways in eukaryotic cells. Among other functions, it has a role in cancer, inflammation, aging, and in the immune defense, and moreover, it is serving as a general stress response [2, 3, 9, 16, 29–31]. Since the regulation of temperature is also predicted to be a fundamental part of especially the immune response, we were interested in studying the interplay between oscillatory NF-κB and variations in temperature. A heat shock protein-dependent mechanism has been proposed as a link between the NF-κB signaling pathway and heat [29], and recently a model introducing a delay of the A20 signaling protein has been suggested [32], but we wanted to test this further, and establish the results for different levels of TNFα induction. Furthermore, little is known about the mechanisms of how the affected NF-κB oscillations could affect downstream protein production.

The theory of how reaction rates were affected by temperature, were pioneered by the work of the polish physicist Marian Smoluchowski [1], who calculated the reaction rate between two spherical particles diffusing in a potential. Even though this theory is more than 100 years old, and is a part of every physics curriculum, it has rarely been applied to systems that show dynamical behaviour such as limit cycles.

In this paper we apply the theory of temperature dependent reactions, to predict how the oscillatory dynamics of the transcription factor NF-κB is affected. We conduct experiments, using both single and double additions of the ligand TNF-α as well as applying this through a custom made flow chamber. This enables us detect clear oscillations in the nuclear concentration of TNF-α, and we succeed in varying the temperature as much as $\pm 5^o$C in the flow chamber, where the oscillations are still maintained. Through the analysis of these data we find a clear dependency of the period on the external temperature, so increasing the temperature leads to faster oscillations. By using a well-tested model of the dynamics of NF-κB, we find a striking correspondence between the model and the experimental findings and our model additionally pre-

*Electronic address: mhjensen@nbi.dk

dicts that lowering the temperature can lower the threshold level of the Hopf Bifurcation. Furthermore we use the model to predict how the change in temperature might lead to a significantly different downstream production level. Finally, we simulate how an oscillatory temperature can affect the NF-κB dynamics and we find, that this can lead to entrainment even for small temperature oscillations. Interestingly, for amplitudes of $\approx 2.5^o$C we find a chaotic transition that we surmise can be used to study the effect of complex dynamics on transcription factors in the future.

Results

A. Quantification of nuclear NF-κB concentration dynamics at different temperatures

We investigate how temperature affects oscillations of NF-κB in mouse embryonic fibroblast (MEF) cells, through three experiments:

- An experiment where TNF-α was added once to the MEF cells,
- An experiment where TNF-α was added twice with 40 min. in between
- An experiment where the MEF cells were exposed to a flow of TNF-α in a flow chamber.

Each type of experiment was conducted at 32.0°C, 34.5°C, 37.0°C, 39.5°C, and 42.0°C while imaged in a fluorescence time-lapse microscope, where DsRed-labeled p65 would give information about the relative nuclear to cytoplasmic concentration of NF-κB in the MEF cells.
In the single addition experiments, TNF-α was added to the MEF cells 2 min. prior to initiation of the experiments and the concentration was increased from 0 ng TNF-α/ml to 10 ng TNF-α/ml. At t = 0 min. the fluorescence time-lapse microscope would start imaging at 10 - 12 different locations every 10th min. Experiments were terminated after 20 - 48 hours. In the double addition experiments, TNF-α was added to the MEF cells increasing the concentration from 0 ng TNF-α/ml to 10 ng TNF-α/ml 2 min. prior to initiation of the experiments. After $\approx$ 38 min. the TNF-α concentration was again increased to 18 ng TNF-α/ml. These experiments were also terminated after 20 - 48 hours. In the flow experiments, the TNF-α concentration converged towards a constant value of 1 ng/ml. These experiments were terminated between 40 hours and 7 days after initialization (See Methods).
The flow setup is presented schematically in Fig. 1A and a more detailed illustration is presented in Fig. 5 in the methods section. For these experiments, all tubing in the system would be filled up with TNF-α-free medium and the syringe connected to the inlet would thereafter inject medium with TNF-α, meaning that the TNF-α level in the flow chamber would increase.
In Fig.1 B an example of a fluorescent image of an MEF cell at 37 ^{o}C is presented at $t = 0$ min, where TNF-α was added to a concentration of 10 ng/ml at $t = -2$ min. The emitted light is from the DsRed-p65 complex and hence the image taken at $t = 0$ is a signature of the NF-κB accumulation in the cytoplasm in all the cells. Additionally to this we also see from Fig.1 B that all nuclei are depleted from NF-κB, thus showing near complete translocation of NF-κB from the nucleus to the cytoplasm. This is also shown in Figure 1C, but at time $t = 30$ min. At this time point the cytoplasm has only a fraction of the NF-κB compared to Fig.1 B, and instead the NF-κB has translocated into the nucleus.
To analyze the dynamics of the nuclear NF-κB concentration, two different analysis methods were used. One for for doing statistics on a large number of cells (see Quantitative Period Extraction Method in methods section) and one for the visualization of the oscillations (see Qualitative Period Extraction Method). Based on the images, we were able to quantify the relative nuclear concentration of NF-κB and plot this as a time series, where we at this temperature(32^oC), observe approximately two periods in this time interval (Fig.1D, below). Here, the image series shows how the cytoplasm is bright and the nucleus is dark at $t = 0$ meaning that NF-κB is accumulated in the cytoplasm (Fig.1D, above). By inspection for a higher temperature (39.5^oC), we find approximately three periods, which can be seen both in the images and in the plot of I_N/I_C ratio (Fig.1E).
We quantified the frequency of these periods, by calculating the power spectrum (see Methods), and by applying this to the time series above, we could extract frequency of $8.26 \cdot 10^{-3}$min $^{-1}$ for the time series at 32^oC, which corresponds to a period of 121 min (Fig.1F). Similarly, we could do the same for the time series at 39.5^oC, finding a frequency of $13.2 \cdot 10^{-3}\text{min}^{-1})^{-1}$ corresponding to a period of 74.1 min (Fig.1F). We further visualized the data (see Methods) of a single addition-, a double addition- and a flow experiment at 37 ^{o}C, by showing the nuclear to cytoplasm intensity ratio, I_N/I_C, plotted versus time (Fig.1H-J). We note that when the TNF-α concentration is increased only once (Fig.1H), a transient peak in the NF-κB concentration appears, followed by periodic oscillations with lower amplitude (Fig.1H). However, when TNF-α is added at $t = -2$ min and again at $t = 38$ min., the transient peak is followed by another peak that has higher concentration than the average amplitudes, which again is followed by oscillations with lower, and slightly decaying amplitudes (Fig. 1 I). Based on this, we note that when the TNF-α concentration is abruptly increased, the following NF-κB peak has an increased amplitude, which is the case for both addition of one and two subsequent doses of TNF-α. These initial peaks after TNF-α addition is expected ([9, 27]), but here we reveal that two succesive additions will create two initial peaks with higher amplitude.

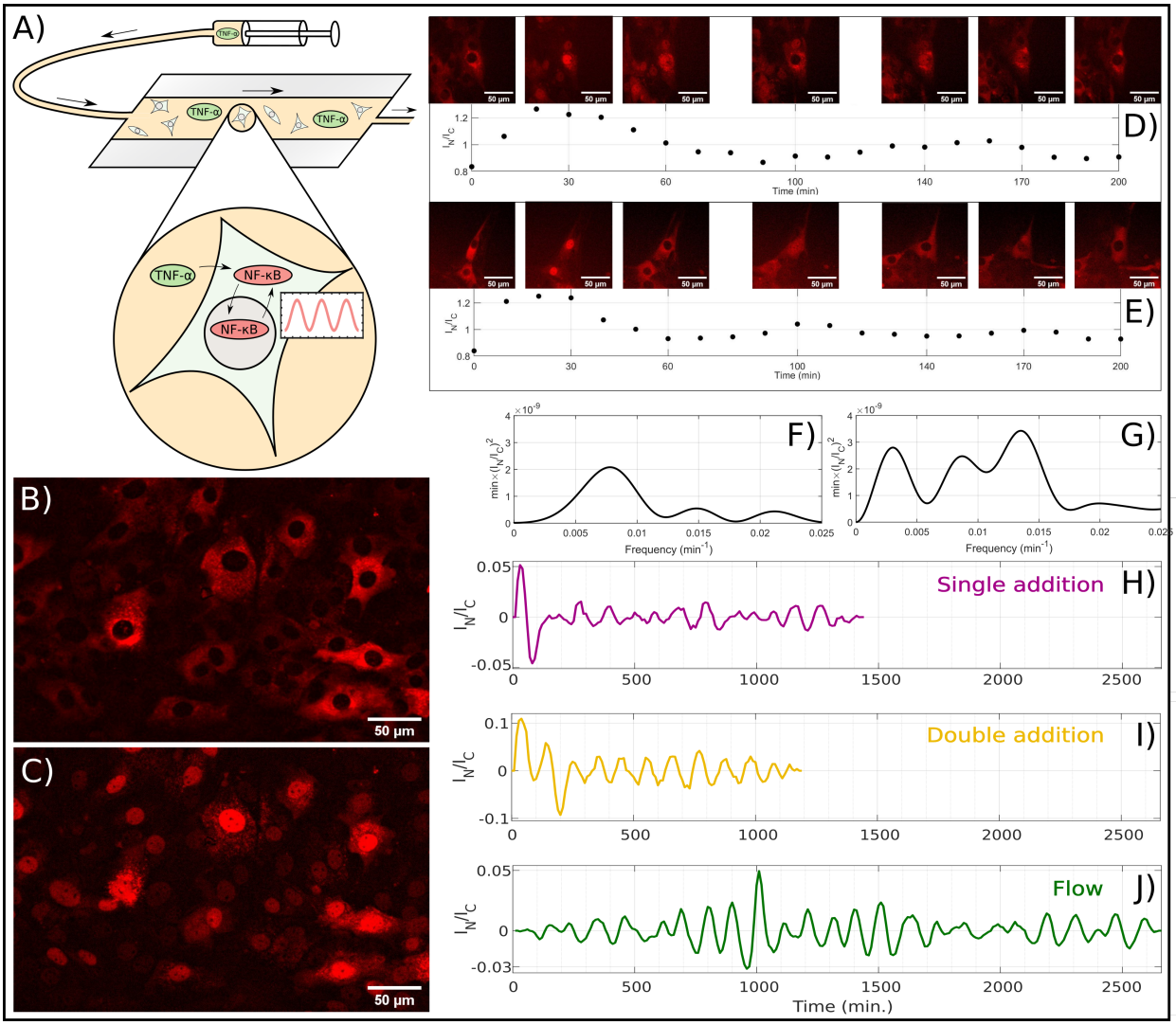

FIG. 1: Experiments in NF-κB oscillations conducted on mouse embryonic fibroblast cells. A) Schematic drawing of the flow experiment with a flow chamber containing NF-κB oscillating cells. Through a syrringe, medium contaninng TNF-α is injected into the flow chamber, which causes NF-κB oscillations. B) Representative example of experiment where NF-κB is primarily located in the cytoplasms. C) Same as B, but with NF-κB is primarily located in the nuclei. D) The top row images show a time-lapse of a single fibroblast cell with p65 fluorescently labeled DsRed. At temperature 32.0 °C the cell is exposed to 10 ng TNF-α/ml at $t = -2$ min and a new concentration increment, to a total of 18 ng TNF-α/ml, at t = 38 min. Each image corresponds to the time points in the plot below. The graph below, shows I_N/I_C ratio of the first 200 min. of the data series. Data is extracted in 10 min. intervals, with image examples every 30 or 40 min. E) Same as D, but for temperature at 39.5 °C. F) Power spectrum of the I_N/I_C ratio of the data presented in D). G) Power spectrum of the I_N/I_C ratio of the data presented in E) H) Ratio (I_N/I_C) versus time, measured after adding 10 ng TNF-α/ml to μ-wells at t = -2 min. I) Ratio I_N/I_C versus time where 10 ng TNF-α/ml was added at t = -2 min and the concentration was again increased at t = 38 min to a total of 18 ng TNF-α/ml. J) Ratio I_N/I_C for the flow experiments where the TNF-α concentration is converging towards 1 ng/ml during the entire range plotted.

B. Inclusion of temperature dependency in mathematical model predicts changes in periods and Hopf bifurcation

Our goal was now to identify the periods of the oscillations in order to measure the difference between the three types of experiments and to finally identify how the temperature affected the period of NF-κB oscillations.

We first compare the oscillations at 37.0 °C, by calculating the power spectrum (see Methods). Here we find the periods to be

- 105.3 min. ± 21.3 min (for the single addition with $n_{37single} = 12$)
- 114.7 min. ± 29.7 min. (for the double addition with $n_{37double} = 10$)
- 100.8 min. ± 10.9 min. (for the flow experiments

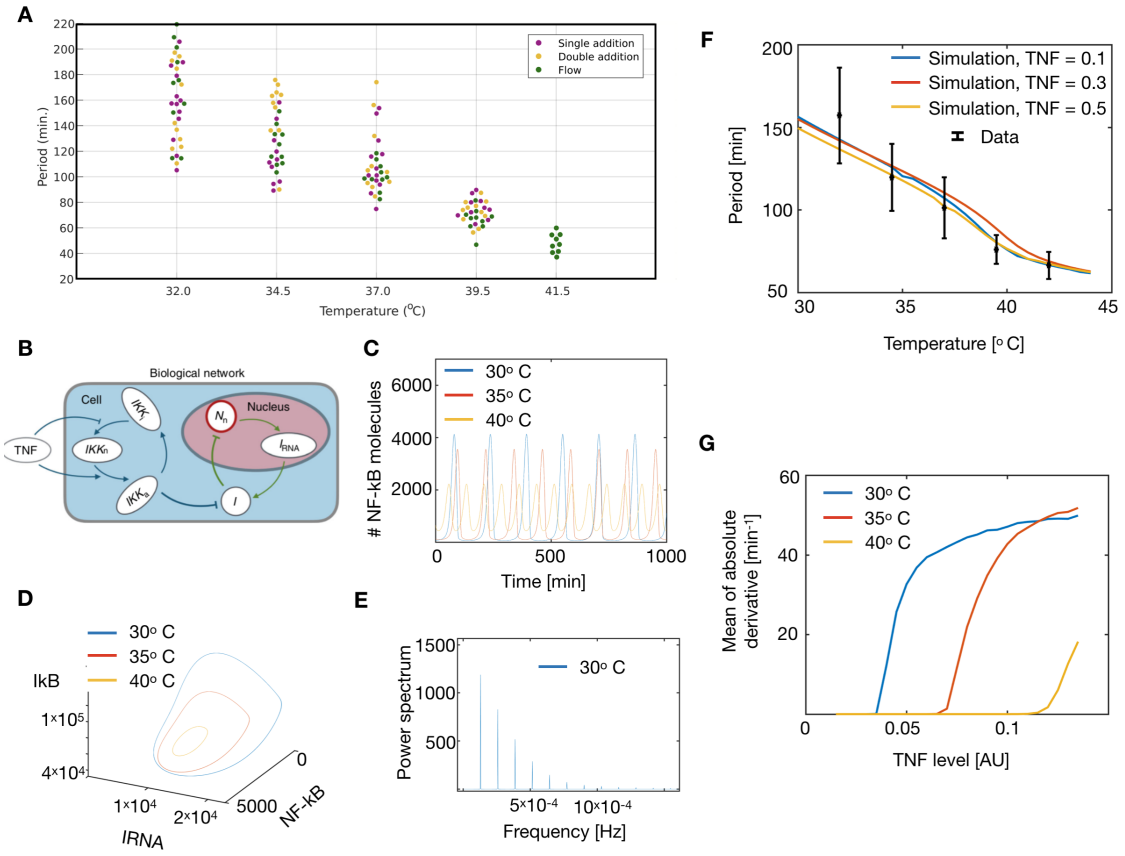

FIG. 2: Temperature dependency in NF-kB frequency. A) Oscillation period of NF-κB in fibroblast cells vs. temperature for the three different types of experiments: Single addition experiment, where 10 ng TNF-α/ml was added at t = -2 min, double addition experiment, where 10 ng TNF-α/ml was added at t = -2 min and followed by another increase of 8 ng TNF-α/ml at t = 38 min, and lastly, flow experiments, where cells were exposed to flow in a flow chamber where the TNF-α concentrationwas converging towards 1 ng/ml. All types of experiments were conducted at 32.0 °C, 34.5 °C,37.0 °C, and 39.5 °C, and the flow experiments were in addition conducted at 41.5 °C. B) Schematic figure, showing the components in the NF-κB network. C)Time traces at three different temperatures. D) Phase space for NF-kB, IRNA and IkB at three different temperatures. C) Power spectrum of the oscillations. The most left peak corresponds to the observed frequency. E) NF-kB oscillation period as a function of the external temperature shown for three different levels of TNF. Points in black corresponds to the experimental findings and their uncertainty. F) Absolute value of the derivative og NF-kB traces, calculated as a mean over the time series, as a function of the applied TNF level. Note that this curve rises at the emergence of oscillations and thereby the point of the Hopf Bifurcation.

with $n_{37\text{flow}} = 10$)

From this, it is concluded that there is no significant difference across the various experiments at this normal temperature, with Student's t-test resulting in p-values > 0.05 when comparing the three populations.

Next, we applied this method to all experiments at different temperatures. Here we measured the dynamics for temperatures down to 32 °C for all three experiments. The maximum temperatures where NF-κB oscillations were successfully extracted, were 39.5 °C for single- and double addition experiments and 41.5 °C for flow experiments, indicating that the flow setup might be more robust in order to measure the dynamics during external stresses. By analysis of these time series, we find that the NF-κB oscillation period decreases as a function of increasing temperature (Fig. 2A). Here we also note, that this behaviour is present in all three experimental conditions, emphasizing the generality if this result (Fig. 2A).

It is clear that there is very little difference in the period when using the three different assays, however, the flow experiments did result in a more smooth curve than in the μ-dish experiments. When grouping the assays as a weighted average the periods are 160.4 min. $\pm$ 32.4 min. and 106.8 min. $\pm$ 22.0 min. for the 32.0 °C and 37.0 °C, respectively. In spite of the similar results across the different types of experiments, the flow experiments have a more constant decrease, and so, for the calculation of the change of period per change of temperature, the flow experiments were used.

From these experiments, the period is constant through-

out different TNF-α concentrations and throughout different methods TNF-α exposure, however, varying the temperature +4.5 °C or -5.0 °C compared to body temperature significantly changes the period, and is found that Δperiod/Δtemperature = -12.64 min/°C.

To gain insight into the mechanism behind the temperature dependency of the oscillations, we tested whether these experimental findings could be explained by the classical theory of temperature dependency of reaction rates. To describe the dynamics of the NF-κB concentration, we used the mathematical model, that is simplified in order to reduce the number of parameters, and that has previously been used to model the dynamics of NF-κB [13, 15, 17] In this model, we consider the NF-κB inside the nucleus (N_n), acting as a transcription factor for many proteins, including I-κB. The equations take the following form:

$$\begin{aligned}
\dot{N_n} &= k_{Nin}(N_{tot} - N_n)\frac{K_I}{K_I + I} - k_{Iin} I \frac{N_n}{K_N + N_n} \\
\dot{I_m} &= k_t N_n^2 - \gamma_m I_{RNA} \\
\dot{I} &= k_{tl} I_{RNA} - \alpha I K K_a (N_{tot} - N_n)\frac{I}{K_I + I} \\
\dot{IKK_a} &= k_a \cdot TNF \cdot IKK_n - k_i IKK_a \\
\dot{IKK_i} &= k_i IKK_a - k_p IKK_i \frac{k_{A20}}{k_{A20} + [A20] \cdot TNF} \\
IKK_n &= [IKK]_{tot} - IKK_a - IKK_i
\end{aligned}$$

Here, N_n is the nuclear NF-κB concentration, I_m is the IkB mRNA level, and I is the concentration of cytoplasmic I-κB protein. This network is schematized in Fig. 2B, and a more detailed description can be found in the appendix, where all the parameters are listed as well.

We now included the temperature dependency into the simulations. In the model, we have 9 rates, and these were all made temperature dependent. We assumed that the fastest ones: α, k_{Nin} and k_t followed a Smoluchowski dependency (i.e. they are diffusion limited, $k^+ \propto D(T)$), whereas the others followed an Arrhenius dependency (i.e. they are reaction limited $k^+ \propto e^{\frac{E}{k_B T}}$).

With this setup we were ready to simulate the dynamics of NF-kB at different temperatures. By varying the temperature we found that the NF-kB oscillations were highly affected by the change in the temperature level and that low temperatures, led to large periods and amplitudes (Fig 2C). We visualized this further in the three-dimensional phase space spanned by the NF-kB, IRNA and IkB. Here we note that the change in temperature affects the entire size of the limit cycle and for high temperatures the limit cycle shrinks, leading to faster oscillations (Fig 2D). To quantify these oscillations, we calculated the power spectrum, by applying the FFT algorithm, finding the leading frequency of the time series. We note that multiples of this oscillation appear as well, but taking the maximal value of the power spectrum we find the correct frequency of the oscillations (Fig. 2E). We now used this algorithm to calculate the period as a function of the applied temperature. Here we found that the curve decreases monotonically for increasing temperature, which is what we would expect by observing the time series, and by comparing these results to the experimental observations we find a striking compliance (Fig. 2F). We tested this for different values of TNF baseline levels, and here we found similar patterns for different levels of the TNF, indicating that this result is quite robust and not sensitive to our initial choice of external TNF level (Fig. 2F). Since the temperature affected the oscillations, we were interested if this meant that changes in the temperature could induce oscillations and thereby affect the point of the Hopf bifurcation. Here we found to our surprise that decreasing the temperature, would lead to oscillations for smaller values of the external TNF levels (Fig. 2G). This means that it would be possible to use regulations of temperature to induce or stop the oscillations in living organisms.

C. Control of downstream protein production by changing the temperature

As we had established how the dynamics of NF-κB could vary with different temperature levels, we wanted to investigate how this could affect the downstream production of proteins stimulated by NF-κB. Here we used a previously suggested model [13], where all genes are divided into groups based on their affinity and cooperativity from stimulation with NF-κB. We assume that NF-κB can bind to an enhancer or operator region, and can form complexes to bind the RNA polymerase, with different affinity, depending on the gene (schematically shown in Fig. 3A). We describe the transcription and translation of each gene, labelled $i = 1, 2, 3, \ldots$, using the differential equations:

$$\dot{m}_i = \gamma_i \frac{N^{h_i}}{N^{h_i} + K_i^{h_i}} - \delta_i m_i, \tag{1}$$

$$\dot{P}_i = \Gamma_i m_i - \Delta_i P_i. \tag{2}$$

Here, the m_i represent the mRNA level transcribed from gene i, and P_i represents the concentration of proteins produced from the correspnding mRNA. The first term in the equation for the mRNA is known as a Hill function; the canonical way to describe the protein production for genes governed by transcription factors where each gene has a specific Hill coefficient and effective affinity [5, 23–26].

The effective affinity K_i is a parameter that combines the strength of binding of the transcription factor to the operator/enhancer region, the strength of binding of RNA polymerase to the promoter and transcription factor, as well as the effect of DNA looping that may be needed to bring the enhancer/operator close to the promoter region. Operationally, K_i sets the concentration of NF-κB that results in 50% of maximal gene expression enhancement.

With this setup, we simulated the model of NF-κB with varying the temperature as shown in Fig. 2, and measuring the produced proteins. For simplicity we will only consider two proteins, Protein 1 and Protein 2, being stimulated from a High and Low affinity gene respectively. Here we see that as we increase the temperature, the steady state level of Protein 1 is enhanced (Fig. 3B). However as we measure the steady state level of Protein 2, we realised that this was significantly reduced and thus these types of proteins would be up-regulated if the cell could lower the temperature (Fig 3C). With this information we simulated the steady state protein level of both proteins as a function of temperature, and here we found a very interesting crossover effect (Fig. 3D) that points out that proteins from High affinity can be upregulated as one increase the temperature whereas proteins from Low affinity genes are monotonically decreased for increasing temperature. This result highlights the very interesting prospect that one can use temperature as a regulator for the downstream production of proteins.

D. Synchronization and chaotic dynamics emerges from temperature oscillations

Since temperature had the ability to affect the oscillatory properties of the NF-κB we wanted to investigate how this would behave if we not oscillated the temperature. This would lead to a system of two coupled oscillators which potentially could lead to interesting dynamics [13, 16, 19, 20]. We note, that we in the experiments already had tested ranges of temperature variations, for which the cells would still survive and oscillations would be maintained. Therefore we can, in the model, predict amplitude variations of $\pm 5^oC$ which should be realistic for the experimental system.
We first oscillated the temperature with an amplitude of 1^oC and by varying the frequency we observed that different entrainment modes emerged. First we found the 1/1 coupling, which means that one full period of the temperature corresponds to one period of the NF-κB system, where the phases are locked (Fig. 4A). By varying the period, it became clear that this temperature dependency could lead to entrainment for different rational numbers, for instance with a 5/3 coupling (Fig. 4B) and strong 2/1 coupling (Fig. 4C). Based on these first observations, we varied the frequency and measured the rotation number of the system. This rotation number we define as the (externally fixed) frequency of the temperature divided by the (measured) NF-κB frequency. By doing this we were able to extract the resulting plot known as a Devil's staircase (Fig. 4D-E) for two different values of the external amplitude. Here we find entrainment plateaus (horizontal regions), were the NF-κB frequency is completely determined by the temperature frequency. This means that inside these regions, one can completely control of behaviour of the NF-κB oscillations and either speed up or slow down the dynamics.

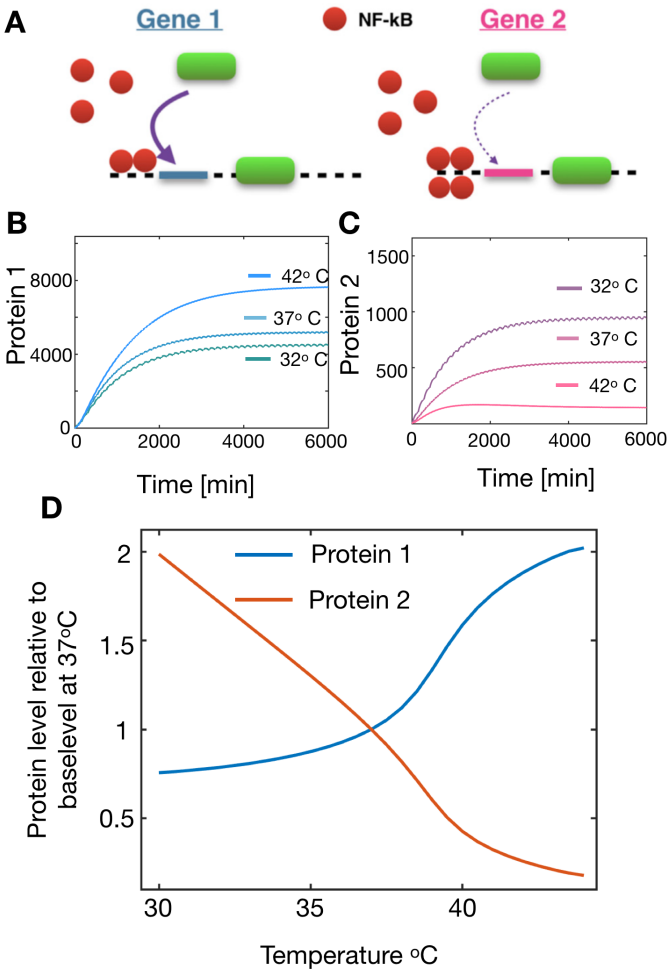

FIG. 3: Temperature dependency in $NF-kB$ frequency. A) Schematic figure showing the stimulation of a high affinity gene (left) and a low affinity gene (right). B) Protein production of Protein 1 (from a high affinity gene) at three different temperatures. C) Same as A but for Protein 2 (from a low affinity gene). D) Relative steady state production of Protein 1 and Protein 2 respectively as a function of temperature.

We note by comparing Fig. 4D-E that the dominating plateaus grow in range, as we increase the amplitude from 0.5^oC to 1^oC. We therefore wanted to measure the width of these entrainment regions especially for the dominating ones. First we tested how this was affected by the external level of TNF, and we found that even though small variations occurred these entrainment regions were quite stable and robust to changes in the TNF level (Fig. 4F). This is a very interesting observation, since it allows future experiments *in vivo* and *in vitro* to focus on the changes in temperature, without worrying about the small differences in the levels of TNF. Next we increased the amplitude of the temperature amplitudes, and here we found that all the dominating regions were growing, whereas the smaller rational regions (such as 5/3) loose their stability as they are being "squeezed" out by the dominating ones (Fig. 4G).

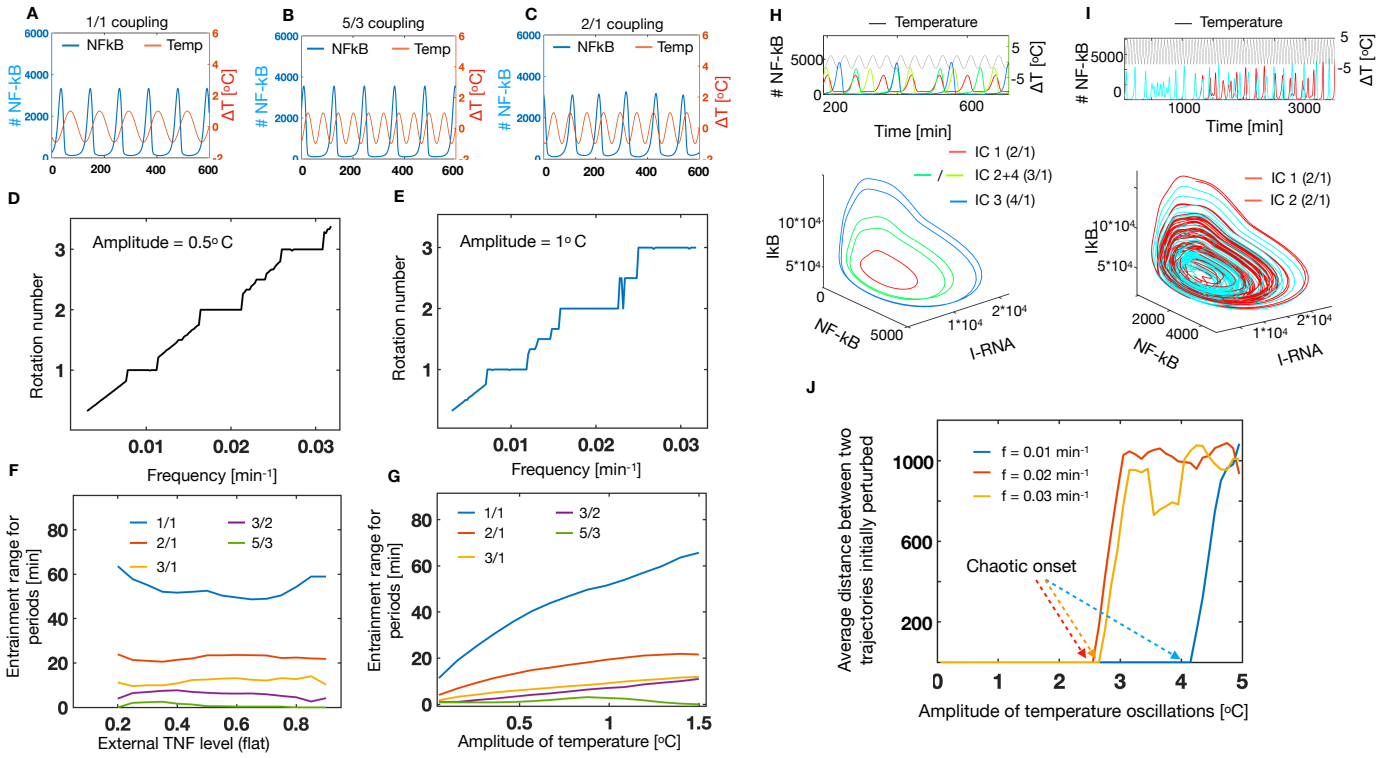

FIG. 4: Temperature oscillations lead to entrainment and chaotic dynamics for NF-κB. A) Oscillations in NF-κB (blue, left axis) coupled to temperature (red, right axis). Temperature amplitude = 1^oC and frequency (f_{tmp}) = $0.01[min^{-1}]$. B) Same as A, but with temperature frequency = $0.018[min^{-1}]$. C) Same as A, but with temperature frequency = $0.02[min^{-1}]$. D) Rotation number measured as $f_{tmp}/f_{NF-\kappa B}$ as a function of the temperature frequency for the temperature. Amplitude of temperature = 0.5^oC. E) Same as D, but with amplitude of temperature = 1^oC. F) Width of the dominating steps in the figures D+E as a function of the external TNF level. Amplitude of temperature oscillations = 1^oC. G) Width of the dominating steps in the figures D+E as a function of the amplitude of temperature oscillations. TNF level = 0.2. H) Dynamics of NF-κB for different initial conditions (indicated by colors) as a function of time (above) and in the phase space spanned as $I_{RNA}\kappa B$ and IκB I) Same as H, but for two initial conditions separated by 10^{-4}%. J) Mean distance of the trajectories, initially separated by 10^{-4}% as a function of the amplitude of the temperature oscillations. Curves shown for three different frequencies of temperature oscillations.

It has previously been observed that for large amplitudes of oscillatory TNF, the dynamics of NF-κB, could show "modehopping" which corresponds to transitions between two stable limit cycles [13, 14]. We were interested if this was also the case, if we used temperature to oscillate, and we realised that already for amplitudes of 2^oC, we found multistability, and we were even able to find three stable limit cycles by varying the initial conditions of the simulation (Fig 4H). We note that for some of these limit cycles, the dynamics could entrain in different phases even though they were in the same attractor in the phase space (see IC2+IC4 in the time series above in Fig 4H). This observation also indicated that the applied amplitude was above the "critical value", and due to a theorem of Poincare, above this line various complex dynamics could emerge and in particular chaotic dynamics. Therefore, we investigated this by increasing the external amplitude, and we found that chaotic dynamics could emerge for amplitudes around 2.5^oC. We vizualised the chaotic dynamics, by simulating the system with identical parameter values, and initial conditions only separated by 10^{-4}%. By studying the time series, it is clear that even though they show completely similar dynamics for a long time, then the time series evolve completely differently (Fig 4I above). We also visualized this in the three-dimensional phase space, where we could see that the trajectories moved on a strange attractor (Fig 4I below). Finally we were interested in studying for what values of the the temperature oscillations, that we could expect to see the chaotic transition. To quantify this, we measured the average distance between two trajectories only separated by 10^{-4}% in the initial conditions. Using this measure we found that for relatively large frequencies of the temperature oscillations (periods of 30-50 minutes), we found a chaotic transition for $\approx 2.5^o$C, whereas for temperature oscillations with a period of 100 minutes, we would expect the amplitude to be around $\approx 4.1^o$C before the chaotic transition emerges (Fig. 4J). However we note that all of these values are in agreement with the observed temperature variances for the flow experiment

and we therefore predict that one could induce chaotic dynamics by applying this experimental setup.

Discussion

Temperature is known to vary in living organisms as a response to external stresses, but a mechanistic understanding of how this can affect the protein production and control transcription factor dynamics has been scarcely investigated. In this work, we have shown how the transcription factor NF-κB can change the properties of oscillation by varying the temperature in a realistic range where the cells can still survive and maintain oscillations. We use theories of statistical physics and in particular the Smulochowski equation to predict how the individual rates are affected by a changing temperature, and show that these are sufficient to describe the results of the experimental data. We further use this calibrated model, to predict how different families of downstream genes are affected by a change in temperature and we point out a crossover effect with strong regulatory implications. Finally, we show that temperature can be used as a strong source to induce more complex dynamics to the NF-κB and we suggest that this can be used as a key measure to investigate the role of dynamics in transcription factors on the downstream gene production.
Even though chaotic dynamics has been investigated theoretically and experimentally for more than 50 years, it has still not been shown to exist and play a role in cellular dynamics. Complex phenomena such as synchronization has been shown to exist [9, 13, 33], and even modehopping that reveals the existence of multistable cycles, when the amplitude of the external oscillator has been sufficiently increased. Theoretically this should also guide a way to induce chaotic dynamics [14, 19, 20], however often cells have trouble surviving the transiently high concentrations of TNF-α, and therefore it has been difficult to predict how chaotic dynamics might be investigated for such systems. Our present results predicts that temperature oscillations is a simple and effective way to induce highly complex dynamics if the temperature is oscillated externally. Since our experimental results reveal that cells can survive and maintain oscillations under temperature variations of $\approx \pm 5^oC$, this system should be stable enough to induce chaotic dynamics under oscillations with temperature amplitudes in this range. If future experiments succeed in using the temperature oscillations, it is possible to distinguish chaotic from oscillatory behaviour with stochastic noise; see for example [16, 21, 22]. We surmise that future directions of experimental investigations might use this fundamental possibility of temperatures as a roadmap to study the emergence of complex dynamics in cells and how this affects and regulates the cellular machinery under different external stresses.
Temperature presents a fundamental, physical property with the potential to control and regulate the dynamical properties of protein concentration in cells. It is our hope that this work will inspire theoretical and experimental exploration these prospects of transcription factors, as the system is affected by either constant or dynamically varying temperatures in living cells.

Acknowledgements

We are grateful to Sandeep Krishna for knowledge about the TNF model.

[1] Smoluchowski, M. V. Über Brownsche Molekularbewegung unter Einwirkung äußerer Kräfte und deren Zusammenhang mit der verallgemeinerten Diffusionsgleichung. Annalen der Physik, **353(24)**, 1103-1112 (1916).
[2] Hoffmann, A., Levchenko, A., Scott, M.L. & Baltimore, D.: The IκB-NF-κB signaling module: temporal control and selective gene activation, Science **298**, 1241-1245 (2002).
[3] Nelson, D. E., Ihekwaba, A. E. C., Elliott, M., Johnson, J. R., Gibney, C. A., Foreman, B. E., ... & Edwards, S. W. Oscillations in NF-κB signaling control the dynamics of gene expression. Science **306**, 704-708 (2004).
[4] Krishna, S., Jensen, M.H. & Sneppen, K.: Spiky oscillations in NF-κB signalling, Proc.Nat.Acad.Sci. **103**, 10840-10845 (2006).
[5] Mengel, B., Hunziker, A., Pedersen, L., Trusina, A., Jensen, M.H. & Krishna, S.: Modeling oscillatory control in NF-κB, p53 and Wnt signaling, Current Opinion in Genetics and Development **20**, 656-664 (2010).
[6] Levine, Joe H., Lin, H. & Elowitz, M.: Functional roles of pulsing in genetic circuits, Science **342** 1193-1200 (2013).
[7] Gonze, D., Halloy, J. & Goldbeter, A.: Robustness of circadian rhythms with respect to molecular noise, Proceedings of the National Academy of Sciences **99** 2, 673-678 (2002).
[8] Lahav, G., Rosenfeld, N., Sigal, A., Geva-Zatorsky, N., Levine, A. J., Elowitz, M. B. & Alon, U. Dynamics of the p53-Mdm2 feedback loop in individual cells. Nature Genetics, **36(2)**, 147 (2004).
[9] Tay, S. & Kellogg, R.: Noise facilitates transcriptional control under dynamic inputs, Cell **160**, 381-392 (2015).
[10] Tay, S., Hughey, J. J., Lee, T. K., Lipniacki, T., Quake, S. R., & Covert, M. W. Single-cell NF-κB dynamics reveal digital activation and analogue information processing. Nature, **466(7303)**, 267-271 (2010).
[11] Chen, S. H., Forrester, W., & Lahav, G. Schedule-dependent interaction between anticancer treatments. Science, **351(6278)**, 1204-1208 (2016).
[12] Heltberg, Mathias L., Sheng-hong Chen, Alba Jiménez, Ashwini Jambhekar, Mogens H. Jensen, & Galit Lahav. Inferring leading interactions in the p53/Mdm2/Mdmx circuit through live-cell imaging and modeling. Cell sys-

tems **9 (6)**, 548-558 (2019).
[13] Heltberg, M., Kellogg, R. A., Krishna, S., Tay, S., & Jensen, M. H. Noise induces hopping between NF-κB entrainment modes. Cell systems, **3(6)**, 532-539 (2016).
[14] Heltberg, M. L., & Jensen, M. H. Locked body clocks. Nature Physics, **15(10)**, 989-990 (2019).
[15] Heltberg, M. L., Krishna, S., & Jensen, M. H. On chaotic dynamics in transcription factors and the associated effects in differential gene regulation. Nature communications, **10(1)**, 1-10 (2019).
[16] Heltberg, M. L., Krishna, S., Kadanoff, L. P., & Jensen, M. H. A tale of two rhythms: Locked clocks and chaos in biology. Cell systems, **12(4)**, 291-303 (2021).
[17] Jensen, M.H. & Krishna, S.: Inducing phase-locking and chaos in cellular oscillators by modulating the driving stimuli, FEBS Letters **586**, 1664-1668 (2012).
[18] "MatTek", "MatTek microwell dishes", "https://www.mattek.com/products/glass-bottom-dishes/", addendum = "(accessed: 13.01.2021)"
[19] Jensen, M. H., Bak, P., & Bohr, T. Transition to chaos by interaction of resonances in dissipative systems. I. Circle maps. Physical review A, **30(4)**, 1960 (1984).
[20] Jensen, M.H., Bak, P. & Bohr, T.: Complete devil's staircase, fractal dimension and universality of mode-locking structure in the circle map, Phys. Rev. Lett. **50**, 1637-1639 (1983).
[21] Amon, A. & Lefranc, M. Topological signature of deterministic chaos in short nonstationary signals from an optical parametric oscillator. Physical review letters, **92(9)**, 094101 (2004).
[22] Gilmore, R. & Lefranc, M. The Topology of Chaos. John Wiley and Sons Ltd, New York, (2002).
[23] Maienschein-Cline, M., Warmflash, M., A. & Dinner, A. R.: Defining cooperativity in gene regulation locally through intrinsic noise. IET systems biology **4.6** 379-392 (2010).
[24] Werner, M., Zhu, L. & Aurell, E. : Cooperative action in eukaryotic gene regulation: physical properties of a viral example. Phys. Rev. E **76**, 061909 (2007).
[25] Kaplan, S., Bren, A., Zaslaver, A., Dekel, E. & Alon, U.: Diverse two-dimensional input functions control bacterial sugar genes. Mol. Cell, **29(6)**, 786-792 (2008).
[26] Sneppen, K., Krishna, S. & Semsey, S. Simplified models of biological networks. Annu. Rev. Biophys, **39**, 43-59 (2010).
[27] Zambrano, S., De Toma, I., Piffer, A., Bianchi, M. E., & Agresti, A. NF-κB oscillations translate into functionally related patterns of gene expression. Elife, 5, e09100 (2016).
[28] Agbanoma, G., Li, C., Ennis, D., Palfreeman, A. C., Williams, L. M., & Brennan, F. M. Production of TNF-α in macrophages activated by T cells, compared with lipopolysaccharide, uses distinct IL-10–dependent regulatory mechanism. The Journal of Immunology, 188(3), 1307-1317 (2012).
[29] Liu, Y., Zhou, G., Wang, Z., Guo, X., Xu, Q., Huang, Q., & Su, L. NF-κB signaling is essential for resistance to heat stress-induced early stage apoptosis in human umbilical vein endothelial cells. Scientific reports, **5(1)**, 1-17 (2015).
[30] Mercurio, F., & Manning, A. M. NF-κB as a primary regulator of the stress response. Oncogene, **18(45)**, 6163-6171 (1999).
[31] Courtois, G., & Gilmore, T. D. Mutations in the NF-κB signaling pathway: implications for human disease. Oncogene, **25(51)**, 6831-6843 (2006).
[32] Harper, C. V., Woodcock, D. J., Lam, C., Garcia-Albornoz, M., Adamson, A., Ashall, L., ... & White, M. R. H. Temperature regulates NF-κB dynamics and function through timing of A20 transcription. Proceedings of the National Academy of Sciences, **115(22)**, E5243-E5249 (2018).
[33] Danino, T., Mondragón-Palomino, O., Tsimring, L., & Hasty, J. A synchronized quorum of genetic clocks. Nature, **463(7279)**, 326-330 (2010).
[34] "Nikon", "Nikon microscopes", "https://www.microscope.healthcare.nikon.com/", addendum = "(accessed: 14.01.2021)",
[35] "Lumencor", "Lumencor Sola Light Engine", "https://lumencor.com/products/sola-light-engine/", addendum = "(accessed: 14.01.2021)",
[36] "Lumencor", "Andor Neo sCMOS", url = "https://andor.oxinst.com/products/scmos-camera-series/neo-5-5-scmos", addendum = "(accessed: 14.01.2021)",
[37] "Warner", "Warner temperature controller", url = "https://www.warneronline.com/dual-channel-temperature-controller-tc-344c", addendum = "(accessed: 14.01.2021)",
[38] "OkoCageIncubator", "Oko cage incubator", url = "http://www.oko-lab.com/live-cell-imaging/cage-incubator", addendum = "(accessed: 14.01.2021)",
[39] "Gene and Cell Technologies", "Human TNF-alpha stability testing", url = "https://www.geneandcell.com/blogs/molecular-biology-methods/human-tnf-alpha-stability-testing? addendum = "(accessed: 04.02.2021)",

II. METHODS

Cell culturing

All cells used in this article were stably transduced 3T3 mouse fibroblast cells obtained from Tay et al. [10]. Using lentivirus, DsRed was introduced into the genome of the cells, resulting in the expression of the fusion protein DsRed-p65. This allowed for tracking of p65 when shuttling between cytoplasm and nucleus of the cells. These cells also had the nuclear marker H2B-GFP which was not utilized in the presented data of this article.

Cells were incubated in 5.0 % CO_2 at 37.0 °C in a HERA CELL VIOS 160i CO_2 incubator. For culturing Gibco^{TM} DMEM culture medium with high glucose, L-Glutamine, phenol red, and no Sodium Pyruvate and no HEPES were used. While performing experiments this medium was substituted with Gibco^{TM} DMEM culture medium with high glucose, HEPES, L-Glutamine, no phenol red, and no Sodium Pyruvate. To both media +10 % Fetal bovine serum (FBS) and+ 1 % Penicillin-Streptomycin (PS) was added.

Single well experiments

48 hours prior to the experiments fibroblast cells were seeded on collagen-coated, γ-radiated, 35 mm, No. 1.5 glass bottom microwell dishes [18]. The microwells were brought from the 37 °C, 5 % CO_2, high humidity incubator into the incubation chamber of the microscope with an atmosphere of 5 % CO_2, high humidity, and a specific target temperature. Approximately 15 minutes after, when the temperature had stabilized, the 10 ng TNF-α/ml was added to a total of 40 ng TNF-α. One to two minutes thereafter the fluorescence microscope timelapse was initiated. This initiation was defined as time = 0 min in the experiments. Timelapse images were obtained every 10 minutes where 10 positions were captured at each time point throughout the entire timelapse series. In the experiments where TNF-α was added twice, the first addition was once again 10 ng TNF-α/ml to a total of 40 ng TNF-α, and the second addition took place one to two minutes before the fourth set of timelapse images at t = $\approx$ 38 min, and consist of a total increase of 8 ng TNF-α/ml. At the second addition 50 ng TNF-α was added and the total TNF-α added to these experiments were 90 ng TNF-α.

Flow experiments

When performing flow experiments, a major task is to prevent gas formation in the perfusion chamber where cells grow. The media utilized in the experiments have to be stored at room temperature but the temperature of the perfusion chamber is approximately 10 - 20 ^{o}C higher than room temperature, and since Gas is extruded from a liquid when it is heated up, gas formation in the perfusion chamber is an inherent problem to flow chamber (MBR) flow experiments. If the perfusion chamber is filled up with gas, even temporarily, in the order of minutes, cells will be injured. They will not be able to fully recover and likely cells will undergo necrosis. If cells survive, however, our preliminary experiments showed that nuclear translocation of NF-κB shuttling was prevented. Following, the extensive measures required to prevent gas formation are described.
Prior to the initialization of the experiments, the medium was degassed for 90 minutes. Subsequently, the medium was brought to a flow hood and filtered using a 0.2 μm filter to remove biological contaminants from the degassing process. The medium was separated into two portions. One where TNF-α was added and one that was left for filling up the flow system before starting the experiment. From degassing, the medium was cooled down, so before injecting it into the flow system5, consisting of tubing, bubble traps, and perfusion chamber, the medium was heated up to room temperature in a sealed falcon tube to prevent new gas from being dissolved in the medium while the medium was heating up. The entire flow system was then filled up with medium in steps and assembled inside the flow hood. In each bubble trap, 3 ml of medium was injected, leaving 2 ml left in each bubble trap for air. The entire flow system was then brought to the microscope setup and inserted into the microscope eclosure. The chamber and 1 meter of tubing were inserted into the incubation chamber, an inlet was connected to the controllable pump outside the enclosure and an outlet was inserted into a glass beaker.
The inlet and outlet of the system were elevated compared to the other devices in the system. This was to create increased pressure in the perfusion chamber and tubing situated in the incubation chamber in order to minimize gas formation. In between the injection and the perfusion chamber, the temperature increases twice. The first increment is close to the target temperature, which serves two purposes: 1) It stabilizes the temperature surrounding the incubation chamber, which will minimize temperature fluctuations herein. 2) When gas forms in the medium due to increased temperature, the temperature has already increased significantly before entering the bubble trap and most gas will be trapped herein. In between the barrier of the microscope enclosure and the bubble trap, extra tubing is inserted to make sure the temperature of the medium is increased and to give the medium time to extrude gas before entering the bubble trap. After the bubble trap, the medium flows into the incubation chamber, where the medium and perfusion chamber is exposed to the target temperature, 5 % CO_2, and high humidity.

Microscopy

A Nikon inverted fluorescence microscope was utilized throughout these experiments [34]. a Lumencor Sola Light Engine[35] solid-state illumination provides fluorescent light combined with excitation- and emission filters in the microscope at 575 nm and 641 nm, respectively. Bright-field images are provided by the build-in lamp in the microscope. Images are captured with an Andor Neo sCMOS model DC-152Q-COO-FI [36] camera.

Temperature control

Temperature control inside the microscope enclosure was provided by Oko lab incubation unit model H201-T-0016 [38]. The temperature of the incubation chamber that was approximately 2.0 ^{o}C higher than the temperature in the microscope enclosure, was provided by the Warner Duel Automatic Temperature Controller TC-344B [37]. Each of its two controllers had two heaters, one control thermometer, and one monitor thermometer. The two heaters connected to one of the controllers were mounted to the bottom stage of the outsides of the incubation chamber and two heaters connected to the other controller were mounted to the inside of the incubation chamber. The heaters outside the incubation chamber

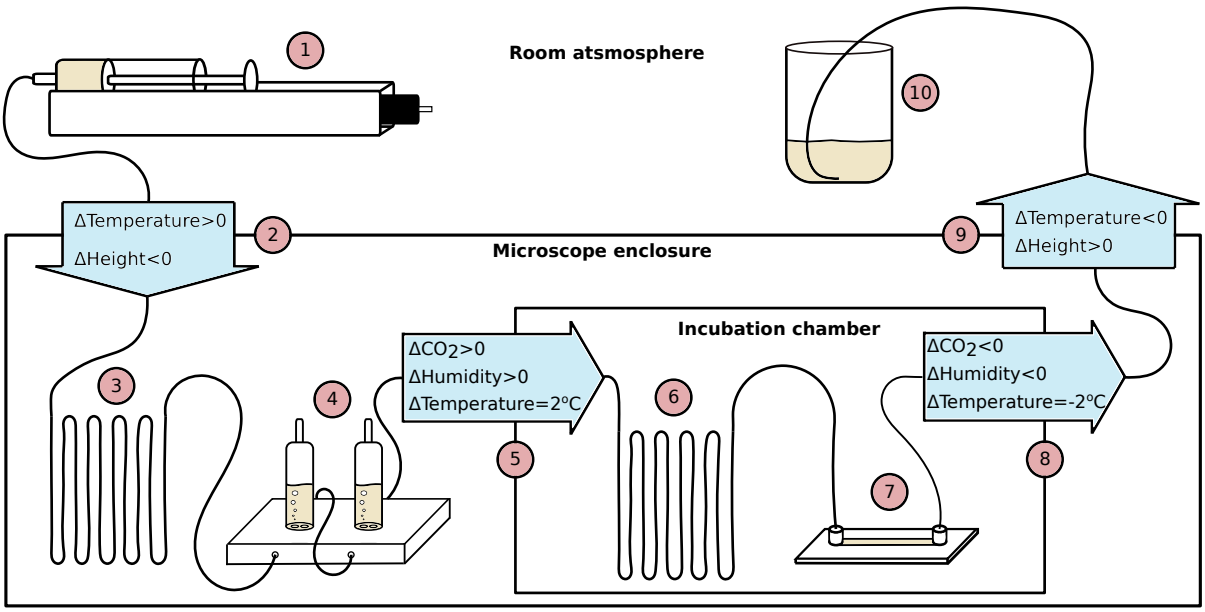

FIG. 5: Schematic of flow system with numbers indicating how the medium flows through the system, chronologically. The solid line connecting devices is gas permeable silicone tubing. 1) Pump injecting medium into the system at a rate controlled by a computer via Labview software. 2) medium flows into the microscope enclosure. Medium changes from room temperature to target temperature -2.0 °C and changes from the starting height to the same level as all devices inside the microscope enclosure (ΔHeight $\sim$ -40 cm) 3) 1.0 m of extra tubing lets the medium reach target temperature -2.0 °C before entering the bubble trap. 4) Two bubble traps capturing excess gas in the tubing. 5) Medium enters incubation chamber and the atmosphere changes from room atmospheric CO_2 and room atmospheric humidity to 5 % CO_2 and high humidity while also the temperature increases with 2.0 °C to the target temperature. 6) Extra tubing allowing for the medium to adjust to CO_2 and temperature. 7) Perfusion chamber where the fibroblast cells grow and the microscopy data is collected. 8) Medium exits incubation chamber and CO_2 and humidity changes to atmospheric levels. Temperature changes to target temperature -2.0 °C. 9) Medium exits microscope enclosure and temperature changes from target temperature -2.0 °C to room temperature. Height of medium is increased (ΔHeight $\sim$ +30 cm). 10) Medium flows out of the flow system and into a glass beaker.

were constantly exposed to 6 V from the controller, while the heaters inside were continuously controlled by a loop, meaning the temperature inside the incubation chamber could be set to a constant value. The control thermometer of the inside heaters was taped on top of the flow slide in the case of flow experiments and taped onto the bottom of the inside of the incubation chamber in the case of micro dish experiments. During flow experiments, the temperature of the cells inside the perfusion chamber was assumed to be equal to the temperature on top of the flow slide, where the control thermometer was attached. In micro dish calibration experiment it was shown that the temperature inside a micro dish containing 4 ml of water was 1.0 °C lower than a thermometer attached to the bottom of the inside of the incubation chamber, so in these experiments, the temperature of the Warner temperature controller was set to 1.0 °C higher than the target temperature.

Data Analysis

A semi-automatic Matlab program was built for the analysis, where nuclear light intensity (I_N) and cytoplasm intensity (I_C) were measured and an oscillation period was extracted for a single cell at the time, by taking the ratio of I_N/I_C. Prior to being analyzed in the Matlab program, cells with clear oscillation patterns were chosen from the visual image analysis in Fiji. In the Matlab program, the average light intensity of a circular area for each of the nucleus and cytoplasm was selected for each timeframe, corresponding to a change in time of 10 min. Depending on the size of the cell, the measured area would be between 3.1 μm^2 and 8.7 μm^2, corresponding to a circle with a diameter between 2 μ m and 3.3 μm, and corresponding to between 27 pixels and 79 pixels for each measured nuclear or cytoplasm intensity.

This approach was used throughout all data analysis, but it was found to be an advantage to both have a qualitative- and a quantitative approach for the total data analysis. The Qualitative Period Extraction Method would visualize the oscillations to give an understanding of the shape of the oscillations as well as give an understanding of how well the system behaved. This method was very time-consuming, so another the Quantitative Period Extraction Method was used to extract statistics on oscillations of a high number of cells in a more time-efficient manner.

A. Quantitative Period Extraction Method

With the analysis in Fiji described above a single area from the cytoplasm and a single area from the nucleus were extracted. Each cell was analyzed in a time span of between 90 min and 770 min, equivalent to be between 2 and 11 oscillations.

The Matlab program would then do a power spectral analysis of I_N/I_C - mean(I_N/I_C) and extract the frequency value of the highest peak, see figure 1 D) and figure 1 E). The inverse of this frequency value would then correspond to the most significant period in the data series. However, in some cases, a peak that did not correspond to the cell's oscillations was the highest peak. This was typically a peak representing an oscillation with twice the period of the timespan of the signal. In these cases, the high peak near the visually observed oscillation was chosen as the frequency for extracting a period.

B. Qualitative Period Extraction Method

In this analysis, four areas of the same size as described above were chosen for both the cytoplasm and for the nucleus. This made the total areas for the calculations of the I_N/I_C ratio larger resulting in local intensity variations being minimized. The I_N/I_C ratio was then smoothed with the Matlab Smooth Function, where span = 4. From experimental errors, the I_N/I_C data had intensity variation on a larger than the typical oscillation period. These variations were found by taking the Matlab Smooth Function with span = 13. The Matlab Smooth function with span = 13 was then subtracted to the Matlab Smooth Function with span = 4, which resulted in a data series well suited for qualitative understanding of the oscillations.

Overdamped Langevin equations

We describe the dynamics of a spherical particle, diffusing in fluid. This movement is governed by the Langevin equation:

$$m\frac{d\vec{v}}{dt} = -\gamma\vec{v} + F(\vec{r}) + \eta(t) \tag{3}$$

Here forces acting on the particle are:

- Viscous force ($-\gamma\vec{v}$), proportional to the velocity, that is known as Stokes law ($F = 6\pi\mu Rv$)
- Spatially distributed force field ($F(\vec{r})$)
- Stochastic movement due to random collisons with other particles $\eta(t)$.

For the stochastic term we assume that it has zero average and that the correlation times are so small that they can be assumed to be zero. Mathematically this means that

$$\langle\eta(t)\rangle = 0 \quad \text{and} \quad \langle\eta(t)\eta(t')\rangle = 2D\delta(t-t') \tag{4}$$

We will (as standard) assume this occurs in the limit of strong friction. This means that: $|\lambda\vec{v}| \gg |m\frac{d\vec{v}}{dt}|$. The latter is called the inertial term, since it stems from Newtons second law, and this we neglect in the rest of this work. This is called the over damped limit. We therefore write our equations of motion as:

$$\gamma\vec{v} = F(\vec{r}) + \sigma\eta(t) \tag{5}$$

Smoluchowski Equation

From the Langevin equation in the overdamped limit we can construct the Fokker Planck equation that describes the probability distribution of the position of a diffusing particle in space and time. This takes the form:

$$\partial_t p(\mathbf{r},t) = \Big(\nabla^2\frac{\sigma^2}{2\gamma^2} - \nabla\cdot\frac{1}{\gamma}\mathbf{F}(\mathbf{r})\Big)p(\mathbf{r},t) \tag{6}$$

Here $p(\mathbf{r},t)$ is actually including some initial conditions, so it should in priciple be written as $p(\mathbf{r},t|\mathbf{r}_0,t_0)$ but to simplify the expressions we will in the following just write $p(\mathbf{r},t)$. Furthermore note that the coordinate $\mathbf{r}$ is a vector

describing the position in space and is therefore not a specified dimension.
From the above equation we introduce as standard that we can define:

$$\mathbf{F(r)} = -\nabla U(\mathbf{r}) \quad \text{and} \quad D(\mathbf{r}) = \frac{\sigma(\mathbf{r})^2}{2\gamma^2} \tag{7}$$

Furthermore, we will later use as a postulate that the distribution should obey the Boltzman statistics. This simply implied that the steady state probability should be:

$$p(\mathbf{r}, t \mapsto \infty) = \mathcal{Z} e^{-\beta U(\mathbf{r})} \tag{8}$$

Where we have as always $\mathcal{Z}$ being the partition function that normalize the probability and $\beta = \frac{1}{k_B T}$ being the temperature dependency.
First we rewrite the Fokker Planck equation. We use the vector calculus identities (on a testfunction f) that: $\nabla^2 f = \nabla \cdot \nabla f$. Using this on the term for $D(\mathbf{r})$ and setting the divergence operator outside of the parenthesis we obtain:

$$\partial_t p(\mathbf{r}, t) = \nabla \cdot \Big(\nabla D(\mathbf{r}) - \frac{1}{\gamma} \mathbf{F(r)} \Big) p(\mathbf{r}, t) \tag{9}$$

This equation is known as the Smoluchowski equation! This is smart since from the continuity equation, if we assume that no mass is generated, we have:

$$\partial_t p(\mathbf{r}, t) = \nabla \cdot \mathbf{J}(\mathbf{r}, t) \tag{10}$$

This means that we can identify the flux as:

$$\mathbf{J}(\mathbf{r}, t) = \Big(\nabla D(\mathbf{r}) - \frac{1}{\gamma} \mathbf{F(r)} \Big) p(\mathbf{r}, t) \tag{11}$$

This can also be identified if we express the fraction of particles (P(t)) inside a small subvolume Ω_0. This is of course the integral over the

$$P(t) = \int_{\Omega_0} d\mathbf{r}^3 p(\mathbf{r}, t) \tag{12}$$

We are interested in the rate of change for this so we take the time derivative:

$$\partial_t P(t) = \int_{\Omega_0} d\mathbf{r}^3 \partial_t p(\mathbf{r}, t) = \int_{\Omega_0} d\mathbf{r}^3 \nabla \cdot \Big(\nabla D(\mathbf{r}) - \frac{1}{\gamma} \mathbf{F(r)} \Big) p(\mathbf{r}, t) \tag{13}$$

Now using Gauss theorem, stating that $\int_V \nabla \cdot f dV = \int_S f \cdot \vec{n} dS$ we obtain:

$$\partial_t P(t) = \int_{\Omega_0} d\vec{\mathbf{a}} \Big(\nabla D(\mathbf{r}) - \frac{1}{\gamma} \mathbf{F(r)} \Big) p(\mathbf{r}, t) \tag{14}$$

This is exactly the about of change in the fraction of particles inside a subvolume, and the amount that crosses the surfaces, in the integral, is exactly the flux. This is again equal to the definition of the flux above.

Fluctuation dissipation theorem

To advance any further, we will investigate the stationary solutions, which are for a great number a systems, typically a good approximation. The definition of the stationary solutions will be that there is no flux, i.e.

$$\mathbf{J}(\mathbf{r}, t) = 0 \tag{15}$$

Furthermore, in this regime, the probability distribution should obey the Boltzmann Distribution:

$$p(r) = \mathcal{Z} e^{-\beta U(\mathbf{r})} \tag{16}$$

Therefore we can insert this for the probability in the definition of the flux above and obtain (dropping the time dependency, since we are looking for stationary solutions):

$$\mathbf{J}(\mathbf{r}) = \Big(\nabla D(\mathbf{r}) - \frac{1}{\gamma}\mathbf{F}(\mathbf{r})\Big)\mathcal{Z}e^{-\beta U(\mathbf{r})} = 0 \tag{17}$$

If we now only consider the first term we calculate:

$$\nabla D(\mathbf{r})\mathcal{Z}e^{-\beta U(\mathbf{r})} = \mathcal{Z}e^{-\beta U(\mathbf{r})}\nabla(D(\mathbf{r})) + D(\mathbf{r})\mathcal{Z}e^{-\beta U(\mathbf{r})}(-\beta\nabla U(\mathbf{r})) \tag{18}$$

$$= \mathcal{Z}e^{-\beta U(\mathbf{r})}\Big(\nabla D(\mathbf{r}) - D(\mathbf{r})\beta\nabla U(\mathbf{r})\Big) \tag{19}$$

$$= \mathcal{Z}e^{-\beta U(\mathbf{r})}\Big(\nabla D(\mathbf{r}) + D(\mathbf{r})\beta\mathbf{F}(\mathbf{r}))\Big) \tag{20}$$

If we insert this in the full expression for the flux we now have:

$$\mathbf{J}(\mathbf{r}) = \mathcal{Z}e^{-\beta U(\mathbf{r})}\Big(\nabla D(\mathbf{r}) + D(\mathbf{r})\beta\mathbf{F}(\mathbf{r})) - \frac{1}{\gamma}\mathbf{F}(\mathbf{r})\Big) = 0 \tag{21}$$

Since the Bolzmann prefactor can never be zero we obtain the relation:

$$\nabla D(\mathbf{r}) + D(\mathbf{r})\beta\mathbf{F}(\mathbf{r})) - \frac{1}{\gamma}\mathbf{F}(\mathbf{r}) = 0 \tag{22}$$

$$\Rightarrow \quad \nabla D(\mathbf{r}) = \mathbf{F}(\mathbf{r})\Big(\frac{1}{\gamma} - D(\mathbf{r})\beta\Big) \tag{23}$$

This is exactly the celebrated Fluctuation dissipation theorem, in a more general form that typically considered, since it includes the possibility of position dependent forces and diffusion coefficient. We note that if the diffusion coefficient is not dependent on position, we of course have $\nabla D(\mathbf{r}) = 0$ and this reduces to:

$$\frac{1}{\gamma} = D(\mathbf{r})\beta \tag{24}$$

$$\Rightarrow \quad \sigma^2 = 2k_B T\gamma \tag{25}$$

Where σ is the function in front of the noise term in the definition of the Langevin equation.
We note that with the fluctuation dissipation theorem, we can rewrite the flux. We have that:

$$\nabla(D(\mathbf{r})p) = D(\mathbf{r})\nabla p + p\nabla D(\mathbf{r}) = D(\mathbf{r})\nabla p + p\mathbf{F}(\mathbf{r})\Big(\frac{1}{\gamma} - \beta D(\mathbf{r})\Big) \tag{26}$$

Where the last equality was obtained by using the Fluctuation Dissipation theorem. If we now insert this in the expression for the flux we obtain:

$$J(\mathbf{r},t) = \Big(\nabla D(\mathbf{r}) - \frac{1}{\gamma}\mathbf{F}(\mathbf{r})\Big)p \tag{27}$$

$$= \Big(D(\mathbf{r})\nabla + \mathbf{F}(\mathbf{r})\Big(\frac{1}{\gamma}\Big) - \beta D(\mathbf{r}) - \frac{1}{\gamma}\mathbf{F}(\mathbf{r})\Big)p(\mathbf{r},t) \tag{28}$$

$$= D(\mathbf{r})\Big(\nabla - \beta\mathbf{F}(\mathbf{r})\Big)p(\mathbf{r},t) \tag{29}$$

Boundary Conditions

In order to find applicable solutions to the differential equation we describe as the Smoluchowski Equation, one needs to specify the Boundary conditions. We imagine that diffusion takes place at some space (i.e. inside the cell), and if we define a boundary condition where the probability can pass through, we have a reactive boundary condition that describes the possibility of a reaction. We remember that we stated above that the flux could be expressed as:

$$\mathbf{J}(\mathbf{r},t) = \Big(\nabla D(\mathbf{r}) - \frac{1}{\gamma}\mathbf{F}(\mathbf{r})\Big)p(\mathbf{r},t) \tag{30}$$

This means that we can define the flux operator as:

$$\mathcal{J}(\mathbf{r},t) = \Big(\nabla D(\mathbf{r}) - \frac{1}{\gamma}\mathbf{F}(\mathbf{r})\Big) \tag{31}$$

Since this operator acts on the probability function to give the flux. But this flux operator defines the spatial boundary conditions, since it allow us to measure the particle probability exchange at the surface of the space where the particles are diffusing. The two classical boundary conditions are 1) the reflective:

$$\mathbf{n} \cdot \mathcal{J}(\mathbf{r},t)p(\mathbf{r},t) = 0 \tag{32}$$

Here $\mathbf{n}$ is the normal vector to the surface, and this basically means that no flux will pass through the boundary and thus be completely reflective. The second possibility is the 2) reactive:

$$p(\mathbf{r},t) = 0 \tag{33}$$

This is equivalent to the absorption and it means that probability current will go through the boundary.
While these two are completely classical in many derivations it is however possible to consider a much more general version, that combines the two above. This is called the Robin boundary condition or the radiation boundary condition and takes the form:

$$\mathbf{n} \cdot \mathcal{J}(\mathbf{r},t)p(\mathbf{r},t) = \kappa p(\mathbf{r},t) \tag{34}$$

From this it is clear that the parameter κ defines whether it is reflective ($\kappa = 0$), reactive ($\kappa \mapsto \infty$) or partially reflective for any value in between these two extremes. This boundary condition will be the most realistic when we consider the situation of reactions between particles and molecules inside the cell.

On capture rates

With this formalism we are ready to derive the actual problem. We will describe the rate of capture for a diffusing molecule, that can get absorbed (i.e. react) with another molecule. We note that instead of considering the diffusion of both molecules, we can consider one of them as being stationary and let the diffusion coefficient be the sum of the two individual diffusion coefficients.
We consider the Smoluchowski equation in spatial coordinates. We assume there is no angular independence, and the D and $\mathbf{F}$ are now functions of a radial coordinate r, instead of the position vector $\mathbf{r}$. Now in the stationary state (where we drop the dependency on t) this takes the form:

$$0 = \nabla \cdot D(r)\Big(\nabla - \beta\mathbf{F}(r)\Big)p(r) \tag{35}$$

With the two boundary conditions:

1. $p(r \mapsto \infty) = c_1 c_2$
2. $D(R_0)\Big(\nabla - \beta\mathbf{F}(R_0)\Big)p(R_0,t) = \kappa p(R_0)$

Here the first boundary condition guarantees that away from the sphere of interest, there is a constant concentration of both species of molecules. The second is the so called Robin or radiation Boundary Condition as described in the section above. This describes the rate of absorption at the surface of a spherical binding site of radius R_0. Note that this radius is actually the sum of the two radii of the interacting molecules, but for our purposes this is not important. Here we have introduced the parameter κ that defines the absorbance of the binding site. For $\kappa \mapsto \infty$ this is a completely absorbing binding site, and for $\kappa = 0$ it is completely reflective. However we are interested in the intermediate regimes and will use thin Boundary Condition.
Integrating with respect to the volume and applying Gauss theorem we obtain:

$$\int_V \nabla \cdot D(r)\Big(\nabla - \beta\mathbf{F}(r)\Big)p(r,t)dV = \int_S \mathbf{n} \cdot D(r)\Big(\nabla - \beta\mathbf{F}(r)\Big)p(r)dS \tag{36}$$

$$= 4\pi r^2 D(r)\Big(\nabla - \beta\mathbf{F}(r)\Big)p(r,t) \tag{37}$$

Now inserting the Boundary Condition 2), we see that the following equation must hold:

$$4\pi r^2 D(r)\Big(\nabla - \beta\mathbf{F}(r)\Big)p(r) = 4\pi R_0^2 \kappa p(R_0) \tag{38}$$

Also we note that we can rewrite the first term as:

$$4\pi r^2 D(r)\Big(\nabla - \beta\mathbf{F}(r)\Big)p(r) = 4\pi r^2 D(r) e^{-\beta U(r)}\partial_r(e^{\beta U(r)}p(r)) \tag{39}$$

Putting all this together we not get:

$$4\pi r^2 D(r) e^{-\beta U(r)}\partial_r(e^{\beta U(r)}p(r)) = 4\pi R_0^2 \kappa p(R_0) \quad \Leftrightarrow \tag{40}$$

$$\partial_r(e^{\beta U(r)}p(r)) = \frac{R_0^2\kappa}{r^2 D(r)} e^{\beta U(r)} p(R_0) \tag{41}$$

Integrating on both sides, from R_0 to ∞ we obtain:

$$e^{\beta U(\infty)}p(\infty) - e^{\beta U(R_0)}p(R_0) = \int_{R_0}^{\infty} \frac{R_0^2\kappa}{r^2 D(r)} e^{\beta U(r)} p(R_0) dr \tag{42}$$

$$c_1 c_2 = p(R_0) R_0^2 \kappa \int_{R_0}^{\infty} \frac{1}{r^2 D(r)} e^{\beta U(r)} dr + e^{\beta U(R_0)} p(R_0) \tag{43}$$

$$c_1 c_2 = e^{\beta U(R_0)} p(R_0)\Big(e^{-\beta U(R_0)} R_0^2 \kappa \int_{R_0}^{\infty} \frac{1}{r^2 D(r)} e^{\beta U(r)} dr + 1\Big) \tag{44}$$

$$\frac{c_1 c_2}{\Big(e^{-\beta U(R_0)} R_0^2 \kappa \int_{R_0}^{\infty} \frac{1}{r^2 D(r)} e^{\beta U(r)} dr + 1\Big)} e^{-\beta U(R_0)} = p(R_0) \tag{45}$$

We remember that the total radial current into the partially absorbing sphere (i.e. the flux integrated over the surface of the partially absorbing sphere) is equivalent to the rate of absorption:

$$I_{rad} = k^* = 4\pi R_0^2 \kappa p(R_0) = 4\pi R_0^2 \kappa \frac{c_1 c_2}{\Big(e^{-\beta U(R_0)} R_0^2 \kappa \int_{R_0}^{\infty} \frac{1}{r^2 D(r)} e^{\beta U(r)} dr + 1\Big)} e^{-\beta U(R_0)} \tag{46}$$

However normally we define the actual on-rate as a constant multiplied by the (probability) concentrations of the two interacting molecules: $k^* = k^+ c_1 c_2$. Therefore removing the dependencies on c_1 and c_2 we arrive at:

$$k^+ = \kappa \frac{4\pi R_0^2}{\Big(e^{-\beta U(R_0)} R_0^2 \kappa \int_{R_0}^{\infty} \frac{1}{r^2 D(r)} e^{\beta U(r)} dr + 1\Big)} e^{-\beta U(R_0)} \tag{47}$$

$$= \frac{4\pi}{\Big(\int_{R_0}^{\infty} \frac{1}{r^2 D(r)} e^{\beta U(r)} dr + \frac{e^{\beta U(R_0)}}{R_0^2 \kappa}\Big)} \tag{48}$$

Limits of interest for capture rates and specific examples

In the previous section we arrived at the on-rate for two interacting spheres. This expression we will now simplify assuming specific limits.
First we assume that $\kappa \approx 0$ and get:

$$k^+_{\kappa\approx 0} = \frac{4\pi}{\Big(\frac{e^{\beta U(R_0)}}{R_0^2\kappa}\Big)} = 4\pi R_0^2 \kappa e^{-\beta U(R_0)} \tag{49}$$

We note that this is exactly the Arrhenius equation. That this arise in this limit makes sense, since we defined the sphere to be almost reflecting and the dependency on diffusion vanishes, whereas the surrounding potential we be "felt" by the particle, since it will spend much time around this potential before absorption.
Next we assume that we have no potential (i.e. $U(r) = 0$) and a constant diffusion coefficient (i.e. $D(r) = D_0$). Here we get:

$$k^+ = \frac{4\pi}{\int_{R_0}^{\infty} \frac{1}{r^2 D_0} dr + \frac{1}{R_0^2 \kappa}} = \frac{4\pi D_0 R_0}{1 + \frac{D_0}{R_0 \kappa}} \tag{50}$$

We see that we here arrive at Diffusion limited reaction rate ($k^+ = 4\pi D_0 R_0$) if we also assume that $\kappa \mapsto \infty$. We note here that the classical result derived by Berg and Purcell, where one assumes a surface of small absorbing disks lead to an on-rate of: $k^+_{BP} = 4\pi D R_0 \frac{Na}{\pi R_0 + Na}$, where a is the radius of the small disks covering the absorbing spheres. These two expressions are therefore equivalent if $\omega = \frac{NaD}{\pi R_0^2}$.

Temperature dependency

Now we are ready to define how we expect the rates should change according to a change in temperature. We have of course as standard that $\beta = \frac{1}{k_B T}$. We we start by considering the limit of low absorbing rate (i.e. $\kappa \approx 0$), where we denote $U(R_0) = E$ as the activation energy and $4\pi R_0^2 \kappa = A$ as an activation constant.With this we have the on rate given by:

$$k^+_{\kappa \approx 0} = Ae^{-\beta E} \tag{51}$$

Now differentiating with respect to temperature gives:

$$\frac{\partial k^+}{\partial T} = Ae^{-\beta E}\frac{E}{k_B T^2} = k^+ ln(\frac{1}{k^+})\frac{1}{A}\frac{1}{T} \tag{52}$$

Now assuming linearity around the value of T, we can rewrite the differential equation into a difference equation:

$$\frac{k^+_n - k^+_0}{T_n - T_0} = k^+_0 ln(\frac{1}{k^+_0})\frac{1}{A}\frac{1}{T_0} \qquad \Leftrightarrow \tag{53}$$

$$k^+_n = k^+_0\Big(1 + ln(\frac{1}{k^+_0})\frac{1}{A}\frac{\Delta T}{T_0}\Big) \tag{54}$$

Here we note that we have no direct knowledge of the constant A, but since $e^{-\beta E} = 1$ for $E = 0$, we know that this should not exceed the value of the rate itself.
Next we consider the case of diffusion limited reactions. This is the other limit in the equations above, where we also assume there is no potential. Here we arrived at the maximal rate:

$$k^+ = 4\pi D_0 R_0 \tag{55}$$

If we apply the Einstein-Stokes relation we have the temperature dependency in D_0 with

$$D_0 = \frac{k_B}{6\pi\eta r}T \tag{56}$$

This means that the rate would simply follow the temperature as:

$$\frac{k^+_n - k^+_0}{T_n - T_0} = 4\pi R_0 \frac{k_B}{6\pi\eta r} \qquad \Leftrightarrow \tag{57}$$

$$k^+_n = k^+_0\Big(1 + \frac{\Delta T}{T}\Big) \tag{58}$$

1. The NF-kB system

In this model, we consider the NF-κB inside the nucleus (N_n), acting as a transcription factor for many proteins, including I-κB. The equations take the following form:

$$\dot{N_n} = k_{Nin}(N_{tot} - N_n)\frac{K_I}{K_I + I} - k_{Iin} I \frac{N_n}{K_N + N_n} \tag{59}$$

$$\dot{I_{RNA}} = k_t N_n^2 - \gamma_m I_{RNA} \tag{60}$$

$$\dot{I} = k_{tl} I_{RNA} - \alpha I K K_a (N_{tot} - N_n)\frac{I}{K_I + I} \tag{61}$$

$$\dot{IKK_a} = k_a \cdot TNF \cdot IKK_n - k_i IKK_a \tag{62}$$

$$\dot{IKK_i} = k_i IKK_a - k_p IKK_i \frac{k_{A20}}{k_{A20} + [A20] \cdot TNF} \tag{63}$$

$$IKK_n = [IKK]_{tot} - IKK_a - IKK_i \tag{64}$$

$$TNF = 0.5 + A\sin(\frac{2\pi}{T}t) \tag{65}$$

Here, N_n is the nuclear NF-κB concentration, I_m is the IkB mRNA level, and I is the concentration of cytoplasmic I-κB protein.
All the parameters used in the NF-κB model are found in the table below.

Parameter in paper	Default value
k_{Nin}	5.4 min^{-1}
k_{Iin}	0.018 min^{-1}
k_t	1.03 $(\mu\text{M})^{-1}.\text{min}^{-1}$
k_{tl}	0.24 min^{-1}
K_I	0.035 μM
K_N	0.029 μM
γ_m	0.017 min^{-1}
α	1.05 $(\mu\text{M})^{-1}.\text{min}^{-1}$
N_{tot}	1. μM
k_a	0.24 min^{-1}
k_i	0.18 min^{-1}
k_p	0.036 min^{-1}
k_{A20}	0.0018 μM
$[IKK]_{tot}$	2.0 μM
$[A20]$	0.0026 μM

TABLE I: Default values of parameters in the model. Here we assume that the slowest rates are governed by the Arrhenius equation, whereas the fastest rates will follow the temperature dependency of the Smoluchowski rate

We will in the following briefly describe the different terms in the model:

- In the equation for $\dot{N_n}$, the first term models the import of NF-κB into the nucleus, which is inhibited by NF-κB-IκB complexes formed in the cytoplasm. The second term models the formation of these complexes in the nucleus followed by their export into the cytoplasm.
- The equation for I_{RNA} describes the NF-κB activated transcription of IκB m_{RNA} and the spontaneous degradation of the m_{RNA} with a half-life of $ln(2)/\gamma_m$.
- The first term in the equation for IκB models translation of IκB m_{RNA} into IκB protein in the cytoplasm, and the second term models the TNF-triggered degradation of IκB in the cytoplasm when it is bound to NF-κB.
- The triggering stimulus TNF, acts by changing the level of active IκB kinase, $[IKK_a]$, which phosphorylates IκB, resulting eventually in its degradation. This degradation rate is set by the parameter α in the model. It is thus only this protein complex with IKK that can phosphorylate the NF-κB - I-κB complex and make NF-κB active again.

This model assumes that there is a constant amount of IKK (IKK_{tot}), which can be in three states: active (IKK_a), inactive(IKK_i) and neutral ($IKK_{tot} - IKK_a - IKK_i$). TNF increases the rate at which neutral IKK is made active, and decreases the rate at which inactive IKK is made neutral